Obscuration, Environments and Host Galaxies of Active Galactic Nuclei.

Jack Mayo

A thesis submitted in fulfilment of the requirements
for the degree of Doctor of Philosophy
to the
University of Edinburgh
May 2014

Lay Summary

The bulk of this work involves the study of the centre of galaxies where supermassive black holes exist (called AGN). There are features which are present in a subset of these AGN which do not exist in others, however, the unified model states that all AGN are intrinsically the same and that the lack of these particular observational features is a result of obscuration. The population statistics of these "obscured"AGN appears to change depending on the regime in which they are observed; in the X-ray regime for instance, it appears that obscured AGN are more common at low luminosities and less common at high luminosities, while in the infrared regime it appears that obscured AGN make up a fixed percentage of the total AGN population across all luminosities.

I develop a model to reproduce the observed trend in the X-ray regime by partially covering the X-ray sources in these AGN with thick material. I argue that the effect of this thick material can go unnoticed and therefore not be corrected for. Using this model it is possible to reproduce the observed trend in the X-ray vs. Infrared luminosity of these sources; both the X-ray and infrared luminosities of these bright sources are thought to measure the intrinsic power of the AGN, however, if the obscuration in the X-ray regime is unaccounted for then the X-ray luminosity will not correlate well with the infrared luminosity; this is indeed what is seen. Many obscured AGN having lower "corrected" X-ray luminosities than predicted from their infrared luminosities. This model shows the consequences of inferring obscuration from crude observational data, and indeed shows how the observed X-ray luminosity dependence of the obscured fraction can simply be accounted for.

I also investigate the "obscured fraction" of AGN observationally by taking a sample selected purely by star formation related emission. I find a result consistent with no luminosity dependence of the obscured AGN fraction. I also find evidence to support the unified model detailed above; I find obscured and unobscured AGN to have similar stellar masses, dust masses and formation ages.

I also investigate the neighbours of the highest mass galaxies at between 10 and 12.5 billion years ago, These highest mass galaxies, with powerful radio emission can have profound effects on the surrounding environment and are believed to trigger star formation. Here, however, I find no correlation between the power of these radio jets and the number of neighbours these galaxies have.

Abstract

The work contained within this thesis
Is made up primarily of two pieces
Both address active galactic nuclei
And the galaxies that live nearby
The obscured fraction of the population
Is the topic of one publication
And the type-II fraction in the optical regime
In chapter four this is the theme
I research the vicinity overdensity
Around radio galaxies in chapter three, you'll see
I reduce some spectra at redshift one
But not all observations in the end got done
With the spectra I have I do what I can
As if all target observations had actually ran
In the end I conclude with results and the theme
of research to be done further downstream.

The works contained herein addresses two major topics in extragalactic astrophysics, namely the Type-II AGN fraction and the Overdensity-Radio power relation.

Quantifying the Type-II AGN fraction has been attempted by many works in many different observational regimes, finding rather contrasting results. Accretion onto supermassive black holes contributes between 5 per cent and 20 per cent of the luminosity of the Universe, and seems to be closely linked to star formation processes. The large uncertainty on this value is due to the ill-determined contribution from obscured accretion, namely the Type-II fraction.

In Chapters 3 and 4 I address this issue from a theoretical standpoint in the X-ray regime and an observational standpoint in the optical regime respectively.

In Chapter 3 I show how crude X-ray spectroscopy of partially obscured AGN can lead to catastrophic underestimations of the intrinsic X-ray luminosity of these sources. Acting over an entire population, these partial obscurers can produce an obscured AGN fraction which decreases as a function of observed luminosity. The results are consistent with observations in the X-ray vs. IR luminosity of AGN classes.

In Chapter 4 I select a statistically significant sample of AGN from an unbiased 250μm galaxy sample. After spectroscopic classification I find the optical Type-II AGN fraction to be consistent across several decades in `[OIII]` luminosity, a common proxy for intrinsic AGN luminosity. I also investigate the relation of AGN activity to host galaxy mass, as well as star formation activity and star formation history.

Probing the environments of protoclusters will help to constrain the models of structure formation in the Universe. Until now, no dataset has been big enough to probe the environments of high redshift radio galaxies at a statistical level; While many believe that the feedback processes of high luminosity radio jets will have a direct impact on star formation in the surrounding medium it has not been tested. In Chapter 2 I investigate this on an statistical level, finding no meaningful correlation between radio galaxy radio power and source overdensity in the vicinities of these sources.

In Chapter 5 I discuss the reduction of a 24μm sample at redshift $z \sim 1$ for direct comparison with a local 12μm sample. With only a fraction of the target sample being observed, no statistically significant results could be derived, but the objects are spectroscopically classified and spectroscopic redshifts are measured where possible. Correlations in the data set are investigated and the limitations of the sample selection strategy are discussed.

Declaration

Except where otherwise stated, the research undertaken in this thesis was the unaided work of the author. Where the work was done in collaboration with others, a significant contribution was made by the author.

Work contained within this thesis has been published in :

Mayo, J. H.; Vernet, J.; De Breuck, C.; Galametz, A.; Seymour, N.; Stern, D. *Overdensities of 24um Sources in the Vicinities of High-Redshift Radio Galaxies.* Astronomy & Astrophysics, 539, 33. **2012**.

Mayo; Jack. H., Lawrence, Andy. *The Effect of Partial Obscuration on the Luminosity Dependence of the Obscured Fraction in Active Galactic Nuclei.*. Monthly Notices of the Royal Astronomical Society. accepted. **2013**.

J. Mayo
May 2014

Acknowledgements

Throughout my studies and research which culminate in this work, there are a number of people who have contributed greatly not only to useful science conversations and advice, but also in the complete opposite. My sanity and hairline have been truly tested over the past 4 years. I would first like to thank Rebekah for all her love and support throughout, and for putting up with my absent mindedness.

I would also like to thank Andy for all of his support and patience with me over the years, especially for his tutorials and constructive feedback throughout.

Thanks to my immediate family, and especially to Mum and Dad for keeping my down to earth; I hope to spend more time seeing you in the future than I have afforded over the last years.

I would also like to *big up* the Vista-Huts Massive for enduring crow battles, Hurricane Bawbag and the brutal murder of innocent bunnies, as well as for turning up the Christmas songs up to 11.

I thank Victoria Bruce and Vinodiran Arumugam for their tip-top conversation and supply of biscuits over my final year[1] in the Ultra-Vista corridor (which views an equalling area of the sky as our office). Also, thanks for putting up with my inane conversations about fish and reptiles.

Thanks to Paula Wilkie and John Barrow for their administrative and computational support respectively, and also thanks to Paula for showing me how poor my grasp on cryptic crosswords truly is.

I would like to thank Carlos De Breuck and Jöel Vernet for their supervisory roles during my visits to ESO. Thanks to Martin Elvis for useful conversations regarding partial obscuration during his visit to the ROE. Thanks for Kirpal Nandra and Avery Meiksin for constructive comments.

---

[1] though Sonday were always as good as Hit. Fact.

Thanks Henry Pearce, Trevor Back and David Harvey for horrendous chat, these made my lunch hours that which I will remember most about being at the ROE.

Cheers to Robert Menzies and Hannah Lester, for being great.

Slàinte

Contents

Chapter 1

Introduction

1.1 Outline

In this chapter, the reader will be taken through an overview of active galactic nuclei (AGN), from a brief outline of discovery through to a more in depth discussion of their observable features and the physics involved. I will describe the unified scheme, and show how this is capable of explaining a myriad of different features seen in different classes of object. I will detail the importance of AGN in the field of galaxy evolution and discuss some of the outstanding problems in the field.

1.2 Discovery of AGN

1.2.1 `NGC1068` and other Core Dominated Galaxies

As early as 1908, Edward Fath reported prominent emission lines within the *spiral nebula*, `NGC 1068` (Fath 1909). Unbeknown at the time, this "spiral nebula" was not within our galaxy but extragalactic; Fath was studying the core of another galaxy. Fath noted the remarkable spectral features in this *nebula* as being quite unlike any other he had observed. Instead of having the absorption features commonly associated with unresolved stellar populations, `NGC1068` was dominated by emission lines, much more commonly associated with planetary nebulae.

Over the following years (1917-1930), Vesto Slipher, Edwin Hubble and Milton

Humason obtained spectra of much greater detail of `NGC 1068` and other similar objects; `NGC1275`, `NGC 4051` and `NGC 4151` (Slipher 1917, Hubble 1926) [1].

In 1943, Karl Seyfert undertook a spectroscopic study of six core-brightened spiral galaxies, the results of which were compelling; Seyfert noted high-excitation emission lines emanating from luminous semi-stellar nuclei at the galactic centres. These high-excitation lines were broader than the (also present) absorption lines, and in some cases the Balmer series of lines (Hα, Hβ, Hγ, …) were much broader even than other high excitation lines. The narrower set of emission lines were observed from both permitted and forbidden lines such as the Balmer series and [OIII], [NII] & [SII].

The importance of this seminal work is reflected in the fact that this class of objects have now become his eponym; the Seyfert Galaxies.

1.2.2 `3C273` and Other Quasars

In the 1930s, Karl Jansky serendipitously detected a radio signal from the centre of the Galaxy, in the Sagittarius constellation (Jansky 1933). Further pioneering observations during the 1930's and 1940's led to the detection of the Sun in the radio regime (Hey, 1943) and the first radio map of our galaxy (Reber, 1938; unpublished).

By 1960 the Third Cambridge Radio Survey (Edge et al. 1959) was published, cataloguing some 471 radio sources. At that time the nature of many of these sources remained a mystery, but gradually optical counterparts were found. One of the first radio sources for which an optical counterpart was found was `3C48`. In the optical regime `3C48` was found to be very blue (Matthews and Sandage 1963), but the stellar nature of the object led the authors to believe that the object was galactic.

`3C273`

In 1963, Hazard et al. identified an optical counterpart to the radio source `3C273` via lunar occultation, a method which uses the lunar position as it occults the source to measure the location of the radio source to a higher level of accuracy. The optical counterpart to `3C273` was also found to be quasi-stellar in nature,

---

[1] Note that by 1926 a consensus was formed as to the existence of galaxies outside of our own

just like `3C48` discovered prior. In the same year, Schmidt obtained a spectrum of this source. The optical spectrum of `3C273` was quite peculiar; not only was it redshifted (at $z = 0.158$), but it also had broad permitted emission lines, and both permitted and forbidden narrow lines, much like those seen in the Seyfert Galaxies. The Balmer series of lines in the `3C273` spectrum exhibit average linewidths (full width half maximum) of $\sim 4000 \mathrm{km\,s^{-1}}$, if the broadening is interpreted as a velocity dispersion (Oke 1965).

Arguments were put forward for two alternative explanations of this quasi-stellar radio source. Either `3C273` was a intragalactic stellar object with a large gravitational redshift, or else `3C273` was an extragalactic source, exhibiting cosmological redshift associated with recession (Schmidt 1963). Arguments put forward for a galactic, gravitationally redshift object would have constrained the size of the object to $\sim$ 10km and would have relied on both permitted and forbidden lines coming from a coincident medium; these arguments were swiftly rejected in favour of the extragalactic regime which held no such constraints.

Further work throughout the 1970's and 1980's found a vast array of bizarre extra galactic objects, including many like `3C273`, which were coined *Quasars* (from QUAsi-StellAr Radio Source). Other objects hosting these *nebular* emission lines but lacking the broad lines seen in quasars were also found.

Work undertaken by Khachikyan and Weedman (1971) was the first to classify broad line objects and narrow line objects as two sub-classes of Seyfert galaxies, called Type-I and Type-II respectively, purely based on line widths. Around the same time, unification of the Seyferts and Quasars was also being discussed (e.g. Lynden-Bell 1971, Weedman 1973)

For many years radio quiet (see Section 1.3.2) Type-II Quasars remained largely undetected, though their existence was suggested by the presence of radio loud counterparts (Lawrence 1991). The reason for the dearth of these objects lay in the fact that they are dominated by narrow lines in the optical, and so are not very bright, they are obscured in the soft X-ray, and are not prominent in the radio regime.

The established understanding is that Seyfert galaxies and Quasars are the same phenomena manifesting at very different scales in luminosity. As such, they are grouped together under the umbrella of Active Galactic Nuclei (AGN). The Type-I Quasars and Seyfert-I's possess broad permitted lines in their spectra and are occasionally referred to *broad line objects*. The Type-II Quasars and Seyfert-II's lack broad permitted lines in the unpolarised spectra and are occasionally referred to as *narrow line objects*.

1.3 Emission in AGN - Observations and Classification

1.3.1 Optical/UV

The Big Blue Bump - In the spectra of Type-I AGN, the most prominent feature in the Spectral Energy Distribution (SED) is a "thermal" spectral feature peaking in the UltraViolet (UV, at $\nu L_\nu \sim 1100$Å). This feature is inconsistent with a single temperature blackbody spectrum, but is often approximately fit by a series of blackbody spectra at a range of temperatures. This feature is commonly referred to as the *Big Blue Bump* (BBB).

The Broad Line Region (BLR) - The broad emission lines - most prominently the Balmer series lines - emanate from an unresolved region at the centre of AGN. A lower density limit for the BLR is constrained by the lack of observed broad forbidden lines, which are suppressed in sufficiently dense media due to collisional de-excitation (this is species dependent, but typical critical densities are around $n_c \sim 7 \times 10^5$ cm^{-3}, for `[OIII]`). Relative strengths of emission lines in the BLR suggest a temperature of $\sim 10^4$K, though this is poorly constrained.

Hidden Broad Line Objects - Spectropolarimetric observations of `NGC 1068` in 1985 (Antonucci and Miller 1985) led to the discovery of "hidden" broad Balmer lines in an otherwise archetypal Type-II AGN. This observation showed for the first time that Type-I and Type-II AGN were intrinsically very similar, supporting that claims that some mechanism or morphological difference made them appear different to the observer such as a medium capable of scattering broad line emission into the observers line of sight.

The Narrow Line Region (NLR) - The narrow emission lines - from both permitted and forbidden species - emanate from resolvable regions extending

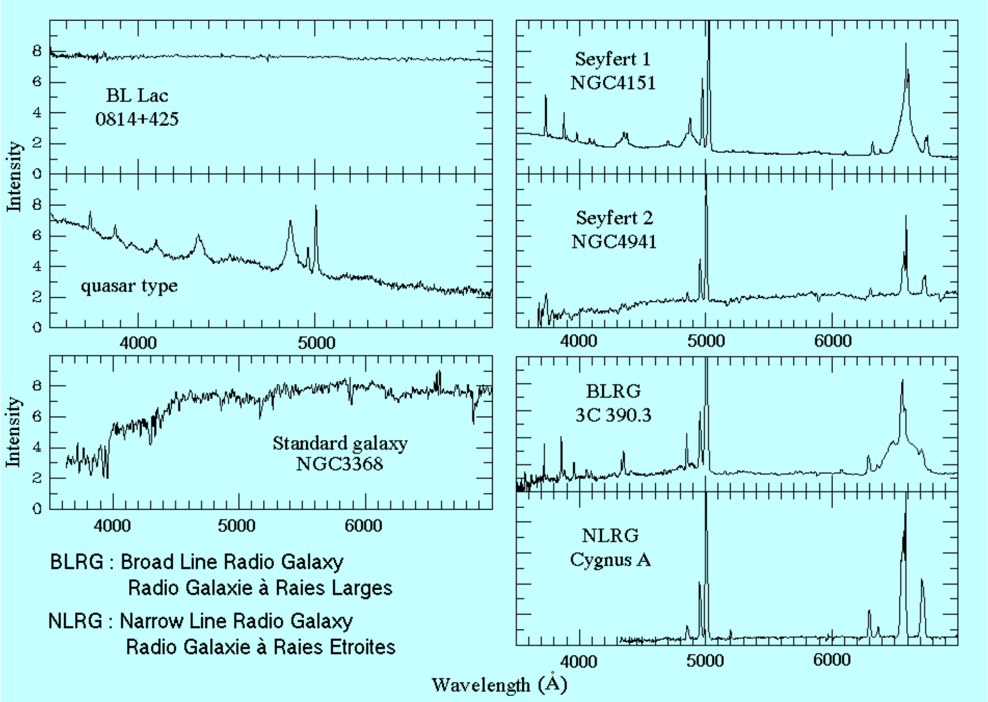

Figure 1.1: Optical spectra from sub-classes of AGN. Note that all have strong emission lines (bar the BL Lac object). The spectrum of a normal galaxy with characteristic 4000Å break is also shown. Credit Maran (1992).

beyond the central AGN. The morphology of these NLRs is very messy, but in the cleanest cases is approximately bi-conical in shape, centred on the AGN. The presence of forbidden lines such as `[OIII]` (`[NII]`) indicate very low density media with densities below $n = 7 \times 10^5$ cm^{-3} ($n = 6.6 \times 10^{-4}$ cm^{-3}) (Osterbrock and Ferland 2006).

Spectral Types - Figure 1.1 shows examples of the optical spectra of different classes of AGN, including the Seyfert classes and a Quasar (Maran 1992). One can see in the Quasar and Seyfert-I class objects broad Balmer series lines (most noticeably at Hβ (λ4861Å) and Hγ (λ4341Å)), while this broad feature is not observed in the Seyfert-II class object. The `[OIII]`($\lambda\lambda$4959Å, 5007Å) doublet longward of Hβ is present in all three subclasses. Notice the rise in continuum toward the blue end of the Quasar and Seyfert-I spectra. This is the BBB. Figure 1.2 shows the extended nature of the NLR in two AGN examples, tentatively showing a biconical shape in each source.

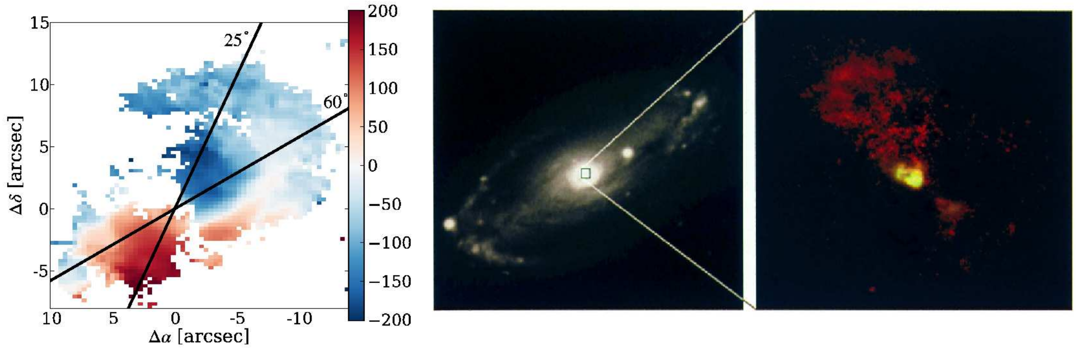

Figure 1.2: Left-hand subfigure shows the `[OIII]` ionisation cone for QSO HE1029-1401 from integral field data (Husemann et al. 2010) while the right-hand subfigure shows the Hα+`[NII]` ionisation cone of Seyfert 2 galaxy NGC5728 from Hubble Space Telescope narrow band data (Wilson et al. 1993).

1.3.2 Radio

Radio Loud vs. Radio Quiet

The two main classifications for AGN in the radio regime are Radio-Quiet, which is the most common population, and Radio-Loud, which are about ten times less common. The distinction between these two groups is usually made from the ratio between the radio and optical fluxes (5GHz and B-band flux (Kellermann et al. 1989)), though the issue of bimodality is still controversial in the literature (Ivezić et al. 2002, Jiang et al. 2007, Singal et al. 2011). Also note that this classification does not mean that Radio-Quiet AGN are radio silent. Indeed all AGN emit radio emission. One must be more careful in the Radio-Quiet regime when deriving AGN based characteristics since star formation related radio emission can heavily contaminate low luminosity AGN related emission.

Lobe Dominated vs. Core Dominated

A number of further classifications within the radio regime are morphologically based. One such morphology based classification is with regards to whether AGN are Lobe or Core Dominated (LD or CD). This classification depends on

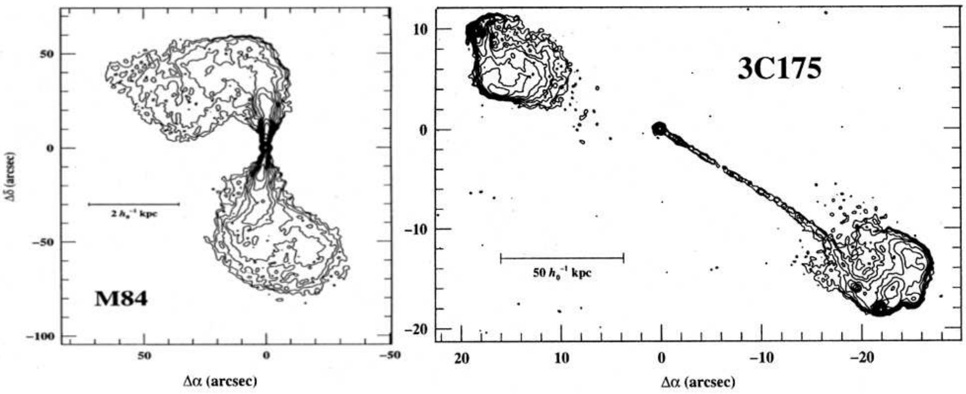

Figure 1.3: A comparison of a FR-I (M84; left-hand plot) and FR-II (3C175; right-hand plot) Radio Loud AGN. Credit Peterson (1997).

the extent and location of the radio emission. In CD objects the locus of radio emission is very close to the optical core of the host, whereas LD Quasars have bright characteristic jets emanating from a central location. This classification goes further in two respects; lobe morphology and spectral characteristics. The brightest region of the jets is usually either part way along bright radio jet or at the end of a faint jet; the radio emission comes from collimated jets travelling kiloparsecs into the Inter-Galactic Medium (IGM) with "radio lobes" at the jet termination. These termination points can extend up to megaparsecs from the central engine (in the case of `3C236`, a radio galaxy at $z = 0.1$ the lobes are separated by 4Mpc, some 36' on the sky).

The two classes of Radio Galaxy, i.e. those where the lobe is part way along the jet, and at the end of the jet are called Fanaroff-Riley I & II classes (FR-I & FR-II; Fanaroff and Riley 1974) respectively. While the FR-I's are usually associated with less luminous sources this association is not absolute, and it is believed that any characteristic boundary between the FR classes could be a function of optical luminosity (Owen and White 1991). Figure 1.3 shows examples of the two different FR classes.

Spectrally in the radio regime, AGN are classified as either flat or steep. These two classes are commonly referred to as *Flat Spectrum Radio Quasars* - FSRQs, $\alpha \leq 0.5$ and *Steep Spectrum Radio Quasars* - SSRQs, $\alpha > 0.5$ (where $f_\nu \propto \nu^{-\alpha}$). The flat spectrum AGN are usually associated with CD AGN, and the steep spectrum AGN are usually associated with LD AGN. In the extreme case that the radio jets are aligned directly along the line of sight, the radio emission is Doppler boosted, resulting in a Blazar/BL Lac type object.

1.3.3 X-ray

The early space-based X-ray satellites (e.g. UHURU, Ariel V), operating between ~ 2 keV - ~ 40 keV cataloged hundreds of galactic and extragalactic sources; pioneering observations of AGN `NGC 4151` and `NGC 1275` (Gursky et al. 1971) using the Uhuru Satellite[2] and just as significantly, a non-detection of X-ray emission from `NGC 1068` led the foundations of much work to come in this area. Elvis et al. (1978) showed X-rays to be a common feature in AGN.

AGN Spectra

The archetypal unobscured AGN X-ray spectrum is dominated by a power law extending from the keV energy regime up to a cutoff typically of energies higher than 100keV. The power law slope in the X-ray is typically $\alpha = 0.5 - 1.5$ where $I_\nu \propto \nu^{-\alpha}$ (Nandra and Pounds 1994, Reeves and Turner 2000, Risaliti 2004, Page et al. 2005, Krolik 1999) is typical of a synchrotron spectrum.

Overlayed upon this power law spectrum is a feature rising (in νL_ν) around 10keV, peaking $\sim 30 - 40$keV before rolling off at higher energies:

With photoelectric absorption having a much greater cross-section than electron scattering below $\sim$ 10keV, below these energies most electron-scattered photons get absorbed. However, above $\sim$ 10keV the photoelectric absorption cross-section falls away and electron-scattered photons can escape. Around the Klein-Nishina limit ($>$ 40keV) photons impart a significant recoil to an electron during scatter, which creates a hot electron medium. Further incoming photons will be Compton or Inverse Compton scattered depending on their frequency relative to the hot electron temperature, but since with the underlying power-law spectrum there is a far greater quantity of lower energy photons, the statistics work in the favour of inverse-Compton scattering, causing a build up of emission around the characteristic peak. Observationally this is around $30 - 60$keV and is

---

[2] two of only 339 X-ray sources detected in the two-year lifetime of Uhuru

referred to as the “Compton hump”.

At these energies, obscuration by a medium of Compton thick material has less effect on the photons and so the inner morphology has less of an effect on the X-ray spectra at these energies (see e.g. Murphy and Yaqoob 2009, which shows the effect of column densities between $N_H = 5 \times 10^{23}$ and $N_H = 10^{25}\mathrm{cm}^{-2}$ over a range of observer lines-of-sight).

As technology and instrumentation improves, the $10 - 100$keV will become increasingly important for detection of AGN that are otherwise obscured at lower X-ray energies. The Compton hump is found to be less significant at high redshifts and high luminosities (Reeves and Turner 2000, Shemmer et al. 2008) but is very important in the lower luminosity Seyferts. The presence of this Compton hump plays a vital role in constraining the AGN population with XRB statistics at hard X-ray energies where the XRB has yet to be resolved.

The Iron Kα (Fe Kα) line at 6.4keV is present in the X-ray spectrum of almost all AGN. It is a fluorescent line of an L $\rightarrow K$ shell electron transition (atomic orbital levels 2-1) where an X-ray photon ionises the atom from the L shell, an outer electron fills this energy state and emits a photon equal to the transition energy (E_t) of the electron (Barr et al. 1985). Theoretically there are several lines making up the observable Fe Kα complex, but X-ray spectrographs lack the resolution to deblend them. Rather, the Fe Kα complex can often become heavily distorted due to gravitational redshifting, doppler broadening, and boosting. The dominant feature has a typical width (FWHM) of $\sim$ 1000-17000$km\,\mathrm{s}^{-1}$ (e.g. Yaqoob and Padmanabhan 2004).

The X-ray “Compton hump” component along with the Fe Kα line can be understood together by considering the X-ray power law illuminating a slab of “cold” gas, that is, a gas that is sufficiently cool to keep metals mostly neutral, but with H and He mostly ionised. Upon entering the slab X-ray photons can undergo either Compton scattering or photoelectric absorption (followed by fluorescent line emission or Auger de-excitation) and so the photon is either scattered out of the slab, can escape the slab (as a fluorescent line photon) or get destroyed by Auger de-excitation.

Many AGN spectra rise smoothly (in νL_ν) over power law extrapolations below $\sim$ 1keV. This feature is known as the “soft excess” above the underlying power law continuum. This soft excess is generally featureless and appears to be a continuum component. However, extrapolating this soft excess as a thermal continuum does not fit well with observations in the extreme UV and does not correlate with disc temperature (Done et al. 2007, Gierliński and Done 2004). Some models fit the soft excess by asserting that Compton upscattering of the thermal disc creates these soft X-rays (e.g. Done and Nayakshin 2001, Done et al. 2012).

The archetypal “obscured” AGN spectrum shows signs of attenuation at the softer X-ray energies, dominated by photoelectric and Thomson scattering processes. The degree of absorption/scattering is dependent on the gas density along the line of sight. The column density in the ISM ranges greatly depending on the line of sight, but is typically $\mathrm{N_H} \sim 10^{20} - 7\times10^{22}$ cm^{-2} (Wakker and Mathis 2000, Willingale et al. 2013) while measured column densities in obscured AGN X-ray spectra measure a broad range between $10^{22} < \mathrm{N_H} < 10^{24}$ cm^{-2}, and beyond. Column densities beyond 10^{24} cm^{-2} are described as Compton thick, as they will completely attenuate photons in the < 10keV X-ray regime. X-ray telescopes capable of probing high energies have revealed thousands of obscured AGN that have previously gone undetected, from their “Compton hump” emission (Tozzi et al. 2001, Alexander et al. 2003, Hasinger 2004, Tueller et al. 2010, Burlon et al. 2011, Corral et al. 2011). Whilst the X-ray unobscured and obscured classes often correspond to optical Type-I and Type-II objects respectively, the populations are not perfectly congruent.

The X-ray absorbing regions can broadly be divided in two regions, the compact nuclear region at less than 10pc from the central source (based on short timescale variability; Ives et al. 1976, Warwick et al. 1988), and an extended medium further out (e.g. Maiolino and Rieke 1995).

The Compton thick absorption seen in a number of AGN implies a absorber column density of $N_H > 10^{24}$cm^{-2}; such a column density cannot exist beyond these inner regions since if they were to reach out to 100pc the mass of the obscurer would exceed the galactic mass (Risaliti et al. 1999).

As previously mentioned, the presence of this X-ray obscuring region (XOR) is not necessarily congruent with optical absorption features; in many cases objects classified as bona fide Type-I objects optically show signs of heavy attenuation in the X-ray (e.g. Wilkes et al. 2002, Szokoly et al. 2004, Barger and Cowie 2005). This detail will become important when I discuss the unified scheme below. The nature of nuclear absorption will be discussed in greater detail in Chapter 3.

As for the extended obscuration; this is a constant varying feature in many AGN, with column densities $N_H \sim 10^{21} - 10^{22}\text{cm}^{-2}$. In many sources this obscuration is often attributed to galactic scale dust lanes.

The X-ray Background

The X-ray Background (XRB) was detected some three years prior to measurements of the Cosmic Microwave background (CMB; Penzias and Wilson 1965). However, unlike the CMB predictions (Doroshkevich and Novikov 1964) no predictions of ubiquitous, extrasolar X-ray emission had previously been made.

The XRB was initially unresolved due to crude collimation and shallow depth of observations with early instruments, and early theories proposed that the XRB came from the diffuse hot Intergalactic Medium (IGM) due to its emission profile fitting well with a bremsstrahlung profile within the limited energy range and resolution. This theory didn't fall out of favour until the COBE satellite, launched in 1990 dismissed the hot IGM model (Mather et al. 1990). Since this time, and with the advent of the XMM and Chandra space telescopes, much of the XRB has been resolved in the $0.5 - 10$keV range, with a large proportion of the emission attributed to AGN. A plot of the integrated XRB is shown in Figure 1.4.

1.3.4 Infrared Emission

Detections of AGN in the Infrared (IR) began in 1964 and 1967 when Johnson (1964) and Pacholczyk and Wisniewski (1967) observed considerable emission from `3C273` and `NGC1068` respectively. Subsequent observations of further AGN (Rieke 1978) made it apparent that IR emission was a common feature of AGN. The field expanded in earnest with the launch of the Infra Red Astronomical Survey (IRAS) telescope in 1983. The survey covered the entire sky in four mid-IR wavebands (12.5,25,60 and 100μm). Early observations fit a power-law to the

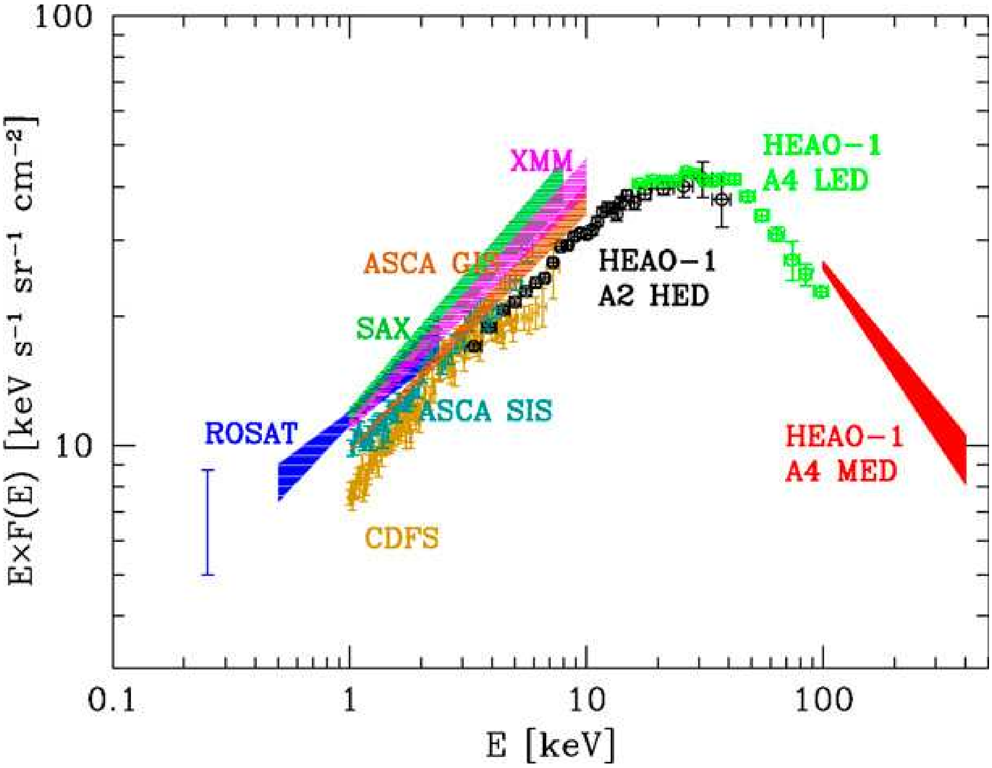

Figure 1.4: A plot of the extragalactic XRB from 0.2 - 400 keV. Different instruments are as labelled. Reference list and credit Gilli (2004).

AGN SED ($S_\nu \propto \nu^{-\alpha}$) around the waveband of the stellar peak, but as further and further data mounted it became apparent that the true IR-SED was much more like a thermal blackbody spectra, covering a wide range of temperatures, with $T_{\rm max}$ close to the dust sublimation temperature ($T\sim 1000-1500$K). Recent interferometric observations in the IR (Raban et al. 2009) have been able to infer a resolved oblate structure centred on the central source. In practice, modelling any such structure with a smooth topology is not a good fit to the IR data, which demands a range of media at different densities and temperatures in a clumpy fashion in order recreate the observed IR SED. This makes it possible to have small high density regions capable of attenuating high energy photons without exceeding the dynamical mass of the system. This is discussed in greater detail in Section 1.5.1.

The IR emission is believed to be a proxy for the true intrinsic luminosity of AGN unbiased by obscuration effects (like the optical/UV/X-ray regimes) or radio-loudness (like the radio regime). Numerous diagnostic techniques have been developed in the IR to separate the AGN from starbursts including IR colours (Lacy et al. 2004, Ivison et al. 2004, Stern et al. 2005, Jarrett et al. 2011), SEDs (Donley et al. 2007; 2010) as well as spectrally by a host of works (e.g. Weedman et al. 2006, Spoon et al. 2007, Polletta et al. 2008, Alexander et al. 2008).

Silicate Feature

One of the strongest mid-IR features observed in the galactic ISM and in AGN spectra is due to `Si-O` stretching and `O-Si-O` bending bonds in silicate materials. Within certain selection criteria, multiple observations of Type-I objects have found a 9.8μm peak in the mid-IR SED (Hao et al. 2005, Siebenmorgen et al. 2005, Sturm et al. 2005, Weedman et al. 2005), while low luminosity AGN display `Si-O` in absorption (Roche et al. 1991, Jaffe et al. 2004, Mason et al. 2003, Hao et al. 2007, Levenson et al. 2007). However, the picture is complicated since there has been emission observed in high luminosity Type-II objects (Sturm et al. 2006) to “mild absorption” found in low luminosity Type-I objects (Wu et al. 2009).
Early observations had insufficient spectral resolution to discern between the Si-O materials being detected, however more recent observations have been able to differentiate between those silicate materials usually seen in the InterStellar Medium (ISM; e.g. Olivine $Mg_{2x}Fe_{2-2x}SiO_4$) and a dominant feature in a

Type-II AGN `NGC1068`, Calcium Aluminium Silicate ($Ca_2Al_2SiO_7$), though any significance of this fact is still to be determined (see Li 2008, and references there in).

Polycyclic Aromatic Hydrocarbons

Polycyclic Aromatic Hydrocarbons (PAHs) are fused aromatic rings of carbon containing no heteroatoms or substituents i.e. the rings are purely Carbon atoms and the terminal bonds are purely Hydrogen atoms. PAHs typically consisting of between 10 and 20 Carbon atoms (e.g. Naphthalene: $C_{10}H_8$, Benzopyrene $C_{20}H_{12}$). It is interesting to note that PAH emission is generally absent in AGN spectra (Li 2008) whilst they are of huge importance to the mid-IR spectra of starburst galaxies (e.g. Valiante et al. 2007), so much so that they can lead to sample contamination when selecting from photometric bands in the mid-IR. PAH molecules are known to be depleted by high energy radiation, such as the X-ray radiation observed in AGN; this is also supported by that fact there is no 2175Å peak in the AGN dust attenuation curve (Gaskell et al. 2004), which is due to graphitic grains.

1.3.5 Multi-wavelength Studies

A very important characteristic of AGN is the fact that they can be luminous across many decades of frequency space from the Gamma regime all the way through to the Radio regime, especially bright in the X-ray, optical, IR and radio, depending on the class of source being observed. In fact with luminosities up to and in excess of 10^{46} erg s^{-1}, the Quasars are among the brightest objects in the Universe, which any feasible energy generation mechanism must address.

Figure 1.5 shows the X-ray-to-Radio SED for a Radio Loud Quasar, a Radio Quiet Quasar and a Seyfert galaxy. One can see the dominant emission in the X-ray (Compton hump), optical (BBB) and IR regimes, and the difference in the synchrotron emission between RL and RQ Quasars.

Many works use empirical relations in unobscured objects to infer the intrinsic properties of obscured objects, such as intrinsic X-ray luminosities from mid-IR

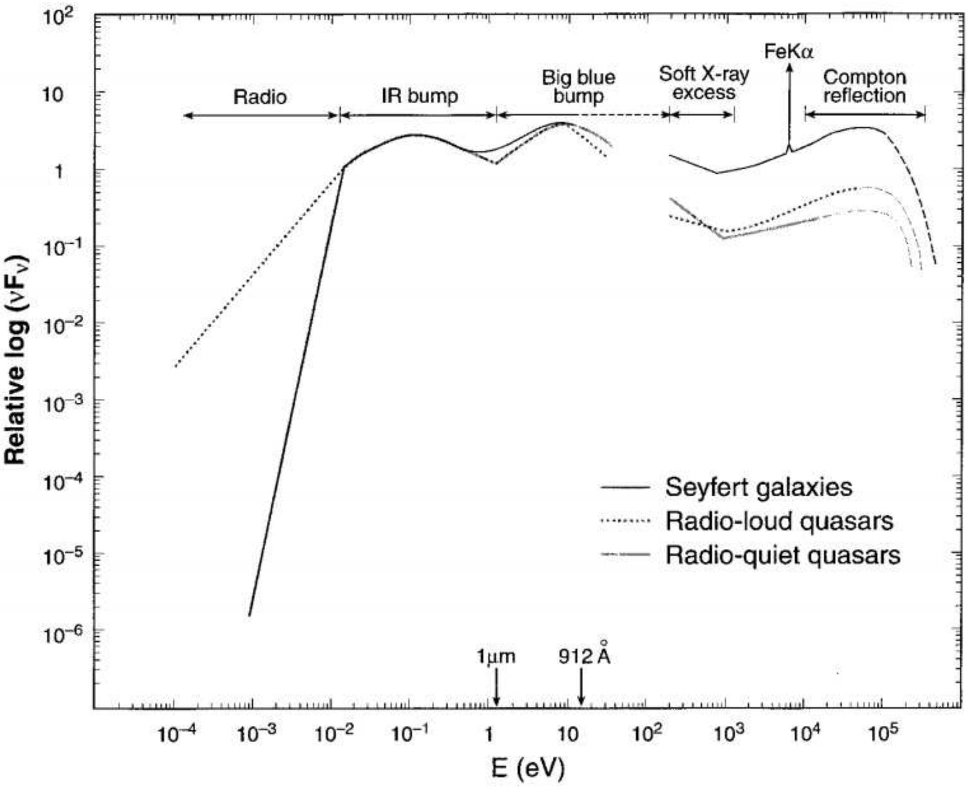

Figure 1.5: A model of the X-ray-to-Radio SED of a RL Quasar, a RQ Quasar and a Seyfert Galaxy. The peaks in the X-ray, optical and IR regimes dominate the distribution. Credit Koratkar and Blaes (1999).

luminosities (Gandhi et al. 2009, Lanzuisi et al. 2009, Asmus et al. 2011; 2013) as well as from the `[OIII]`λ5007Å luminosity (Mulchaey et al. 1994, Heckman et al. 2005). In order to characterise AGN, and the host galaxies of AGN, multi-wavelength data can help to decouple star-forming from AGN related emission.

1.3.6 Variability Studies

AGN, and particularly the Quasars are highly variable objects, especially in the optical and X-ray regimes. Any mechanism which creates photons in these regimes (and indeed, attenuates photons in these regimes) must be on sufficiently small physical scales to address this issue. Figure 1.6 shows the variability of three AGN in the X-ray, optical and radio regimes.

Since both Componisation and recombination can work simultaneously to produce X-ray photons from UV photons and vise-versa, this can complicate matters: Observations in the X-ray/UV marginally show a UV lag, thus supporting the underlying mechanism of X-ray variability as the source of UV variability (Breedt et al. 2010, Alston et al. 2013). However, X-ray variability is seen to correlate and lag with respect to IR variability (McHardy et al. 2007), thus the mechanism producing IR variability may be responsible for UV variability. This is briefly mentioned as an example of correlations between different observational regimes, and to show how any model will be complicated by different physical processes. The matter of X-ray variability lead and lag will not be discussed in any further detail in this work. The reader is referred to (Lawrence 2012) for a more in depth discussion.

1.4 Physics of the AGN and Origins of Emission

1.4.1 The Black Hole and Accretion Disk

As previously mentioned, Quasars can be extremely luminous (L$\sim 10^{46}$ erg s^{-1}) an order of magnitude brighter than the brightest galaxies, yet we know due to their variability timescales, of the order of hours, that they are relatively small. Thus we know we need a small and extremely efficient means of energy generation (Lynden-Bell 1969). Any structure capable of energy generation on this scale

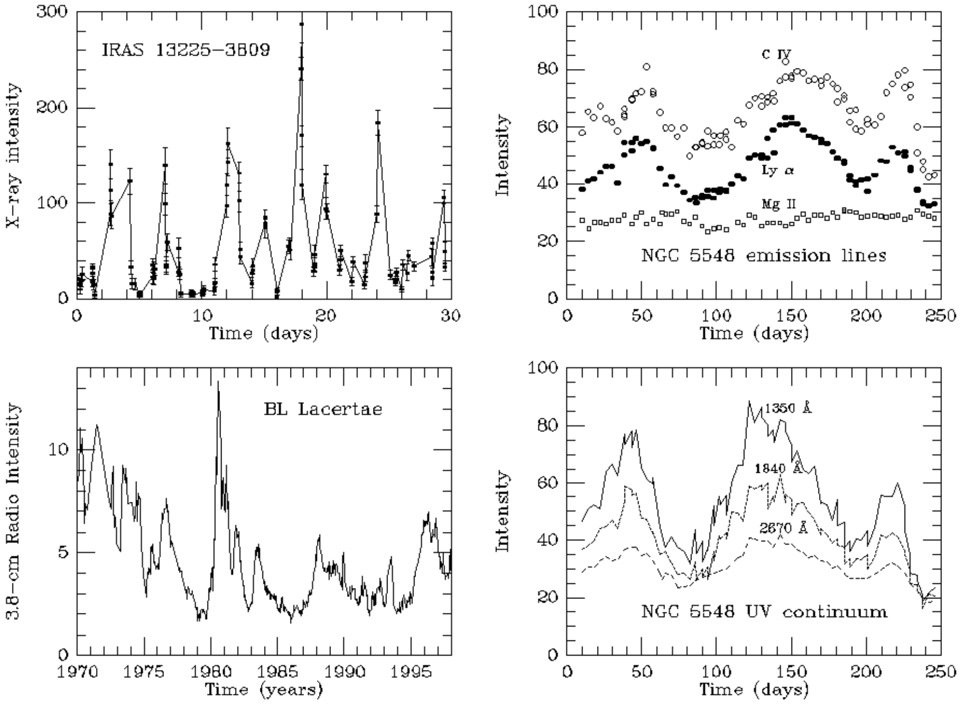

Figure 1.6: The variability of three different AGN in X-ray, line emission, radio and UV continuum respectively. Credit William C. Keel (http://www.astr.ua.edu/keel/agn/)

through thermonuclear fusion would be large enough to create the energy required through gravitational contraction alone! Large linewidths of many lines seen in AGN (Broad Balmer lines, FWHM = 2000-10,000 km s^{-1}; Fe Kα sometimes up to 100,000 km s^{-1}) implies deep gravitational wells. Also, stable long-lived collimated jets are most simply made by a single mass gyroscopic model. This evidence points to a SMBH, which is widely regarded as the centrepiece of all AGN, the main driver of *activity* (Lynden-Bell 1969).

It is favourable from the viewpoint of angular momentum transfer, for infalling material around such a compact body to lie in a single plane, such as those observed in protostellar discs, only on a much larger scale. The accretion mechanism causes material to flow inward, heating up as it loses gravitational potential energy. In this process the accretion disc will emit photons according to its local temperature. This accretion disc is widely regarded as being where the BBB is emitted.

1.4.2 Origins of BLR and NLR

The theoretical principles underpinning the mechanisms of line emission, both for permitted and forbidden lines is firmly established; electron de-excitation from one defined energy level to one of lower energy, resulting in the emission of a photon at the energy difference between the two levels. The only difference between permitted and forbidden lines is the stability of the upper energy level; in forbidden lines the energy level lifetime is much longer. For forbidden line emission to occur the medium must be sufficiently sparse such that spontaneous emission occurs before collisional de-excitation[3]. The densities needed to observe forbidden lines are characterised per species and quantified by the "critical density" of said given species. For example, the densities needed to observe the `[OIII]` doublet is $n_e \leq 7 \times 10^5 cm^{-3}$ (at T$= 10,000$K, taken from Osterbrock and Ferland (2006)), since above this density `[OIII]` the collisional de-excitation rate is greater than the radiative decay rate. Thus the NLR, or at least, the regime in which any given forbidden line is observed must be an extremely sparse medium, typically $n_e \approx 10^4$ cm^{-3}

The photons responsible for creating NLR lines, must also be accounted for.

---

[3] The reason for these lines being called forbidden is that they had, at the time of discovery, and indeed until this day not been reproducible in any laboratory experiment.

For example, the ionisation potential energy for O^{2+} (the species responsible for `[OIII]`) is 35.1eV, corresponding to an incident photon wavelength of ~ 350Å, and many other ionisations are seen, from [OI] and [SII], through to [Ne V] and [Fe X].

There are no such restrictions placed on the emission of permitted lines when it comes to the medium density; observations of the Hydrogen lines can be observed in standard physics laboratory experiments; the BLR is only observed in the permitted lines, thus the density of this region can be far greater than that of the NLR, typically $n_e \approx 10^9$ cm^{-3}. Finding details of the morphology of the BLR remains difficult; the innermost regions of AGN are still unresolved in the optical regime. Any information about the geometry of the BLR (which is believed to comes from the inner region, this will be discussed below) comes purely from spectroscopic data. The BLR structure is very complex and much is still under debate(Nikołajuk et al. 2005, Gaskell 2009, Gaskell et al. 2007). Studies show there to be two components in the BLR, the High-Ionisation Lines (HILs, $E \gtrsim$ 50eV), such at C IV $\lambda 1549\mathring{A}$, which are blueshifted with respect to the NLR lines, implying an outflow of material, and the Low-Ionisation Lines (LILs; $E \lesssim$ 20eV), such at MgII $\lambda 2800\mathring{A}$ and the Balmer series which are not blueshifted and are less broad ($\sim$ 2000km s^{-1} versus $\sim$ 7000km s^{-1} for HILs). Recent works have shown that the LIL clouds exist at $\sim 1,000$K and so are capable of hosting dust without irradiation leading to sublimation (Czerny and Hryniewicz 2012).

One assumes that since the NLR and BLR species require ionising photons, and that the BBB is assumed to emit them, that the BBB is responsible for producing the BLR and NLR. The physical size of the BLR is determined by studying line variability in response to continuum measurement. This technique is called Reverberation Mapping (RM) and requires extensive and intensive data acquisition, hence reverberation mapping has only been performed on a handful of sources (Blandford and McKee 1982, Netzer and Peterson 1997). None the less, RM shows that LIL variability lags continuum variability by on the order of tens of days, whilst the HIL variability lags continuum variability by the order of days, showing that the HIL medium exists much closer to the BBB continuum source.

Modern theories of BLR creation involve an accretion disc-wind (see Kollatschny and Zetzl 2013, and references therein), the disc being capable of producing the LILs while the wind is necessary to produce the HILs (since simple disc-only photoionisation models cannot produce these). This is in agreement with observations since winds would produce high-velocity, blue-shifted HILs. Superficially, complexity is added when considering Broad Absorption Lines (BALs) that are observed in some 10 per cent of Broad Line Objects, but if a mechanism capable of producing very fast winds is adopted (such as radiation pressure, or magnetic pressure) then this wind can be responsible for both the BALs and the Broad Emission Lines (BELs), the bulk of which will originate in the highest density regions closest to the accretion disc (where it is indistinguishable from the accretion disc atmosphere).

In reality the velocity field in the BLR might be a superposition of components due to random motions, turbulence, rotation, inflows and outflows, and shocks, with the final line profiles being comprised of a convolution of the different components present. Gaussian profiles are characteristic of random motions (Peterson and Wandel 1999; 2000), Lorentzian profiles of extended accretion disc turbulence and shocks (Véron-Cetty et al. 2001), while logarithmic profiles can be produced by outflowing gas. Furthermore, electron scattering can broaden the lines. Deconvolving individual velocity components has shown relative contributions to vary from line to line, as well as from source to source, and thus deciphering the true nature, morphology and dynamics of the BLR is a minefield.

1.4.3 Radio Emission

Radio Spectrum and its Origins

As previously mentioned, the radio emission from AGN is characteristic of a synchrotron spectrum, in which charged particles (in this case, relativistic electrons) are gyrated around magnetic fields. For the flat spectrum objects is possible to superimpose a series of synchrotron spectra peaking at different energies together in such a way as to reproduce a flattening of the spectrum.

Suffice to say that the topic of synchrotron emission is in itself a thesis worthy subject, as are the mechanisms which could possibly produce a magnetic field in AGN, and indeed many works have been written on it (see Blandford and Znajek 1977, Blandford and McKee 1982, Longair 1994).

1.5 The Unified Scheme

In the literature of the early 1970's are discussions of unification of the exotic phenomena discussed above. The seminal work of Rowan-Robinson (1977) attempted to unify the characteristics of radio sources with the characteristics of Seyfert galaxies. A model was produced such that an AGN is present within of all these sources, ascribing the observed differences between broad line objects and narrow line objects (the Type-I and Type-II objects) to dust obscuration alone. Later Lawrence and Elvis (1982) described an orientational effect, accounting for more dust obscuration in Type-II than in Type-I objects, thus making intrinsically identical objects appear differently depending on their orientation with respect to the observer. The idea of a torus model was suggested by Antonucci and Miller (1985) alongside the discovery of a hidden BLR in a Type-II object lying within "an optically and geometrically thick disc". The important hidden BLR was key to showing that the Type-I and Type-II objects could indeed be intrinsically similar. A theoretical model for a geometrically thick disc was produced when Krolik and Begelman (1988) modelled a swollen torus by collision induced viscous heating near a galactic nucleus. These collisions resulted in velocity dispersions of order the orbital speed of the accretion discs, thus creating a geometrically thick structure.

The unified scheme attributes the variation in all sources to orientational effects. The model has an accretion disc around an SMBH centred within a dusty, optically and geometrically thick torus between $1 - 100$pc in radius. The BLR exists within 1pc of the accretion disc and the NLR extends up to a kiloparsec perpendicular to the torus plane. The BLR and NLR arise from the photoionisation of gas by high energy emission from the central accretion disc continuum (BBB). The torus obscures the central continuum as well as the BLR to observers along the line-of-sight (i.e. in Type II objects) whilst the more extended NLR is observed in all objects, and occasionally shows a characteristic biconical morphology. Radio jets emanating from (or near to) the central regions project orthogonally to the torus plane. In the RL subset of sources the accompanying radio-lobes extend several kiloparsecs-to-megaparsecs into the intergalactic medium along the same axis as the radio jets.

Figure 1.7 shows a cartoon of the simple unified model with locations of the BLR, accretion disc, NLR, radio jets, torus and SMBH. Note that the relative sizes of the regions in this carton are not to scale, since fitting a sub-parsec accretion disc, kiloparsec scale NLR and megaparsec scale radio jet on the same schematic is unreasonable.

1.5.1 Torus Models

It has been shown that a “hidden” BLR is found in the polarised emission of many Type-II objects. This leads one to believe that the obscuring medium must be anisotropically distributed, allowing light through only certain scattering angles; i.e., if the obscuring body were just a simple line-of-sight cloud then the light would not get polarised, thus spectropolarimetric measurements would not “amplify” a hidden BLR.

As previously mentioned, there is direct observational evidence suggesting a compact obscuring structure. Taken from mid-IR interferometry, a warm dusty structure (T=320K) at the centre of `NGC 1068` (Jaffe et al. 2004) is observed, 2.1pc thick and 3.4pc in diameter encompassing a 0.7pc hotter ($T > 800$K) component.

Indirect evidence links Quasar and Radio Galaxy classifications to orientational effects; we often see radio jets aligned with the NLR, and core dominated radio emission associated with Broad Line objects (Fine et al. 2011, Drouart et al. 2012). We also observe hidden BLR polarisation mostly perpendicular to the radio axis, implying scattering by clouds along the radio jet axes (di Serego Alighieri et al. 1989).

These observations imply an anisotropic obscuring medium, with an opening to allow BLR and BBB light to emanate, for the ionisation and emission of the NLR, and to allow a magnetic field with associated radio emission to emanate. The most simple shape satisfying these criteria is a wedge, however a torus is usually depicted to most simply explain the variety of attributes seen in AGN.

However, there is still much to be understood regarding the stability of such a torus. If the torus is cold and molecular, has a mass constrained by x-ray absorption (column densities of $N_H > 10^{21}$ cm^{-2}) and physical extension constrained by the dust sublimation radius, is geometrically thick (in order to

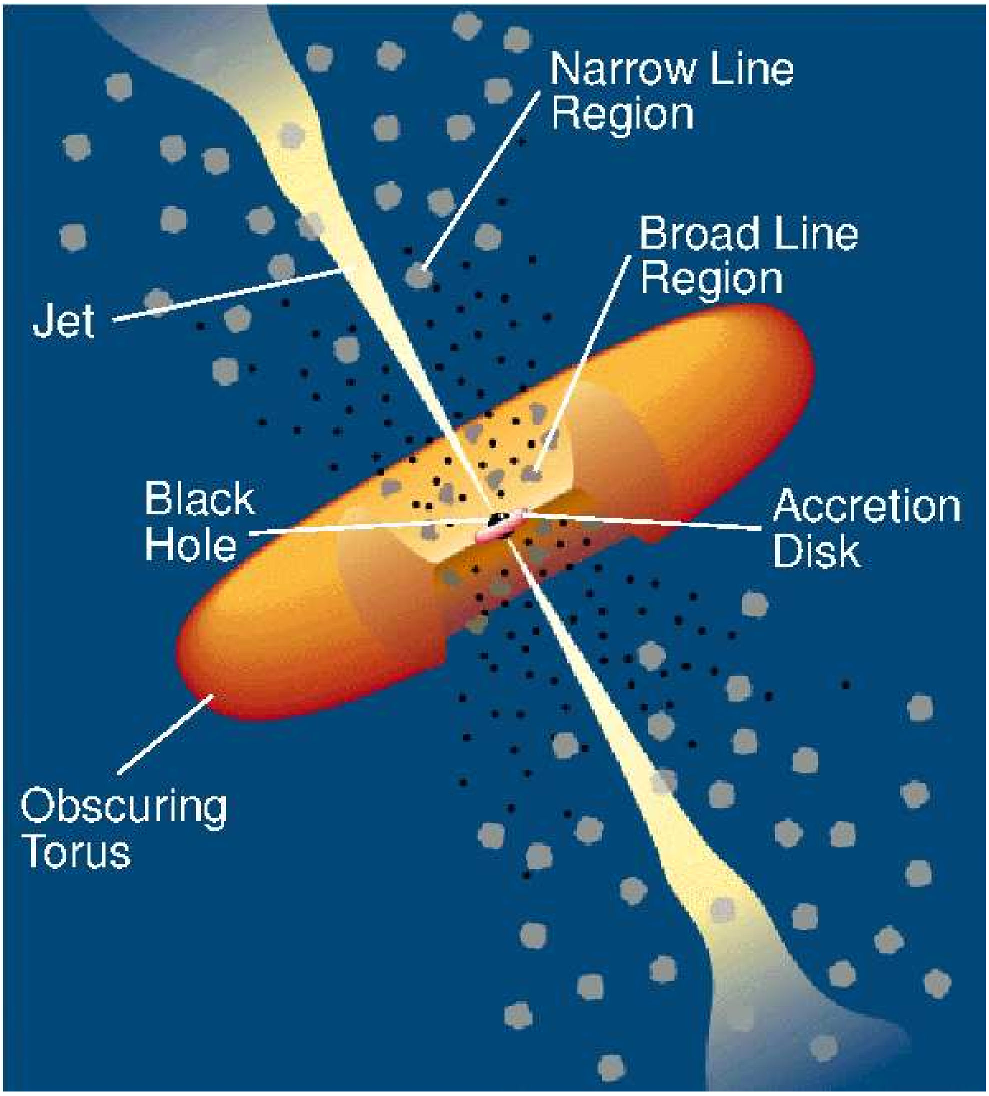

Figure 1.7: A cartoon of the unified torus model of AGN, showing the locations of BLR, NLR, SMBH, accretion disc and dusty obscuring torus, along with collimated radio jets. Note that the relative scales in this cartoon are far from accurate, the scales of the jet and NLR are far greater than that of the BLR and central accretion disc (by 3-4 orders of magnitude). The depicted opening angle of the torus would indicate a Type-II fraction of circa 20 percent, far from the fraction proposed by many observations. Credit: C.M. Urry and P. Padovani, 1995.

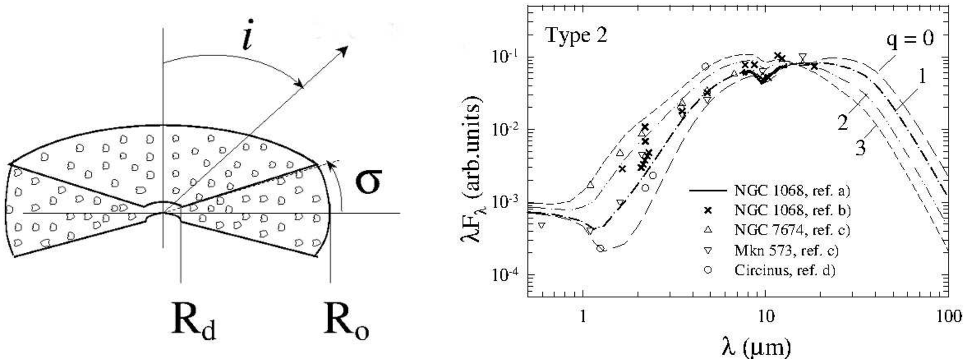

Figure 1.8: a cartoon with model fit to mid-IR data for a clumpy obscuring structure in the locus of a wedge/torus. Data from Type-II AGN. Credit Nenkova et al. (2008).

obscured the BLR and BBB in Type-II objects), and has a typical orbital velocity of 100km s^{-1}, with a scale height of order the orbital radius (making a intrinsic Type-II fraction of 0.5), the vertical velocity component must be of order the orbital velocity. This implies[4] a temperature of $10^5 K$, which is far in excess of the dust sublimation temperature. Thus using naive assumptions a geometrically thick and cold torus is hard to sustain (Krolik and Begelman 1988).

Early attempts to solve this instability issue used models with heavily clumped clouds travelling with supersonic velocities and with collisional losses being mitigated by strong magnetic fields (Krolik and Begelman 1988, Beckert and Duschl 2004). The presence of clumped clouds is supported by observations, since in order to fit the mid-IR Spectral Energy Distribution (SED) the torus must contain multiple dust components of different temperatures and densities. These models (and others using magnetocentrifugal winds to puff up the torus) have fallen out of favour since they require improbably high magnetic field strengths.

Figure 1.8 shows a cartoon of a clumpy torus, along with a series of IR SED templates according to viewing angle (Nenkova et al. 2008).

In a more recent model, the torus structure is supported by infrared radiation pressure from the re-emission surface of the torus (Krolik 2007), though this method of support becomes more difficult when anisotropic radiation is taken

---

[4] if this velocity is interpreted as thermal motions

into consideration (Liu and Zhang 2011). An alternative model has outflows of clouds embedded in a hydrodynamic disk wind, where the "torus" is simply a region in the wind where the clouds are optically thick and dusty such that they can provide toroidal obscuration (e.g. Blandford and Payne 1982, Elvis et al. 2002, Elitzur and Shlosman 2006, Everett 2005). Although there are multiple observations in favour of winds and cloud motions (Arav et al. 1997, Elvis 2004) and supporting disk-wind geometries (Hall et al. 2003), questions regarding the cloud-uplift and wind driving mechanisms remain (Emmering et al. 1992, Ferreira 2007) [5].

A further model has a starburst disc in the host galaxy, with the turbulent motions and geometrical thickness being sustained by supernova heating. The reason that such a model is considered relies on the fact that fuelling gas for the black hole must be funnelled toward the centre of the galaxy, producing favourable conditions for star formation (Fabian et al. 1998, Wada and Norman 2002, Thompson et al. 2005, Ballantyne 2008). Also, a clumpy medium is also common in the star forming regions of starburst galaxies. This model is, as well the other models discussed above, also supported by observations: high-spatial resolutions, down to parsec scales in nine local Seyfert galaxies have shown post starburst populations, which indicates that such a obscuring-starburst torus may be commonplace (Davies et al. 2007).

The size of the torus is yet another interesting, if contentious issue. In early models, torus sizes were inferred by the requirement to obscure the BLR (the size of which is constrained from RM studies), whilst still remaining small enough to not to obscure the NLR, of which the extent can be directly measured. The aforementioned clumpiness of the torus, as suggested by IR observations and models suggests that multiple absorbers, on quite different physical scales are present. X-ray observations measuring variability show there to be gas absorption within the dust sublimation radius typically on sub-parsec distances from the central source: A particular example shows intra-day variability between a Compton thin ($N_H \sim 10^{23}\mathrm{cm}^{-2}$) and reflection dominated-Compton thick ($N_H > 10^{24}\mathrm{cm}^{-2}$) regime (Risaliti et al. 2005; 2007; 2009). By constraining

---

[5] including interaction between disk and SMBH, time dependence (non-steady state), high efficiencies requiring additional disk heating

the ionisation parameter of the obscuring cloud (which is calculated from the intrinsic X-ray luminosity of the source as determined from the X-ray reflected component), it is possible to estimate the radius of the obscuring cloud to be $R \sim 10^4 R_G$, where R_G is the gravitational-*Schwarzschild* radius of the central BH (the reader is referred to Risaliti et al. (2007) for more details of this calculation, and the assumptions made in getting to it). This radius lies far within the dust sublimation radius at the locus of the BLR. Furthermore, the same work calculates estimates for the radius and density of such an obscuring cloud at 10^{13}cm and $10^{11} - 10^{13}$cm^{-3} respectively, making it typical of a BL emitting cloud. While such observations are only present for a handful of local sources (and indeed, at *this* quality only one source to date; `NGC 1365`) the result implies that the short timescale-occultation clouds and BLR clouds are one and the same, thus making the physical extent of the torus dependent on the regime in which you are observing it.

1.5.2 Disc-Torus Alignments

The simplest unified model assumes that the accretion disc, torus and any associated outflows occupy the same axis of rotation. This model is justified by assuming a symmetric mass transfer from the torus to the accretion disc, inward towards a rotating black hole, thus being favourable for angular momentum transfer. Outflows will be collimated by the geometrically thick nature of a torus.

Doubt has been cast on whether this most simple of models is correct; firstly, from a hypothetical point of view if a BH is grown by several minor accretion events from randomly infalling material, there is no reason why the BH spin would be co-planar with a torus. Observationally, high resolution interferometric measurements of a torus-like structure in `NGC 1068` in the mid-IR suggest a substantial misalignment of a torus-outflow structure (Raban et al. 2009). Further observations show misalignments between NLR ionisation cones (presumably constrained by torus geometry) and radio jets (presumably constrained by the orientation of the accretion disc's innermost regions) measuring in the tens of degrees (Bergmann 2012). Such observations are still in their early stages owing to the difficulty of mid-IR interferometry and high-resolution radio interferometry of AGN inner regions. Thus we only have evidence supporting disc-torus misalignments in a handful of sources. We are unsure whether such misalignments are commonplace, however, if it turns out that there are, then serious questions regarding the true differences between AGN classes must be discussed. For example, can disc warping reproduce the observed covering factors of different AGN classes? Is there a covering factor luminosity dependence?

1.5.3 Receding Torus Models

Observations in the X-ray and `[OIII]` regimes show the Type-II fraction (that is, the number of Type-II AGN as a fraction of the total AGN population) to decrease as a function of luminosity (e.g. Lawrence 1991, Ueda et al. 2003, Simpson 2005, Hasinger 2008).

One can argue that with a fixed height torus whose inner edge is defined by the dust sublimation radius (and hence temperature, and hence the central engines luminosity), this trend for more Type-I objects to be observed at higher luminosity is a natural conclusion. This is referred to as the receding torus model (Lawrence 1991) However, this luminosity dependence is not something that is matched in other observational regimes. In volume limited optical samples, IR and radio surveys, the Type-II fraction appears to be fixed across many decades of Luminosity (see Chapter 3). This problem is very much still an open matter, and is one that will be discussed in further detail in both Chapters 3 and 4

1.5.4 The Warped Disc Model

The Warped Disc Model is a competitor model to the torus model in which random inflow of material from kiloparsec scales realigns to a well-defined central accretion axis at smaller scales. Furthermore, the self gravity of the disc at intermediate scales (between the kpc scales and sub-parsec SMBH sphere of influence) has been shown to be capable of inducing warp (Nayakshin 2005).

Warped discs have observational support; the first sub-parsec observations of a central engine taken via radio interferometry, revealed evidence of a rotating warped disc through water maser emission in the disc. Whilst this evidence appears compelling it is also noteworthy that this maser-emission only traces the highest maser amplification regions of the disc (within $\sim 15^\circ$ to the line of sight), and thus may not trace the overall morphology of the molecular gas.

Asserting that a kpc scale torus is co-planar with the disc does not fit entirely with observations (Lawrence and Elvis 2010): studies of individual cases of RL objects that the radio axis (which is shown to be roughly perpendicular to the parsec scale maser emission, and so assumingly the disc (e.g. Raban et al. 2009)) is randomly oriented with respect to the kpc scale dust disc (Schmitt et al. 2002). Also, BLR linewidths seem to be dominated by orbital rotations (see Smith et al. (2005) for a description of how such a conclusion can be reached), requiring a large angle between viewing at the disc rotation axis. This is simply not feasible in a coplanar disk-torus model. Thus at some scale and in some objects, misalignment of the torus and disc, and some level of warp between them is necessary.

1.5.5 Other Problems, Curiosities and Open Issues

Host Galaxy Obscuration

Another issue which must be raised when regarding obscuration of the BLR is that of the host galaxy itself. Many works show a strong correlation between host galaxy inclination and AGN obscuration (Keel 1980, Lawrence and Elvis 1982, de Zotti and Gaskell 1985, McLeod and Rieke 1994, Simcoe et al. 1997), so this must also be considered when regarding a unified scheme; observations (e.g. Malkan et al. 1998) have shown there to be significantly more nucleus obscuring dust lanes in Type-II objects than Type-I objects.

True Type-II Objects

In recent years, the existence of *true* Type-II objects, that is, objects which lack a BLR have emerged. These are still a real novelty within the field. If we are to truly believe that Type-I and Type-II objects are analogous and depend only on orientation, then what has happened to the BLR in these objects? Are the mechanisms responsible for their creation suppressed or extinguished?

BLRs seem to have an upper limit on their velocity dispersions with no BLR having a measured linewidth $\sigma_{BLR} > 25,000$km s^{-1} (Eracleous and Halpern 1994). Applying Keplerian motion approximations allows us to arrive at a relation between this linewidth and the bolometric luminosity (L$_{bol}$) which, when combined with the linewidth upper limit gives us a minimum L$_{bol}$ for a BLR to survive (see Laor 2003, for details). In these cases the lack of BLR would not necessarily imply a significantly different structure in the inner regions compared to “normal” AGN, and so will not contradict the unified scheme. However, there are notable sources (e.g. `NGC 3147`; Bianchi et al. 2008) within the true Type-II class with bolometric luminosity extrapolations in excess of this cutoff and so cannot be explained by the simple unified scheme. Again, progress on this topic is blighted by the difficulty of observations. Many targets that have previously been classified as true Type-II candidates turn out to have extraordinarily weak - but nonetheless present - broad lines, whilst other sources have Hα lying outwith the optical spectral window and so classification relies solely on the detection of Hβ, which is intrinsically weaker than Hα (e.g. 273x; Bianchi et al. 2012).

The Big Blue Bump

There are numerous open problems with regard to the BBB; I will briefly detail a few of these following the discussion of Lawrence (2012):

- The Temperature Problem: while the BBB feature itself is not well fit by a single temperature blackbody, the BBB universally peaks around 1100Å (in νL_ν), characteristic of a temperature of $T \sim 30,000$K (e.g. Zheng et al. 1997, Telfer et al. 2002, Shang et al. 2005). However, using the Stephan-Boltzmann equation and reasonable estimates of the Eddington rate, black hole mass and emitting region size, the temperature of the BBB should be $\sim 100,000$K.

- The Ionisation Problem: the observed UV continuum cannot be extrapolated in a simple way so as to provide sufficient photons to ionise the gas in the BLR.

One suggested solution to these two problems is for the BBB to be double peaked, with the extreme-UV peak near $75,000 - 100,000$K, the Wein tail of which is observed as the soft X-ray excess (Korista et al. 1997, Lawrence 2012). Physically this can be produced by a “harder than observed” continuum at $T \sim 100,000$K which is blurred and reflected from high density and nearby clouds, which produce the 1100Å peak.

- The Co-ordination Problem: the variability at different UV/optical wavelengths are almost in phase - the delay timescale between wavelengths is small compared to the variability timescale itself.

A suggested solution to this lies in the central accretion disc being partially heated by the central X-ray source, such that the co-ordination timescale is dictated purely by light travel time from the X-ray source to the accretion disc regions, such that the measured variations are artifacts of reprocessed X-ray variability. Alternatively, the BBB could be a reprocessing of the extreme UV emission.

1.6 AGN with relation to Galaxies and their Environments

AGN are seen to be hosted typically by galaxies with stellar masses in excess of 10^{10} $M_\odot$ (Kauffmann et al. 2003), and there are many convincing correlations suggesting AGN-host galaxy interactions:

$M - \sigma$ Relation - A tight relation between $M_{\rm BH}$−stellar bulge velocity dispersion ($\sigma_{\rm bulge}$) as well as bulge luminosity and bulge mass are found (e.g. Magorrian et al. 1998, Ferrarese and Merritt 2000, McLure and Dunlop 2002, Woo and Urry 2002, Häring and Rix 2004, Greene and Ho 2006, Bentz et al. 2009, Woo et al. 2010, Vika et al. 2012); by plotting the radial dependence of the stellar velocity dispersion it is possible to find both the median σ as well as that in the sphere of influence of the black hole, the shape and peak of the $\sigma(r)$ profile dictating the black hole mass. Figure 1.9 shows this empirically derived relation for a number of sources, with values derived using a number of methods (details given in Gültekin et al. 2009).

Prevalence of AGN - It is firmly established that higher mass galaxies are significantly more likely than lower mass galaxies to host AGN (e.g. Sanders et al. 1988, Dunlop et al. 2003, Floyd et al. 2004, Veilleux et al. 2009). Studies of the population of AGN as a fraction of the total galaxy population reveal a variety of results, dependent both on the observational regime and environments being studied; while AGN have been found to be more prevalent in field (as opposed to cluster) environments (e.g. Kauffmann et al. 2004,

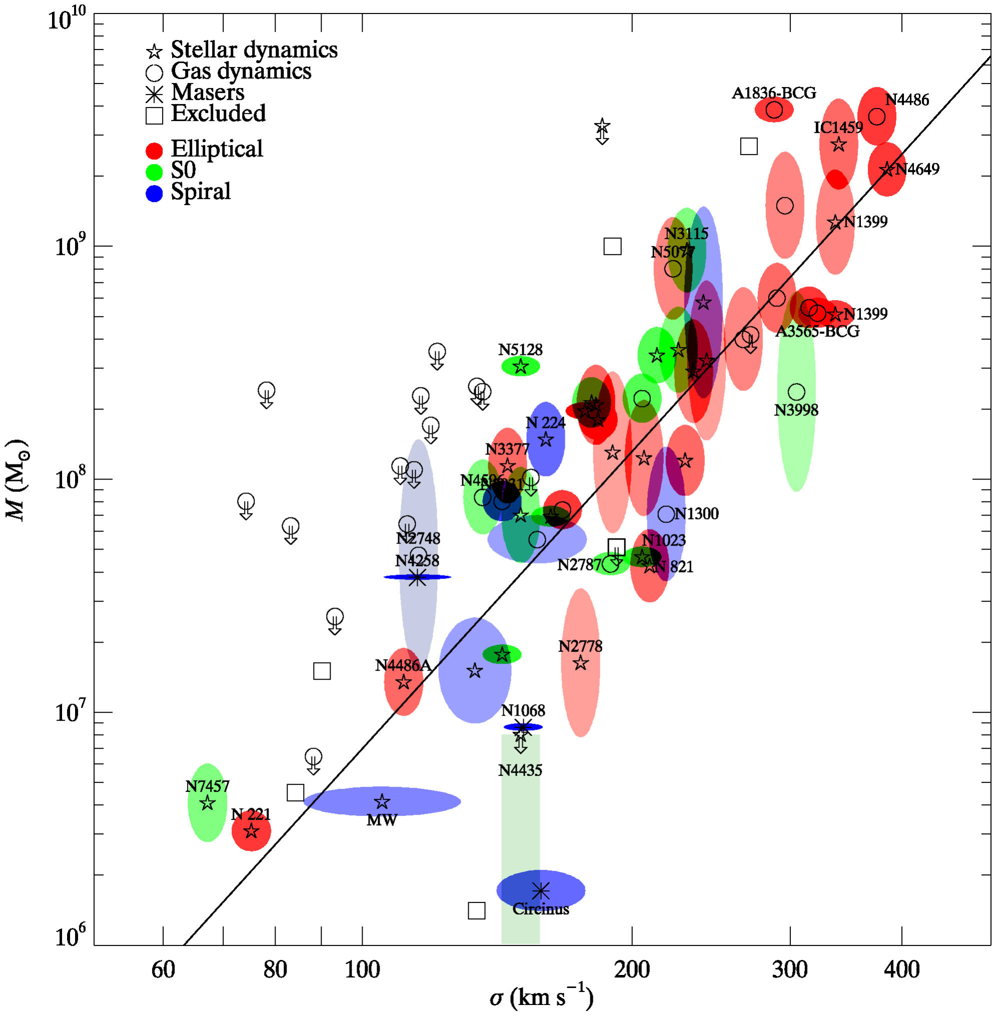

Figure 1.9: A plot to show the M-σ relation, with values derived using different methods. Credit (Gültekin et al. 2009).

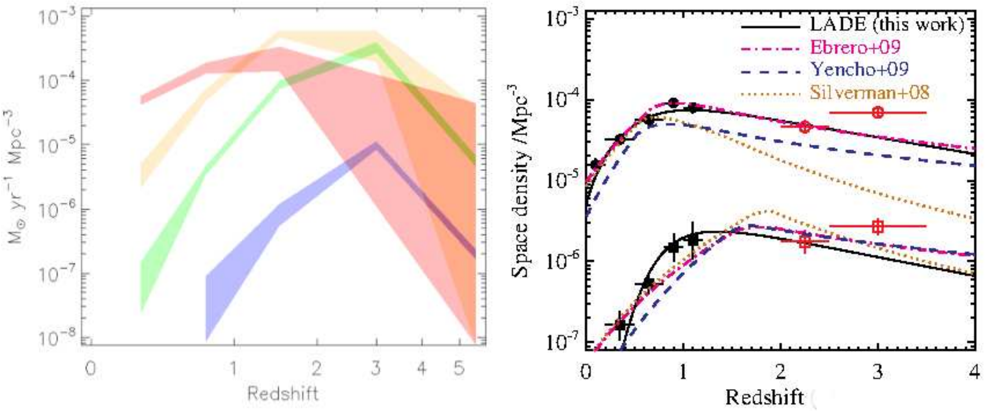

Figure 1.10: A side by side presentation of the star formation rate density evolution and space density AGN evolution. The left subfigure represents the star formation rate density evolution for Quasar hosts inferred from 100μm rest-frame luminosities, for QSOs with $22 > I_{AB} > 24$ (red), $24 > I_{AB} > 26$ (orange), $26 > I_{AB}28$ (green) and $I_{AB} < 28$ (blue) (Serjeant et al. 2010). The right-hand subfigure shows the evolution of the space density of AGN based on models and binned estimates are shown from hard X-ray samples at $z < 1.2$ (solid symbols) and the colour pre-selected samples at $z \sim 23$ (open symbols) from Aird et al. (2010). other Models from Ebrero et al. (2009, dot-dashed line), Yencho et al. (2009, dashed line) and Silverman et al. (2008, dotted line) are also shown.

Montero-Dorta et al. 2009), this result is contentious since other works find no evidence for an "anti-correlation" (e.g. Miller et al. 2003, Haggard et al. 2010). Statistics of the populations range from circa 1-3 percent in X-ray/optical surveys (Alexander et al. 2005), through to 75 percent of X-ray observed galaxies in sub-mm+optical+radio selected samples (Pope et al. 2008), though these result depend hugely on the sample criteria, including the mass, luminosity and star formation rate scales being probed.

Tracing the Star Formation Rate Density - the AGN activity and star formation rate density of the Universe closely trace one another, typically peaking at $z \sim 2$ (e.g. Lilly et al. 1996, Madau et al. 1996, Ueda et al. 2003, Nandra et al. 2005, Hasinger et al. 2005, Silverman et al. 2008, Yencho et al. 2009, Ebrero et al. 2009, Aird et al. 2010, Patel et al. 2013). Figure 1.10 shows the SFRD evolution and AGN space density for a range of data (details given in the caption and in Serjeant et al. (2010), Aird et al. (2010).

Down-Sizing - Both star forming galaxies and AGN show a "down-sizing" effect in which stellar/accretion activity predominantly occur in less massive-lower luminosity systems at a later epoch than their higher mass-higher luminosity counterparts (Cowie et al. 2003, Ueda et al. 2003, McLure and Dunlop 2004, Hasinger et al. 2005, Bongiorno et al. 2007). AGN feedback is typically evoked as a star-formation quenching mechanism in semi analytical galaxy evolution models in order to reconcile theoretically and observationally derived galaxy luminosity functions, especially at high stellar masses (e.g. Granato et al. 2001; 2004, Springel et al. 2005, Bower et al. 2006). There is also mounting observational evidence for AGN induced quenching of star formation (e.g. Schawinski et al. 2007, Salim et al. 2007). One can see the effects of downsizing in Figure 1.10 also, since in the left-hand plot the peak of star formation rate density is dependent on the luminosity of the sources, with more luminous sources peaking in star formation rate density at earlier epochs.

AGN Feedback

The importance of AGN feedback to galaxy evolution has been realised over the past decade. The interaction of the host galaxy gas and the radiation/energy produced in its central engine can have a major impact on the evolutionary path of the galaxy. AGN feedback must be included in simulations of galaxy evolution in order to suppress star formation in the highest mass objects. In the radiative mode, that is when the AGN is believed to be accreting at a maximal rate, cold gas is pushed out of the host galaxy, quenching star formation. Interestingly, by making simple assumptions about the accretion process, one can balance the radiation and gravitational forces and arrive at a formula describing an $M - \sigma$ as detailed above. Any such calculation is outwith the scope of this brief overview, but it described in more detail in Fabian (2012), and references therein.

Outflows

Many works detail AGN outflows over kiloparsec scales, which can have a profound effect on star formation within the host galaxy (see e.g. Cattaneo et al. 2009). Indeed it has been suggested that extended outflows, acting far beyond the host galaxy, can be used to constrain X-ray Luminosity - X-ray temperature correlations observed within the ICM of groups and clusters (see e.g. Stott et al. 2012), by proving required heating. This implies AGN can have a substantial impact on the evolution of the environment beyond their own host galaxy (indeed, this would be a suitable explanation as to why HzRGs are observed to lie in protocluster/cluster environments)

The Environments of High Redshift Radio Galaxies

Radio galaxies (RL Type-II AGN) are extremely rare objects. Estimates of their space density at $z \sim 2$ are around a few $\times 10^{-8}$ Mpc^{-3} (Dunlop and Peacock 1990, Willott et al. 2001). However, since they are extremely luminous it is also possible to observe them at high redshifts (e.g. TN J0924-2201 at $z = 5.197$). These high luminosity radio galaxies are extremely rare at the current epoch (Willott et al. 2001, Jarvis et al. 2001); there are almost no local analogues with identical characteristics. Despite this, we know that HzRGs are among the most massive galaxies at high redshift (Seymour et al. 2007), radio galaxies are almost exclusively giant ellipticals (e.g. Matthews et al. 1964) and they are seen to live in overdense regions (e.g. Roettgering et al. 1996, Pascarelle et al. 1996, Le Fevre et al. 1996). The only local analogues that fit this scenario are the cD galaxies that exist at the centre of clusters.

Whilst conventionally the study of new cluster environments relies on the detection of hot cluster gas in the X-ray regime, by targeting observations around HzRGs we can probe the evolution of clusters up to much higher redshifts, not limited by the sensitivity of current X-ray telescopes.

1.7 Scope of this Thesis

The aims of this work is to address first a few of the previously discussed issues. First and foremost is the issue of the Type-II AGN fraction, which I have already said is seen to decrease as a function of X-ray and `[OIII]` luminosities in a numerous works, despite this not being found in all regimes.

In Chapter 2 I investigate the environments of high redshift radio galaxies (these are galaxies (Type-II Radio loud AGN) in the mid-IR regime, where I probe the possible protocluster environments. In Chapter 3 I develop an observationally motivated model for explaining the observed Type-II fraction luminosity dependence in the X-ray regime, using distributions of partial covering, Compton thick clouds. In Chapter 4 I analyse a multiwavelength dataset reaching from the optical to sub-mm regimes, with spectroscopic data allowing for the optical classification of a sample of AGN that is unbiased by core accretion activity. I investigate the Type-II fraction in this dataset, as well as discuss many other issues such as the AGN fraction, characteristics of the Low Ionisation Narrow Emission Region (LINER) vs. bona fide Type-II AGN populations. In Chapter 5 I reduce and analyse a dataset of 24μm selected targets in the UDS field.

Chapter 2

Overdensity of 24μm sources in the vicinities of High Redshift Radio Galaxies

2.1 Prologue

The majority of this work in this chapter was undertaken whilst working with collaborators at the European Southern Observatory, and was published in Astronomy & Astrophysics (A&A) in December, 2012.

2.2 Abstract

I present a statistical study of the environments of 63 high-redshift radio galaxies (HzRGs) between redshifts $1 \leq z \leq 5.2$, using the 24μm waveband of the MIPS instrument aboard the *Spitzer Space Telescope*. Using a counts-in-cell analysis, a statistically significant source overdensity is found in $1.75'$ radius circular cells centred on the HzRGs when compared to reference fields. I report an average overdensity of $\delta\,(= \bar{N}_{targets}/\bar{N}_{reference}) = 2.2 \pm 1.2$ at a flux density cut of $f_{24\mu\mathrm{m}} = 0.3\,\mathrm{mJy}$. This result implies that HzRGs are likely to lie in protoclusters of active and star-forming galaxies at high redshift. Over 95 percent of our targeted HzRGs lie in higher than average density fields. Further, 20 (32 percent) of our selected fields are found to be overdense to at least a 3σ significance, of which 9 are newly identified protocluster candidates. I observe a weak correlation between redshift

and 24μm source density, and discuss the populations being probed at different redshifts. In this uniformly selected sample, which was designed to cover two orders of magnitude in radio luminosity throughout $z = 1 - 4$, I find that the 24μm source density does not depend on radio luminosity. I also compare this result with recent work describing IRAC source overdensities around the same HzRGs and find correlations between the results.

2.3 Introduction

Observations of high-redshift radio galaxies (HzRGs: defined as $z > 1.0$ with a rest$-$frame 3GHz luminosity greater than $10^{26}\,\mathrm{W\,Hz^{-1}}$) provide evidence that such galaxies are the progenitors of the current day giant elliptical (gE) and cluster-dominant (cD) galaxies (see e.g. De Breuck et al. 2002, Seymour et al. 2007, De Breuck et al. 2010). As such, we expect HzRGs to be signposts of high-density regions. Studies have shown overdensities of Lyα emitters in HzRG environments between $2.2 \leq z \leq 4.1$ (e.g. Venemans et al. 2002; 2003, Overzier et al. 2008). The formation of filamentary structures out to high redshifts (Croft et al. 2005, Matsuda et al. 2005) and of Extremely Red Object (ERO) overdensities in high-redshift active galactic nuclei (AGN) fields have also been observed (e.g. Chapman et al. 2000, Hall et al. 2001). Overdensities of Hα emitters (Kurk et al. 2004a, Tanaka et al. 2011), Lyman Break Galaxies (Miley et al. 2004), BzK-selected sources (Galametz et al. 2009) and red sequence galaxies (Doherty et al. 2010) have also been reported in the vicinities of HzRGs. Large rotation measures within the HzRG environments (Carilli et al. 1997) are indicative of dense, X-ray emitting cluster atmospheres. All of this evidence suggests HzRGs trace protoclusters, and indicate that protoclusters can be in place from early epochs (when the Universe was only $\sim 1 - 2$Gyr old). These studies have been performed on limited samples of less than a dozen each; prior to this work, a systematic study of HzRG environments has not been undertaken.

High-energy continuum emission from a central accretion disc in an AGN is believed to be re-processed by the dusty toroidal structure encompassing it, and re-radiated in the mid-IR ($10 - 30\mu$m; Elvis et al. 1994). All AGN are thought to emit strongly in the rest-frame mid-IR. However, mid-IR observations will not only detect AGN; starburst galaxies have strong polycyclic $-$ aromatic hydrocarbon (PAH) features, strongest at $\sim 3.3\mu$m, 6.2μm, 7.7μm, 8.6μm, 11.2μm and 12.7μm attributed to vibrational modes of these complex molecules (Gillett et al. 1973). These attributes make mid-IR detection ideal for selection of star-forming galaxies at high redshifts as well.

In order to find protoclusters, large-area surveys are needed and so efforts can be both time and resource intensive. If we can pre-select targets that are thought to preferentially reside within rich environments, we can quickly identify larger numbers of robust cluster candidates. Selecting HzRGs (which have been found to lie in overdense regions at other wavebands and at lower redshifts) and analysing their fields in the mid-IR allows us to probe the AGN and starburst populations simultaneously, without obvious selection effects.

2.3.1 The Environmental Dependence of Galaxy Properties

Much work has been done in investigating the environmental dependence of galaxy and AGN properties. Work by Cooper et al. (2006) shows that blue galaxies (rest frame U-B optical colour) typically lie in lower density regions than red galaxies at $z \sim 1$, mirroring the trend seen in the local Universe (e.g. Hogg et al. 2003). Interestingly, Hogg et al. (2003) also find that there is an overdensity-luminosity relation for red sources but not for blue sources, something which Cooper et al. (2006) do not find at higher redshifts; at $z \sim 1$ an overdensity-luminosity relation exists for both red and blue sources. The fact that an overdensity-luminosity relation is observed in blue objects at $z \sim 1$ but not by the current epoch is attributed to quenching; high luminosity sources at $z \sim 1$ have their star-formation quenched and migrate on to the red sequence by $z \sim 0$.

Further work by Cooper et al. (2010) has shown that higher stellar mass objects typically lie in higher density regions already at $z \sim 1$, though these results are controversial (e.g. Iovino et al. 2010).

It is therefore expected that the presence of AGN - with their prevalence in high stellar mass objects and *contamination* of photometric colours (primarily in Type-I objects) - may also depend on environment. This is indeed what is seen. Works by Wake et al. (2004), Coil et al. (2007) show that AGN up to quasar luminosities and $z \leq 1$ cluster in much the same was as star forming galaxies at the same epochs[1]. On the other hand, work undertaken by Constantin and Vogeley (2006) much more locally ($z \leq 0.3$) shows that Seyfert galaxies do not cluster as strongly as "average" galaxies.

Further works undertaken by Georgakakis et al. (2007), Coil et al. (2009) investigates the clustering of X-ray AGN. Georgakakis et al. find X-ray AGN to follow similar clustering to non-AGN with similar colours and luminosities. Coil et al. find that at $z \sim 1$ this population clusters in a similar amplitude to red, quiescent galaxies, much stronger than blue, star-forming galaxies. They also find that X-ray AGN cluster significantly more strongly than optically selected AGN, inferring that they lie in more massive dark matter haloes

The companion paper to this work, Galametz et al. (hereafter referred to as G12), undertakes the analysis of 48 HzRG fields between redshift $1.2 \leq z \leq 3.0$ using the NASA *Spitzer Space Telescope* (Werner et al. 2004) Infra-Red Array Camera (IRAC; Fazio et al. 2004) to isolate high redshift sources. Their work shows that HzRGs lie preferentially in medium-to-high density regimes when compared to a reference sample, though the colour criterion used in that work does not differentiate between passive and active galaxies.

Throughout this chapter many references to the HzRG fields are made. They are addressed with the same IDs as the HzRGs, though typically we are discussing the environments and not the radio sources. In this paper we refer to all significantly overdense regions as protoclusters or protocluster candidates. Though at low redshifts these structures may be gravitationally bound, at higher redshifts these structure are not yet gravitationally bound. The term protoclusters is used throughout for the sake of consistency.

2.4 Observations

2.4.1 HzRGs

A sample of HzRGs is taken from both flux−limited surveys such as 3C, 6CE, 7C and MRC for their unbiased radio properties, as well as ultrasteep radio spectra

---

[1] Interestingly, Wake et al. (2004) also find that the clustering strength of AGN varies as a function of narrow-line `[OIII]` luminosity ($L_{[OIII]}$) with $L_{[OIII]}$ AGN clustering more strongly than high $L_{[OIII]}$ AGN

surveys (e.g. De Breuck et al. 2000) to cover the higher redshift ($z > 2$) range. This sample is specifically designed to mitigate the luminosity-redshift correlation that affects flux-limited samples; the reader is referred to De Breuck et al. (2010, Fig. 2) for further details.

I present observations of the first statistically significant sample of HzRG fields to date. The 70 target *Spitzer*-HzRG sample is described in more detail by Seymour et al. (2007) where targets were preferentially selected based on their amount of supporting data (*Hubble Space Telescope* and SCUBA observations) and existing guaranteed time observations (GTOs) with *Spitzer*. With no 24μm data (one source) and insufficient coverage (seven sources), this sample size is reduced to 62 targets. The source `LBDS53W069`, although not meeting the HzRG radio luminosity selection criterion, has been included in this sample as it is a known radio galaxy with the relevant data available (Stern et al. 2006), making the HzRG sample 63 fields in total.

The HzRG sample was observed at 24μm using the Multiband Imaging Photometer for *Spitzer* (MIPS; Rieke et al. 2004). The majority of observations (59 sources) have been undertaken as part of Program ID's 40093 (39 sources) and 3329 (20 sources) as part of *Spitzer* proposal cycles 1 and 4 respectively. Exposure times for the former 59 sources were determined based on 24μm background levels as determined with the Leopard software. Data for three remaining sources were taken from much deeper GTO programs.

2.4.2 Reference Fields

The reference set against which the HzRG fields are analysed is that of the *Spitzer* Wide-area InfraRed Extragalactic Survey (SWIRE; Lonsdale et al. 2003). SWIRE, the widest area cryogenic *Spitzer* legacy program, imaged 49 sq. deg. of the sky over six[2] high−latitude extragalactic fields in all seven available bands[3] and detected over two million objects up to $z \sim 4$ (Rowan-Robinson et al. 2008). The field choices for SWIRE required low Galactic cirrus emission, large contiguous areas and low foreground contamination such as bright stars and local galaxies. The observing strategy for the SWIRE survey involved mapping of the fields such that each point is covered by four 30-second exposures with the IRAC

---

[2] ELAIS N1, ELAIS N2, ELAIS S1, Lockman, XMM−LSS, CDFS

[3] IRAC: 3.6μm, 4.5μm, 5.8μm, 8.0μm. MIPS: 24μm, 70μm and 120μm.

instrument and 44 four-second exposures with the MIPS instrument. The SWIRE observations were taken throughout 2004 with over 800 hours of observations.

After initial analysis of the SWIRE fields I opt to remove the ELAIS S1 field from comparison, due to its shallow depth compared to the remaining five SWIRE fields. By doing this, I manage to cut at a deeper flux density without jeopardising the signal to noise, whilst still allowing the reference sample to be large enough to mitigate cosmic variance.

2.4.3 Reduction

Data reduction was performed using MOPEX (Makovoz and Khan 2005) as described by Seymour et al. (2007); basic calibrated data are drizzled to reach an increased sampling of 1″.25 per pixel from the intrinsic pixel scale for MIPS 24μm frames of 2″.5 per pixel[4].

2.5 Source Extraction and Photometry

2.5.1 Creation of Variance Maps

Fully reduced data and corresponding exposure maps are used to produce accurate variance maps: the pixel flux densities are binned and plotted according to their exposure, Gaussian profiles are fit to the lower part of the resultant histograms (ignoring the positive skew due to sources), then finally RMS noise values are extracted for each exposure value. Plotting of the root mean square (RMS) noise values vs. exposure (and using $\sigma^2 \propto 1/\mathcal{W}$, where σ is RMS noise and $\mathcal{W}$ is the weight, equivalent to exposure) allows the exposure maps to be converted directly to *absolute variance* maps. An example of a fit to a variance vs. exposure (named “coverage” as a remnant of the MIPS data header) plot is shown for HzRG field 3C239 in Figure 2.1.

---

[4] note that the SWIRE data is rescaled to 1farcs2 per pixel

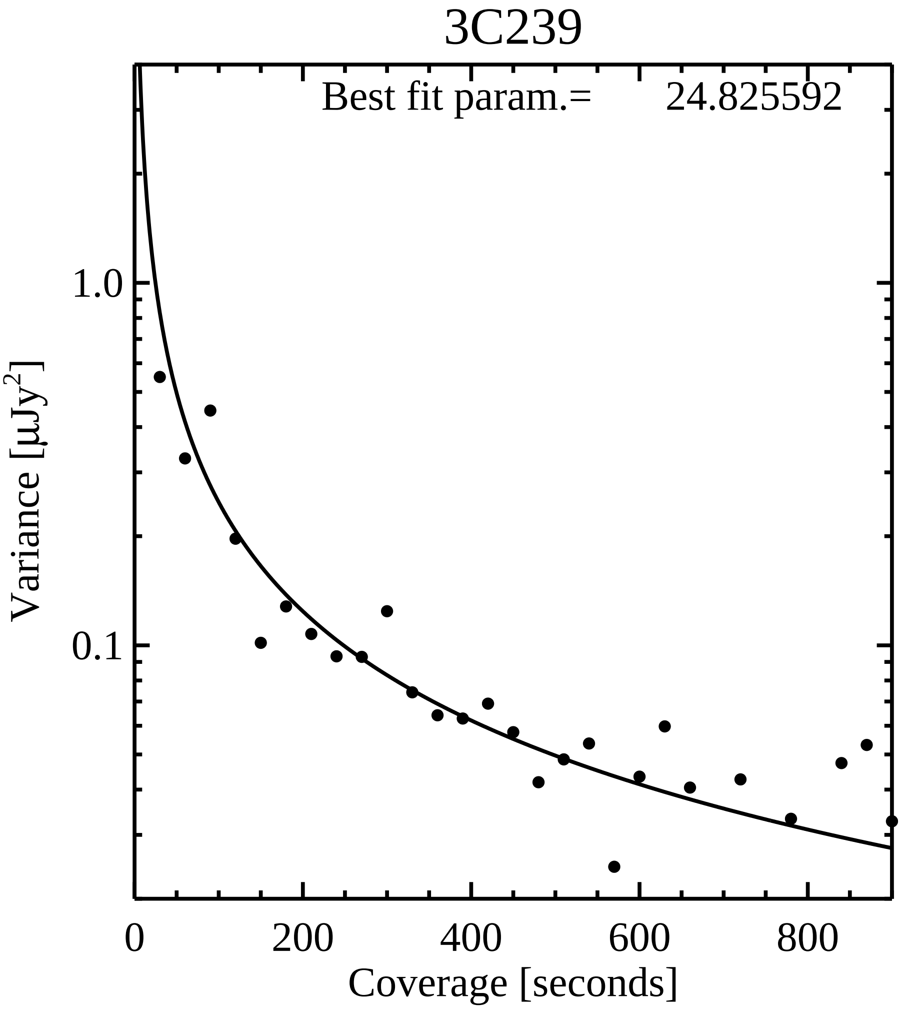

Figure 2.1: A plot showing the variance vs. coverage for HzRG field 3C239, along with the best fit line.

2.5.2 Detection and Extraction

Source detection and photometry are undertaken using the SExtractor software (Bertin and Arnouts 1996). Parameters are set as to minimise false detections and to optimise the separate detection of sources in close proximity. The parameters chosen are included in Appendix A. The flux density from extended sources[5] is taken to be the Kron flux density, with the aperture correction to the flux density being calculated from the *effective* Kron radius. Elsewhere, the resultant flux density from point-like[6] sources is taken to be that calculated within a $5\farcs25$ aperture radius. Aperture corrections are calculated using the *Spitzer* MIPS data handbook (see the MIPS data handbook[7], p.37).

2.5.3 Flux Density and Region Cut

Due to the dithering pattern adopted during the HzRG field observations for which the central region of each frame has a higher coverage, I restrain the present analysis to the central $1\farcm75$ radius circular fields centred on the HzRGs. This rejects areas in the frame with lower coverage.

To determine a suitable flux density cut to the data, I first calculate the $5\farcs25$ radius aperture errors for each frame. This is done by placing random apertures upon the frame (within $1\farcm75$ radii circles), binning of source flux densities, and plotting the flux density distribution. I again perform a Gaussian fit to the lower part of the distribution, so as to avoid the positive skew due to flux from sources, and calculate the Gaussian width; this width gives me the RMS noise for each frame (RMS values are included in Tables 2.1 and 2.2). An example half-Gaussian fit to calculate the noise for field SWIRE-XMM is shown in Figure 2.2. The RMS values calculated for the SWIRE fields are smaller than those of Shupe et al. (2008) by a factor of ~ 1.35; however, the results here are consistent with their signal-to-noise measurements. For comparison, the average RMS noise for the HzRG fields is $23.0\,\mu$Jy, while for the SWIRE fields the average RMS noise is $29.6\,\mu$Jy. I adopt a flux density cut of $f_{24\mu\mathrm{m}} = 0.3\,\mathrm{mJy}$, corresponding to a minimum $S/N \sim 5$ for the fields with the highest RMS, after aperture correction (both for the HzRGs and for reference SWIRE fields, this is limited by

---

[5] area > 100 pixels and stellarity < 0.8

[6] area < 100 pixels or stellarity > 0.8

[7] http://ssc.spitzer.caltech.edu/mips/dh/mipsdatahandbook3.3.1.pdf

Table 2.1: SWIRE fields. In Col. 1 are the field names, in Col. 2 are the areas analysed, in Col. 3 are the RMS values calculated for $5''.25$ radii apertures (not aperture corrected). Column 4 states the average number of sources per $1.75'$ radius circular cell. The total number of $1.75'$ radius circular fields analysed in SWIRE is 9981 (area 26.7 deg^2), totalling 72295 sources.

Field Name (1)	Area (deg^2) (2)	RMS (μJy) (3)	$\bar{\text{N}}_{sources}$ ($1.75'$ rad) (4)
ELAIS N1	6.73	28.0	7.16
ELAIS N2	4.60	28.3	7.83
CDFS	7.69	27.9	7.16
Lockman	7.81	29.6	7.27
XMM-LSS	7.40	34.3	6.03

the SWIRE XMM-LSS fields). As will be shown in Sec. 2.6.5, the HzRG RMS values are found to be independent of 24μm source densities, which is indicative of a conservative cut free of questionable sources.

2.5.4 Densities in $1.75'$ circular cells

Contiguous $1.75'$ circular cells are placed on a grid (without overlap) within the five SWIRE fields, totalling some 9981 cells. The 24μm source densities are then calculated in each of these cells, with an imposed flux density cut of $f_{24\mu\mathrm{m}} = 0.3\,\mathrm{mJy}$. Source densities in the HzRG fields are calculated by centring the $1.75'$ radius apertures on the radio galaxy locations. When undertaking a sources-in-cell count for our HzRG fields, the HzRG itself is removed from the statistics. Uncertainties are calculated from small number statistics, following the method of Gehrels (1986).

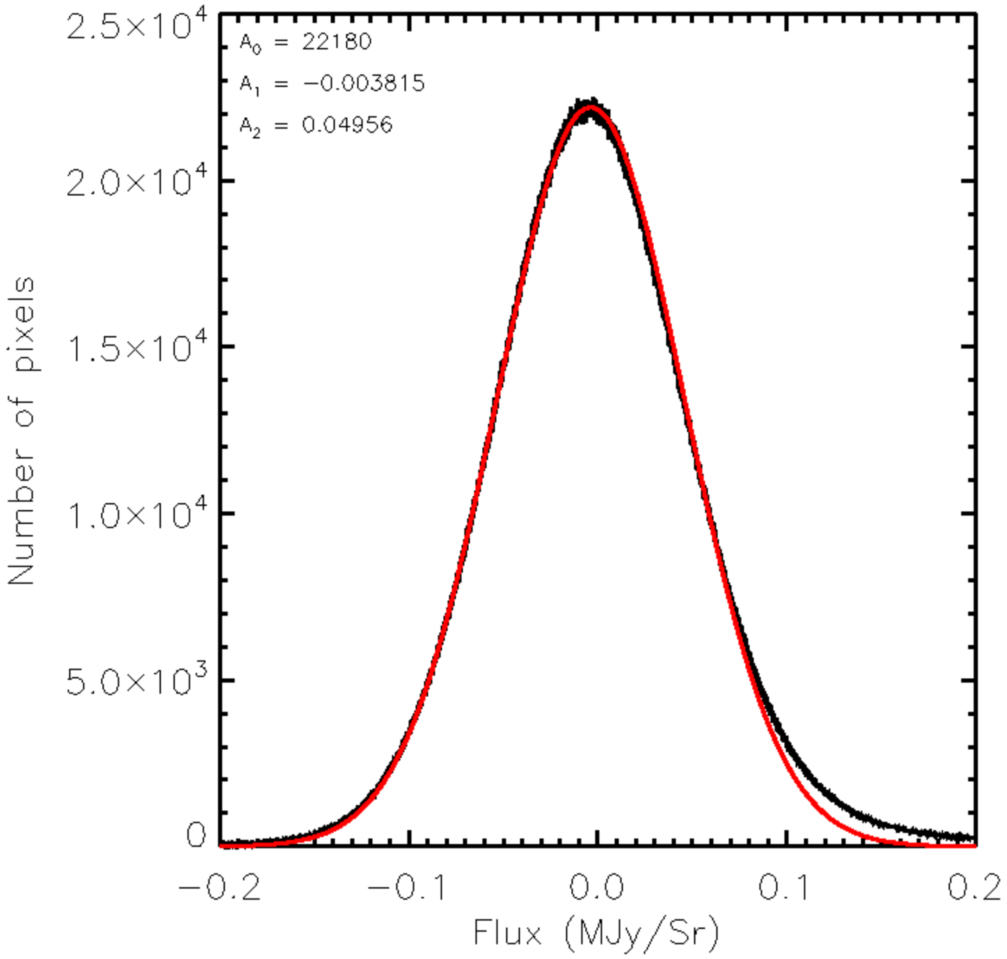

Figure 2.2: A plot showing a Gaussian (red) of which the lower half is fit to the noise (black) in reference field SWIRE-XMM. The high flux tail due to sources is obvious.

HzRG (1)	Redshift (2)	RMS Noise (3)	BG (4)	Exposure (5)	$\log_{10}(L_{500\mathrm{MHz}})$ (6)	# Sources (7)	$\delta\pm$Err (8)	$\delta(\sigma)$ (9)	P_{Poisson} (10)
3C356.0	1.079	19.5	0.76	450	28.35	8	$1.5^{+0.7}_{-0.5}$	1.1	0.073
MRC0037-258	1.100	22.1	0.75	900	27.72	7	$1.3^{+0.7}_{-0.5}$	0.7	0.113
3C368.0	1.132	27.6	0.73	450	28.52	11	$2.1^{+0.8}_{-0.6}$	2.3	0.010
6C0058+495	1.173	24.1	0.85	450	27.33	17	$3.2^{+1.0}_{-0.8}$	**4.7**	$2\times10{-5}$
3C65	1.176	24.0	0.89	900	28.63	15	$2.8^{+0.9}_{-0.7}$	**3.9**	$2\times10{-5}$
3C266	1.275	17.3	1.07	900	28.54	15	$2.8^{+0.9}_{-0.7}$	**3.9**	$2\times10{-5}$
MRC0211-256	1.300	20.6	0.79	900	27.78	12	$2.3^{+0.9}_{-0.6}$	2.7	0.005
MRC0114-211	1.410	18.8	0.79	900	28.66	16	$3.0^{+1.0}_{-0.7}$	**4.3**	$7\times10{-5}$
LBDS53w069	1.432	15.8	0.73	2100	26.30	20	$3.8^{+1.0}_{-0.8}$	**5.8**	$4\times10{-7}$
7C1756+6520	1.480	18.7	0.78	450	27.40	15	$2.8^{+0.9}_{-0.7}$	**3.9**	$2\times10{-5}$
7C1751+6809	1.540	18.0	0.78	450	27.46	9	$1.7^{+0.8}_{-0.6}$	1.5	0.042
LBDS53w091	1.552	12.6	0.73	2100	27.04	10	$1.9^{+0.8}_{-0.6}$	1.9	0.022
3C470	1.653	25.4	0.83	450	28.79	16	$3.0^{+1.0}_{-0.7}$	**4.3**	$7\times10{-5}$
MRC2224-273	1.679	27.6	0.75	900	27.52	11	$2.1^{+0.8}_{-0.6}$	2.3	0.010
6C0132+330	1.710	28.3	1.18	900	27.64	9	$1.7^{+0.8}_{-0.6}$	1.5	0.042
MRC1017-220	1.768	23.0	0.72	900	27.94	15	$2.8^{+0.9}_{-0.7}$	**3.9**	$2\times10{-5}$
3C239	1.781	26.7	1.07	900	29.00	10	$1.9^{+0.8}_{-0.6}$	1.9	0.022
3C294	1.786	25.2	0.49	900	28.96	9	$1.7^{+0.8}_{-0.6}$	1.5	0.042
7C1805+6332	1.840	18.5	0.78	450	27.78	21	$4.0^{+1.1}_{-0.9}$	**6.2**	$1\times10{-7}$
6CE0820+3642	1.860	23.3	0.78	900	28.28	7	$1.3^{+0.7}_{-0.5}$	0.7	0.113
6CE0905+3955	1.883	17.5	0.78	900	28.17	8	$1.5^{+0.7}_{-0.5}$	1.1	0.073
MRC0324-228	1.894	16.2	0.79	900	28.49	7	$1.3^{+0.7}_{-0.5}$	0.7	0.113
MRC0350-279	1.900	27.0	0.78	450	28.25	13	$2.5^{+0.9}_{-0.7}$	**3.1**	0.002
MRC0152-209	1.920	20.6	0.79	360	28.20	12	$2.3^{+0.9}_{-0.6}$	2.7	0.005
MRC2048-272	2.060	23.1	0.76	900	28.72	11	$2.1^{+0.8}_{-0.6}$	2.3	0.010

PKS1138-262	2.156	9.2	1.08	9300	29.07	16	$3.0^{+1.0}_{-0.7}$	**4.3**	8×10^{-5}
4C40.36	2.265	22.3	0.77	450	28.79	13	$2.5^{+0.9}_{-0.7}$	**3.1**	0.002
TXS0211-122	2.340	25.2	0.53	900	28.48	8	$1.5^{+0.7}_{-0.5}$	1.1	0.073
USS1707+105	2.349	17.7	0.79	900	28.63	10	$1.9^{+0.8}_{-0.6}$	1.9	0.022
USS1410-001	2.363	33.7	1.24	900	28.41	9	$1.7^{+0.8}_{-0.6}$	1.5	0.042
LBDS53w002	2.393	22.8	0.66	450	27.78	14	$2.6^{+0.9}_{-0.7}$	**3.5**	7×10^{-4}
6C0930+389	2.395	23.5	1.39	900	28.41	7	$1.3^{+0.7}_{-0.5}$	0.7	0.113
MRC0406-244	2.427	28.7	0.76	450	29.03	9	$1.7^{+0.8}_{-0.6}$	1.5	0.042
4C23.56	2.483	32.3	0.77	450	28.93	17	$3.2^{+1.0}_{-0.8}$	**4.7**	$2\times10-5$
MRC2104-242	2.491	28.4	0.78	900	28.84	12	$2.3^{+0.9}_{-0.6}$	2.7	0.005
WNJ1115+5016	2.540	19.2	1.47	900	27.82	8	$1.5^{+0.7}_{-0.5}$	1.1	0.073
PKS0529-549	2.575	30.5	0.79	450	29.16	18	$3.4^{+1.0}_{-0.8}$	**5.1**	7×10^{-6}
MRC2025-218	2.630	25.9	0.76	900	28.74	27	$5.1^{+1.2}_{-1.0}$	**8.7**	1×10^{-11}
USS2202+128	2.706	21.4	0.98	900	28.54	13	$2.5^{+0.9}_{-0.7}$	**3.1**	0.002
MG1019+0534	2.765	22.3	1.44	900	28.57	10	$1.9^{+0.8}_{-0.6}$	1.9	0.022
4C24.28	2.879	20.4	0.76	900	29.05	10	$1.9^{+0.8}_{-0.6}$	1.9	0.022
4C28.58	2.891	22.3	0.76	900	28.91	10	$1.9^{+0.8}_{-0.6}$	1.9	0.022
USS0943-242	2.923	17.3	0.66	450	28.62	9	$1.7^{+0.8}_{-0.6}$	1.5	0.042
WNJ0747+3654	2.992	31.5	0.81	900	28.14	15	$2.8^{+0.9}_{-0.7}$	**3.9**	$2\times10-4$
B3J2330+3927	3.086	19.4	0.69	450	28.33	11	$2.1^{+0.8}_{-0.6}$	2.3	0.010
MRC0316-257	3.130	23.1	0.79	900	28.95	16	$3.0^{+1.0}_{-0.7}$	**4.3**	8×10^{-5}
MRC0251-273	3.160	15.9	0.79	900	28.54	4	$0.8^{+0.6}_{-0.4}$	-0.5	0.168
WNJ1123+3141	3.217	25.9	1.45	900	28.51	4	$0.8^{+0.6}_{-0.4}$	-0.5	0.168
6C1232+39	3.220	19.2	1.10	900	28.93	8	$1.5^{+0.7}_{-0.5}$	1.1	0.073
TNJ0205+2242	3.506	26.5	0.77	900	28.46	6	$1.1^{+0.7}_{-0.4}$	0.3	0.151
TNJ0121+1320	3.516	28.3	0.78	900	28.49	5	$0.9^{+0.6}_{-0.4}$	-0.1	0.175
TXJ1908+7220	3.530	26.0	0.48	450	29.12	12	$2.3^{+0.9}_{-0.6}$	2.7	0.005

USS1243+036	3.570	29.4	1.45	900	29.23	12	$2.3^{+0.9}_{-0.6}$	2.7	0.005
WNJ1911+6342	3.590	19.4	0.77	450	28.14	7	$1.3^{+0.7}_{-0.5}$	0.7	0.113
MG2144+1928	3.592	25.6	0.85	900	29.08	12	$2.3^{+0.9}_{-0.6}$	2.7	0.005
6C0032+412	3.670	21.4	0.77	450	28.75	11	$2.1^{+0.8}_{-0.6}$	2.3	0.010
4C60.07	3.788	31.4	0.77	450	29.20	9	$1.7^{+0.8}_{-0.6}$	1.5	0.042
4C41.17	3.792	23.1	0.78	900	29.18	11	$2.1^{+0.8}_{-0.6}$	2.3	0.010
TNJ2007-1316	3.840	18.7	0.76	900	29.13	9	$1.7^{+0.8}_{-0.6}$	1.5	0.042
TNJ1338-1942	4.110	32.0	0.78	900	28.71	10	$1.9^{+0.8}_{-0.6}$	1.9	0.022
8C1435+635	4.250	21.0	0.76	450	29.40	9	$1.7^{+0.8}_{-0.6}$	1.5	0.042
6C0140+326	4.413	24.3	1.39	900	28.73	18	$3.4^{+1.0}_{-0.8}$	**5.1**	7×10^{-6}
TNJ0924-2201	5.195	23.1	0.74	450	29.51	7	$1.3^{+0.7}_{-0.5}$	0.7	0.113

Table 2.2: HzRG field Densities. HzRG names, redshifts, RMS noise values (for 5".25 radius apertures, not aperture corrected) and calculated background values in Cols. 1-4. Exposure time is stated in Col. 5. 500 MHz radio luminosities quoted in Col. 6 are taken from De Breuck et al. (2010). 1.75′ radius cells source counts and each field overdensity (with respect to the calculated SWIRE 1.75′ radius fields Gaussian peak, as per Fig. 2.3) along with their associated small-number statistical error in Cols. 7 and 8. Column 9 shows the field overdensities as a function of σ_N, corresponding to the probability of finding that given number of sources in a blank, non targeted field. Column 10 shows the Poisson probabilities for source overdensities (compared to the median field density of 5.2 sources. Fields classified as protocluster candidates (20) are in bold font.

2.6 Analysis

2.6.1 Comparison with SWIRE data

Figure 2.3 shows the source density distribution of the five reference SWIRE fields. The grey histogram represents the percentage of cells containing a given number of sources in SWIRE. The dashed line shows the Gaussian fit to the lower portion of this distribution, and exemplifies the positive skew in the SWIRE data due to clustering. The values for the Gaussian fit are $\langle N \rangle = 5.28$ with $\sigma_N = 2.52$. Superimposed upon this plot is a histogram of the HzRG field densities, whereby the histogram height represents the number of HzRG fields for a given number of sources. Along with the HzRG histogram the HzRG field names are included. I also overplot my criterion for protocluster candidacy of $N_{HzRG} \geq \langle N \rangle + 3\sigma_N = 12.84$, a cut which only six percent of SWIRE cells exceed. This comparison of the HzRG field data with the SWIRE fields shows such an overdensity in a significant minority (20 [32 percent]) of HzRG fields. The mean density of the HzRG fields is 11.6 ± 6.3, translating to a mean overdensity ($\delta = \frac{\bar{N}_{HzRG}}{\bar{N}_{SWIRE}}$) of 2.2 ± 1.2 over the reference SWIRE data, with a Kolmolgorov-Smirnov probability that the two datasets are drawn from the same distribution of 1.2×10^{-12}. Individual field source densities are included in Table 2.2

2.6.2 Comparison with IRAC

G12 study the environments of $1.2 \leq z \leq 3.0$ HzRGs and compare the densities of sources with IRAC $[3.6] - [4.5] > -0.1$ (AB) (within a certain flux density cut) found within one arcminute of the HzRG. The imposed colour cut selects against galaxies below $z \sim 1.2$, but does not distinguish between passive and active galaxies (Papovich 2008). Comparing the main result of this chapter, a significant fraction of the sources confirm the protocluster candidacies proposed in G12. The result of this comparison is shown in Fig. 2.4, where the 24μm source number in $1.75'$ radius circular cells is plotted against radio galaxy redshift. The dotted line, dark shaded region and light shaded region represent the SWIRE mean density, $\langle N \rangle$, $1\sigma_N$ and $3\sigma_N$ deviations, all extracted from the Gaussian fit described above. Plotted star symbols represent those sources with an overdensity in this work of

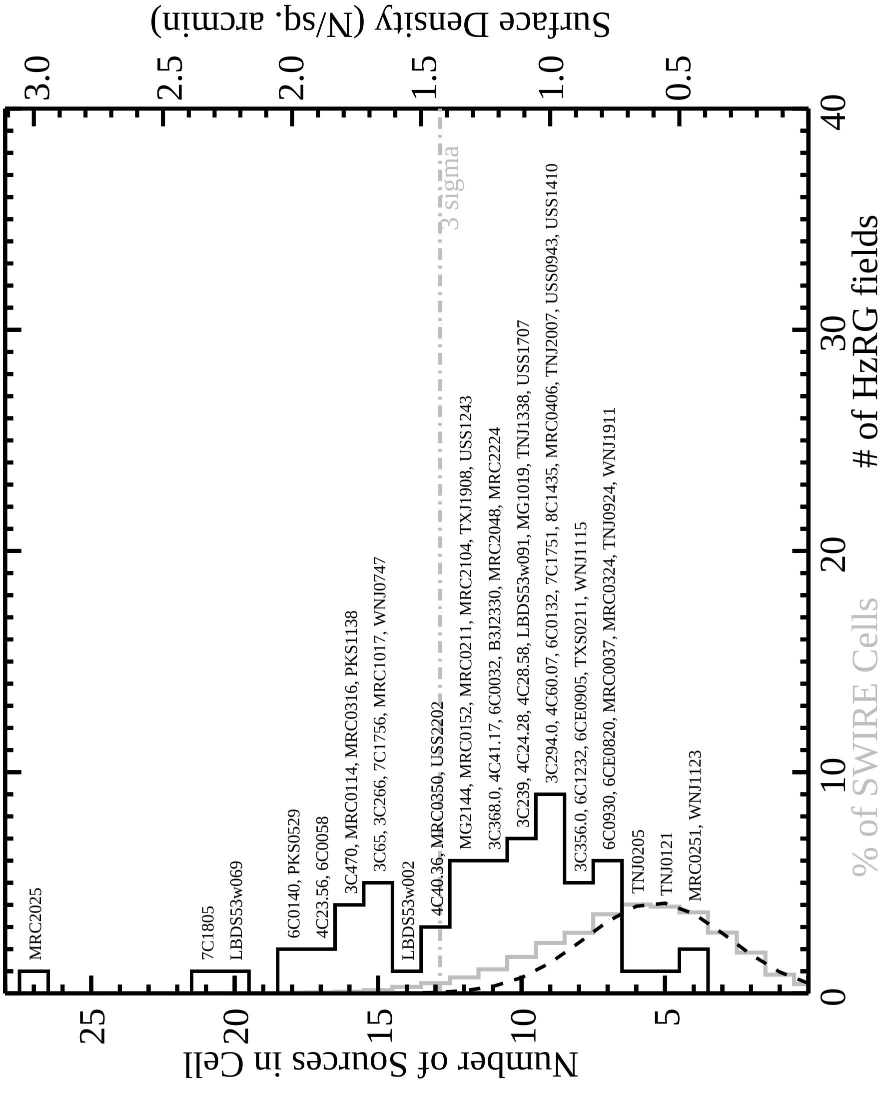

Figure 2.3: A comparison of HzRG source counts with the reference SWIRE fields. The distribution of the SWIRE 24μm source counts in $\sim 10,000$ circular cells of $1.75'$ radius, representing five SWIRE fields, is plotted as a grey histogram. A Gaussian fit to the lower part of this distribution is overlayed as a dashed line. A 3σ above the SWIRE mean is indicated as a dot-dash line. A histogram of HzRG field densities is overlayed along with each HzRG name. The corresponding source number density is indicated on the right-hand axis.

$\delta_{MIPS} \geq \langle N \rangle + 3\sigma_N$ and in G12 with an overdensity of $\delta_{IRAC} \geq \langle N \rangle + 2\sigma_N$. Plotted circles represent those remaining sources present in both catalogs, and the plotted plus symbols represent the fields which are not analysed in G12: **3C65** (z=1.176) and **LBDS53W059** (z=1.432). Notes on protocluster candidates are included in Sec. 2.7.1 and shown in Fig. 2.9.

Figure 2.5 shows the source field densities as measured in IRAC by G12 versus the 24μm source densities measured here. The source selection criteria in G12 is slightly different to that used here, since in G12 a colour cut is used to eliminate low-redshift interlopers. A strong correlation between the two values is found, despite the wavebands probing different populations. Of particular interest for further study may be those environments which are found to be significantly dense in one waveband but unremarkable or even underdense in the other, as these abnormalities may enlighten us with regard to structure formation. The Spearman Rank correlation is $\rho = 0.577$, implying a statistically significant correlation (e.g. there is a 99.992 percent probability that the two parameters are correlated).

As a check of the quality of our data, the RMS noise is plotted against the 24μm source density (Fig. 2.6). We expect there to be no obvious correlations between these values, and indeed no correlation is found. The Spearman Rank Correlation coefficient for these data is $\rho = 0.08$, implying only a 48.6 percent probability of a correlation between the values.

2.6.3 Dependence on Radio Luminosity

Plotting of 24μm, source density versus HzRG 500MHz luminosity (Fig. 2.7) shows no significant correlation between the two parameters. Though no work in the literature has had a large enough sample to statically prove or disprove any correlation, suggestions that high luminosity radio galaxies lie within a more dense medium have been put forward (Venemans et al. 2007, Miley and De Breuck 2008, Falder et al. 2010). The motivation for this is that higher luminosity radio galaxies

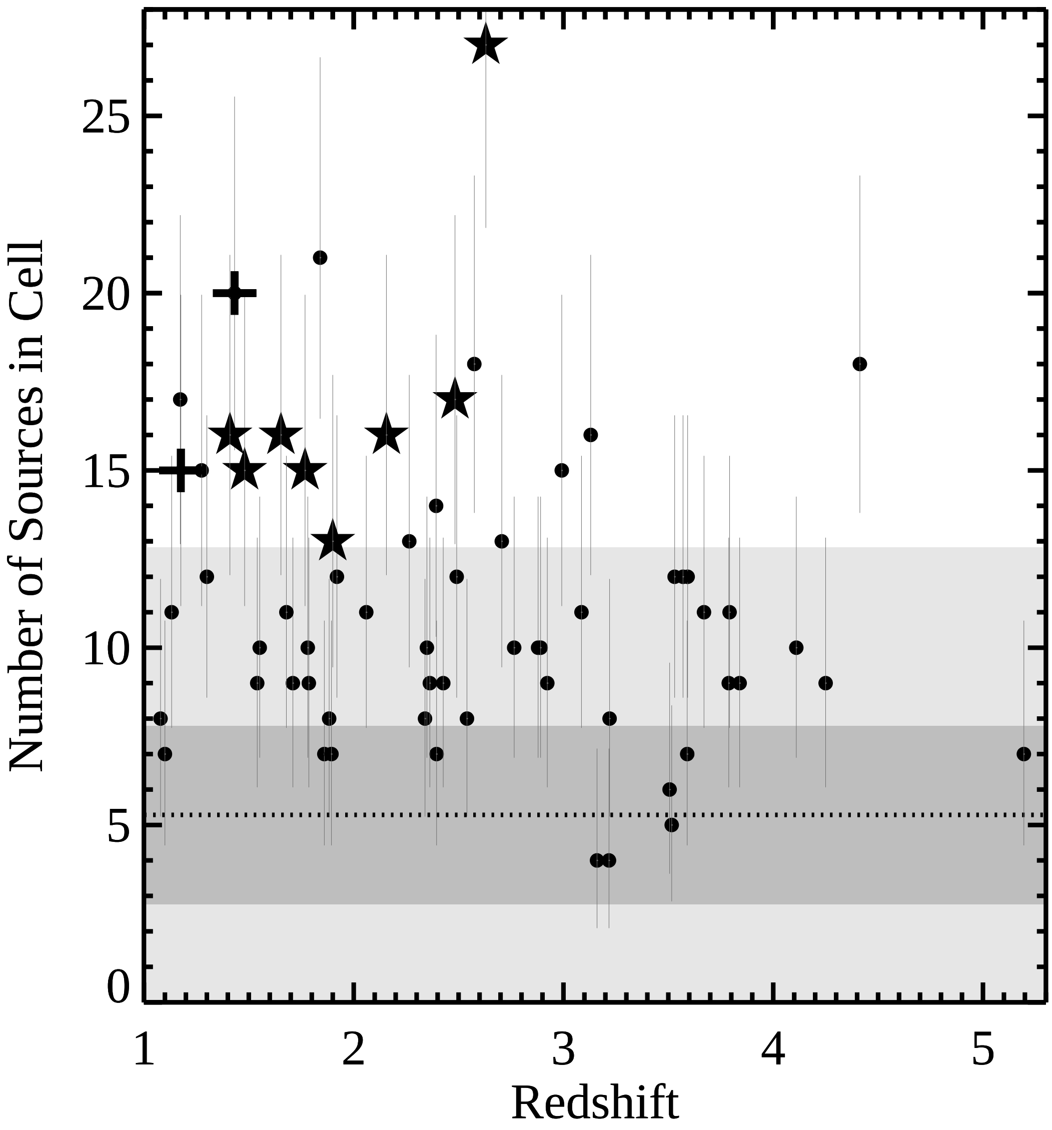

Figure 2.4: Source counts around each HzRG versus HzRG redshift. The dotted line indicates the SWIRE mean source count for a 1.75′ radius cell, the dark shaded region denotes ±1σ and the light shaded region denotes ±3σ on the SWIRE data. Starred symbols denote those sources which are considered candidate clusters in both this work and G12 (8) whilst the plus symbol sources (2) are those which are not studied in G12. Note that $z > 3$ sources are not deep enough to clarify protocluster candidacy in G12. The uncertainties on the source counts are derived from small number statistics.

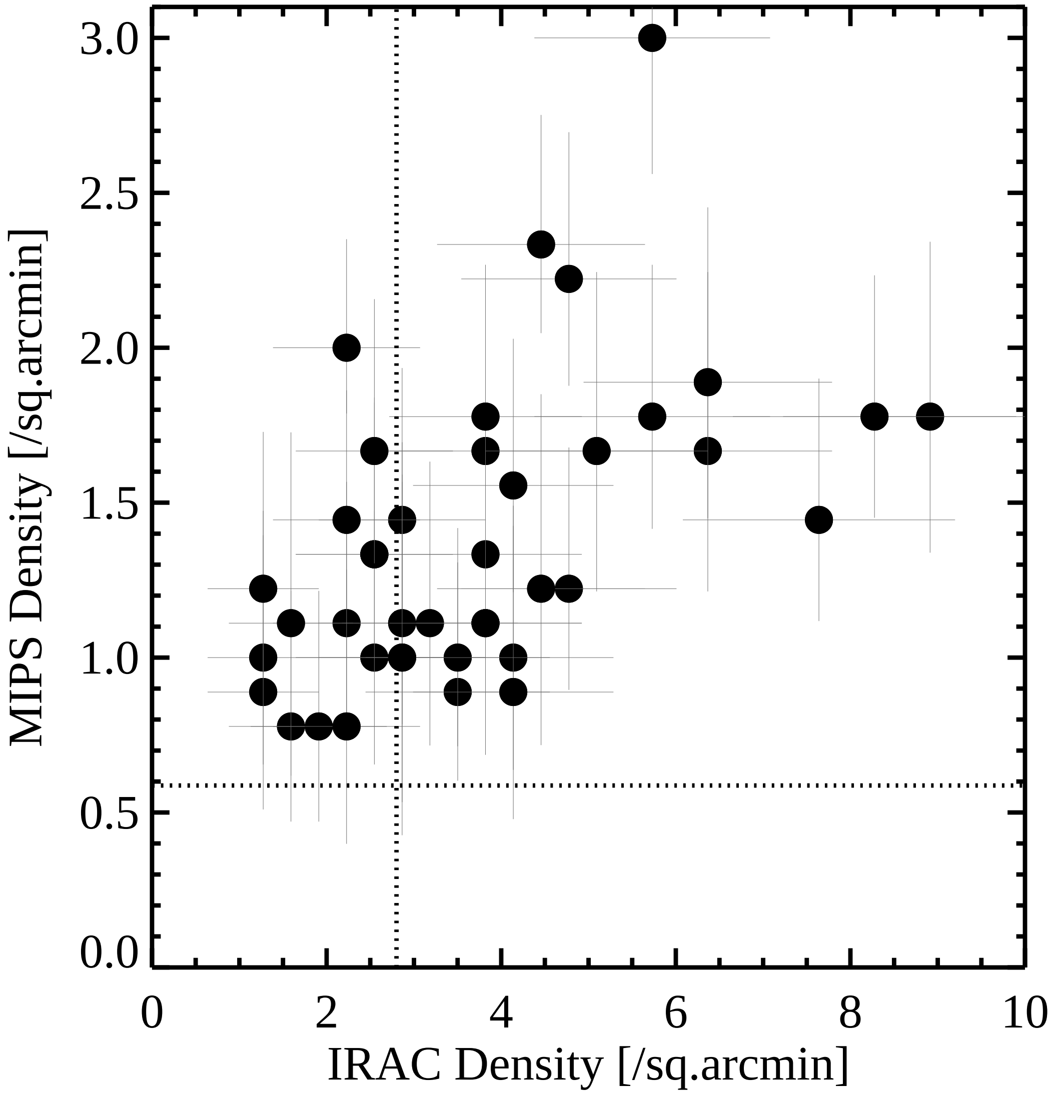

Figure 2.5: Comparison of MIPS field densities with IRAC $[3.6]-[4.5]>-0.1$ field densities from G12 ($1.2 \leq z \leq 3.0$). The horizontal and vertical dotted line correspond to the mean SWIRE 24μm and IRAC colour-selected values from SWIRE, respectively. A relatively strong correlation between source densities is found.

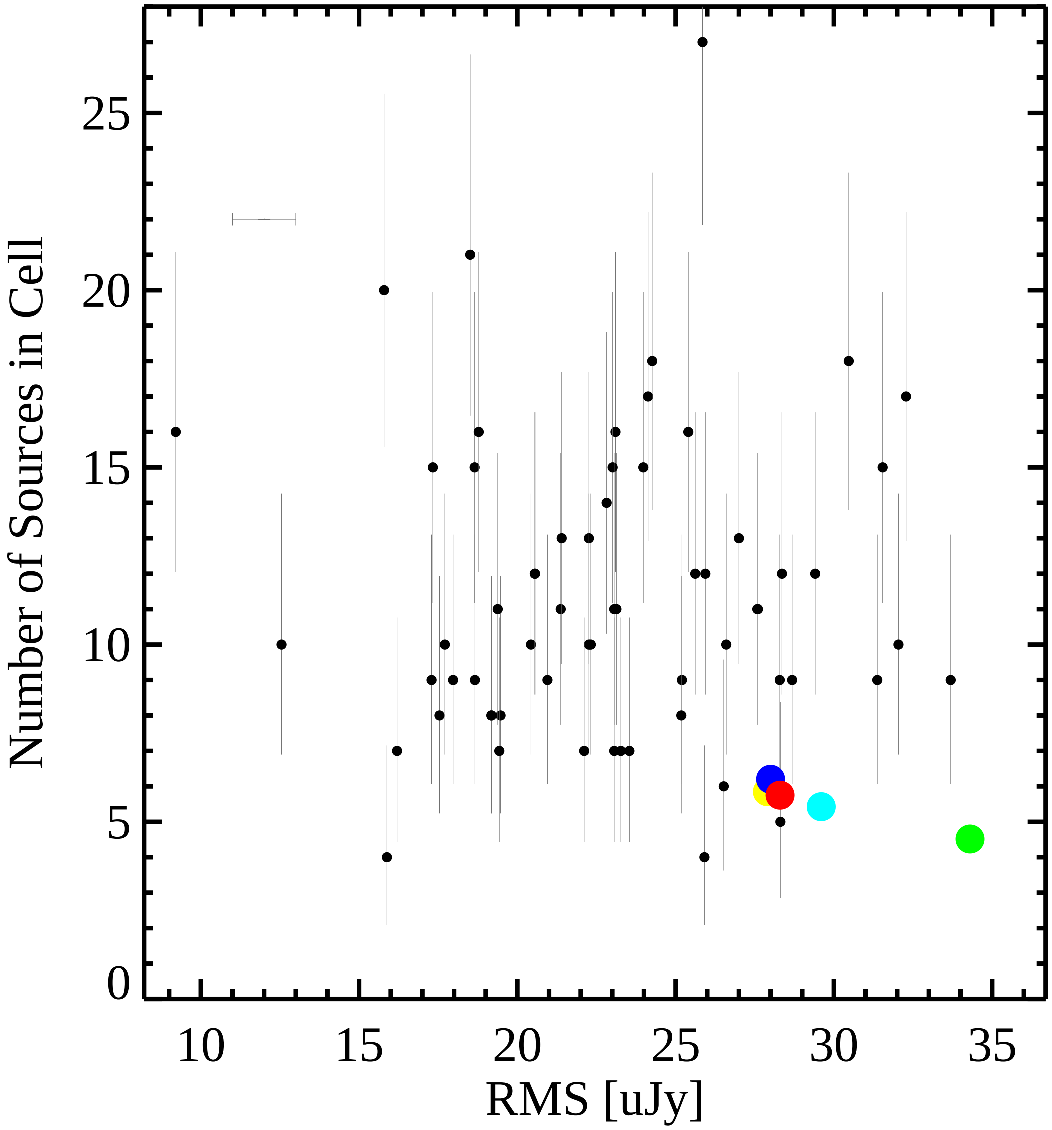

Figure 2.6: A plot of HzRG field density versus RMS noise. No obvious correlation between the two values is found. The error bar plotted in the upper left in included to give an indication of a typical uncertainty in the RMS values. SWIRE field values are plotted as larger circles where yellow, blue, red, green and cyan correspond to CDFS, EN1, EN2, XMM-LSS and Lockman fields respectively.

lie in a medium with a higher than average density, thus being more conducive to cluster formation. This work, alongside that of G12 are the first capable of making such a statistically significant comparison. Both find no such correlation between source density and HzRG 500 MHz luminosity. The Spearman Rank correlation coefficient recovered for these data is $\rho = 0.04$, implying only a 25 percent probability that the two parameters are correlated. Note that there is a small redshift-radio power degeneracy in this sample (especially at $z > 3$, see Fig. 2.7). Given that redshift and density are clearly correlated (see Fig 2.4) this may imprint a correlation between source density and radio power. We take this into account by using the Spearman Partial Rank correlation coefficient (Macklin 1982) which reduces the correlation coefficient to $\rho = 0.01$. We conclude that the 24μm source density does not depend on radio power.

2.6.4 K-correction and Population Type

This sample covers a wide range in redshifts, and the observed 24μm, band therefore covers significantly different rest-frame wavelengths.

To examine the K-correction effects, I map the SEDs of a starburst galaxy (Siebenmorgen and Krügel 2007) as well as face- and edge-on quasars (Pier and Krolik 1992) through the MIPS 24μm transmission window for redshifts $1 < z < 5.2$ (Fig. 2.8). The starburst galaxy has Star Formation Rate (SFR) = $1000\,\mathrm{M}_\odot/\mathrm{yr}$. The face-on and edge-on quasars have $L_{24\mu\mathrm{m}} = 10^{45}\,\mathrm{erg\ s}^{-1}$. These are plotted black continuous, green dashed and blue dot-dashed lines respectively. The 0.3 mJy flux density cut in indicated by the black dot-dot-dot-dashed line.

It is interesting to note a number of things; (1) the relative flatness of the quasar flux density over the entire redshift range, due to hot dust entering the MIPS transmission window; and (2) the bump in the starburst SED at $z \sim 1.5$, due to the PAH emission lines (dominated by 7.7μm) entering the MIPS transmission window. Note that the smoothness of the starburst line is due to the broad MIPS 24μm transmission window covering some 9μm between $\sim 20-29\mu$m, thus smoothing out the more narrow PAH features. Also note that even for such a high SFR starburst, galaxies fall below the flux density cut beyond redshift three. Finally, the orientation of quasars will have a large impact on their detectability at lower luminosities.

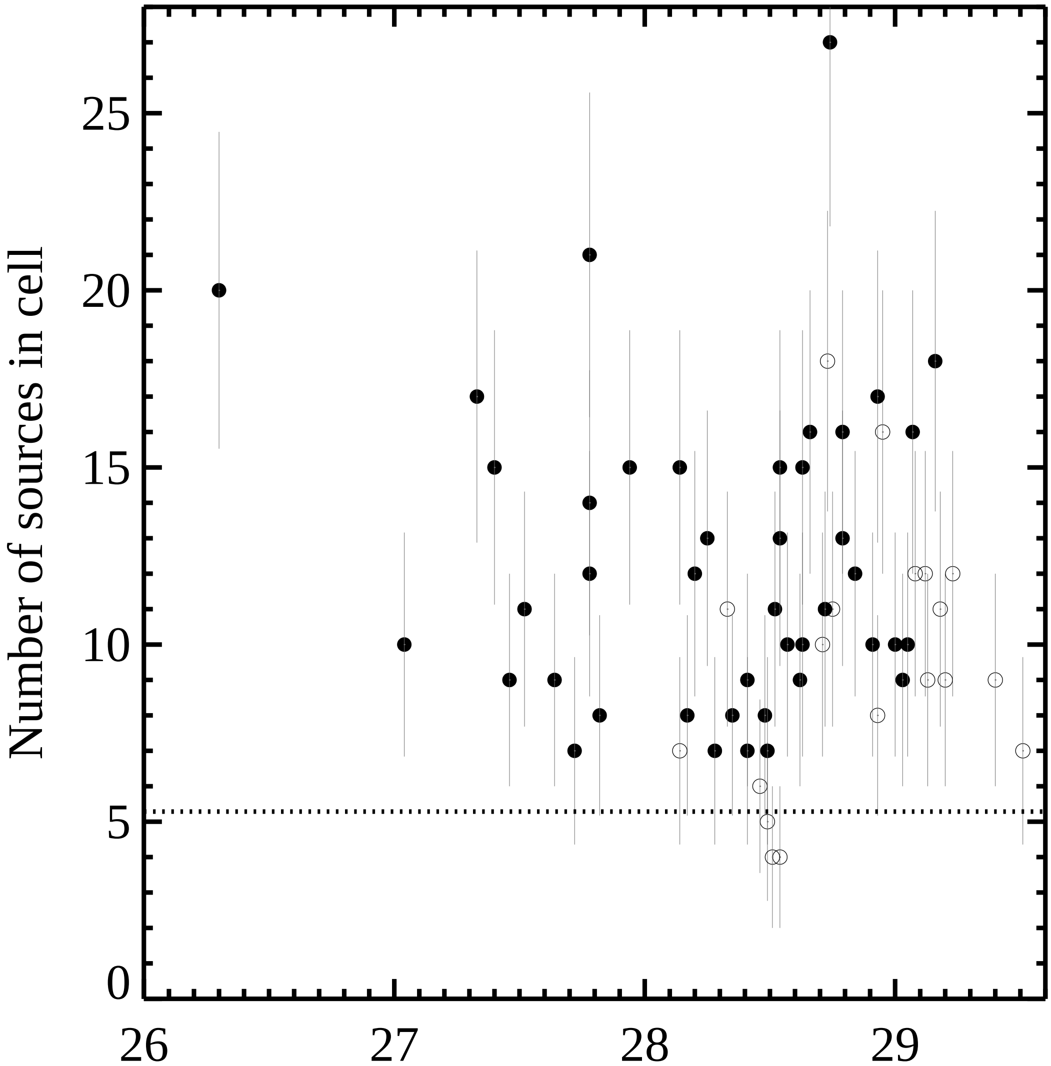

Figure 2.7: HzRG 24μm, field densities versus HzRG 500 MHz luminosities (taken from De Breuck et al. 2010). The HzRGs with $z > 3.0$ are plotted as open symbols.

By comparing a high SFR starburst to a moderately luminous quasar, as shown in Fig. 2.8, we can make the assumption[8] that above a redshift of $z \sim 3$ I am probing almost exclusively the quasar population. On the other hand, below $z \sim 3$, I am simultaneously probing the quasar and starburst populations, with starbursts become ever-more important at redshifts two and below.

Since we are probing down to different luminosities at different redshifts, it is entirely likely to see higher densities in fields at lower redshifts. This is indeed what we observe; as shown in Fig. 2.4 the *highest* density fields ($\delta(\sigma) \gtrsim 4.5$) almost exclusively lie below a redshift of three. Reddy et al. (2006, see Fig. 2) compare spectroscopically confirmed 24μm sources in the GOODS-North field between redshifts $1 \leq z \leq 2.6$. For a flux density cut of $f_{24\mu\mathrm{m}} \geq 0.3\,\mathrm{mJy}$, they find only Sub-Millimetre Galaxies (SMGs) and X-ray sources in the field, consistent with probing the starburst galaxy and AGN populations.

The minimum AGN luminosities which I can probe with a flux density cut of 0.1mJy are $3.4 \times 10^{41}\,\mathrm{erg\,s^{-1}}$ at $z = 1$ to $1.9 \times 10^{43}\,\mathrm{erg\,s^{-1}}$ at $z = 5.2$. Compare this with the minimum SFRs which can equivalently be probed; SFR$= 100\,\mathrm{M_\odot\,yr^{-1}}$ at $z = 1$ to a SFR $\sim 1000\,\mathrm{M_\odot\,yr^{-1}}$ at $z = 3$. These values have been calculated using the relevant formulae from Rieke et al. (2009).

Since I do not know the physical nature of every object in each frame, let alone the redshift of each of these sources, it is not possible to perform K-corrections. For K-corrections to be calculated one will need to scrutinise the complimentary IRAC data for these fields, as well as gain data in the Far-IR. This process is currently being undertaken (Wylezalek et al. 2013). However, it is beyond the scope of this work, which concentrates only on the statistical properties of HzRG fields.

2.6.5 Evolution with Redshift

Figure 2.4 also shows the HzRG field densities versus HzRG redshift. If **6C0140+326** (z=4.413) is a lensed system (as suggested in Lacy 1999) and as such possibly contaminated by artificially brightened sources, then this field should be removed from my sample. If I do remove this field, then I begin to

---

[8] if we assume no evolution of the luminosity functions.

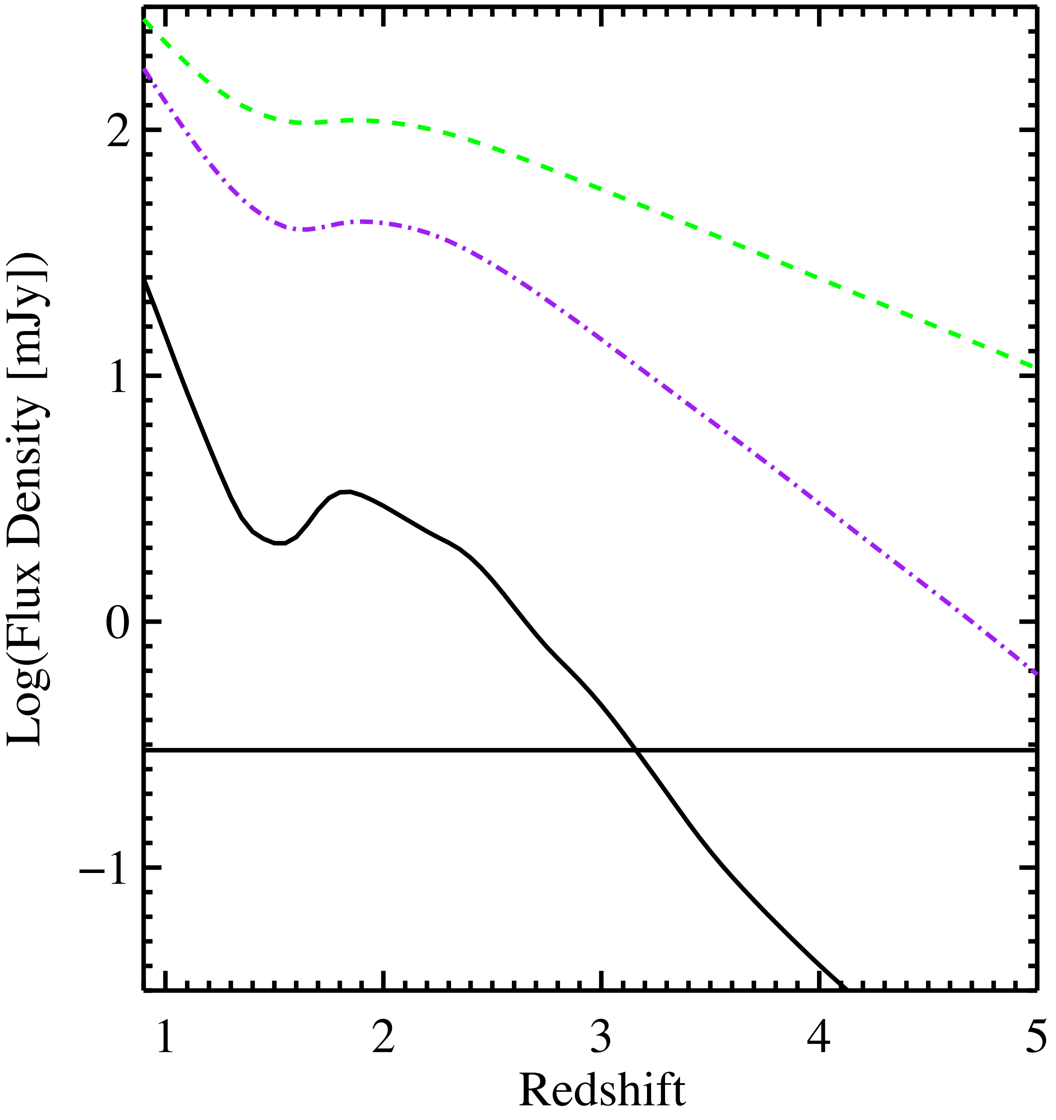

Figure 2.8: predicted MIPS 24μm, flux density versus redshift. Solid black line represents a starburst galaxy with a star formation rate of 1000 $M_{\odot}\,yr^{-1}$. The dashed green line and dot-dash blue line represent a face-on and an edge-on quasar with $L_{24\mu m} = 10^{45}$ erg s^{-1}. The horizontal line represents the 0.3 mJy flux density cut.

see a general trend towards smaller-overdensities at early epochs. This could be interpreted in two ways: (1) the cluster luminosity function is truly evolving over time; or (2) the imposed flux density cut is too high to probe comparable populations at higher redshifts, as discussed above.

Since I am probing different populations at lower ($z = 1 - 2$) and higher ($z = 3 - 5$) redshifts, with a transitory region between them, higher source densities at later epochs is the behavior that one would expect. However, since we also expect structure formation to be evolutionary, and not instantaneous, observations of higher overdensities at lower redshifts may not be due to selection bias alone. The mid-IR luminosity function has been measured to $z \sim 2.5$ through stacking analysis (Caputi et al. 2007, Rodighiero et al. 2010) though is essentially unconstrained at $z > 2.5$. We do not expect a significant increase in number density at higher redshifts as this would be inconsistent with star-formation rate density-evolution(Lilly et al. 1996, Madau et al. 1996); the high-end of the mid-IR luminosity function must drop off at high redshift, though constraints are too poor to infer population statistics.

2.7 Discussion

The above work appears to confirm that HzRGs lie in overdense regions of the Universe, but that the source overdensity in the HzRGs vicinities does not depend on the radio power of the HzRG itself. It is well known however that Radio Galaxies are predominantly associated with high stellar mass galaxies, which in turn are found to occur in larger dark matter haloes. Thus in order to undertake a more fair comparison one must investigate differences in the environments of these HzRGs with those of high redshift high stellar mass objects which are not Radio Galaxies at or near the same epochs. Photometric redshift data exist for many galaxies in the SWIRE fields, and subsequent work may benefit from selecting "like-for-like" samples non-radio galaxy high redshift sources, whether by 24μm luminosity or otherwise (perhaps by multiband photometric SED-fitting for stellar masses/star formation rates. Undertaking such an analysis may help to mitigate problems with comparing these HzRG fields with blank fields, but maybe subject to a raft of different selection effects based on the method of SED fitting and flux limits in a number of different wavebands.

It is paramount that spectroscopic observations be taken for these protocluster candidate fields in order to either confirm or deny their candidacy. Many works have undertaken detailed spectroscopic follow-up observations of protocluster candidates; the works of Venemans et al. (2005; 2007), Maschietto et al. (2008), Kuiper et al. (2010), Kuiper et al. (2012), for example, have undertaken followup observations of protocluster candidate MRC0316-257 (studied here), confirming the field's protocluster candidacy. Previous observations of the fields studied here are detailed below.

2.7.1 Notes on Individual Sources

For the sake of a well defined sample, I only select 24μm targets with an $N_{\rm HzRG} > \langle \rm N_{SWIRE} \rangle + 3\sigma$ as cluster candidates. This accounts for 20 (32 percent) of the HzRG sample. For all sources that meet this criterion, cutouts are included in Fig. 2.9. Fields are sorted by increasing redshift. Quoted sigma values correspond to the probability of finding protocluster candidates compared to a blank, non-targeted field.

6C0058+495 (z=1.173)

I find a 24μm source overdensity of 4.7σ, with the sources in this field having a clumpy structure. This field is my lowest redshift protocluster candidate.

3C65 (z=1.176)

This field was first studied by Best (2000), who found a K-band overdensity. My study confirms an overdensity in 3C65 at a 3.9σ level.

3C266 (z=1.275)

This field has also been studied in G12, but its source overdensity was not significant enough to declare protocluster candidacy. This work however finds a 24μm source overdensity of 3.9σ, making it a firm candidate.

MRC0114-211 (z=1.41)

With an overdensity of IRAC sources significant at a 6σ level compared to the field, MRC0114-211 is the densest field and most promising cluster candidate in

G12. I also find an overdensity of 24μm sources at the 4.3σ significance.

LBDS53W069 (z=1.432)

This is formally not a radio galaxy according to the radio luminosity cutoff defined by Seymour et al. (2007). Nevertheless, this work shows a significant 24μm source overdensity at 5.8σ; observationally this field is very dense with no preferred spatial segregation. This field was not included in G12's $[3.6] - [4.5] > -0.1$ analysis, but it has been calculated that this field would represent a 4.8σ overdensity.

7C1756+6520 (z=1.48)

This field is a known protocluster, first identified in Galametz et al. (2009) and spectroscopically confirmed in Galametz et al. (2010). This work confirms that 7C1756+6520 is also a protocluster candidate at 24μm with a source overdensity of 3.9σ.

3C470 (z=1.653)

This field was first studied in G12, with a source overdensity of 2.9σ. This work quotes a 24μm source overdensity of 4.3σ.

MRC1017-220 (z=1.768)

This field was first studied by Cimatti et al. (2000), who found an overdensity of EROs. Studies of near-IR selected galaxies (Galametz et al. 2010) and IRAC-selected galaxies (G12), however, did not find a significant overdensity. This work finds a 24μm source overdensity at the 3.9σ level.

7C1805+6332 (z=1.84)

This field was first studied in Galametz (2010), where no near-IR overdensity was reported. This field was also studied in G12, which again did not find a significant overdensity. This work finds a 24μm source overdensity at 6.2σ, making it a very strong protocluster candidate. Observationally, sources lie in a filamentary structure in the NE-SW direction.

MRC0350-279 (z=1.9)

Field studied in G12, with an IRAC source overdensity of $\sim 5.2\sigma$ derived. Here, the 24μm source overdensity is 3.1σ. Observationally the field is very much clustered towards the East of the HzRG.

PKS1138-262 (z=2.156)

PKS1138-262 is a well studied protocluster environment with overdensities of Lyα and X-ray sources (Pentericci et al. 2000; 2002), as well as Hα emitters and EROs (Kurk et al. 2004a;b). This work finds an overdensity of 24μm sources at 4.3σ.

4C40.36 (z=2.265)

This field was studied in G12, who found an underdensity of red IRAC sources. This work quotes a 24μm source overdensity of 3.1σ. Sources appear to lie in a filamentary E-W structure.

LBDS53W002 (z=2.393)

This field was studied in G12, but no significant overdensity was found. The 24μm source overdensity quoted here is 3.5σ. The structure appears to have some form of preferred direction, though this remains ambiguous without a larger field of view.

4C23.56 (z=2.483)

There are many works covering this field, beginning with Knopp and Chambers (1997) that quote a "marginally significant excess of objects" in the K-band. Other works have found overdensities in the near-IR (Kajisawa et al. 2006), of Hα emitters (Tanaka et al. 2011) and mid-IR (G12). This work finds a 24μm source overdensity at a 4.7σ level.

PKS0529-549 (z=2.575)

This field was studied in G12 and its environment was found to be underdense. Here, however, a significant 24μm source overdensity of 5.1σ is found. The sources appear to be very strongly clustered within the 1.75′ radius frame, making this field a firm protocluster candidate at 24μm.

MRC2025-218 (z=2.63)

This is our highest density field, and has recently been studied by G12, quoting a 2.9σ overdensity. Our result shows a 24μm source overdensity at 8.6σ, with 27 ($f_{24\mu\mathrm{m}} > 0.3\,\mathrm{mJy}$) sources in a 1.75′ radius field. This exceeds the number of sources in every 1.75′ radius SWIRE sub-field from our analysis.

USS2202+128 (z=2.706)

This field was studied in G12, who found no overdensity. Here, the 24μm source overdensity is quoted as 3.1σ making it a firm protocluster candidate. Clustering appears mostly in the North of the frame, centred on a bright object $\sim 30''$ from the HzRG.

WNJ0747+3654 (z=2.992)

A 24μm overdensity of 3.9σ is found in this field, making **WNJ0747+3654** a strong protocluster candidate. Upon visual inspection, local clustering of sources (within the 1.75′ radius cell) appears to be taking place, though on larger scales (outside of the cell) no spatial segregation appears to be present.

MRC0316-257 (z=3.13)

This target is a known Lyα and `[OIII]` protocluster (Venemans et al. 2005; 2007, Maschietto et al. 2008, Kuiper et al. 2010), which our work also confirms with a 24μm source overdensity of 4.3σ.

6C0140+326 (z=4.413)

This is a known protocluster, having recently been studied by Kuiper et al. (2011), with a Lyα overdensity of 9 ± 5 over a random field distribution. My result confirms a 24μm source overdensity in the vicinity of 6C0140+326 at 5.1σ. However, if it is lensed as suggested in Lacy 1999, then this field may be contaminated by artificially brightened sources.

2.8 Conclusions

Mid-IR emission is a powerful tracer of both AGN (torus-dust) and starburst galaxies, making mid-IR observations ideal for finding galaxy clusters in the early Universe. Using targeted observations in the mid-IR, I have investigated the fields of 63 HzRGs and find a statistically significant source overdensity over SWIRE reference fields data. I find a large minority of the targeted fields, 20, or 32 percent, to be overdense to at least a 3σ significance, confirming 11 known protoclusters (or existing protocluster candidates). I identify nine new protocluster candidates. Targeted mid-IR observations of HzRG fields shows to be a powerful technique for protocluster candidate selection.

These overdensities are indicative of the presence of protoclusters with active and star−forming galaxies at high redshifts. My results indicate a redshift evolution of source density, but this may be due to an insensitivity to star-forming galaxies at high redshifts. My dataset is compared with recent results of IRAC colour selected densities and correlations between the data are found.

Further work with regard to these data will involve spectroscopic follow-ups for each of the cluster candidates in order to confirm members. Meanwhile Far-IR photometry currently being undertaken, in conjunction with the existing *Spitzer* data will allow a more complete knowledge of the population which make up these overdense fields.

HzRGs are extremely useful beacons for observing the early Universe, especially in high density environments - the birth places of present day clusters. What is still not truly understood is why these active galaxies are so prevalent at early times and so rare in the current epoch. Several threads of research arise from the study of HzRGs; large scale structure, AGN evolution, AGN host galaxy evolution, to name a few, and HzRGs remain exciting phenomena in their own right. Continued study of these objects and their environments will allow us to eventually bring together these topics to form a more complete understanding of the evolution of AGN, and their impact on host galaxies and their surroundings.

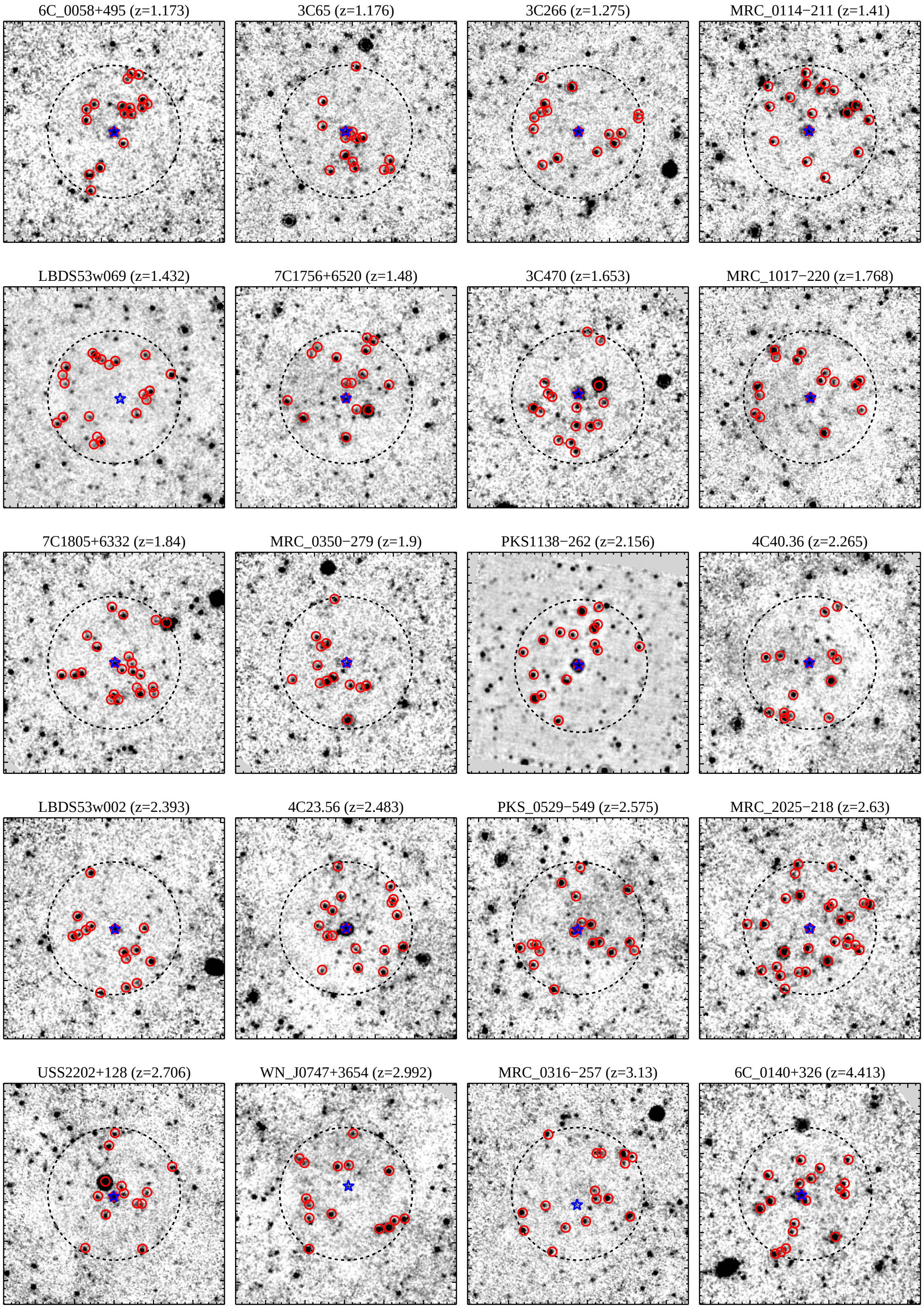

Figure 2.9: Cutouts of all HzRG 24μm, fields with a 3σ significance source overdensity. The dotted circle represents the $1.75'$ radius circular sub-field that is analysed further, and plotted in red are the source for which $f_{24\mu m} \geq 0.3\,$mJy. All fields are scaled to the same $5.8' \times 5.8'$ angular size, with North/East facing up/left. The HzRG is plotted as a blue star in each frame. Note that **PKS1138-262** is much deeper GTO data.

Chapter 3

The Effect of Partial Obscuration on the Obscured Fraction *vs.* X-ray Luminosity Trend Observed in Active Galactic Nuclei

3.1 Abstract

Surveys of AGN in different observational regimes seem to give different answers for the behaviour of the obscured fraction with luminosity. Based on the complex spectra seen in recent studies, I note that partial covering could significantly change the apparent luminosities of many AGN, even after apparent X-ray absorption correction. I explore whether this effect could reproduce the observed dependence of the obscured fraction on the apparent X-ray luminosities seen between 2 and 10 keV. I can reproduce the observed trend in a model where 33 per cent of AGN are unobscured, 30 per cent are heavily buried and 37 per cent have a range of intermediate partial coverings. This model is also tentatively successful at reproducing observed trends in the X-ray versus infrared luminosity ratio for AGN.

Throughout this chapter I use the term “obscured sources” to mean those sources showing signs of attenuation either in the X-ray regime (i.e. a characteristic drop in the flux at low X-ray energies, deviating away from the assumed intrinsic power-law spectrum) or the optical regime (i.e. no broad lines or BBB; more commonly referred to as Type-II objects).

I differentiate between partially obscured sources and partially covered sources. To clarify, I define partially obscured sources to be partially covered with a medium of *some* given column density, which will generally range of $N_{\mathrm{H}} \sim 10^{19} - 10^{26}\mathrm{cm}^{-2}$, – from negligible to Compton Thick (CT) and beyond. Partially covered sources on the other hand are taken to be partially covered with an assumed CT fraction such that all X-ray flux ($E_{\gamma} < 10$keV) in that region is completely attenuated.

During the discussion I make several references to partially covered sources, however, since these are physically indistinguishable (both observationally and mathematically) from *totally covered* sources plus a back-scattered fraction, I use the term to correspond to either phenomenon in equal weight. To clear any further confusion, the *obscured fraction* is used to mean the total fraction of sources showing *some* level of obscuration in their X-ray spectra. Typically the *measured* obscuration in these sources is Compton thin, as the sources still have a measurable flux at $E_{\gamma} < 10$keV.

3.2 Introduction

3.2.1 The Obscured Fraction

The first work on a sample large enough to test the obscured AGN fraction-luminosity dependence in a statistical fashion (Lawrence and Elvis 1982) found that fraction of obscured objects (f_{obsc}) to decrease as a function of X-ray luminosity. This trend has also been found as a function of radio luminosity in radio loud sources (Lawrence 1991) and further works have confirmed this trend in soft X-rays (< 10keV) (Hasinger 2008), hard X-rays (Tueller et al. 2010) and using optical `[OIII]` luminosities (Simpson 2005). This result remains controversial since the observed trends are largely regime dependent and subject to associated selection effects. It has been argued (Lu et al. 2010) that the observed anti-correlation in the obscured fraction-$\mathrm{L}_{\texttt{[OIII]}}$ can be accounted for purely on grounds of selection effects and extinction correction.

For instance, more recent radio, IR and volume limited optical samples find f_{obsc} consistent with being fixed across many decades in luminosity (de Grijp et al. (1992), Rush et al. (1993), Lacy et al. (2007), Ogle et al. (2006), Ho et al. (1997), Willott et al. (2000), see Lawrence and Elvis (2010) for discussion), though quantifying f_{obsc} in these regimes still remains inconsistent:

The major example is the difference in classification between the optical and X-ray regimes. In the optical regime one uses the presence of broad permitted lines and of a BBB to classify an object as a Type-I AGN, whilst in the X-ray, one classifies *unobscured* objects as those which so no signs of attenuation in their characteristic power law spectrum.

Therefore, one naively assumes optical Type-II objects as routinely having some form of optical obscuration of their BLR and BBB, whilst their X-ray counterparts show X-ray obscuration. We may indeed be selecting different classes of object; these two obscuring phenomena may or may not be related to one another, therefore classification diagnostics which use only one observational regime may be subject to strong selection effects. Classification of radio AGN into Type-I and Type-II objects still relies on optical diagnostics but is obviously biased towards RLAGN over RQAGN. Any results regarding a derived f_{obsc} must take into account the sample selection bias.

While at the lower luminosities the observational evidence supporting the unified scheme is substantial, at higher luminosities there are still major issues. One such issue is that of the “torus” opening angle; an attempt to explain the f_{obsc} vs. luminosity trend observed in X-ray and some optical regimes argue for a torus opening angle-luminosity dependence i.e. the obscured to unobscured fraction is dependent on the intrinsic luminosity (Lawrence 1991, Simpson 2005). This *receding torus model* relies on tori having a defined height but with inner radii as defined by the dust sublimation radius of the AGN, which is determined by the local temperature and hence the luminosity of the central engine.

In the hard X-ray (> 10keV) (e.g. Tueller et al. 2010), one should still be able to observe sources which are attenuated at softer energies. As such, this should mitigate much of the selection effects associated with softer X-ray observations. Wang and Jiang (2006) have argued that by removing very heavily obscured

(CT) sources, much of the aforementioned observed luminosity trend disappears. It is interesting to note the presence of the well studied archetypal Type-II AGN `NGC 1068` within the Tueller et al. Burst Alert Telescope (BAT) sample, given at a quoted X-ray luminosity some two decades fainter than its intrinsic X-ray luminosity inferred from hard X-ray model extrapolations.

3.2.2 Attenuation

In modelling the attenuation of an X-ray spectrum, one must characterise the cross-section. The total cross section is dependent on dominant phenomena in this energy range; photoelectric absorption and Thomson/Compton scattering. The cross section for the first phenomena, photoelectric absorption is taken from laboratory measurements and is a complex function highly dependent on the ionisation edges of elements present in the medium. The formulism used here is taken from laboratory experiments carried out by Morrison and McCammon in 1983:

Energy Range (KeV)	c_0	c_1	c_2	Edge
0.030 - 0.100	17.3	608.1	-2150	–
0.100 - 0.284	34.6	267.9	-476.1	C
0.284 - 0.400	78.1	18.8	-4.3	N
0.400 - 0.532	71.4	66.8	-51.4	0
0.532 - 0.707	95.5	145.8	-61.1	Fe-L
0.707 - 0.867	308.9	-308.6	-294.0	Ne
0.867 - 1.303	120.6	169.3	-47.7	Mg
1.303 - 1.840	141.3	146.8	-31.5	Si
1.840 - 2.471	202.7	104.7	-17.0	S
2.471 - 3.210	342.7	18.7	0.0	Ar
3.210 - 4.038	352.7	18.7	0.0	Ca
4.038 - 7.111	433.9	-2.4	0.75	Fe
7.111 - 8.331	629.0	30.9	0.0	Ni
8.331 - 10.00	710.2	25.2	0.0	–

where the photoelectric absorption cross section per hydrogen atom, σ_{PE} is:

$$\sigma_{PE} = (c_0 + c_1 E + c_2 E^2) E^{-3} \times 10^{-24} \text{cm}^2 \tag{3.1}$$

and the energy E is in units of keV. The second and third cross-section components, those due to Thomson and Compton scattering can be combined, since Thomson scattering is the low-energy limit to Compton scattering. In Thomson scattering **elastic** scattering of a photon by a charged particle, while Compton scattering is the equivalent **inelastic** scattering. At lower energies ($\lesssim$ 1keV) the correction to the cross section is negligible, whilst at higher energies the correction can become substantial. The Thomson/Compton cross-section can be derived from quantum electrodymanics, was done so by Klein and Nishina in 1929 can be parametrized as follows:

$$\sigma_{KN} = \frac{2\pi e^4}{m^2 c^4}\left[\frac{1+\beta}{\beta^2}\left(\frac{2(1+\beta)}{1+2\beta} - \frac{1}{\beta} ln(1+2\beta)\right) + \frac{1}{2\beta} ln(1+2\beta) - \frac{1+3\beta}{(1+2\beta)^2}\right] \tag{3.2}$$

where e is the electron charge (1.6×10^{19} C), m is the electron mass (9.11×10^{-31}kg), c is the speed of light ($3 \times 10^8 \mathrm{m\,s^{-1}}$) and β is

$$\beta = \frac{E}{mc^2} \tag{3.3}$$

and E is the photon energy. The left-hand term $\frac{2\pi e^4}{m^2 c^4}$ is simply the Thomson cross section (which is simply $\sigma_T = 0.66524... \times 10^{-24}\,\mathrm{cm}^2$), while the right-hand term is the Compton correction to this value which is asymptotic to unity at low energies, and decreases with increasing energy. The total cross section as:

$$\sigma_T = \sigma_{PE} + \sigma_{KN} \tag{3.4}$$

Using this total cross section, is it now possible to calculate the optical depth (τ) of a medium with column density N_H as

$$\tau = N_H \sigma_T \tag{3.5}$$

and in turn to calculate the output spectrum:

$$f_E \propto E^{-\alpha} e^{-\tau} \tag{3.6}$$

with the same proportionality constant as the unattenuated spectrum. In Figure 3.1 is shown the effect of different column density media on a power law spectrum

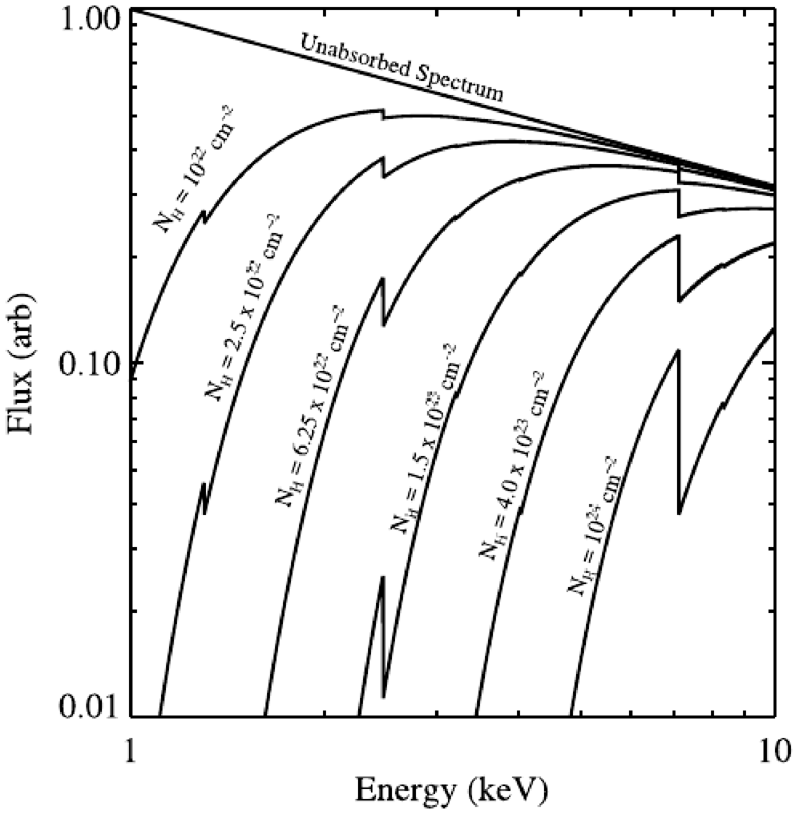

Figure 3.1: A plot of the effects of attenuation on a power-law spectrum. The unattenuated power law is attenuated by media of varying column densities as denoted in the annotations.

3.2.3 The Luminosity Function

The formulation of the XLF is typically in the form:

$$\phi(L) = \frac{1}{L}\frac{d\,\Phi(L)}{d\log_{10}(L)} = \frac{N}{L}\left[\left(\frac{L}{L_*}\right)^{\gamma 1} + \left(\frac{L}{L_*}\right)^{\gamma 2}\right]^{-1} \tag{3.7}$$

between 2-10keV Aird et al. (2010) where typical best fit parameters are given as $\log_{10}(N)$ = -5.1, $\gamma1$ = 0.7, $\gamma2$ = 3.14 and $\log_{10}(L_*)$ = 44.96 and are representative of the normalisation, low luminosity slope, high luminosity slope and characteristic break luminosity (at the knee of the luminosity function) respectively.

3.2.4 The X-ray Background

If we are to correctly constrain the obscured fraction in AGN, we must account for those sources which are completely obscured in the $2 - 10$keV energy range. The most efficient means of doing this is by using the XRB (which peaks at ~ 40keV) since we can infer the population of heavily obscured sources required to reproduce it. At lower energies ($E_\gamma < 10$keV), 80 percent of the XRB has been resolved into discrete sources (Hasinger et al. 2001, Rosati et al. 2002), with the bulk made up of both obscured and unobscured AGN. However, at harder X-ray energies the XRB is still unresolved due to instrumental limitations.

The number ratio of unobscured to obscured sources as measured at $2-10$keV is not in agreement with hard-X-ray background population synthesis models (Gilli et al. 2001, Yu and Tremaine 2002); the obscured sources in question must have column densities of $N_H \sim 3 \times 10^{23}$ cm^{-2} up to in excess of the CT regime, $N_H > 5 \times 10^{24}$ cm^{-2}. XRB population synthesis models expect these heavily obscured objects to account for some 5-15 percent of the total $10-30$keV emission (Luo et al. 2011), contrasting with a 40 percent obscured fraction at lower energies.

The high levels of obscuration within the CT objects makes it very difficult to gain sufficient statistics for population and evolution studies. At X-ray energies hard enough to mitigate obscuration effects ($\gtrsim$ 10keV), large area surveys capable of constraining the highly obscured and CT fractions at multiple evolutionary epochs have yet to be carried out. Current surveys, with their pencil beam nature, can do little to mitigate cosmic variance, and as such provide real problems in constraining the CT fraction.

3.2.5 Partial Covering

The idea of partial covering absorbers in AGN was first suggested in 1980 by Holt et al. They found that the X-ray spectrum of a local Seyfert galaxy, `NGC4151`[1] could not be fit by a single uniform density absorber, but could be fit with a partial covering obscurer where $\sim$10 percent of the intrinsic spectrum between $0.5 - 5$keV remains unabsorbed but a further 90 percent is covered by

---

[1] one of the archetype Seyfert galaxies Karl Seyfert's sample, in fact.

a $N_H = 6 \times 10^{22}$ cm^{-2} column. Work in 1985 by Reichert et al. (1985) showed three further sources with similar X-ray spectral features to `NGC4151`, covering a broad region of parameter space, with covering factors (CF) anywhere between 60 and 99 percent. This result suggested that not only could partial coverings be commonplace in AGN, but that there can be great variation from source to source. There have been many more AGN spectra that are best fit by partial covering obscurers (Matsuoka et al. 1990, Piro et al. 1990; 1992, Celotti et al. 1992), so much so that contemporary spectral fitting routines include partial obscuration as a key parameter (see Arnaud 1996, for example).

Recent work has published results for a source `1H 0419-577` which has a excess of counts in the hard X-ray (> 10keV) compared to extrapolations from models based on previous data (Turner et al. 2009). The authors suggest that partial obscuration by a CT absorber with column density $N_H \gtrsim 1.25 \times 10^{24}$ cm^{-2} and CF of 70 percent, along with a further intermediate obscurer of column density $N_H \gtrsim 1.25 \times 10^{22}$ cm^{-2} and CF $\sim$ 16 percent are responsible for this observed excess over model extrapolations.

The vital importance of this discovery lies in the miscalculations of intrinsic luminosities from different X-ray wavebands;

Observations which have hard (> 10keV) X-ray data allow one to correct for a Compton thick partial fraction since the photons at these energies are less attenuated by such a medium. However, if observations *only* exist in softer wavebands (< 10keV) then the presence of a Compton thick partial fraction will not be known. And so, without this full information the observer will correct only for the "*intermediate*" obscuration, leading to catastrophic differences between the inferred and true intrinsic luminosities. If we take the example of `1H 0419-577` described above, once the milder absorption component has been corrected for the observer would state the intrinsic X-ray luminosity at 30 percent of the true value; this is a huge problem! Any higher CT covering factor values will only make matters worse. For instance, if we assume the CFs published by Reichert et al. (1985) to be typical then a 99 percent CF as observed in `NGC 9582`, if CT, this would result in a two order of magnitude discrepancy between the *inferred* and *true* intrinsic X-ray luminosities.

And so, if partial CT obscurers are present in a large proportion of obscured objects, the statistics based on X-ray luminosities for these sources is going to be heavily biased towards the less obscured systems. While sources are binned in X-ray luminosity for statistical analyses such as measuring the obscured fraction vs. luminosity, the high luminosity-heavily obscured (both high in CF and column density) sources are going to contaminate lower luminosity bins occupied by only mildly-to-intermediately obscured sources.

In Figure 3.2 I show a cartoon of three X-ray sources, ranging from unobscured, partially obscured by a Compton thin medium, partially covered by a CT medium, through to both partially covered by both a CT and a Compton thin medium. The associated model spectrum for each object is included. These spectra will be described in more detail in the coming section.

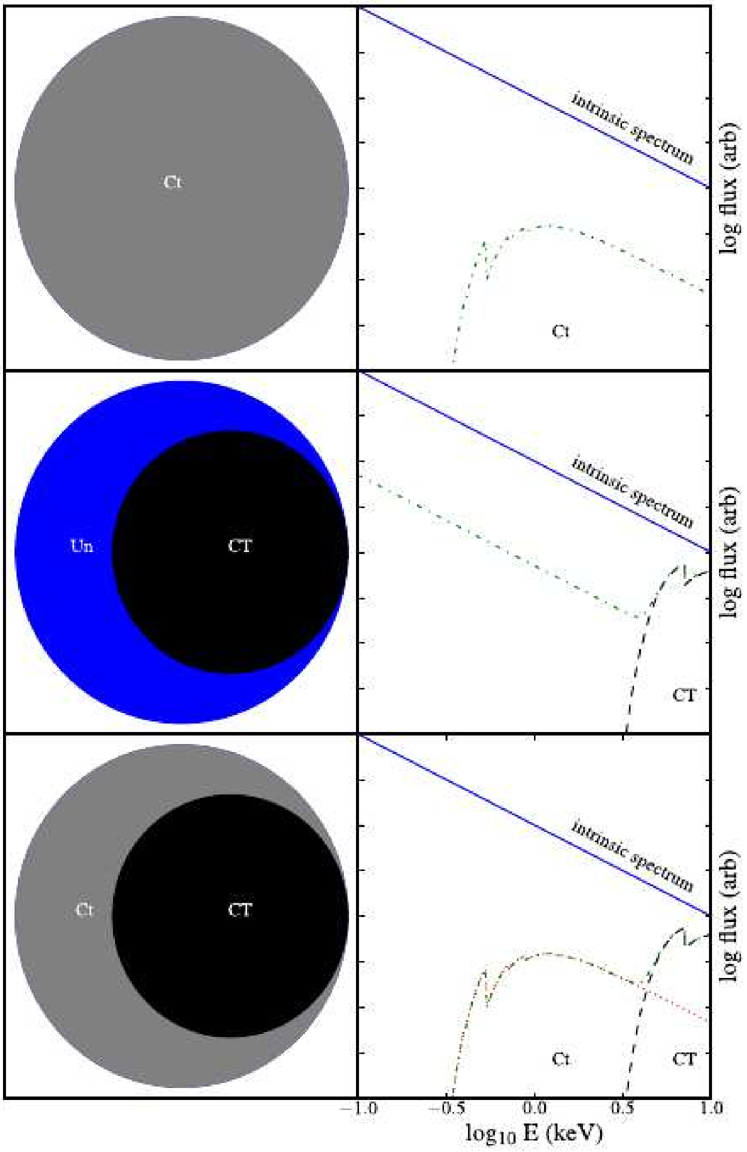

Figure 3.2: A cartoon of three X-ray sources with a different levels of obscuration, Compton thin (Ct) = light grey, Compton thick (CT) = black, unobscured (Un) = blue/dark grey'. Corresponding X-ray spectra are included in right-hand plots, with the intrinsic power law shown as a solid line (blue), the Compton thin contribution to the spectra is shown as a dotted (red) line, the CT contribution to the spectra is shown as a dashed (black) line, while the final observed spectra are shown as a dot-dashed (green) line. Note that the effects of partial obscuration are exaggerated in the spectra so as to be visible.

3.2.6 Scattering

A complicating but important component of the X-ray spectrum is the scattered fraction.

Analogous to the hidden BLR in the optical regime, X-ray photons can be scattered along the line of sight. This scattered fraction must be carefully modelled when attempting to calculate the intrinsic X-ray luminosity, alongside partial obscuration. A reflection component can be indistinguishable from a partial obscurer, however, scattered fractions typically make up between $\sim 0.1 - 10$ percent (Noguchi et al. 2010) of the intrinsic luminosity, and not the much higher ~ 70 percent quoted for `1H 0419-577` in Turner et al. (2009).

The reflection component of the X-ray spectrum is believed to originate from the accretion disc with X-ray photons emanating from the corona above the disc being reflected by a CT medium. Evidence supporting this claim comes from the detection of fluorescent Ke Kα lines, which can uniquely probe the circumnuclear region.

The X-ray spectra of AGN is likely to be complex, with contributory components from the primary continuum, Compton reflection from the accretion disc, partial obscuration from a number of clouds (with different covering factors and densities), re-emission from these clouds, fluorescent features within the reflection component, absorption edges from metals and the broadening features due to various kinematic and relativistic effects. Thus studying any single feature of the X-ray spectrum remains a very difficult task.

3.3 Aim

Based on the evidence that partial obscurers are present in a number of AGN, the aim is to show what possible effect this phenomenon could have on the observed obscured fraction vs. luminosity trend seen in the X-ray regime (E$<$ 10keV).

3.4 Modelling Partial Obscuration

If we have a partial obscuring component (or n non overlapping partial obscuring components across the source) then the Equation 3.6 generalises to:

$$f_E \propto \sum_i^n C_i E^{-\alpha} e^{N_{Hi}\sigma_T} + \left(1 - \sum_i^n C_i\right) E^{-\alpha} \tag{3.8}$$

where C_i is the fraction of the total that the obscurer i covers, with column density N_{Hi}. Note that $\sum_i^n C_i \leq 1$. In Figure 3.3 is shown the effect a combination of a partial covering CT medium and a partial obscuring Compton thin medium on a power law spectrum. The a population of covering factor C, the apparent luminosity K will be:

$$K = (1 - C)L \tag{3.9}$$

and so if there are N objects, intrinsically in the luminosity range dL, we observe them in the range dK, where

$$dK = (1 - C)dL \tag{3.10}$$

and so the density of objects in observed luminosity space is:

$$\psi(K) = \phi\left(\frac{K}{(1 - C)}\right)/(1 - C) \tag{3.11}$$

If we consider a simple power law luminosity function $\phi(L) = AL^{-\alpha}$ then

$$\psi(K) = AK^{-\alpha} \cdot (1 - C)^{\alpha - 1} \tag{3.12}$$

and so for $\alpha < 1$ the effect is to increase the number density, while for $\alpha > 1$ the effect is to decrease the number density. Thus, the adjusted XLF ψ, as a function of the *observed* X-ray luminosity K, for a fraction f of the total population (i.e. $f < 1$, $\Sigma_i f_i = 1$) is:

$$\psi(K) = \frac{N}{K}\frac{f}{(1 - C)}\left[\left(\frac{K}{(1 - C)L_*}\right)^{\gamma 1} + \left(\frac{K}{(1 - C)L_*}\right)^{\gamma 2}\right]^{-1} \tag{3.13}$$

NB compare this with Equation 3.7. $\psi(K)$ will increase the number density below L_* (where $\alpha \simeq \gamma 1 = 0.7(< 1.0)$) and decrease the number density above the L_* (where $\alpha \simeq \gamma 2 = 3.14(> 1.0)$). Consider a simple two population model. Population-1 is unobscured, with covering factor $c_1 = 0$, and is a fraction f_1 of the total. Population-2 has covering factor c_2 and fraction $f_2 = (1 - f_1)$. Figure 3.4 shows the result for $f_1 = 0.5$ and $c_2 = 0.99$. The obscured fraction is given by the ratio of the two luminosity functions, and shows a marked trend with apparent $\mathrm{L_X}$. Figure 3.4 shows the effect of partial covering on the XLF, and the drop in the obscured fraction what would be observed.

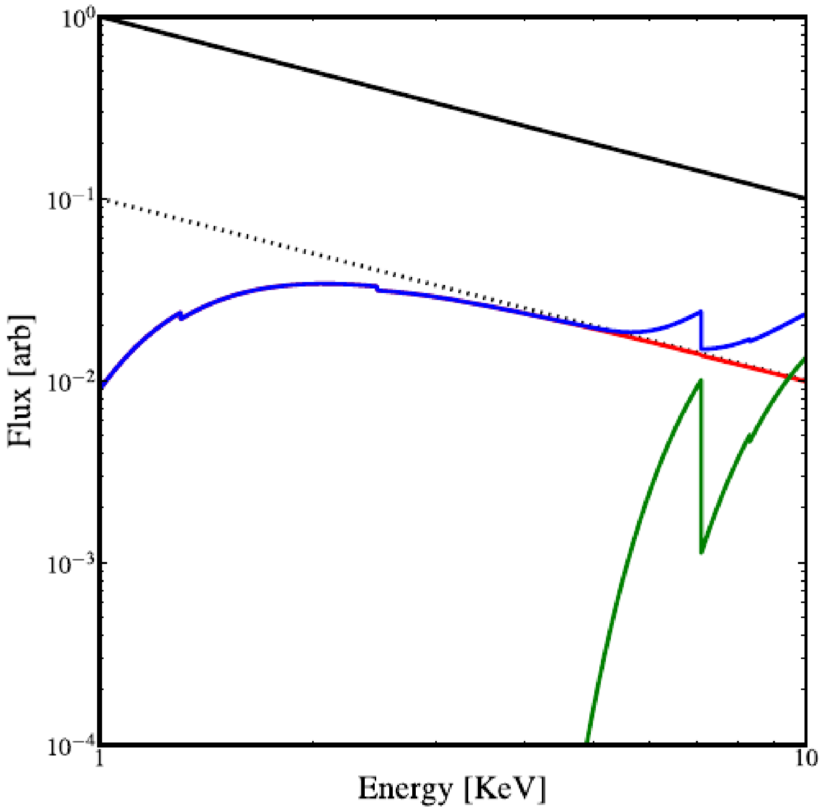

Figure 3.3: A plot of the effects of partial obscuration on a power-law spectrum. An unattenuated power law is partially covered (95 percent) by a CT absorbed ($\mathrm{N_H} = 2 \times 10^{24}$ cm^{-2}) as shown in green, with the remainder (5 percent) covered by a $\mathrm{N_H} = 1 \times 10^{22}$ cm^{-2} column, as shown in red. The combined flux from these two regions is shown and blue as would be measured by an observer, and the dotted line shows a possible “corrected” value for the spectrum after the thin component is corrected for, a factor of twenty below the intrinsic value.

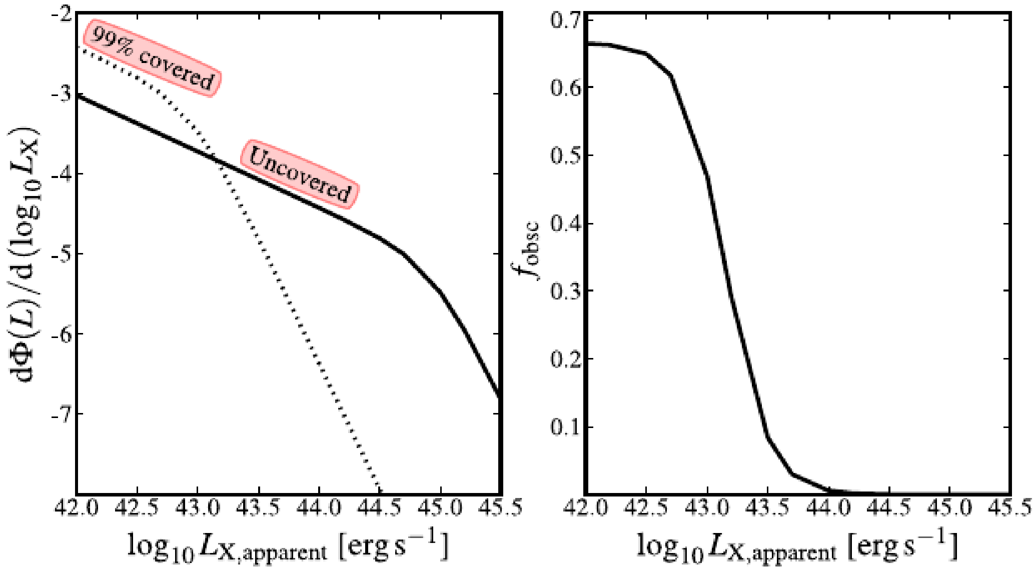

Figure 3.4: A plot showing the effects of partial covering on the XLF. The left-hand figure show the intrinsic (uncovered) XLF as taken from Aird et al. (2010) (solid line) and the change that is produced in the XLF when every object is covered over 99 per cent of its surface with a Compton thick obscurer (dotted line). The right hand figure shows the observed f_{obsc} for an intrinsic obscured population making up 50 per cent of all AGN, all being partially covered over 99 per cent of their X-ray surfaces.

3.4.1 The Data

In order to develop models of partial covering fractions, it is necessary to compare to a suitable observational data set: The data used here are taken from Hasinger (2008). In this work Hasinger used a combination of optical spectroscopy and $0.5 - 10$keV X-ray data to classify AGN as either "unabsorbed" (type-I) or "absorbed" (type-II). First, sources with X-ray luminosity $\log(\mathrm{L}_x) < 42$ erg s^{-1} were rejected since below this cutoff it becomes very difficult to differentiate between low luminosity AGN and luminous star forming galaxies. Next, a hardness ratio (HR) for the X-ray sources was measured:

$$HR = \frac{(H - S)}{(H + S)} \tag{3.14}$$

where H and S are the X-ray count rates in the hard and soft bands, $2-10$keV and $0.5 - 2$keV respectively. A HR cutoff of -0.2 was used to best separate obscured and unobscured objects, since only 3.4 percent of Broad Line AGN (i.e. optically classified as having permitted lines with linewidths $> 1,000\mathrm{km\,s^{-1}}$) are “softer” than -0.2 (i.e. higher than -0.2). Sources which were ambiguously classified in the optical regime are classified according to their hardness ratio alone.

3.5 Two-Population Model

Starting with the simplest model with two populations, one partially covered the other uncovered, I first plot representative XLFs for both, illustrating the aforementioned redistribution of sources from higher luminosity bins to lower luminosity bins for the partially covered sources. The only way that such a redistribution of sources will lead to the observed obscured fraction-luminosity relation is if the partially obscured sources have some form of *visible* (but Compton thin) obscuration such that they can be spectrally classified as obscured sources, otherwise they will just appear as less luminous unobscured objects. This assumption seems reasonable since partial CT obscuration without any associated Compton thin obscuration is unlikely. For this model I have two free parameters representing the fraction (f_{2a}) of the total population with a fraction of their X-ray region totally covered (c_{2a}). The fraction of uncovered sources f_1 is constrained to $1 - f_{2a}$, and by definition the uncovered sources have covering factor $c_1 = 0$.

I fit this model to the data described above using chi-squared minimisation:

$$\chi^2 = \sum_i \frac{(O_i - E_i)^2}{\sigma_{Ei}^2} \tag{3.15}$$

where O_i and E_i represent the observed and expected datum respectively and σ_{Ei} represents the uncertainty on the observed datum. Therefore I want to minimise this value to give the best fit of my model to the data. More generally it is important to consider how many free parameters there are in my model, since if I have more free parameters it should in principle be easier to fit the resulting more complex model to the data; we must therefore use a metric that it capable of comparing arbitrarily complex models with any number of free parameters.

The key parameters in doing this is the *degrees of freedom*, ν which is defined as $\nu = N - n - 1$, where N is the number of observations and n is the number of fitted parameters. The reduced chi-squared is given as:

$$\chi_\nu^2 = \frac{1}{\nu} \sum_i \frac{(O_i - E_i)^2}{{\sigma_{Ei}}^2} \tag{3.16}$$

As a rule of thumb, a high χ_ν^2 (i.e. $\gg 1$) is a poor fit to the data, and a very low χ_ν^2 (i.e. $\ll 1$) usually indicates an overestimate of the error variance, while $\chi_\nu^2 = 1$ is desirable. As one can see, if $n > N$, $\nu < 0$ and so $\chi_\nu^2 < 0$, this shows that highly complex models with many free parameters can only be investigated with large observational datasets.

Including confidence limits with my best fit model parameters, I do so by obtaining a value for $\Delta\chi_\nu^2$ from a χ^2 distribution table for ν degrees of freedom. In order to maintain simplicity I marginalise the errors (meaning that all other parameters are held fixed at their best-fit values). Thus for a 1σ (68 percent) confidence interval, I search within a $\Delta\chi^2 = 1.0$). And so, once I have found a minimum chi-squared value for a model fit, I find the confidence limits by finding the values where

$$\begin{aligned} \chi^2 &= min(\chi_\nu^2) + \frac{\Delta\chi^2}{\nu} \\ &= min(\chi_\nu^2) + \frac{1.0}{\nu} \end{aligned} \tag{3.17}$$

When I fit this simple two population model to the data, I find a poor fit. The best fit parameter values, reduced chi-squared and associated probability for this, and subsequent discrete population models are shown in Table 3.1

Figure 3.5 shows the best fit-two free parameter model overlayed upon the Hasinger (2008) data. The figure shows that whilst it is possible to match the obscured fraction for any given small luminosity range, the “drop” in the obscured fraction is much too steep to match the data.

Table 3.1: Best fit parameters with marginalised errors for the discrete population models, along with reduced chi-squared values χ^2_ν and the associated model probabilities, p.

Parameter	**2-Pop Model**	**3-Pop Model**	**4-Pop Model**
f_1	$0.578^{+0.02}_{-0.01}$	$0.453^{+0.022}_{0.022}$	$0.313^{+0.0229}_{-0.0114}$
c_{2a}	$0.915^{+0.008}_{-0.008}$	$0.283^{+0.120}_{-0.122}$	$0.999^{+0.0002}_{-0.0002}$
f_{2a}	$0.422^{+0.01}_{-0.02}$	$0.126^{+0.010}_{-0.010}$	$0.476^{+0.018}_{-0.020}$
c_{2b}	–	$0.959^{+0.004}_{-0.006}$	$0.941^{+0.008}_{-0.009}$
f_{2b}	–	$0.327^{+0.020}_{-0.020}$	$0.139^{+0.0085}_{-0.0085}$
c_{2c}	–	–	$0.254^{+0.120}_{-0.130}$
f_{2c}	–	–	$0.068^{+0.0062}_{-0.0061}$
χ^2_ν	5.56	2.41	1.154
p	3.1×10^{-10}	0.005	0.320

3.6 Three-Population Model

Increasing the complexity of the model to include a further partially covered population, I now have a four free parameter model (f_{2a}, c_{2a} and f_{2b}, c_{2b} where f_{2b} and c_{2b} represent the fraction and covering factor of a new population) with $f_1 = 1 - f_{2a} + f_{2b}$ constraint. With this increased complexity, running a simple full parameter space exploration as undertaken for the two-population model would become much too time-consuming, and so a grid search algorithm was adopted:

This method minimises chi-squared for each parameter in turn by calculating chi-squared at a random value, n, of that parameter, along with the chi-squared values for the grid points either side of n, $n \pm \delta n$. the value of n, $n \pm \delta n$ with the lowest chi-squared value is taken as the new centre, and the local minimum is iterated towards. The best fit value is taken at this chi-squared and the parameter is fixed whilst the same process is undertaken for all other parameters in succession. This process is repeated until a local minimum is converged upon. The process gets repeated several times, starting with different random parameter values, so as to make sure that the minima are global in the parameter space and not just local minima. When this is confirmed the resolution of the parameter space is increased, the best fit parameters are taken as the initial parameters and a higher resolution fit takes place. The best fit parameters for a three-population model are again shown in Table 3.1. While this model fits the data far better that the two-population model, it still does not make for a satisfactory fit ($\chi^2_\nu = 2.41$). Interestingly, however, we see two very different populations emerging, one with a

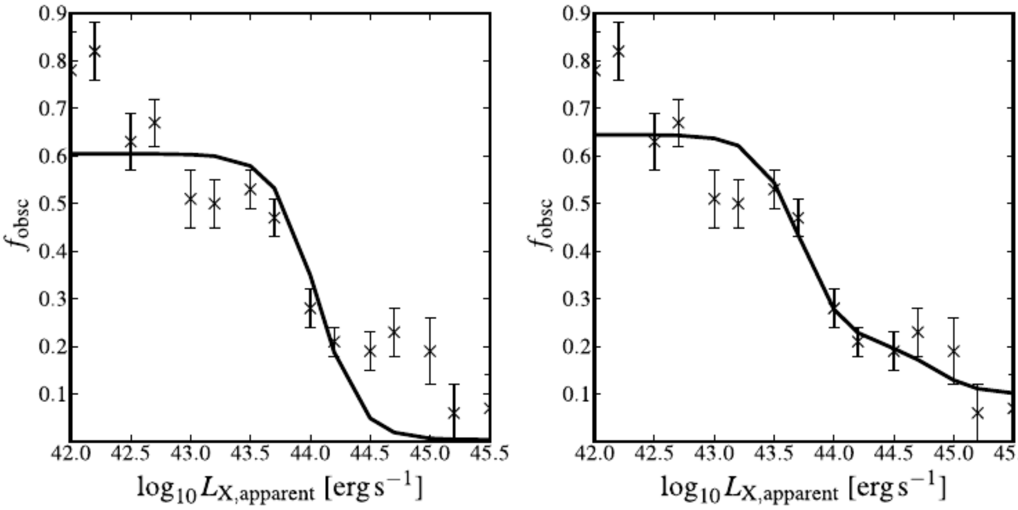

Figure 3.5: A plot showing the best fit-two (left hand) and three (right hand) population models to the Hasinger (2008) data.

very high CF (c_{2b}) and another with a much lower CF c_{2a}, much like what is seen in the individual object `1H 0419-577`. The three population model best fitting the Hasinger (2008) data is shown in Figure 3.5 .

3.7 Four-Population Model

Extending the model yet further to include a third partially covered population (with free parameters f_{2c} & c_{2c}) appears the next logical step. Looking at the data set taken from Hasinger (2008) one observes three distinct plateaux, which may well not be real in the general population, but are nonetheless present in this sample. Quantitatively we see these plateaux at log $L_x \simeq 43$, 44.5, 46 erg s^{-1}. Because of this, I see a significantly better fit to the data when I adopt the four-population model with three distinct partially covered populations. When I perform a chi-squared minimisation on this model I get a quite intriguing result. The unobscured fraction is significantly reduced in this scenario with $f_1 \simeq 0.3$, and I begin to see the significance of the three very different obscured populations; the extremely covered objects with covering factor in excess of 99.9 percent, but making up the most significant fraction of the total population (∼50 percent) which vitally boosts the observed low luminosity obscured fraction at log $L_X \leq 44$ [erg s^{-1}], the heavily partially covered sources with around 95 percent obscuration accounting for some 14 percent of the AGN population dominating the statistics at log $L_X \simeq$ 44-45 erg s^{-1}, and a mildly partially covered population with ∼25 percent obscuration, which whilst making up only a very small fraction of the total population ($f_{2c} = 0.07$) is key to explaining the rather *slow* decline in the observed obscured fraction at high luminosities (log $L_X \simeq$ 45-47 erg s^{-1}). Figure 3.6 shows the best fitting four population model to the Hasinger (2008) data set. Figure 3.7 shows the marginalised error ellipses for the parameters in the four population model.

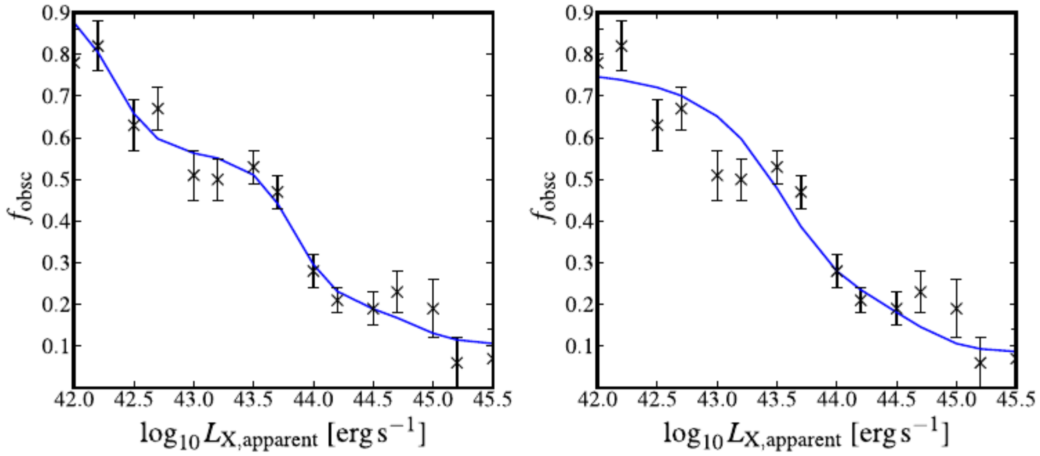

Figure 3.6: A plot showing the best fit-four population (left hand) and Gaussian continuous fraction population (right hand) models to the Hasinger (2008) data.

3.8 Continuous Fraction Distribution Model (CFDM)

It follows from an ever increasingly complex model with up to four separate populations that the next logical step would be to have a more general model where the obscured population exhibits a continuous distribution of partially covered fractions. Put more phenomenologically, each source would have a anisotropically distributed number of clouds, which depending on the sources relative orientation to the observer will show different degrees of partial covering in the X-ray regime.

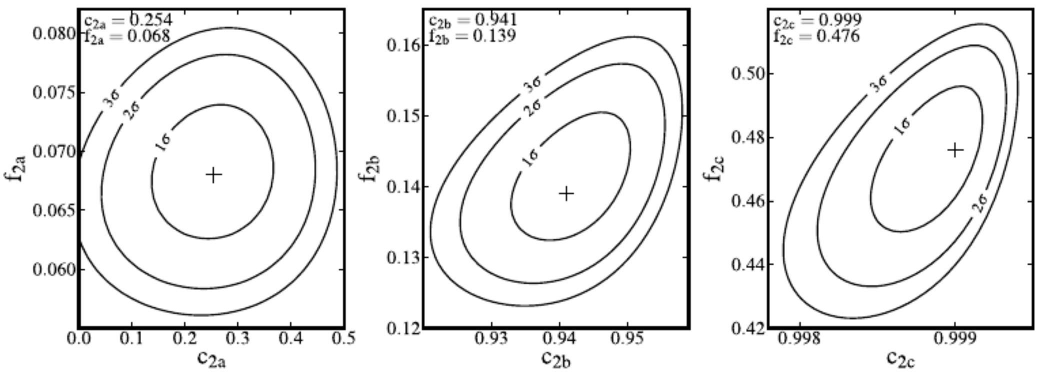

Figure 3.7: A plot showing the marginalised uncertainties for the best fit parameters in the four population models to the Hasinger (2008) data.

If we naively assume a torus based model, then the opening angle of the torus defines the unobscured fraction, whilst the geometry of both individual clouds within the torus, of the torus itself, and of their relative orientation to the observer will dictate whether any individual source will be mildly partially covered, heavily partially or extremely partially covered in the X-ray regime.

The first continuous distribution model to be tested is that taken from a half-Gaussian distribution of covering factors. By looking at the general trend set by the four population model, a small fraction with low covering factor increasing to larger fractions at higher covering factors will be required. First I assume an uncovered population with $c_1 = 0$ and fraction f_1, and a second population with a range of covering factors such that $f(c)dc$ is the fraction of objects with c in the range c to c+dc. The overall fraction of partially covered objects is $f_2 = \int_0^1 f(c)dc$, and the normalisation of $f(c)$ is constrained such that $f_2 = 1 - f_1$.

$$\begin{aligned} f(c) &= Ae^{\frac{-z^2}{2}} + k \\ z &= \frac{c-\mu}{\sigma} \end{aligned} \tag{3.18}$$

where the free parameters A, μ, σ and k where A is the physical height of the Gaussian peak, μ is the location of the peak of the half Gaussian (in c), σ is the Gaussian width, and k is a constant. c is the set of covering factors running from uncovered (0.0) to totally covered (1.0). I constrain A according to f_2 and place a reasonable constraint on μ of 1.0, since in the four (discrete) population model

Table 3.2: Best fit parameters with marginalised errors for the Continuous Distribution Models

Parameter	Gaussian + const.	log-Gaussian + const.
f_1	$0.381^{+0.01}_{-0.01}$	$0.333^{+0.007}_{-0.009}$
σ	$0.028^{+0.007}_{-0.006}$	$0.028^{+0.008}_{-0.006}$
k	$0.016^{+0.002}_{-0.002}$	$0.045^{+0.005}_{-0.01}$
f_b	–	$0.300^{+0.02}_{-0.03}$
c_b	–	0.9989
χ^2_ν	2.03	1.38
p	0.018	0.173

the extremely obscured population makes up a significant fraction of the total population. This leaves the model with only three free parameters; f_1, σ and k. Using the same chi-squared minimisation technique as previously described, the best fit parameters for this model are included in Table 3.2. The best fit model is a very narrow half Gaussian, combined with a very small contribution across the all covering factors from k. This model is promising given its relative simplicity (only three degrees of freedom) but is not as good as the four population discrete model detailed above. I attempt further distributions; logarithmic, linear, sinusoid, sigmoid and log-Gaussian, but of these, only the log-Gaussian provides a reasonable fit to the Hasinger (2008) data.

3.8.1 A log-Gaussian distribution model

The next model tested is a Gaussian in $\log_{10}$c, i.e. with $f\,dc$ as defined above but with $z = (log_{10}c - \mu_{log\,c})/\sigma_{log\,c}$. Again by setting the same constraint that the distribution peaks at $c = 1$, $\mu_{log\,c}$ is set to zero. An added layer of complexity is added here; It seems that all continuous distributions are hindered by requiring such a high fraction of *extremely* obscured objects, I therefore introduce another free parameter. The "buried" fraction that I introduce is reminiscent of the extremely obscured fraction in the four population model above (f_{2c},c_{2c}), and the covering factor of this fraction is fixed accordingly ($c_b = 0.999$). Thus only one further free parameter is introduced; f_b is the fraction of "buried" objects, and thus $\mathcal{F} = 1.0 - (f_1 + f_b)$. So the log-Gaussian model has four free parameters, $\sigma_{log\,c}$, k, f_1 and f_b. The best fitting model parameters to the Hasinger (2008) data set are also shown in Table 3.2 along with the reduced chi-squared value for this fit. This model shows a far better fit to the model that the half Gaussian model. The log-Gaussian best fitting model is compared to the Hasinger (2008) data in Figure 3.8.

The "Buried" Fraction

Interestingly, the "buried" fraction, f_b, is necessitated only by the two lowest luminosity points in the Hasinger (2008) data set. If one ignores these two data points, then the log-Gaussian model is equally well fit without this fixed fraction. This result is also shown in Figure 3.8 along with the log-Gaussian model fit. Indeed at such low X-ray luminosities ($log_{10}\mathrm{L_X} < 42.5$ erg s^{-1}) one must begin to worry about contamination due to other activities in the X-ray regime (e.g. X-ray binaries, supernova remnants), and so one must be very careful in interpreting this result.

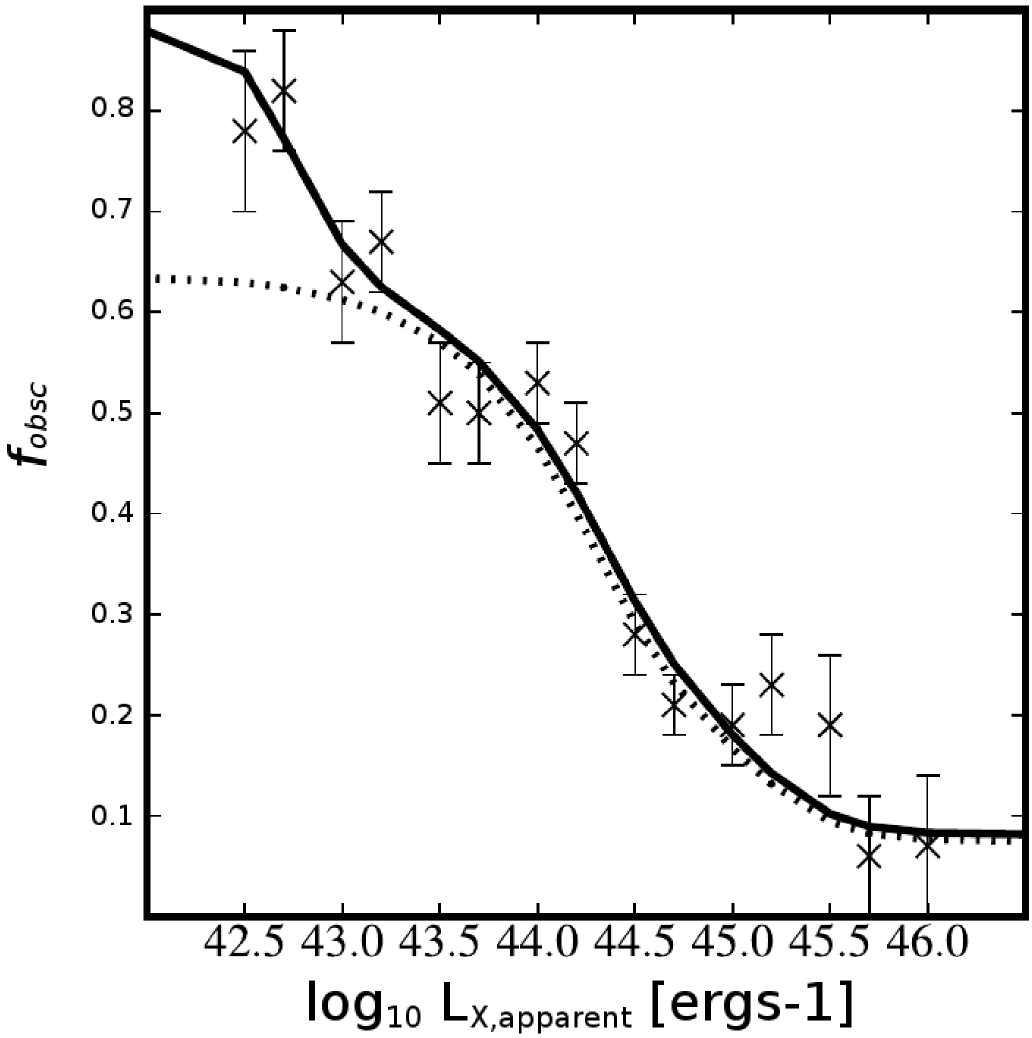

Figure 3.8: A plot showing the best fit log-Guassian continuous fraction population model to the Hasinger (2008) data. The dotted line represents a fit to the data excluding the two lowest luminosity bins, with a model not having a "buried" fraction.

3.9 The X-ray/IR ratio

Ideally one would measure the UV emission to infer the intrinsic luminosity of an AGN. In reality however, much of the UV emission is attenuated and re-emitted in the IR. We therefore use the IR as a proxy for the intrinsic luminosity of the AGN, and as such one hopes to see a correlation in the IR vs. attenuation corrected X-ray luminosity ratio.

Gandhi et al. (2009) have shown a tight correlation between X-ray and small-aperture mid-IR luminosity. Their data is reproduced in the upper panel of Figure 3. Note that Gandhi et al made careful efforts to correct for both standard X-ray absorption and Compton thick absorption - partly from the use of hard X-ray data from Suzaku/Integral/SWIFT, and partly from the use of other data such as `[OIII]` luminosity, which allowed them to estimate the scattered fraction in Compton-thick cases. The degree of correction sometimes necessary is indicated by the two starred points, which show the apparent and corrected luminosities of the archetypal Type 2 AGN, `NGC 1068`. Overall, the Gandhi et al study shows that when full information and high quality data is available, IR and X-ray emission are tightly correlated.

A rather different picture is shown in the lower panel of Figure 3.9, which uses data from LaMassa et al. (2011) and Brightman and Nandra (2011). LaMassa et al. correct only for the observed X-ray column. Brightman and Nandra also use the observed equivalent width of the Fe-Kα (6.4keV) line to infer additional Compton thick absorption, using reflection models, but it is far from clear this will find all the additional absorption, and will be much less accurate. These two samples show a large spread in the IR/X-ray ratio. The figure shows the expected effect of various amounts of partial covering, using the Gandhi et al line as the upper envelope. The spread seen is roughly consistent with the range of partial coverings implied by the model fits of Section 3.7. It is also clear objects optically classified as Type 1.8-1.9 or Type 2 have a systematically different IR/X-ray ratio. (We note that when there are objects in common between the LaMassa et al. and Brightman and Nandra samples, there is sometimes considerable disagreement on the X-ray luminosity, but perhaps this shows how hard X-ray luminosity correction is).

The contrast between the upper and lower panels of Figure 3.9 shows that while it is possible to fully correct X-ray luminosity, standard 2-10keV surveys are unlikely to do so - considerable unrecognised Compton-thick absorption may be present.

As well as the careful correction, the other key difference between the Gandhi et al. (2009) study and the LaMassa et al. (2011) and Brightman and Nandra

(2011) studies, is that Gandhi et al. (2009) used newly measured small aperture mid-IR fluxes, whereas the other two studies use IRAS large aperture fluxes. This could add a spread in the IR/X-ray ratio due to starburst contamination. We have included the X-ray vs IR correlation for starburst galaxies from Asmus et al. (2011) in Figure 3.9. Vasudevan et al. (2010) have quantified this issue. The correction will vary from object to object of course, but in general no source with $\log_{10}$ $L_X > 43$ erg s^{-1} has greater than 50 percent contamination, while some sources below $\log_{10}$ $L_X = 43$ erg s^{-1} have stellar contamination a factor of several. While this is therefore important, it does not explain the effect shown.

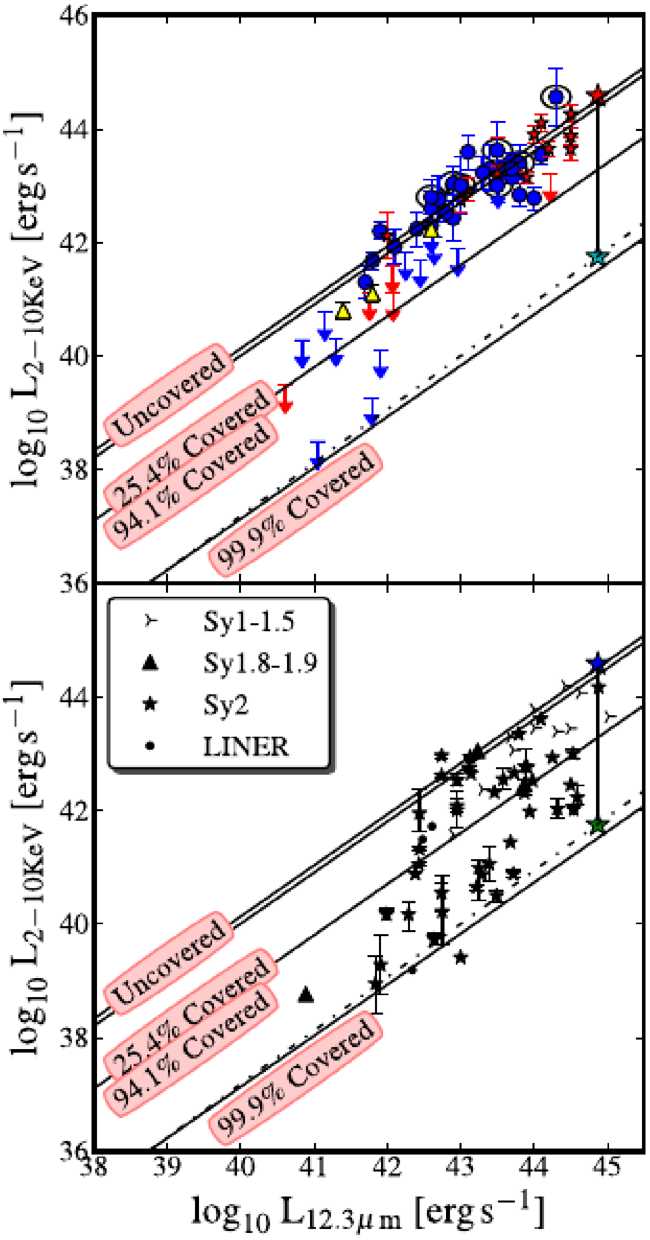

Figure 3.9: A plot of IR *vs.* "corrected" X-ray luminosities for a sample of sources taken from Brightman and Nandra (2011), over-plotted with best fit model lines from Gandhi et al. (2009) with varying degrees of partial obscuration. We have also included `NGC 1068` (star symbols) at both intrinsic and corrected X-ray luminosities, data being taken from Pounds and Vaughan (2006) and Pier et al. (1994) for the observed and intrinsic X-ray luminosities respectively, and Marco and Brooks (2003) for the IR luminosity

Star Formation

Could the IR/X-ray luminosity ratio observed be accounted for by a difference in star formation rates? Evidence for Type-II AGN having higher star formation rates than their Type-I counterparts is disputed in the literature; results from Maiolino and Rieke (1995), Hiner et al. (2009) claim a statistically significant difference (by up to a factor of 50 percent), while results from Netzer (2009), Meléndez et al. (2008) and this work (Chapter 4 show no such difference in star formation rates. If such a discrepancy does exist between star formation rates then this would not be seen in the IR luminosities of the Gandhi et al. (2009) data in Figure 3.9, since the data here are from small apertures probing only the central regions. Even if we allow for this effect, a 50 percent difference in star formation rates between Type-I and Type-II objects does not account for the 2-3 order of magnitude spread in IR luminosity in the Brightman and Nandra (2011) and LaMassa et al. (2011) samples.

Variability

Could variability account for the spread in X-ray vs. IR luminosities that are observed in the Brightman and Nandra (2011) and LaMassa et al. (2011) datasets? Infrared variability is unimportant. Although near-IR variability in Seyfert galaxies is well known (e.g. Suganuma et al. 2006) it is typically only a few tenths of a magnitude; in the mid-IR, variations are seen on a timescale of years with Spitzer, but they are of typical size 0.1 mag (Kozłowski et al. 2010). In the X-ray regime variability is a common trait, with flux variations of order 50 percent on intra-day timescales (e.g. Uttley et al. 2003, Arévalo et al. 2008, Breedt et al. 2009). The absolute variability measured in a number of objects cannot feasibly account for the 2-3 order of magnitude spread seen in the data. However, variability is an issue that will hinder measurements of X-ray vs. IR luminosities which can only be overcome by simultaneous measurements in both regimes.

3.10 Discussion

3.10.1 The Implications and Comparisons to Other Models

The log-Gaussian model proposed above predicts that there is a fixed fraction of extremely obscured, or “hidden” sources, and a further population with a continuous distribution of covering factors across all values from $c = 0 - 1$. This continuous distribution population is a necessary addition to the model, since it models the gradual decline observed in the obscured fraction with increasing luminosity, whilst the extremely obscured sources are responsible for the low luminosity boost in observed obscured sources. The model predicts that ~ 30 percent ($f_b = 0.300$) of all AGN are extremely obscured (99.9 percent covered) along the line of sight, and a further $\sim$37 percent ($\mathcal{F} = 1 - f_1 + f_b = 0.367$) belong to this population displaying *some* amount of CT obscuration.

If one adopts the torus model commonly used in the unified scheme, then such a configuration is representative of a torus with a opening half-angle of 55°, while the “buried” fraction corresponds to an opening half-angle of 72°. In between these two angles would be a rather substantial graded region where the torus is not opaque, but produces partial covering. This is quite hard to understand in a traditional smooth torus model, but may happen fairly naturally in a clumpy torus model (e.g. Stalevski et al. 2012, and references therein). If the mean number of clouds in the line of sight is μ, then assuming that along different sight lines this quantity is Poisson distributed, then the fraction of sight lines with one or more clumps, i.e. the covering factor, will be $c = 1 - e^{-\mu}$. So for example $\mu = 1$ would give $c = 0.63$ whereas $\mu = 7$ would give $c = 0.999$. This general point about clumpiness also applies to alternatives such as disc wind or misaligned disc models.

Do small high density clouds exist in the vicinities of AGN central engines? It has been possible to observe a cloud transiting an X-ray emitter within an AGN, with central column density of $\sim 3 \times 10^{23}$ erg s^{-1}, reducing down to $\sim 3 \times 10^{22}$ erg s^{-1} in the envelope (Maiolino et al. 2010) which could also be evoked to explain the higher levels of variability that are observed in obscured objects over unobscured objects Beckmann et al. (2007). One could indeed use these column densities along with variability measurements as a starting point for further development of a cloud distribution model.

The predicted "hidden" fraction, unobscured fraction and partial obscuring fraction are in line with direct observations (Winter et al. 2009), whilst reproducing the obscured fraction vs. luminosity relation as well as the putative model, the receding torus model (see below), and are consistent with X-ray/IR ratio results.

3.10.2 Receding Torus Model

The current favoured model used to explain the observed trend of the obscured fraction vs. luminosity is known as the receding torus model (Lawrence 1991). This model prescribes a fixed height torus around all AGN accretion discs, with the inner radius (and hence the torus opening angle) determined by the dust sublimation temperature, which in turn scales with the luminosity of the central engine. Hence higher luminosity sources would have smaller sky covering fractions and so there are more unobscured objects than obscured objects at high luminosities. While this model is supported by many works (e.g. Hill et al. 1996, Willott et al. 2000, Grimes et al. 2004), a critical assumption that the torus has a fixed physical height across all objects is one which may be at odds with physical motivations. The problem here is twofold, firstly AGN-induced star formation will result in more feedback due to supernova, thus "puffing-up" a torus, and secondly, more luminous AGN require more accreting material and so a higher mass reservoir. This will result in a modification to the receding torus model whereby the torus height becomes a function of the central engine luminosity (which, only in an extreme case would cancel out the radial effect resulting again in a fixed ratio torus). Results from Cao (2005) and Simpson (2005) show that a shallow slope in obscured fraction vs. luminosity is observed, predicting a non-constant torus scale height.

Work undertaken by Lu et al. (2010) shows that by careful correction of reddening in an `[OIII]` sample, any fractional dependence on luminosity can be removed. Combining this with the calculated Type-II fractions from optical volume limited, IR and radio samples, which all show no luminosity dependence of the Type-II fraction (i.e. a fixed Type-II fraction), it is difficult to reconcile the receding torus model with these results. This is discussed in more detail in

Chapter 4

3.10.3 Warped Disc Model

An alternative to the torus model is the warped disc model (Sanders et al. 1989, Lawrence 2007, Lawrence and Elvis 2010, e.g.) in which fueling material infall occurs from completely random directions only a well defined central accretion axis. The obscured objects (or more precisely, the Type-II objects in the optical) are, on average, those sources with larger misalignment and so have larger covering factors. This model can be used to explain phenomena including the prominence of dust lanes in Type-II objects, why Type-II objects have weaker narrow-line emission for a given radio power, and why Type-II objects are more luminous in the IR as a fraction of their bolometric luminosity. This model does not predict a luminosity dependence of the obscured fraction. See Lawrence and Elvis (2010) for a full discussion.

3.10.4 Cloud Locations

In order for a cloud to partially cover a source, it must realistically be smaller in projection than the object which it obscures (or else in the special case, of grazing angle along the line of sight). Thus to be smaller in projection, the cloud must both lie very close to the object it is obscuring and be physically smaller than the source itself. For this to be the case for X-ray obscuration, the clouds must lie well within the BLR. Thus in such a model, there would not necessarily be any correlation between the classification of optically Type-I and X-ray unobscured AGN sources.

The idea of such clouds in the central regions of AGN is not a new one (see e.g. Celotti et al. 1992, Bond and Matsuoka 1993, Nandra and George 1994). The work undertaken by Nandra and George (1994) shows the X-ray spectra for systems with such clouds including light scattered *into* the line of sight; such modelling shows that the resultant X-ray spectra do not have a dramatic drop in flux at low X-ray energies (compare with Figure 3.2) but is more or less indistinguishable for unobscured objects at low X-ray energies.

Work by Krolik and Kallman (1987) shows the forward scattered X-ray radiation to be not insignificant in any torus-like geometry. This is reinforced by models developed by Ghisellini et al. (1994) and Krolik et al. (1994).

heavily obscured objects are often reflection dominated (see e.g. Reynolds et al. 1994). Note that the model spectrum used in this work to describe a possible "under-correction" of the intrinsic X-ray luminosity does not account for the possibility of reflection dominated Compton thick sources. Indeed, by including a (dominant) reflection component in each heavily covered source much of this effect will be negated.

3.10.5 Future Work

In order to be considered viable, the above model must be extended to include optical obscuration effects, allow for the soft X-ray excess and intra-day variability seen in many sources, account for reflection dominated sources (and the associated line flux contributions to the soft X-ray flux), as detailed above, as well as explain the X-ray Baldwin effect-luminosity dependence seen in AGN (Iwasawa and Taniguchi 1993, Ricci et al. 2013). The model could then be either evolved using XLF evolution models to see whether the relative fractions of each population remain constant, or else infer constraints on the unobscured XLF at high redshifts.

These aims are outwith the scope of this work, which simply address the obscured fraction X-ray luminosity dependence in light of recent spectral observations of individual AGN in the $2 - 10$keV X-ray regime.

Sample selection and modelling will also play a vital role in the development of this work. For instance, sources with higher levels of obscuration (either in the X-ray or optical regime) will be subject to higher contamination due to stellar processes, and so careful modelling and extensive observations capable of deblending contributions from both processes will be very important for calculating intrinsic luminosities for the central engines of heavily obscured objects. Also since highly obscured sources are less likely to be detected optically it is imperative that one creates a volume limited sample within a feasible column density range, such as to minimise selection effects.

Whilst recent results in the hard X-ray regime (> 10keV) confirm the findings at lower energies (< 10keV), that is, a decrease in the number of obscured sources relative to unobscured source as a function of luminosity, it has been argued that these observations may still be strongly influenced by CT sources: Theoretical calculations show that hard X-ray surveys can still be biased against obscured sources, with unobscured sources (i.e. with CT material but *not* along the line of sight) having enhanced X-ray luminosities of up to 40 percent over their obscured counterparts, so it seems that an unbiased sample in the X-ray regime may not be possible for some time. (Yaqoob and Murphy 2010) .

Results showing a similar trend in the optical regime, using `[OIII]` luminosity as a proxy to the intrinsic AGN luminosity, have been shown to be falsifiable if reddening corrections are carefully handled.

Spectral observations of individual AGN in the $2 - 10$keV energy range have shown a number of sources to have complex spectral features, including partial obscuration by different column density media. With these observations in mind, this work has developed a model making use of partial obscuration as a means to explain the observed obscured fraction vs. X-ray luminosity seen at these energies.

3.11 Conclusions

In this chapter I have developed a partial obscuration model to explain the observed obscured fraction vs. X-ray luminosity trend seen in AGN. While the best fitting model is a four discrete population model (one unobscured and three obscured at very different levels), this motivates a continuous distribution model in which there is a unobscured population and a further obscured population in which the level of covering is determined by a distribution of covering factors. Such a model is best fit to a particular observational data set (Hasinger 2008) but introducing a “buried” population of sources with 99.9 percent covering factor, representative of 30 percent of the total population, and a further 37 percent of the population having covering factors dictated by a log-Gaussian distribution. For the best fitting model parameters, the unobscured fraction is found to be one third of the total population. The introduction of the “buried” population is dependent on the quality of the results in the low-luminosity X-ray regime ($\log_{10} L_{\rm X} < 42.5$ erg s^{-1}, which can become contaminated by galactic sources. If these luminosity bins are rejected, this negates the need of a “buried” fraction all together.

Not only does this model reproduce the observed obscured fraction vs. X-ray luminosity trend observed by Hasinger (2008), but it also explains much of the variation seen in the X-ray/IR ratio (Brightman and Nandra 2011, LaMassa et al. 2011) in AGN samples.

Chapter 4

Classification and Characterisation of H-ATLAS 250μm Selected Sources

4.1 Abstract

Using spectral line diagnostics, *Herschel* 250μm sources in the H-ATLAS and GAMA + SDSS overlapping fields are classified and characterised. A sample of 7433 sources spanning redshift range $0 < z < 0.38$ contains 36 broad line (type-I) objects, 146 narrow line (type-II) objects, 234 LINERs and 2090 star forming galaxies, as well as 229 ambiguously classified objects (either composite star forming-AGN, or type-II/LINER objects) and 4697 passive galaxies. The sample has a median stellar mass, star-formation rate and infrared luminosity of $2 \times 10^{10}\,\mathrm{M}_\odot$, $1.3\,\mathrm{M}_\odot\,\mathrm{yr}^{-1}$ and $2.7 \times 10^{10}\,\mathrm{L}_\odot$ respectively, hence probing quiescent star-forming objects far from the Ultra Luminous Infra-Red Galaxy (ULIRG) regime.

No evidence is found for a type-II AGN fraction (f_2) vs. `[OIII]` luminosity dependence, at odds with predictions from the receding torus model.

By decomposing the AGN fraction into type-I+type-II AGN vs. LINERs a positive correlation in the AGN fraction vs. galaxy formation time, t_{form}, is found that is entirely dominated by the LINER population. Negative correlations in the AGN fraction vs. 250μm luminosity, $\mathrm{L}_{250\mu\mathrm{m}}$ and vs. dust mass, $\mathrm{M}_{\mathrm{dust}}$ are reported that are also entirely dominated by the LINER population. The type-

I+type-II AGN fraction shows no significant change vs. t_{form}, $L_{250\mu\mathrm{m}}$, M_{dust}. An AGN fraction vs. stellar mass, M_* dependence is also reported in both the type-I+type-II AGN and LINER populations, but with a shallower dependence than found in previous works.

The LINER population is found to be significantly older than the type-II AGN population, with a much lower star formation rate and significantly less dust for a given stellar mass. The type-II AGN have a larger range of colour excesses ($E(B-V)$) in nebular lines compared to LINERs. Further significant - though weak - trends are found in the evolution of spectral line ratios with stellar age. The passive population, which makes up the majority of the sample, is found to be older, more far-infrared luminous, more quiescent and to have less dust for a given stellar mass than the star forming population. A classification bias due to the aperture effect is investigated, but shown to have a minimal effect on the conclusions.

4.2 Introduction

Observations in the far-IR (FIR) reveal emission from cold dust in galaxies. While dust represents a tiny fraction of the mass density of the Universe, stars form in dense gas and dust clouds with the dust getting heated by UV radiation from these stars. Also, starlight from the general stellar population contributes to heating the dust. Thus measuring the FIR emission from galaxies allows us a relatively unbiased view of their star formation. With general dust temperatures in the 10-100K region, we are far from the hot dust emission associated with Active Galactic Nuclei (AGN), which lies at $100-300$K (and up to $\sim 1,000$K, close to the dust sublimation temperature).

4.2.1 Photometric Modelling of Dust

The photometric FIR data of star forming regions can be well modelled by a greybody spectrum at characteristic dust temperature, T_d, a blackbody modified by the emissivity index, β, which is frequency dependent:

$$\begin{aligned} S_\nu &= \epsilon_\nu B_\nu \\ &= \nu^\beta \left(\frac{2h\nu^3}{c^2} \frac{1}{exp(h\nu/kT_d) - 1} \right) \end{aligned} \tag{4.1}$$

where S_ν is the flux density, ϵ_ν is the emissivity equal to ν^β where ν is the frequency. T_d is the characteristic temperature of the medium, B_ν is the spectral radiance for a black body, defined as the bracketed term in the above equation, k is the Boltzmann constant, h is Planck's constant, c is the speed of light in a vacuum.

4.2.2 Where does the dust come from?

The main production of dust is believed to occur in type-II supernovae and in low-intermediate mass Asymptotic Giant Branch (AGB) stars. Type-II supernovae are large, singular stars than have undertaken thermonuclear fusion up to iron in the core, as well as lighter metals in shells, before exploding and enriching the Interstellar Medium (ISM) with these elements (Todini and Ferrara 2001). In low-intermediate mass AGB stars heavier elements are dredged up from the cores before being expelled through stellar winds (Valiante et al. 2009; 2011).

4.2.3 Reddening

Dust acts to extinguish and redden the light emitted from a host galaxy. Studies of dust from the Milky Way have shown a simple relation between wavelength and extinction (Cardelli et al. 1989) with a characteristic feature at 2175Å associated with small carbonaceous grains (Mathis et al. 1977). Studies of dust in the Magellanic Clouds have, however, found a much flatter relationship between wavelength and extinction, with little to no sign of a 2175Å feature.

Calzetti et al. (2000) undertook observations in order to constrain the dust extinction for starburst galaxies. They found the dust extinction to be steeper than that of the Milky Way and Magellanic Clouds

It is the combined knowledge of these extinction laws which make up modern ISM models for dust. The mean extinction law depends on only one parameter, which is chosen to be R_v, where

$$R_v = \frac{A(V)}{E(B-V)} = \frac{A(V)}{A(B) - A(V)} \tag{4.2}$$

where $A(V)$ and $A(B)$ are the total extinction in the V and B bands respectively. This parameter, R_v is typically taken to be ~ 3.1 for the Milky Way, whilst for the SMC is significantly lower at ~ 2.93 (meaning that the SMC has much larger far-UV extinction than the Milky Way). The derived mean starburst R_v from Calzetti et al. (2000) is $R_v = 4.05 \pm 0.8$.

Studies of starburst galaxies have shown the stellar continuum to suffer less attenuation due to dust than the nebular regions as measured from Balmer decrements (Calzetti et al. 1994, Storchi-Bergmann et al. 1994), by up to a factor of two. It is clear that the dust distribution in galaxies is very clumpy with young stars and their associated nebulae being more extinguished while older populations (which have cleared their birth clouds) are attenuated by only the diffuse ISM. Rhee and Larkin (2005) report that type-II AGN show higher levels of reddening in their NLR than type-I AGN. Together these results naively imply an AGN classification that depends on host composition, however, Rhee and Larkin (2005) have attributed this to an extended dusty torus, reconciling their result with the unified model.

4.2.4 Star Formation Rate Indicators

Star Formation Rate (SFR) indicators are defined from the X-ray through to the radio regime, all probing the SFR of high mass objects where the stellar lifetime is short, and so all have minimal contamination from older objects. Using an assumed Initial Mass Function (IMF) and population synthesis model, one can infer the total SFR of any galaxy. Each SFR indicator has associated strengths and weaknesses, usually associated with dust attenuation and contamination from AGN and old stellar populations. The most commonly adopted SFR indicator, the Ultra-Violet (UV) luminosity traces high mass stars directly. However, since UV photons are easily attenuated by small amounts of dust, direct measurement of the UV luminosity is often not possible. To a lesser extent this measurement can also be contaminated by emission associated with accretion activity in an AGN, but this can often be flagged using proxies of AGN activity such as `[OIII]`, hard X-ray, mid-IR (10-30μm) and radio emission.

The next most commonly used SFR indicator is the $H\alpha$ line. This line is produced by gas that has been ionised by hot, young stars and so should also give a direct measurement of the current SFR, provided reddening is not significant and can be quantified. Not surprisingly the $H\alpha$ line can also be heavily contaminated by AGN activity, and using the same flagging methods as previously described becomes necessary here also.

The FIR emission, that is a re-emission of attenuated UV photons by dust, can also be an effective measure of the SFR. However, with the majority of dust lying in the InterStellar Medium (ISM) and heated by the general stellar radiation field, the FIR emission is associated with current star formation in lower mass objects also i.e. those objects which do not emit significant amounts of UV radiation. One must study the SED from UV to sub-mm in order to constrain the SFH effectively. Many contemporary calculations rely on a combination of UV and FIR flux measurements in order to estimate the unobscured and obscured SFRs respectively.

4.2.5 Type-II Fraction

In the unified scheme type-I and type-II objects differ only in orientation to the observer; the line of sight for type-I objects is often taken to be perpendicular to a "torus" plane, whilst for type-II objects the central engine is obscured by the dusty torus.

In the optical regime one commonly used proxy to the intrinsic luminosity of the central engine is the narrow forbidden line `[OIII]`: studies of type-I objects have found ratios for the `[OIII]` to 5100Å luminosities, and then inferred 5100Å to bolometric luminosities based on the an average type-I Quasar SED, before finally relating the derived luminosities to those found in X-ray studies (see Lamastra et al. 2009, and references there in).

Simpson (2005) and references therein find the optical type-II fraction to depend heavily on the inferred intrinsic luminosity of the central engine, the `[OIII]` luminosity, with type-II objects accounting for some $60-80$ percent of the population at low luminosities ($\log_{10} L_{\rm [OIII]} \sim 41$ erg s^{-1}), gradually declining to around 30 percent at high luminosities ($\log_{10} L_{\rm [OIII]} \sim 45$ erg s^{-1}). Results from Lu et al. (2010) show a result consistent with a fixed type-II fraction of between 75 − 80 percent

In general, an unbiased measurement of the Type-I to Type-II AGN fraction are very difficult, given that the detection methods are often biased towards Type-I objects. This is an issue which I address here.

4.3 Data

Here, I describe in more detail the overlapping equatorial survey fields from which the sample has been drawn. The sample is a 250μm selected galaxy sample from the H-ATLAS Survey, where optical spectra from the SDSS and GAMA surveys are available. The data includes medium resolution optical spectroscopy and 13 bands of photometry.

4.3.1 The H-ATLAS

The Phase 1 (P1) catalogue of the *Herschel*-Astrophysical Terahertz Large Area Survey (H-ATLAS; Eales et al. 2010, Valiante et al., in prep) consists of five bands of photometry at 100, 160, 250, 350 & 500μm. Observations at 100 and 160μm are taken with the Photodetecting Array Camera and Spectrometer (PACS; Poglitsch et al. 2010) and at 250, 350 and 500μm using the Spectral and Photometric Imaging Receiver (SPIRE; Griffin et al. 2010). The survey is taken out aboard the *Herschel* Space Observatory (Pilbratt et al. 2010).

The P1 data release covers three equatorial regions of the Galaxy And Mass Assembly survey (GAMA; Driver et al. 2011), see below. Sources brighter than 5σ in any single band of the SPIRE data were extracted using the MAD-X algorithm (Maddox et al., in prep) applied to the maps, which are made using the method described in Pascale et al. (2011). Fluxes at 100 and 160μm were derived using apertures placed on the PACS maps (Ibar et al. 2010) at the locations of the 250μm source positions; the H-ATLAS catalogue is described in detail in Rigby et al. (2011).

The master H-ATLAS catalog is a 250μm selected flux limited sample with $f_{250\mu\mathrm{m}} > 30.4$ mJy (5σ) amounting to 66552 sources. Photometry is provided across all Herschel PACS and SPIRE bands at 5σ point source flux limits of 130, 130, 30.4, 36.9, and 40.8 mJy in the 100, 160, 250, 350 and 500μm bands, respectively, with corresponding angular resolutions of approximately 9”, 13”, 18", 25" and 35" full width half maximum. Photometry for 100, 160, 350 and 500μm is performed at the locations of the 250μm sources.

4.3.2 Optical

I select of subset of 250μm selected galaxies that have available spectra from GAMA survey or the SDSS:

GAMA

The GAMA survey has undertaken spectroscopic observations of some $340,000$ galaxies to a magnitude of $r_{\rm pet} < 19.8$ over a 310 square degree field, at a resolution of $R \sim 1300$. The Petrosian system is defined by the Petrosian radius at which aperture photometry is recorded; the Petrosian radius, $r_{\rm pet}$ is defined such that the local light intensity that radius is equal to the average of the integrated light intensity within that radius (Petrosian 1976).

Observations commenced in 2008 with the AAOmega multi-object spectrograph at the Anglo-Australia Telescope (AAT). The fields that have been observed for the GAMA survey are among those which have subsequently been selected for observation in the H-ATLAS survey, roughly centred at RA $=09^{\rm h}$ (G09), $12^{\rm h}$(G12) and $14.5^{\rm h}$(G15)

As well as spectra and reliable redshifts for 98 percent of their sample, the GAMA dataset has an abundance of ancillary data from multiple facilities.

SDSS

The *Sloan* Digital Sky Survey (York et al. 2000, SDSS) has mapped more than one quarter of the entire sky ($14,500$ square degrees) in five band optical photometry (ugriz) to petrosian magnitudes of 22.0, 22.2, 22.2, 21.3, and 20.5 respectively and spectroscopic observations covering more that $9,300$ square degrees between 3800 and 9200Å at a resolution of $R \sim 2000$. The SDSS is now in its third stage (SDSS-III) which is due to complete in 2014. Here only data from the SDSS-II Data Release 7 (Abazajian et al. 2009) is used, which contains $\sim$ 1.15 million spectroscopic extragalactic objects.

4.3.3 Additional Data

The UKIDSS-LAS

The UKIRT[1] Infrared Deep Sky Survey (Lawrence et al. 2007, UKIDSS) contains five separate survey fields ranging from wide-shallow galactic to small-deep extragalactic fields. The UKIDSS survey is undertaken using the Wide Field CAMera (Casali et al. 2007, WFCAM) on the United Kingdom InfraRed Telescope (UKIRT) with observations for four near-IR bands (YJHK) to a depth of $K = 18.4$. The Large Area Survey (UKIDSS-LAS. PI Richard Jameson) covers some $4,000$ square degrees split over three high Galactic latitude fields.

4.3.4 Combining the H-ATLAS+GAMA+SDSS+UKIDSS-LAS Data

Combined coverage at FIR wavelengths from the H-ATLAS, optical photometry and spectroscopy from SDSS and GAMA, along with the near-IR data from the UKIDSS-LAS, making a sample with 13 bands of photometry and spectra of sufficient quality for velocity dispersion measurements and optical emission line deblending.

Catalog matching between the H-ATLAS and GAMA data is performed by Smith et al. (2012) using a likelihood estimator

$$R_j = \frac{L_j}{\sum_i L_i + (1 - Q)} \tag{4.3}$$

where R_j represents the probability that object j is the correct identification, L is the likelihood ratio, the sum $\sum_i$ is over all possible cross match candidates and Q is the integrated probability distribution function in magnitude over an ensemble of sources (see Sutherland and Saunders 1992, for a detailed derivation). In practice any source with $R \geq 0.8$ is deemed to have a reliable optical counterpart.

---

[1] The United Kingdom Infrared Telescope is operated by the Joint Astronomy Centre on behalf of the Science and Technology Facilities Council of the U.K.

4.3.5 My Sample

The H-ATLAS P1 (version 1) sample contains 66552 unique 250μm sources, of which 10935 have GAMA ID's. Within the redshift window $0 < z < 0.38$ are some 9740 sources, of which 4690 and 2746 have GAMA and SDSS spectra respectively. This redshift range excludes windows z= $0.245-0.255$,$0.265-0.275$ since at these redshifts skylines interfere with Hβ and `[OIII]` lines in the optical spectra, and so will not allow for optical spectral classification (see later). This gives us a sample of 7433 sources. Some 1437 of these 7433 sources have at least three far-IR bands of photometry above the flux limits defined above. The redshift upper limit is chosen to coincide with the spectral window for emission lines used for the Baldwin-Philips-Terlovich diagnostic technique described below.

The rest of this chapter discusses the derivation of paramaters for the 250μm sample, followed by their subsequent classification and characterisation.

4.4 Deriving Parameters from Spectra and Multi-Band Photometry

I process each source spectrum further using a spectral line extraction technique to derive line fluxes and to quantify the reddening in the optical regime. I perform full Spectral Energy Distribution (SED) fitting in a flux conserving manner across the 13 photometric bands in order to derive parameters such as stellar mass (M_*), dust masses ($M_{\rm dust}$), formation times ($t_{\rm form}$) and star formation rates (SFR). The emission line fitting routine is adapted for this work from Sarzi et al. (2006), and the SED fitting routine is the MagPhys software (da Cunha et al. 2008). Each of these steps is now described in detail.

4.4.1 Spectral Continuum and Absorption/Emission Line Fitting

The Gas And Absorption Line Fitting software (GAndALF; Sarzi et al. 2006), originally written for use with the SAURON integral field instrument on the William Herschel Telescope in La Palma, has been adapted to analyse SDSS and GAMA spectra: adaption for SDSS spectra is performed by Schawinski et al. (2007), adaptation for GAMA spectra is undertaken in this work.

The objective of the software is the simultaneous fitting of stellar continuum and absorption/emission lines associated with nebular regions (including lines associated with AGN and/or hot stars). The crude continuum subtraction method adopts stellar continuum templates modified by a linear combination of Hermite polynomials while masking out emission-line and sky-line regions in the spectra.

The result is continuum subtracted absorption and emission line fluxes, line widths, stellar velocity dispersions and reddening values from both the stellar continuum and for emission lines. Velocity dispersions are derived by using the penalised pixel fitting (pPXF; Cappellari and Emsellem 2004) method, which convolves model spectra with parametrized Line-of-Sight Velocity Dispersion (LOSVD) models, before performing a χ^2 mimimisation. Reddening values are derived as colour excesses, E(B-V). For the stellar continuum, this makes use of the Calzetti et al. (2000) extinction law. The attenuation of the nebular lines is calculated in a different manner, instead using theoretically prescribed intrinsic decrements of emission line series. Most commonly used is the Balmer decrement values which are calculated for a "*case-B*" scenario.

It is also possible for GAndALF to fit broad-line features seen in type-I AGN features, most prominent in Balmer series lines. Each of these must be checked and flagged by eye since imposing broad-line fit where one is not present can adversely affect continuum subtraction. Those sources with "false-positive" broad lines features are re-run through the GAndALF software without mandatory broad-lines.

Figure 4.1 shows the best fit solution from GAndALF for type-I source, $\mathrm{ID_{SDSS}}$ =51663-0307-166. Figure 4.2 shows the best fit solution from GAndALF for type-II source, $_{\mathrm{SDSS}}$ =51913-0469-014.

4.4.2 SED fitting

The MagPhys software (da Cunha et al. 2008) fits the SED of sources over the UV- to sub-mm regime, accounting for dust attenuation in a flux conserving manner i.e. the attenuation of signal in the UV/optical regime must be accounted for by re-emission in the IR.

The software uses a combination of cold dust, warm dust and PAH features as reradiation components. The cold and warm dust components are taken

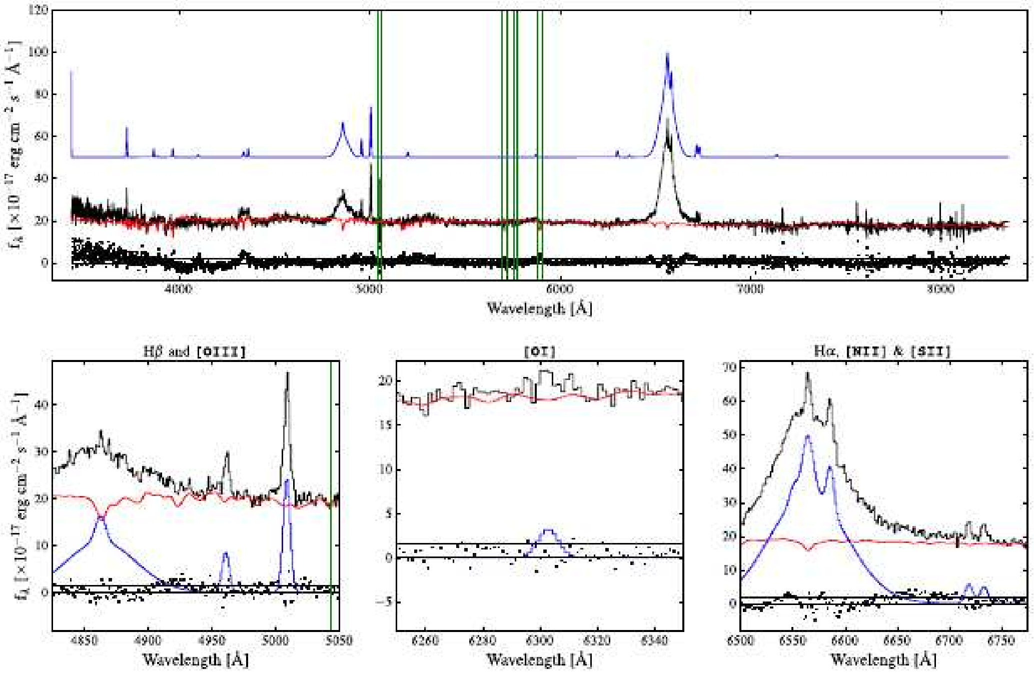

Figure 4.1: A plot of the spectrum of SDSS source $_{\mathrm{SDSS}}$ =51663-0307-166. The best fit GAnDALF solution is also shown. The spectrum itself is shown in black, the best fit spectral continuum is shown in red, the best fit emission lines in blue, the residual points are shown as black dots. Note the masked skyline regions shown in green. The bottom sub-plots show zoomed regions of the spectrum around the Hβ+`[OIII]` complex, `[OI]` emission line and Hα+`[NII]` complex.

to be grey-bodies with emissivities of $\beta = 1.5$ and $\beta = 2.0$ respectively, with dust temperature as a free parameter for each component. The PAH emission is taken from a mid-IR template of three local starbursting dwarf galaxies (Madden et al. 2006) and is combined with a hot dust black body (at 850K), whose luminosity is taken as a fixed fraction of the PAH luminosity. The free parameter for this PAH + host dust component is its luminosity, i.e. a simple normalisation constant. In the optical regime, stellar templates are taken from stellar population synthesis models for a range of different age galaxies, stellar masses, star formation rates and metallicities (Bruzual and Charlot 2003). The fitting routine uses the dust absorption model of Charlot and Fall (2000) to attenuate the optical light, enforcing a re-emission component in the FIR in a flux conservating manner. Full SED fitting using the MagPhys software allows one to calculate likelihood estimates of the star formation rates, stellar masses,

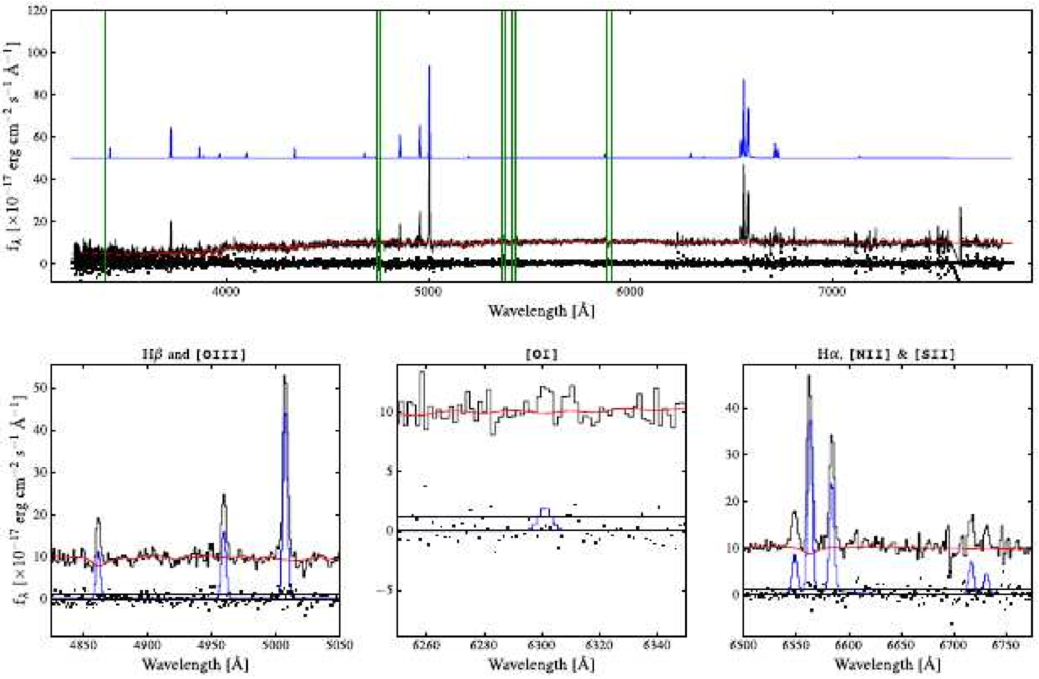

Figure 4.2: A plot of the spectrum of SDSS source $_{\mathrm{SDSS}}$ =51913-0469-014. The best fit GAnDALF solution is also shown. Lines and subplots as per Figure 4.1.

dust masses, dust temperatures and effective dust optical depths. While PAH contributions can be constrained where sufficient mid-IR data are available, with insufficient data for the H-ATLAS fields this is not performed here.

4.4.3 Classification of the Sample - BPT Diagnostic

It is necessary to classify our sample. The standard practice for classification of AGN uses optical spectral lines; a method which uses narrow emission line ratios combined with theoretically derived demarcations allows for star-forming galaxies to be separated from both LINERs and AGN. Many of the diagnostic narrow emission lines which are used are associated with low density, highly excited media; `[OI]`$\lambda 6300\mathring{A}$, `[OII]`$\lambda\lambda 3726, 3729\mathring{A}$, `[OIII]`$\lambda 5007\mathring{A}$, `[SII]`$\lambda\lambda 6717, 6731\mathring{A}$ and `[NII]`$\lambda\lambda 6548, 6584\mathring{A}$.

The Baldwin-Phillips-Terlevich (BPT Baldwin et al. 1981) technique was first used in a heuristic fashion to plot the spectral characteristics of known AGN against star-forming galaxies. The contemporary technique makes use of theoretically derived boundaries between the classes relying on a combination of stellar population synthesis and self-consistent photoionisation models to produce a "maximum starburst" line (Kauffmann et al. 2003). This "maximum starburst" line is a calculation of the maximum theoretical line ratios used in the BPT technique purely based on star formation related emission alone.

The modern technique uses pairs of lines that are similar in wavelength so as to minimise reddening effects. The most common diagnostic diagram uses [OIII]/Hβ *vs.* [NII]/Hα. Note that this diagnostic relies on spectra of sufficient quality as to be able to deblend [NII] and Hα lines.

Empirically derived lines to distinguish between star forming and composite star forming-AGN galaxies, and between Seyfert and LINER galaxies are also used (Kewley et al. 2006): The star forming/composite star forming-AGN galaxiess demarcations are derived from luminosity binning of sources, which at low luminosities produces an *AGN tail* which deviates from the star-forming locus, but exists far below the theoretical AGN demarcation line. The type-II AGN/LINER galaxy demarcation is derived such as to give a maximum bimodality in the AGN wing.

As previously discussed, masked regions in the spectral analysis at sky-line wavelengths $\lambda = 6300$Å and 6363Å coincide with the emission lines at redshifts $z = 0.245 - 0.255, 0.265 - 0.275$, and so sources in these spectral windows are not included in the sample. Sources that have a $S/N \geq 2$ in both `[OIII]` and $H\alpha$, and at least in `[NII]`, `[SII]` or `[OI]`, and with no broad Balmer features are classified according to the BPT diagnostics, whereas sources with lower signal-to-noise in these lines are classified as passive galaxies. Sources with evidence of broad lines (visually confirmed and with linewidths $\sigma_{\mathrm{H}\alpha} > 1,000$km s^{-1}) are classified as type-I AGN. Figure 4.3 shows the BPT diagram for the 2699 H-ATLAS sources which are neither passive nor broad line objects.

Objects present in the BPT diagram are classified as follows:

- Star forming galaxies are those which lie in the star-forming region of BPT-1 (`[OIII]`/Hβ vs. `[NII]`/Hα) and also in at least BPT-2 (`[OIII]`/Hβ vs. `[SII]`/Hα) or BPT-3(`[OIII]`/Hβ vs. `[OI]`/Hα).

- Unequivocal AGNs and LINERs must lie in the AGN region in BPT-1 and AGN/LINER (respectively) in either BPT-2 or BPT-3, or else where the signal-to-noise for `[NII]` is insufficient the sources must lie within the AGN or LINER loci in both BPT-2 and BPT-3 respectively.

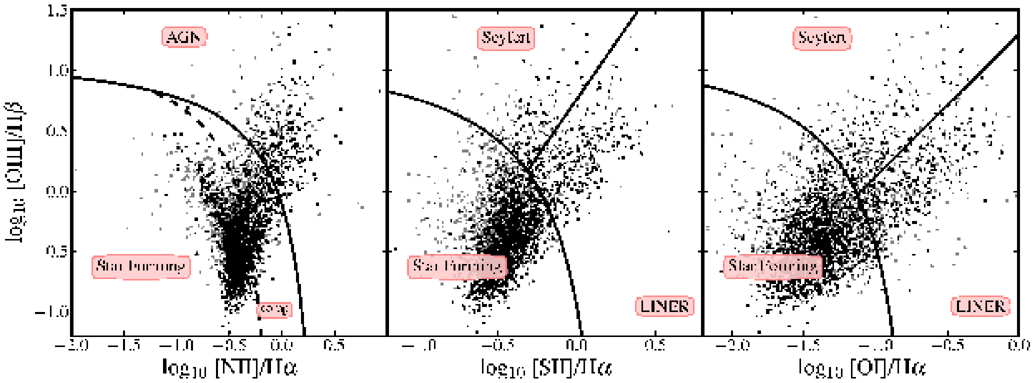

Figure 4.3: A plot of spectral line diagnostic diagrams (BPT) with Star Forming-AGN demarcation lines taken from photoionisation models, and empirically derived Seyfert-LINER demarcations taken from Kewley et al. (2006) where the classes are separated according to maximum bimodality. Classification of ambiguous sources is performed as described in the text.

- Composite sources are classified ambiguously as star-forming galaxies in BPT-1 and as AGN or LINER in each of BPT-2 and BPT-3, or as an AGN in BPT-1 and star-forming in both BPT-2 and BPT-3 or as classified as AGN in BPT-1 and star-forming in either BPT-2 or BPT-3 (where data are insufficient to allow three diagram classification).
- LINER/type-II AGN type objects are classified as AGN in BPT-1 and AGN & LINER in BPT-2 & BPT-3 or LINER & AGN in BPT-2 & BPT-3.

4.4.4 Aperture Effect

Does the spectral fibre size in the GAMA or SDSS instrumentation, and its effective sampling at different redshifts (the so called *aperture effect*) have an impact on the results? For instance, am I more likely to be classifying nearby objects differently to those further away due to aperture sampling?

Local sources are more dominated by their core emission within the spectral fibres than their more distant counterparts. So, for example, local *true* LINERs are less “contaminated” by star formation activity in their observed spectra than more distant counterparts, which leads to a more concrete classification as a LINER. Conversely, those sources at higher redshift will have higher contamination from star-formation activity and so less likely to be classified as

Table 4.1: A table showing the derived parameters, and the method from which they are derived, for the H-ATLAS sample.

Parameter	**Method of Derivation**
Line fluxes (e.g. Hα,Hβ,`[OIII]`,`[NII]`)	GAndALF
Continuum Reddening E(B-V)$_{\mathrm{cont}}$	GAndALF
Emission Line Reddening E(B-V)$_{\mathrm{EL}}$	GAndALF
Stellar Mass (M$_*$)	MagPhys
Dust Mass (M$_{\mathrm{dust}}$)	MagPhys
Star Formation Rate (SFR)	MagPhys
Stellar Age (t$_{\mathrm{form}}$)	MagPhys
Class (e.g. Star forming galaxy, Passive, LINER)	BPT Diagram

LINERs (or indeed AGN in general). Hence the observation that the old LINERs have lower star formation rates than similarly aged star forming galaxies is going to be subject to a selection bias.

I estimate the magnitude of the aperture effect by showing the $\log_{10}$ `[OI]`/Hα ratio sampling across my redshift range. Taking characteristic $\log_{10}$ `[OI]`/Hα ratios for a star forming galaxy and a median LINER of -1.41 and -0.68, respectively (taken from the relevant BPT diagram in Figure 4.3) I calculate relative contributions from star formation and LINER activity by a star-formation rate tied Hα luminosity (derived from the Kennicutt (1998), 1M$_\odot$ yr^{-1} corresponds to $\mathrm{L}_{\mathrm{H}\alpha} = 1.27 \times 10^{41}$ erg s^{-1}) and sampling a range of LINER Hα luminosities (0.01L$_{\mathrm{SF}}$,0.1L$_{\mathrm{SF}}$ and 1L$_{\mathrm{SF}}$. I assume the LINER emission to be concentrated at a central peak and the star formation to be spread across a 50kpc diameter symmetric disc. Using the SDSS fibre width of 3” diameter, I show the aperture effect upon this line ratio in Figure 4.4, the change in `[OI]`/Hα to be minimal across our redshift range compared to differences in the absolute star formation vs. LINER Hα luminosities. Therefore, I conclude that the aperture effect will have a minimal effect in biasing the sample against core activity at higher redshifts.

4.4.5 Derived Parameters

In Table 4.1 I show a list of the parameters and the method by which they are derived.

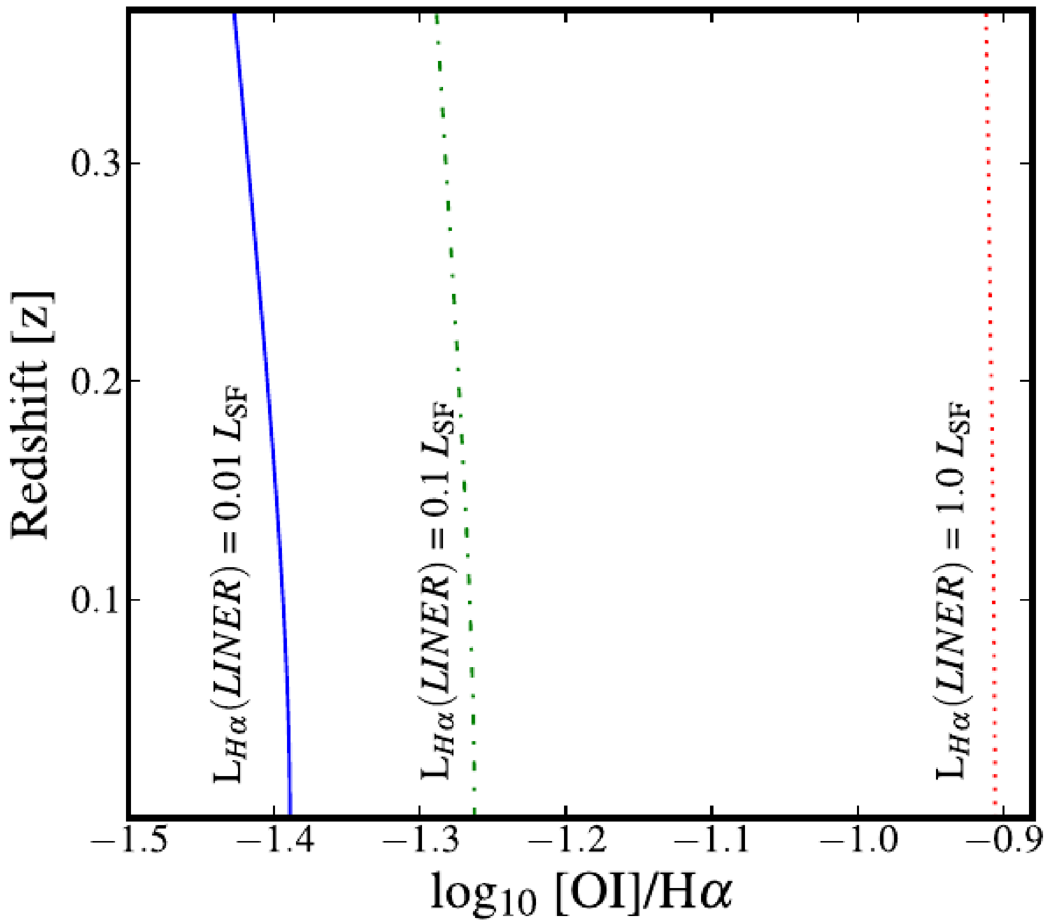

Figure 4.4: A plot of the observed `[OI]`/Hα ratio for 3 objects with intrinsic star formation and LINER activity.

Table 4.2: A table showing the population statistics for the H-ATLAS sample at an emission line $S/N \geq 2$.

Type	**SDSS**	**GAMA**	**Total**
Star Forming Galaxies	1415	675	2090
Type-I AGN	26	14	36
Type-II AGN	85	61	146
Composite star forming/AGN	109	51	160
LINER	192	42	234
LINER/Type-II AGN	54	15	69
Passive	865	3832	4698

4.5 Results

4.5.1 Redshift Distribution

Figure 4.5 shows the 250μm luminosity vs. redshift for the sample. No significant evidence is found that type-I and type-II AGN have different redshift distributions, with a Kolmolgorov-Smirnoff (KS) p-value of 25.0 percent. There is also no significant evidence of a different redshift distribution for the Star forming galaxies vs. type-I, type-II, LINERs or passive galaxies . Masked regions representing the aforementioned skylines are shown at the appropriate redshifts to coincide with Hβ λ4861Å and `[OIII]` λ5007Å emission lines. The 250μm flux limit of 30.4μJy is also shown. Note that the visible difference in the histogram from the Type-I AGN (red dashed line) compared to all other classes is merely due to the small Type-I AGN sample size, and is not statistically significant

4.5.2 Population Statistics

Spectral analysis using the BPT technique described above classifies Herschel 250μm selected sources as shown in Table 4.2.

4.5.3 Assessment of Uncertainties within the BPT classification

Does the classification of sources depend on the S/N cut used? If a more conservative S/N cut in the BPT diagnostic be adopted, S/N $\geq$ 3 say, then

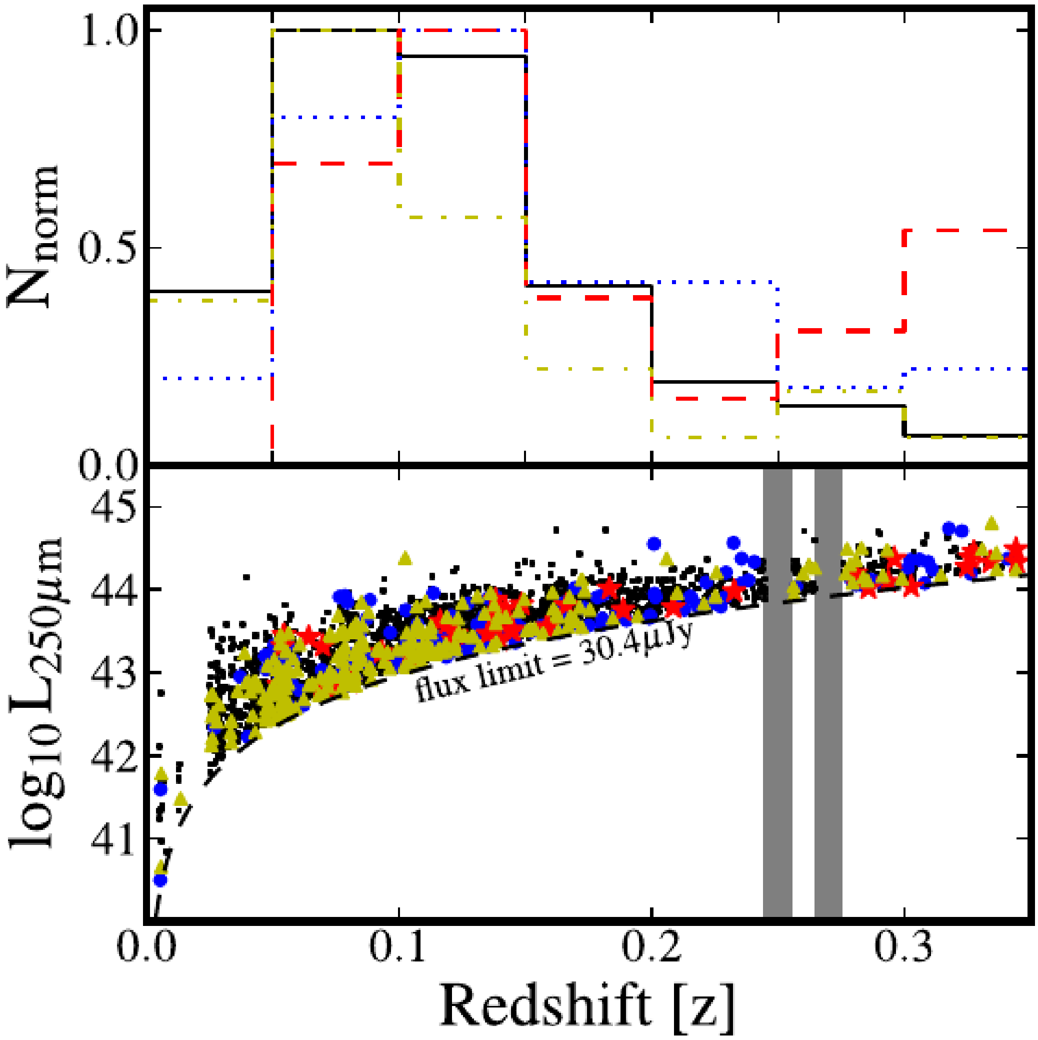

Figure 4.5: A plot of the redshift distribution of star forming galaxies, type-I AGN, type-II AGN, and LINERs over our redshift range. Symbols are: *Star forming galaxies*; black: squares in central plot and solid line in histogram, *type-II AGN*; blue: circles in central plot and dotted line, *type-I AGN*; red: stars in central plot and dashed line and *LINERs*; yellow: triangles and dot-dashed line. The projection of the normalised redshift distributions is shown in the top sub plot. i find no significant evidence of different redshift distributions for any two pairs of class. Log_{10} $L_{250\mu m}$ is in units of erg s^{-1}. Excluded redshift windows at $z = 0.245 - 0.255$ and $0.265 - 0.275$ are shown in grey.

Table 4.3: A table showing a comparison of the population statistics for the H-ATLAS sample at an emission line S/N ≥ 2 and S/N ≥ 3.

Type	**Total**, S/N ≥ 2	**Total**, S/N ≥ 3
Star Forming Galaxies	2090	1447
Type-I AGN	36	36
Type-II AGN	146	120
Composite star forming/AGN	160	93
LINER	234	139
LINER/Type-II AGN	69	50
Passive	4698	5548

the total fraction of passive sources increases (as expected) to circa 75 percent of the entire sample. The fractions of composite objects and LINER drop by ~ 40 percent, while the fraction of star forming galaxies drops by 30 percent. The bona fide AGN classes suffer least in this respect; the type-II objects see a decline of ~ 18 percent. Note that the statistics for the type-I AGN do not change since these objects are visually classified and not according to BPT diagnostic. The change in the population statistics for an increase in S/N ≥ 2 to S/N ≥ 3 is shown in Table 4.3. Subsequent work in this chapter uses the S/N ≥ 2 as detailed earlier.

I show in Figure 4.6 the change in the classification of sources according to the S/N cut used. The top sub plot shows the total fraction of sources that are classified as passives, which as expected increases with more conservative restrictions. The bottom plot shows what fraction of emission line sources i.e. non-passive galaxies that are classified as Seyfert-II, LINER, Composites and Seyfert-II/LINER objects, the "Total" fraction is the total number of emission line galaxies that are not classified as pure star forming galaxies.

4.5.4 Far-IR Luminosity vs. Class

The FIR luminosity is dominated by cold dust emission with minimal contamination from hot dust, and so my parent sample should be unbiased by AGN core activity. To check this I plot the luminosities of our sources according to their classifications: Figure 4.7 shows the 250μm luminosity vs. `[OIII]` luminosity

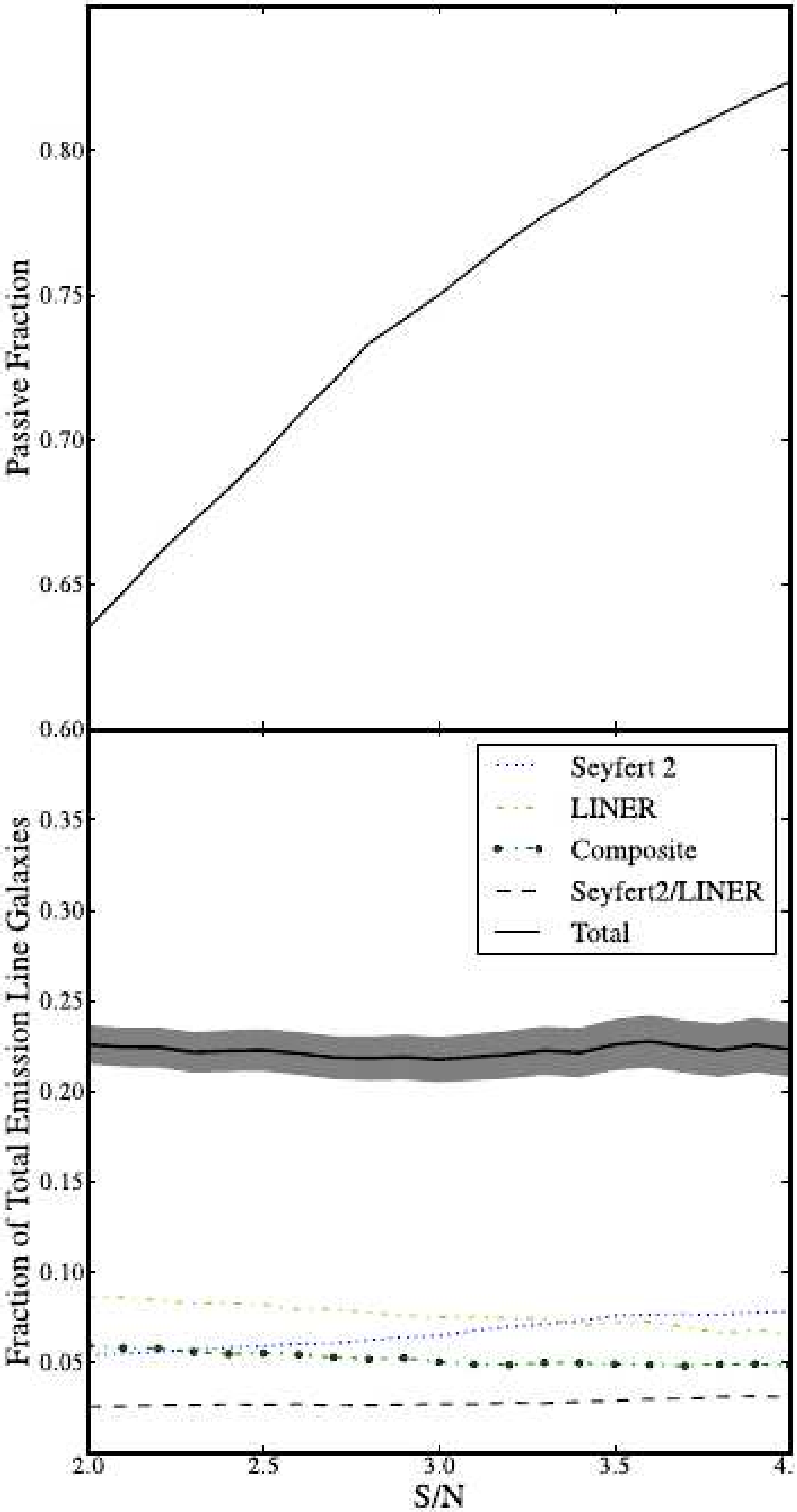

Figure 4.6: A plot of the classification of H-ATLAS sources according to different signal-to-noise cuts. The top subplot shows the total fraction of passive galaxies, while the bottom plot shows the fraction of Seyfert-II, LINER, Composite and Seyfert-II/LINER objects as a fraction of the total emission line galaxies.

for star forming galaxies, type-II AGN, type-I AGN and LINERs with projected distributions associated with the two axes plotted accordingly. One can see from the 250μm luminosity that the peak and shape of these distributions are broadly similar. Note that any discrepancies seen in the type-I objects is largely due to the small size of the sample. KS statistics reveal that the AGN population (type-I+type-II+LINERs) is drawn from the same distribution at 250μm as star-forming galaxies with a p-value of 11.9 percent. Note that the type-I and type-II objects have a very different distribution in $\mathrm{L}_{[\mathrm{OIII}]}$ to the star forming galaxies and LINERs. The median 250μm luminosity of the sample is $\mathrm{L}_{250\mu\mathrm{m}} = 2.7 \times 10^{10}\,\mathrm{L}_{\odot}$, far from the ULIRG regime. Figure 4.8 shows a histogram of the SED derived SFR of the sample.

4.5.5 Star Formation Rate vs. Class

Calculations of the star formation rates are taken from the SED fitting of the full photometric profile of each source with the MagPhys software. Stellar templates are generated from stellar population synthesis code from Bruzual and Charlot (2003) with a Chabrier (2003) Galactic disc initial mass function (IMF). With a median star formation rate of $= 1.3\,M_{\odot}\,\mathrm{yr}^{-1}$, our sample lies far from the Starburst/SMG regime, with only circa one per cent (80/7433) of sources having starburst-like activity (SFR $> 100 M_{\odot}\,\mathrm{yr}^{-1}$) and only seven of these sources can be classified as ULIRG galaxies (with $\mathrm{L}_{\mathrm{IR}} > 100\mathrm{L}_{\odot}$). Around 12 percent of the sample (903/7433) have “high” SFRs of $> 10 M_{\odot}\,\mathrm{yr}^{-1}$.

I compare SED derived SFRs from optical colours to Hα star formation rates derived from the relation given in Kennicutt (1998, eqn 2). No evidence is found for type-I or type-II AGN having a boosted or suppressed star formation rates when compared with star forming galaxy.

No evidence is found for type-II AGN having a different star formation rate distribution to type-I AGN. However, the LINER population SFR is significantly lower than star forming galaxies, when measured in both regimes. This is shown in Figure 4.9 in which the star formation rates according to full SED fitting and that from Hα are compared, with subplots representing different formation ages as detailed in the top left of each sub plot. The SED SFR vs. $\mathrm{L}_{250\mu\mathrm{m}}$, separated by stellar mass is plotted in Figure 4.10. There appears to be a trend for the low

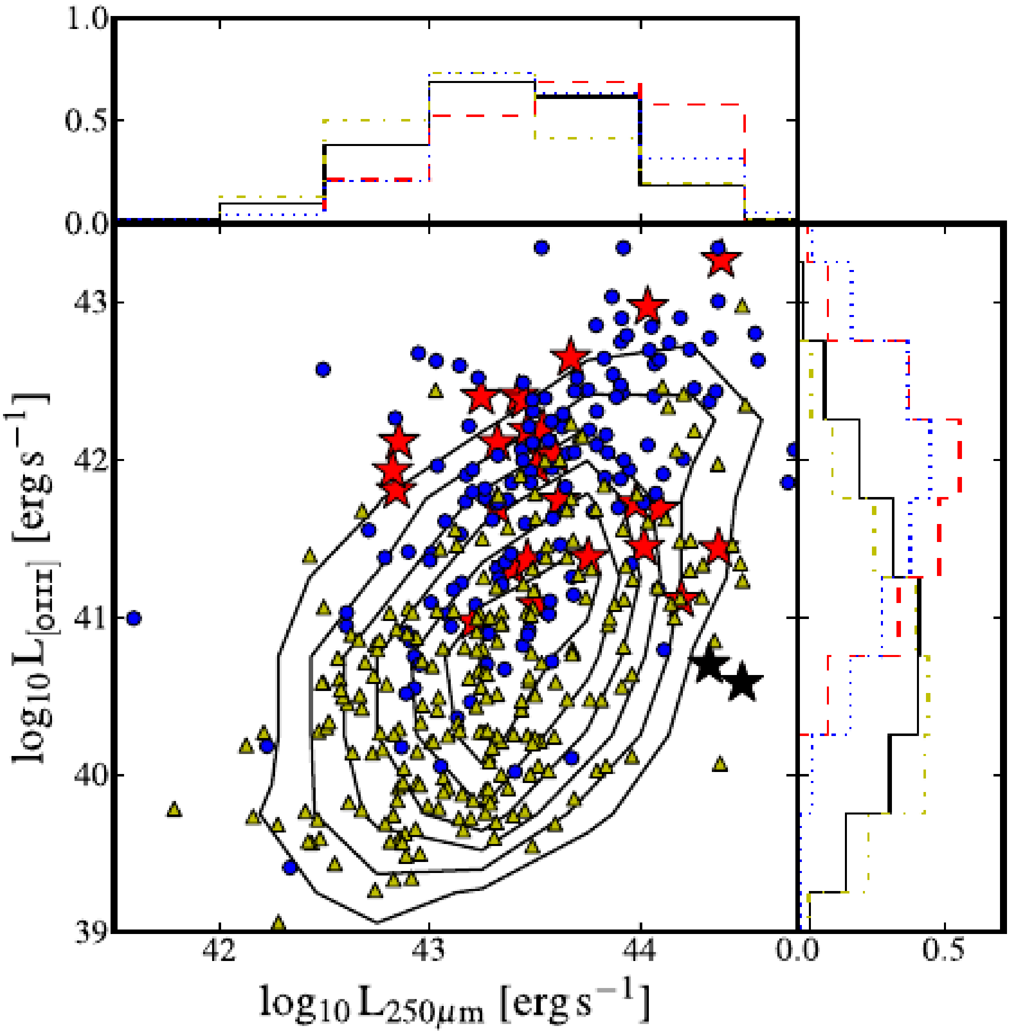

Figure 4.7: A plot of the 250μm luminosity vs `[OIII]` luminosity for all emission line objects in our H-ATLAS sample. Symbols are: *Star forming galaxies*; black: contour in central plot and solid line in histograms, *type-II AGN*; blue: circles in central plot and dotted line, *type-I AGN*; red: stars in central plot and dashed line and *LINERs*; yellow: triangles and dot-dashed line. I note the minimal difference between the classes at 250μm, but the noticeable `[OIII]` boost for the type-I and type-II AGN classes.

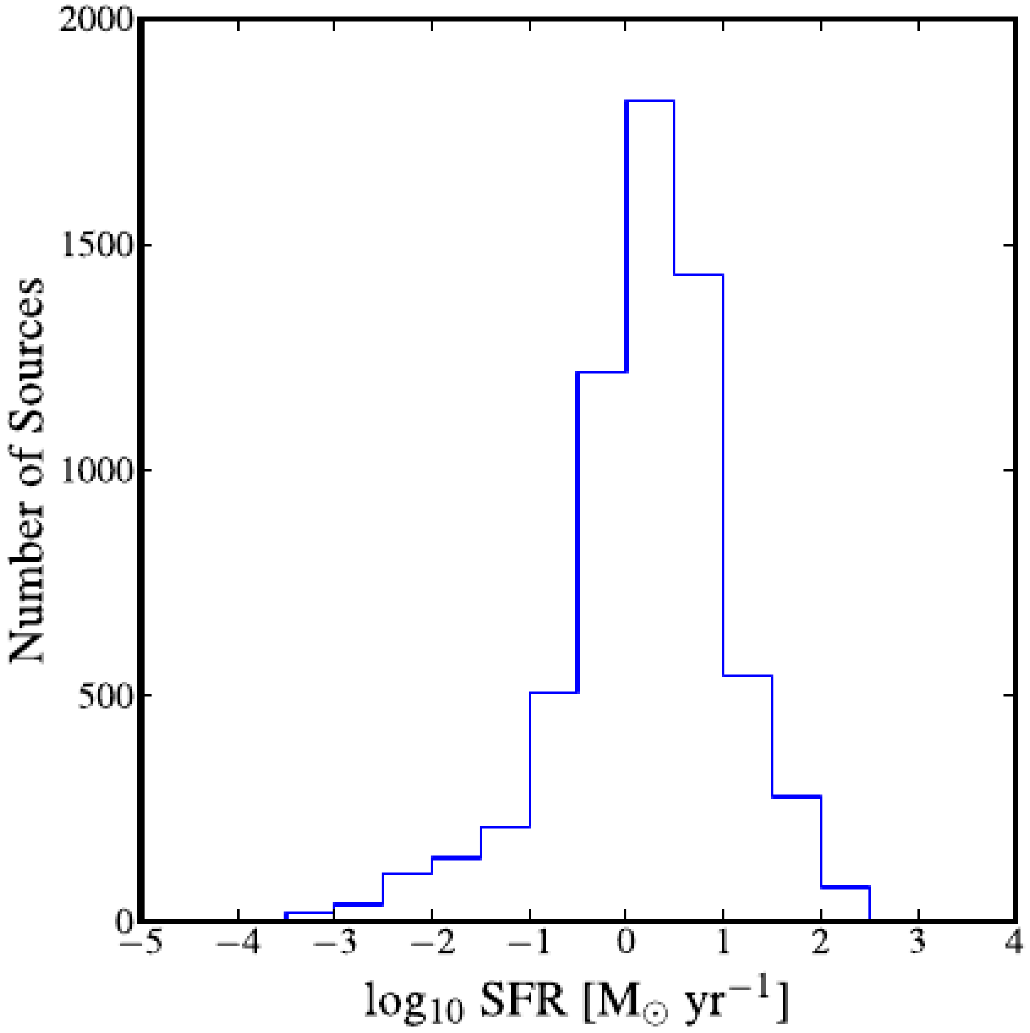

Figure 4.8: A histogram of the $\log_{10}$ SFR of the HATLAS $250_{\mu\mathrm{m}}$ $z < 0.38$ sample. The median SFR of this sample is 1.3 $\mathrm{M}_\odot\,\mathrm{yr}^{-1}$, with only circa one per cent (80/7346) of sources have starburst-like activity (SFR$>100\mathrm{M}_\odot\,\mathrm{yr}^{-1}$). A total of 903 sources have SFR $> 10 M_\odot\,\mathrm{yr}^{-1}$.

star formation rate - high stellar mass objects (especially the LINERs) to have an increased $L_{250\mu m}$ compared to extrapolations from lower mass objects. This can be easily attributed to a mix of cirrus and star formation related dust emission.

4.5.6 The Cirrus Contribution

Can the objects with high $L_{250\mu m}$ compared to SFR derived from optical colours have their "excess" 250μm luminosities attributed to cirrus emission? The $L_{250\mu m}$ contribution from cirrus emission is estimated by using an approximation to the L_{IR}/L_{opt} taken from Rowan-Robinson et al. (1987) $\log_{10} L_{IR}/L_{opt} = -0.7$. An approximation to the cirrus fraction to the IR luminosity is taken from Sauvage and Thuan (1992) who state a cirrus fraction, η of between 0.03 for Sdm galaxies and 0.86 for Sa galaxies. Here I use 86 percent as an upper limit for the general population, to show the maximum cirrus contribution. A mass-to-light ratio (i.e. a *stellar* mass-to-*optical* light ratio) of $MLR = 2$ is adopted, as taken from the Milky Way. Using these crude approximations allows us to estimate, for a given stellar mass, the cirrus luminosity in the FIR:

$$L_{\mathrm{cirrus}} = \eta \times \frac{1}{ML} \times 10^{-0.7} \times \mathrm{M}_* \tag{4.4}$$

where L_{cirrus} and M_* are in units of $L_\odot$ and $M_\odot$, respectively. Cirrus contributions to the FIR luminosity are shown in Figure 4.10 as horizontal dashed lines, and are detailed in the figure caption. One can see in this figure that the high $L_{250\mu m}$ of the low star formation rate-high stellar mass objects can reasonably be explained by the cirrus contribution.

4.5.7 Emission Line Reddening vs. Class

Reddening due to dust is measured from the spectroscopic observations. Separate values for nebular and stellar colour excesses are measured. The nebular colour excess is taken from Balmer decrement measurements vs. the theoretical "Case B" Balmer line ratios (in which the medium as optically thick the Lyman series of emission lines, especially that of Lyα). The stellar colour excess is taken from measurements in the stellar continuum.

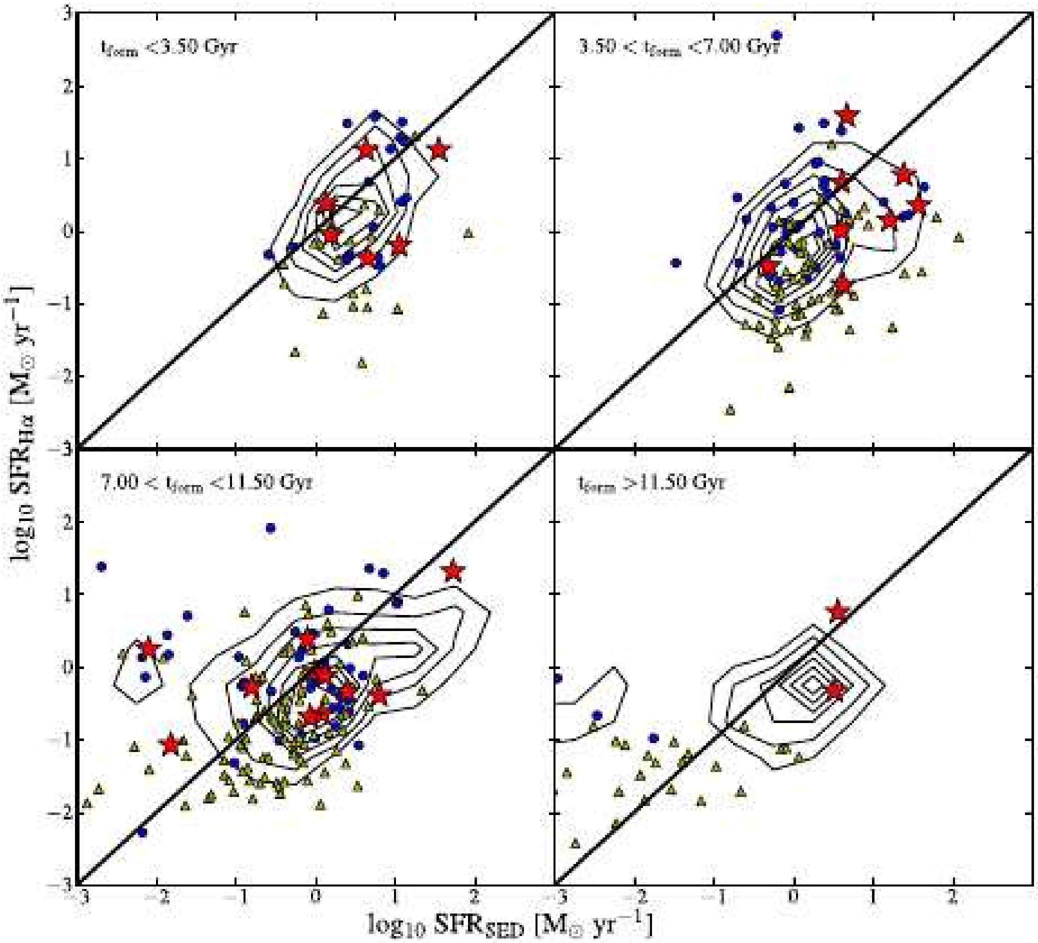

Figure 4.9: A plot comparing the star formation rates derived from SED fitting, and the Hα star formation rate derived from Kennicutt (1998). Symbols are as per Figure 4.7. The subplots are separated according to formation age of the sources taken from SED fitting, as detailed in the top-left corner of each subplot. There is no evidence showing a boost or suppression of SFR in the type-I and type-II AGN classes when compared to star forming galaxies, but the LINER population does show a suppression in the SFR compared to star forming galaxies, as described in the test. Note than the spread in the $\mathrm{SFR}_{\mathrm{H}\alpha}$ is likely due to emission line contamination due to non-stellar activity. Dotted line in included as a guide only and is in no way fit to the data.

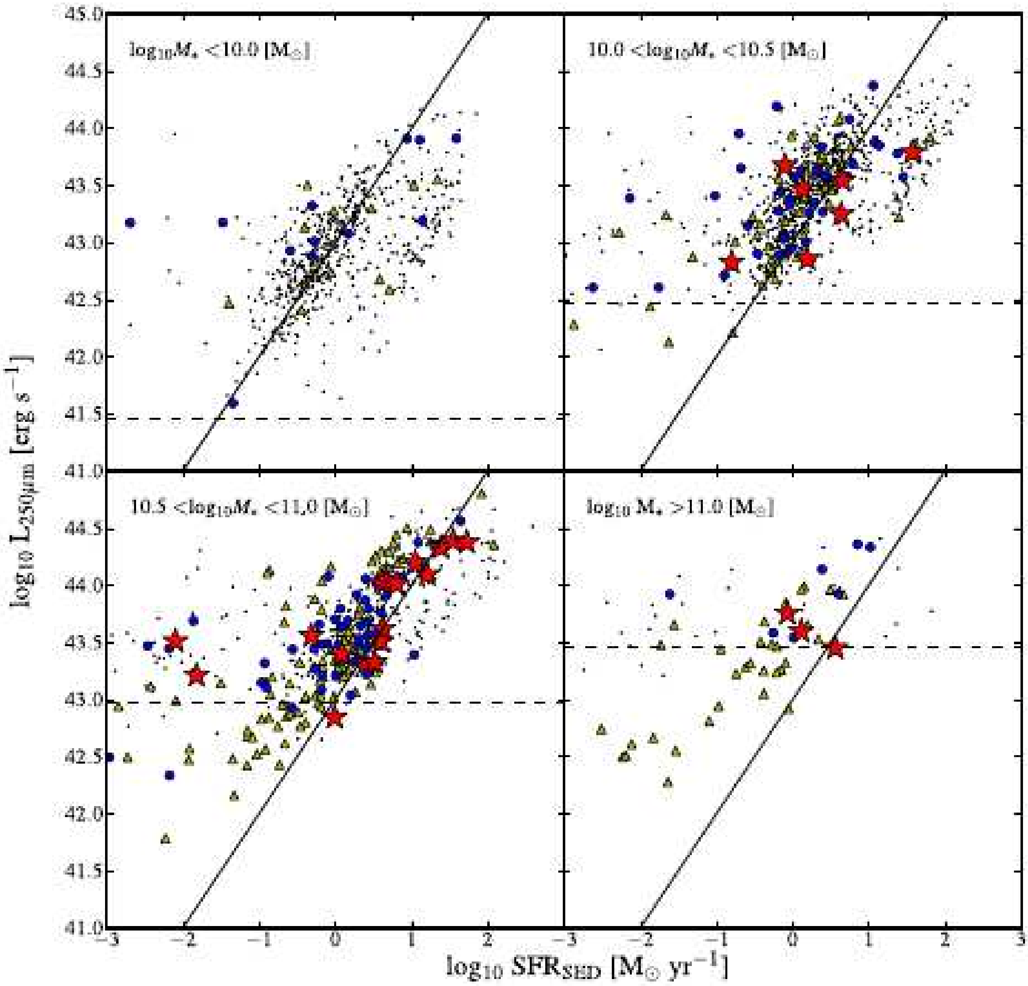

Figure 4.10: A plot of the SFRs derived from SED fitting vs. 250μm luminosity of the H-ATLAS 250μm sample. Colours and symbols as per Figure 4.7. Data are separated according to stellar mass, as detailed in the upper left corner of each subplot. The solid line is included as a guide only, and is not a fit to the data. The dashed line represents an approximation of the 250μm luminosity that can be attributed to cirrus emission as described in the text, and can be used to explain the observed scatter in the 250μm luminosity. The cirrus contributions are representative of stellar masses of $\log_{10}\mathrm{M}_* = 9.5,10,10.5$ and 11 $\mathrm{M}_\odot$ in left to right subplots respectively.

Measurements of the colour excess in the nebular regions reveal type-II objects to have a greater spread in E(B-V) than both type-I and LINER type objects (see Figure 4.11). This result is in agreement with results from Rhee and Larkin (2005) and Ho et al. (2003) respectively. The dichotomy found between type-I and type-II objects in this regard should be taken with caution however, since the narrow Balmer lines will be heavily contaminated by the broad Hα and Hβ components in the type-I objects, possibly introducing measurement errors. However, this will not be the case for LINER objects. Colour excess measurements in the stellar continuum reveal no major differences between any subclasses.

4.5.8 Dust Mass vs. Class

Work by Heckman et al. (1989) has shown the CO masses of type-II objects to be higher than those in type-I objects, again implying a host composition AGN classification dependence. Here, I find no evidence that type-II objects have higher dust masses than type-I objects, in line with the unified model. I show in Figure 4.12 the dust mass per unit stellar mass for all sources in our sample. KS testing reveals that the type-I and type-II objects have the same distribution as each other with p-value= 98.2%. LINERs are found to have significantly less dust (per unit stellar mass) than the type-II AGN with a KS p-value= 0.01 percent, confirming the conclusions reported in Kewley et al. (2006).

4.6 Analysis

4.6.1 Type-II Fraction

Depending on the observational regime used, the type-II AGN fraction statistics vary. In the X-ray and `[OIII]` regimes, works have quoted a luminosity dependence of the Type-II AGN fraction, where as volume-limited optical, infrared and radio observations report a fixed Type-II AGN fraction across several decades (See Chapter 1 for a more length discussion and references). Controversially, Lu et al. (2010) report a fixed Type-II AGN fraction in the

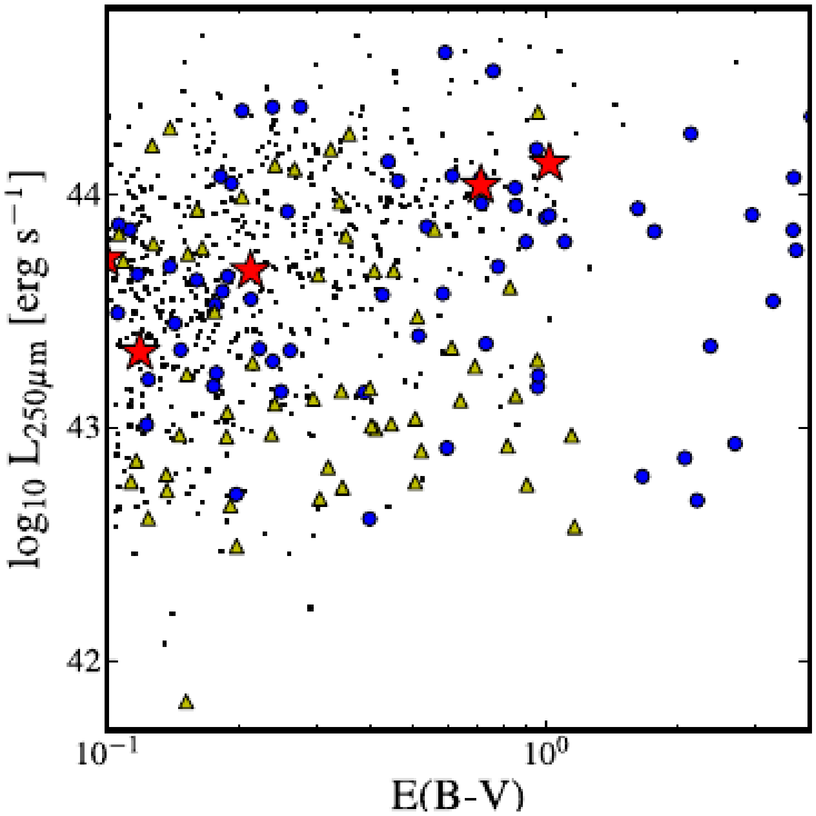

Figure 4.11: A plot of the E(B-V) excess as measured in the spectral emission lines Colours and symbols as per Figure 4.7.

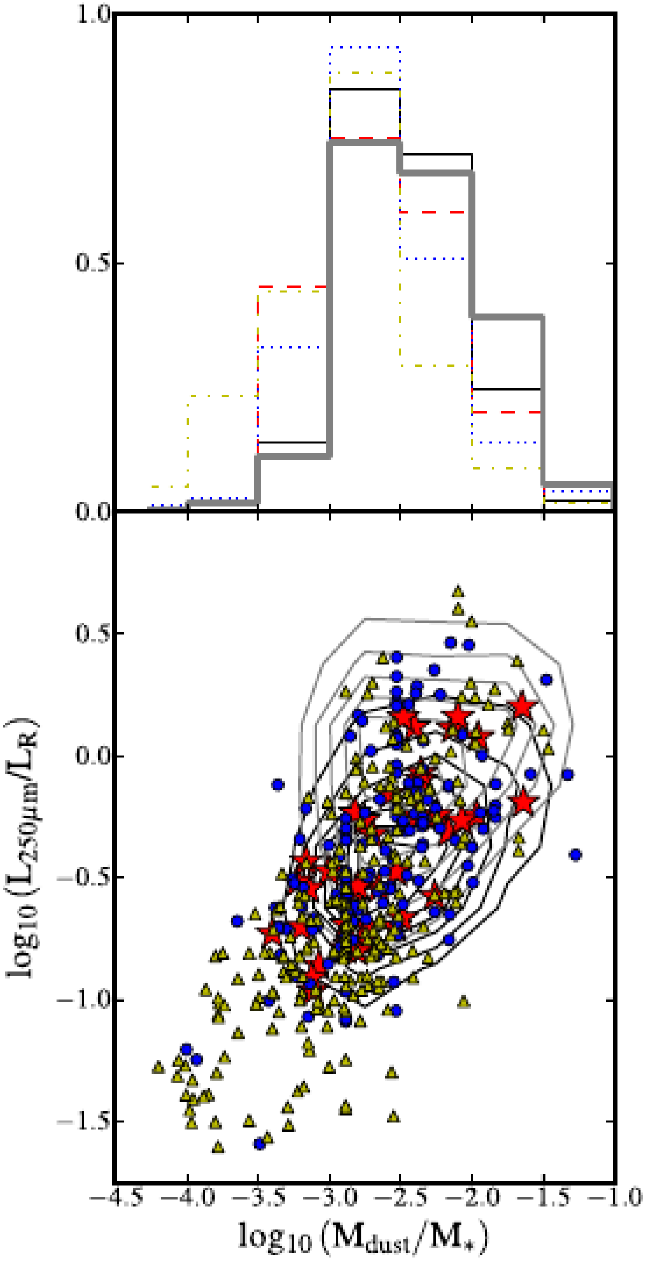

Figure 4.12: A plot and histogram of the dust mass to stellar mass ratio vs 250μm/R-band luminosity of sources by class. Grey contours and histogram represent the passive galaxies. Other colours, symbols and line styles as per Figure 4.7. Dust masses and stellar masses are derived from SED fitting.

`[OIII]` regime, with a fairly high statistic of 0.8. Here I find a Type-II AGN fraction that is consistent with being fixed across several decades in `[OIII]` luminosity, at a value of ~ 0.85: I find no evidence for an `[OIII]` luminosity dependence of the type-II fraction, which is shown in Figure 4.13.

Why such a high value? This could possible be due to one of two reasons. Firstly, the LINER population is far more populous than the Type-II AGN fraction, a number of the sources classified as Type-II AGN may have been scattered in from the LINER region of the diagnostic, increasing the measured Type-II AGN fraction. Secondly, the GandALF software may miss weak broad-line objects. The manner GandALF fits a stellar continuum may mask much of the presence of weak broad lines. this is tested for in a subset of sources by visual inspection, and shown to be minimal.

The size of the uncertainties in the derived values are relatively large, this is down to the statistics of my AGN population being relatively small when split across multiple luminosity bins. None the less, this result is in agreement with that of Lu et al. (2010); I find no evidence for an `[OIII]` luminosity dependence of the type-II AGN fraction, and that this fraction is relatively high at around 80-85 percent.

4.6.2 The AGN Fraction

It is accepted that the AGN fraction is a function of stellar mass, with AGN being far more prevalent in high-mass galaxies (see Chapter 1). Kauffmann et al. (2003) have shown the AGN fraction as a function of stellar mass for an optically selected sample. It is possible to show how the AGN fraction changes as a function of stellar mass for this sample also, as well as how the AGN fraction change with age and FIR luminosity (250μm luminosity). I show this in Figure 4.14. The left-most plot shows the AGN fraction vs. stellar mass, M_*. This shows a prevalence of AGN in higher stellar mass objects, though the observed trend does not appear to be as steep as that found in Kauffmann et al. (2003)[2]. My result are in broad agreement with those of Pimbblet et al. (2013), with AGN making up in excess of 10 percent of the population at stellar masses in excess of $10^{10.5}$ $M_\odot$.

---

[2] Note that the AGN fraction in the Kauffmann et al. (2003) does not include type-I objects and LINER objects, however, since type-I objects represent less than 8 percent of the AGN+LINER sources in my sample this will not make a marked difference to the result.

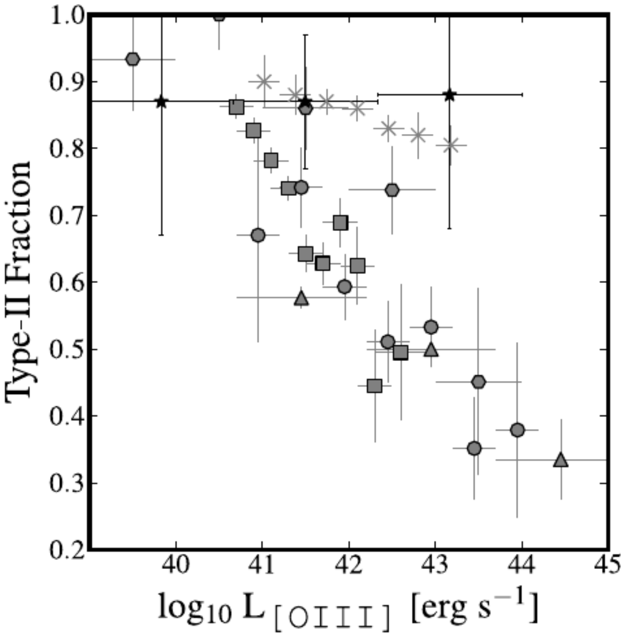

Figure 4.13: A plot of the type-II fraction vs. `[OIII]` luminosity. Data from Simpson (2005) are represented as solid black symbols, Hasinger (2004) as filled circles, Grimes et al. (2004) as filled triangles, Lu et al. (2010) as crosses and our data over plotted as solid star symbols.

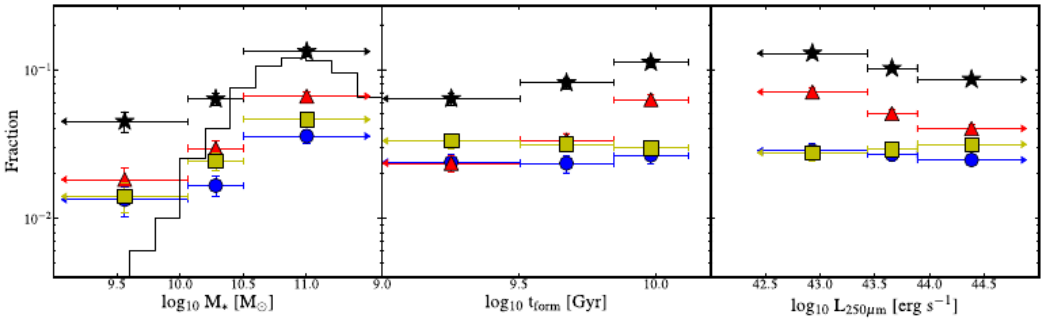

Figure 4.14: A plot of the AGN fraction vs. stellar mass, formation age and 250μm luminosity for our sample. Blue circles = All bona fide AGN (type-I+type-II), red triangles = All Possible LINERs (LINERs+type-II/LINERs), black stars = all possible AGN (bona fide AGN + Possible LINERs) and yellow squares are all possible AGN with L`[OIII]` $> 10^7$L$_\odot$, respectively. In the left-most subplot, data from Kauffmann et al. (2003) (black histogram). The Kauffmann et al. (2003) data show the LINER+type-II/LINER+type-II+composite population with L`[OIII]` $> 10^7$L$_\odot$ for a population of optically selected galaxies at $z < 0.3$.

In the second subplot we see an overall trend for the AGN fraction to increase with age, however, when I split this between type-I+type-II (blue circles) and LINER+type-II/LINER (red triangles) we see that this trend is entirely dominated by the LINER+type-II/LINER population. It has been argued by Kauffmann et al. (2003) that the presence of AGN light in the optical continuum will cause a shift toward an overestimation of the stellar age, and since type-I/type-II objects are typically more luminous than LINER type objects the overestimate of their stellar ages will typically be larger than in LINER objects, thus the difference between the fraction vs. $t_{\rm form}$ for the type-I+type-II objects compared with the LINER+type-II/LINER objects could realistically be even greater than that shown.

Subplot 3 of Figure 4.14 shows the AGN fraction vs. $L_{250\mu m}$. No $L_{250\mu m}$ dependence on the type-I+type-II AGN fraction is seen.

In summary I find that both AGN and LINERs preferentially live in massive host galaxies. I find, however, that LINERs are typically found in older galaxies, whereas AGN are not.

4.6.3 Emission Line Ratios vs. Age

Using the 4000Å break, $D_n(4000)$, as a proxy for stellar population age, Wang and Wei (2008) report a correlation between $\log_{10}$ `[OI]`/Hα and $D_n(4000)$. This is implied as an evolution from a high state with a soft ionising (AGN) spectrum to a low state with a hard ionising (AGN) spectrum, and it is suggested that the `[OI]`/Hα ratio could be used as a potential indicator of age of a stellar population. Plotting the formation time, t_{form} as derived from SED fitting vs. `[OI]`/Hα as derived from our spectral fits, a correlation between the two parameters is found; a Spearman-Rank correlation test is run on the both `[OI]`/Hα vs. t_{form} and `[SII]`/Hα vs. t_{form}, returning correlation coefficients. 0.076 and 0.068, with p-values of $1-(2.86\times10^{-8})$ and $1-(5.34\times10^{-7})$ percent respectively. The data are shown in Figure 4.15.

By splitting into separate populations, this correlation is entirely set by the LINERs. I find no evidence for a correlation in either star forming galaxies of Type-II AGN. I therefore propose that the correlation reported in Wang and Wei (2008) may be due to LINER contributions in the older populations creating a trend in the $D_n(4000)$ vs. $\log_{10}$ `[OI]`/Hα.

Also in Figure 4.15 a histogram of the formation times of the sample is shown. No significant differences in age distributions between type-I and type-II classes is reported (KS p-value = 60.8 percent), but there is a significant difference between LINERs and type-II AGN age distributions (KS p-value = 0.02 percent), with the LINERs typically being older than then type-II AGN.

4.6.4 The Low Mass AGN

One intriguing population in this sample is the low MASS AGN; those AGN with stellar masses of $M_* < 10^{10} M_\odot$. Figure 4.16 shows their locations on the BPT diagram, and Figure 4.17 plots the 250μm luminosity vs. SFR and t_{form} for these AGN compared the overall AGN population. These objects are typically younger and have higher SFRs than other AGN of similar 250μm luminosities.

Work by Johnson et al. (1997) investigates the unusual nature of dwarf galaxy A0951+68, which has a knot of emission that would, according to BPT diagnostics would make the galaxy a type-II AGN. However, the nature of the line emission in this galaxy is attributed to one or multiple O-Type stars. Could these sources

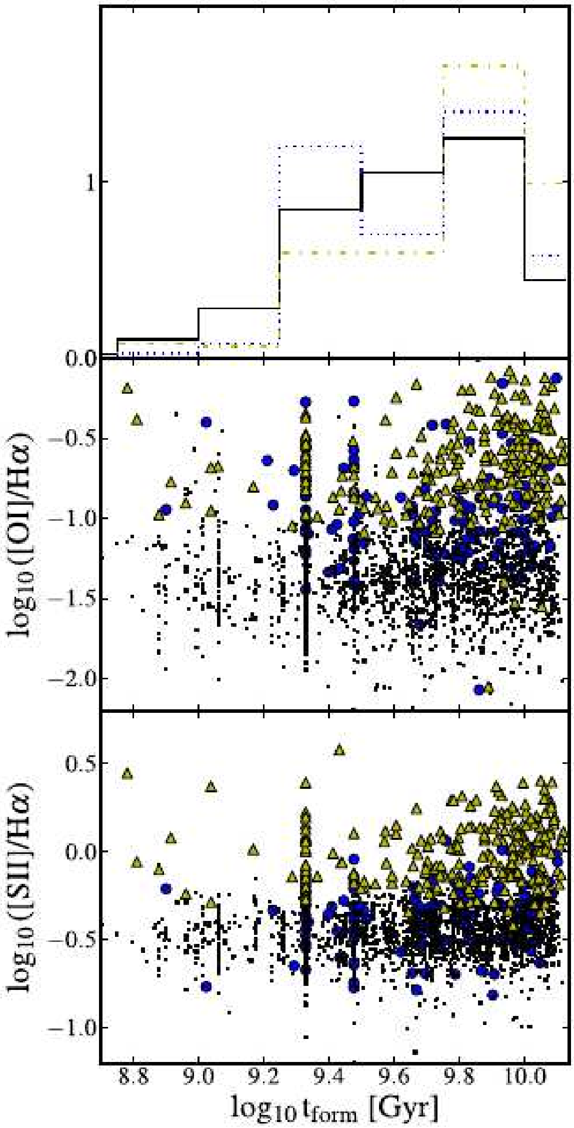

Figure 4.15: A plot of the formation age in Gyr vs. `[OI]`/Hα and `[SII]`/Hα line ratios. Colours, symbols and line styles as per Figure 4.7. We find further evidence for evolution of the spectral line ratios with stellar population age, confirming the suggestion made by Wang and Wei (2008) for an evolution of these line ratios with redshift. However, any such trend should be carefully consider any bias introduced by a fixed spectral fibre size.

Table 4.4: A table showing a names and stellar masses of the low-mass AGN.

Name	**$\log_{10}$ M$_*$**
G09_Y1_EN1_218	9.96
G09_Y1_FS1_223	9.90
G09_Y1_FN1_069	9.63
spSpec-51929-0470-080	9.67
G12_Y1_AT_191	9.83
G12_Y1_DN1_243	9.86
spSpec-51930-0285-094	9.77
G15_Y1_AS1_011	9.46
spSpec-51615-0303-298	9.88
G15_Y1_FS2_247	9.27
G15_Y1_FS1_172	8.92
spSpec-51662-0308-239	8.18
G15_Y1_IN2_106	9.04

that are classified as low mass AGN actually just highly star-forming and the nebular emission simple be associated with young giant stars?

Table 4.4 shows the names and stellar masses of these low-mass AGN.

4.6.5 The Passive Galaxies

What are the passive galaxies? These sources make up some 63 percent of the entire sample. Figure 4.12 shows the passive sources to have a higher $L_{250\mu\mathrm{m}}/L_{\mathrm{R}}$ than star forming galaxies and they are also more luminous in the FIR than star forming galaxies. Figure 4.12 shows the passive galaxies to be more dusty (M_{dust}/M_*) than any other class of source. They have larger stellar masses, they are older and they have lower star formation rates (as derived from optical SED and Hα luminosities). Perhaps none of these facts are intrinsically illuminating, since older galaxies are going to be more massive and have lower star formation rates than younger objects on average. Galaxies with a higher dust content are also more likely to have high $L_{250\mu\mathrm{m}}$ luminosities. Thus the passive sources are

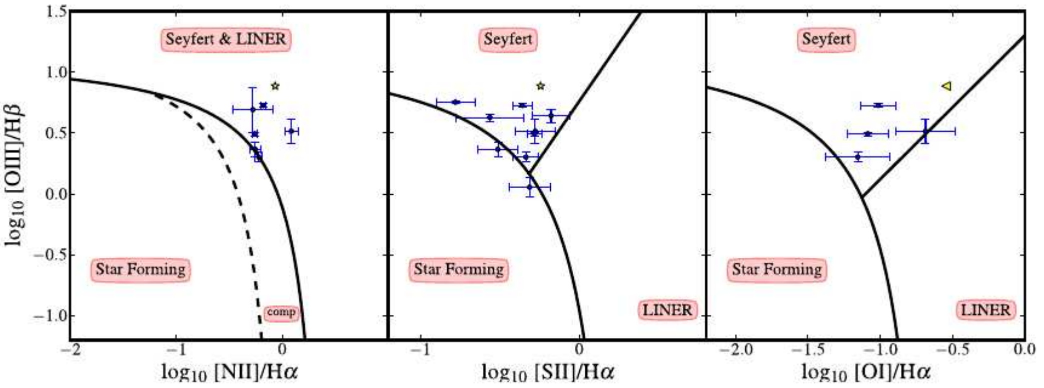

Figure 4.16: A BPT plot of the low stellar mass ($M_* < 10^{10} M_\odot$) AGN in the H-ATLAS sample. The yellow symbol represents the emission line region of dwarf galaxy A0951+68 from Johnson et al. (1997).

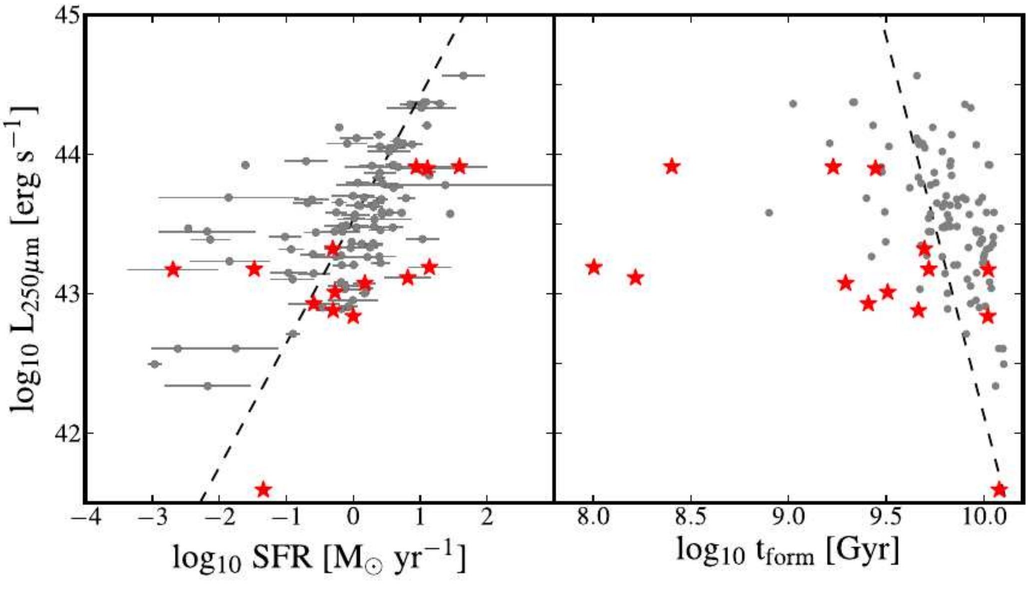

Figure 4.17: A plot of 250μm luminosity vs. SED derived dust-corrected SFR and t_{form} for the AGN in the H-ATLAS sample. The grey circles represent the total AGN sample, while the red stars are the low stellar mass ($M_* < 10^{10} M_\odot$) objects.

likely to be the older quiescently evolving population, with FIR emission possibly dominated by cirrus emission.

One possible explanation for the high $L_{250\mu\mathrm{m}}$ of the passive galaxies compared with the star forming galaxies is that the passive galaxies are colder than the star forming galaxies. Figure 4.18 shows for a thermal source of fixed bolometric luminosity, the normalised (vs. T=15K) 250μm luminosity that would be measured. One can see an order of magnitude difference between the warm and cold ends of this temperature range. This should be evident in the FIR colour of these galaxies also; passive galaxies, if colder than star forming galaxies should appear redder. In Figure 4.19 I show the [250]-[350] colour of the passive galaxies (thick grey line), star forming galaxies (black line) and star forming galaxies with a 10σ detection at 250μm (blue dot-dashed line). The passive galaxies are indeed shown to be significantly redder than the star forming galaxies.

4.7 Discussion

The above work details the study of spectroscopically classified AGN and LINERs from a sample of 250μm sources at a redshift of $z < 0.38$. Based of the BPT-diagnostics and conservative line signal-to-noise cuts, I classify 182 AGN sources (36 broad line, 146 narrow line) and 234 LINER sources out of a possible 7433 250μm with optical spectroscopic counterparts. Detailed SED fitting from the optical through to the far-IR ($< 500\mu$m) allows for the calculation of stellar masses and star formation rates for the entire sample; such calcultions reveal that, as found previously, AGN lie in higher stellar mass objects than non-AGN. Evidence for type-II AGN having higher star formation rates than their type-I counterparts is disputed in the literature; results from Maiolino and Rieke (1995), Hiner et al. (2009) claim a statistically significant difference (by up to a factor of 50 percent), while results from Netzer (2009), Meléndez et al. (2008) show no such discrepancy between the classes. In section 4.5.5 I show that there is no statistical difference between type-I and type-I objects in this respect; the distributions of their star formation rates are consistent with being drawn from the same population.

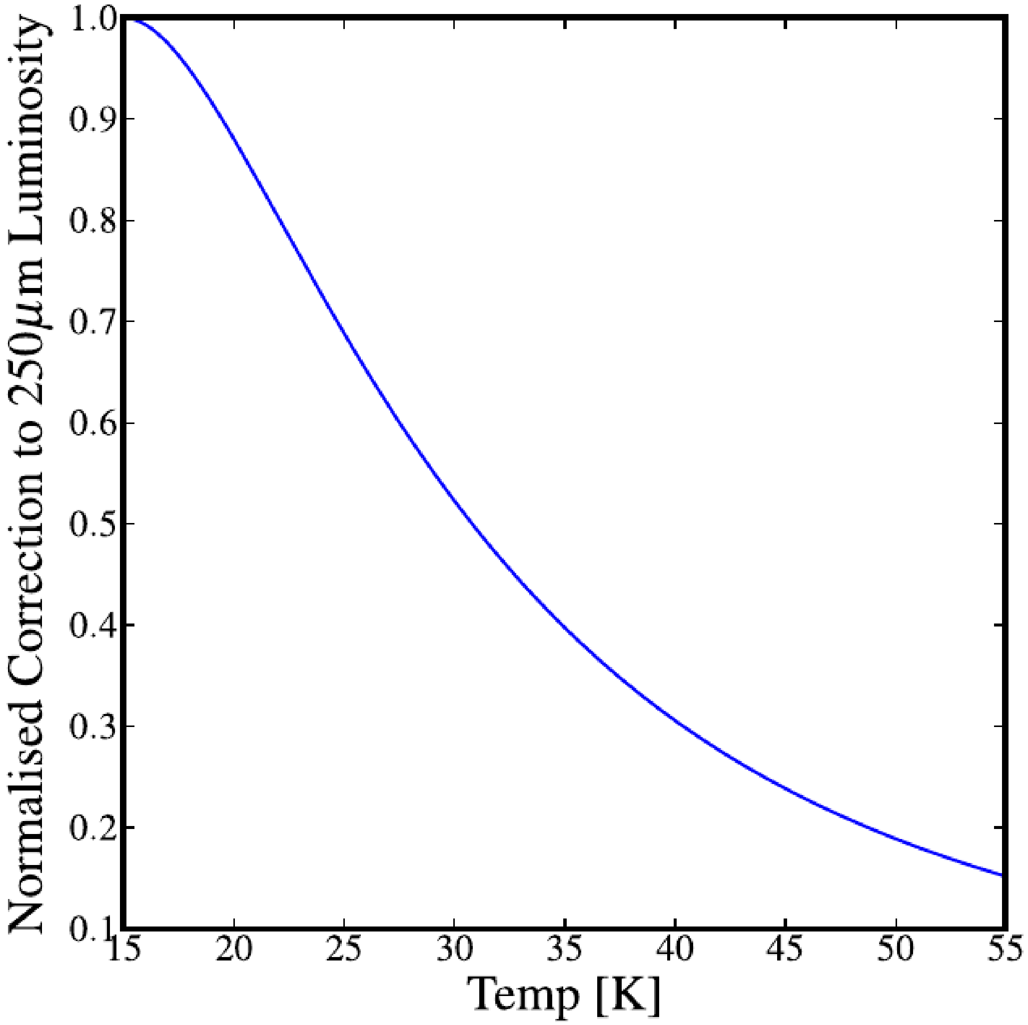

Figure 4.18: a plot of the normalised (to T=15K) 250μm luminosity for a fixed-bolometric luminosity black body at a range of temperatures. Note that the colder the object, the more luminous it will be at 250μm.

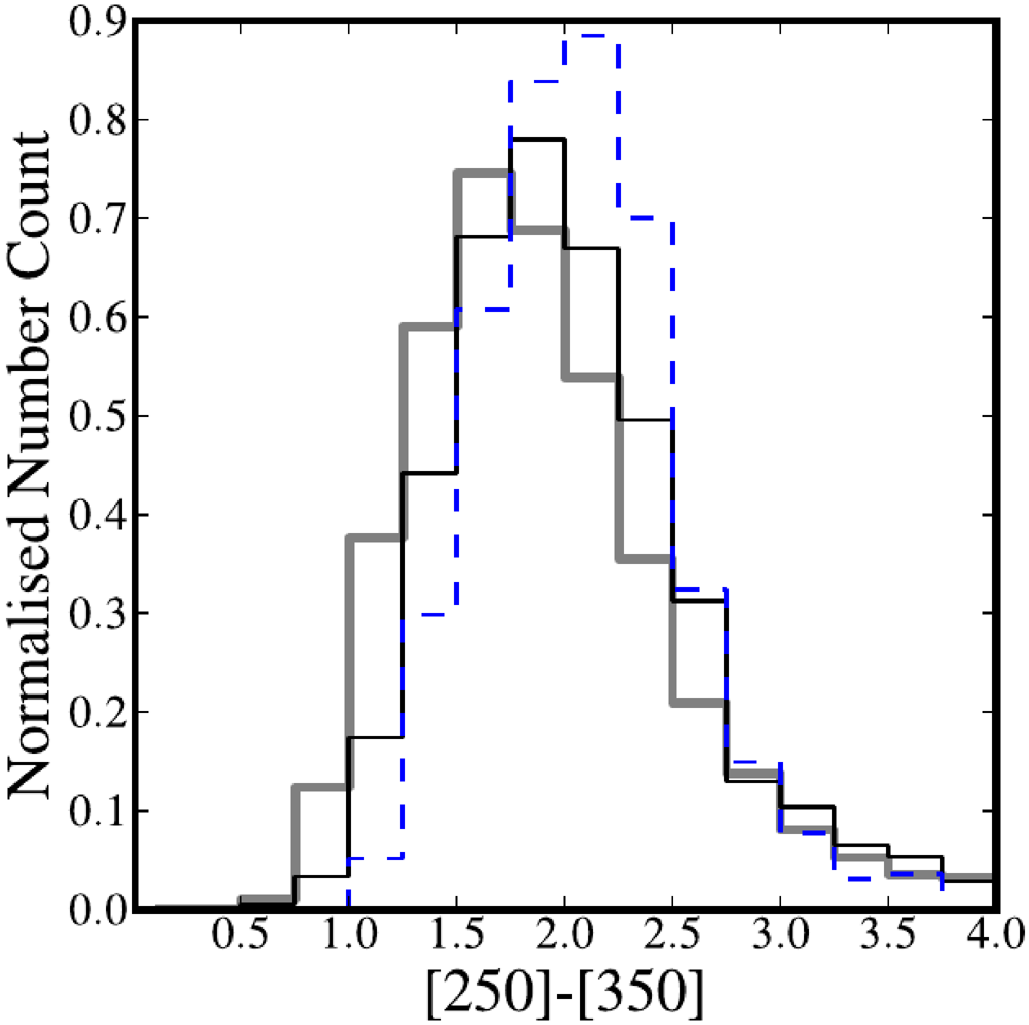

Figure 4.19: a [250]-[350] colour histogram for passive (thick grey), star forming (black) and star forming galaxies with 10σ 250μm detection (blue, dot-dashed). Note that the passive galaxies are significantly redder (and hence inferred to be colder) than star forming galaxies.

By decomposing the AGN fraction into type-I+type-II AGN vs. LINERs a positive correlation in the AGN fraction vs. galaxy formation time, $t_{\rm form}$, is found that is entirely dominated by the LINER population. Negative correlations in the AGN fraction vs. 250μm luminosity, $\rm L_{250\mu m}$ and vs. dust mass, $\rm M_{dust}$ are reported that are also entirely dominated by the LINER population. The type-I+type-II AGN fraction shows no significant change vs. $\rm t_{form}$, $\rm L_{250\mu m}$, $\rm M_{dust}$. An AGN fraction vs. stellar mass, $\rm M_*$ dependence is also reported in both the type-I+type-II AGN and LINER populations, but with a shallower dependence than found in previous works.

The LINER population is found to be significantly older than the type-II AGN population, with a much lower star formation rate and significantly less dust for a given stellar mass. The type-II AGN have a larger range of colour excesses ($E(B-V)$) in nebular lines compared to LINERs. Further significant - though weak - trends are found in the evolution of spectral line ratios with stellar age. The passive population, which makes up the majority of the sample, is found to be older, more far-infrared luminous, more quiescent and to have less dust for a given stellar mass than the star forming population. A classification bias due to the aperture effect is investigated, but shown to have a minimal effect on the conclusions.

An interesting subpopulation of low stellar mass AGN ($\rm M_* < 10^{10} M_\odot$) is reveiled to be younger than expected for the general AGN population, though the significance of this finding is still to be uncovered.

No evidence is found for a type-II AGN fraction (f_2) vs. `[OIII]` luminosity dependence, at odds with predictions from the receding torus model. It is worth noting, however, that the above derived statistics are not necessarily representative of an *unbiased* sample of AGN, but of AGN with a cold dust signature; in total population, much of the observed trends may be nullified or even reversed if one were to investigate those AGN with no cold dust signature.

4.7.1 The Unified Scheme

The unified scheme dictates that the observational attributes of AGN are caused by the orientation of the central engine with respect to the observer. In this scheme, type-I and type-II objects are intrinsically identical. The torus model uses a geometrically thick, axisymmetric obscurer to block much of the emission emanating from the central engine along particular sight lines.

As such, one would expect to find no difference in host galaxy characteristics for type-I and type-II objects. I find type-I and type-II AGN to be indistinguishable in many regards; their dust mass distributions, their star formation rates, their stellar masses, their ages and the $L_{250\mu m}$ distributions, in agreement with predictions of the unified scheme.

4.7.2 The Receding Torus

The receding torus is a physically motivated model which places the inner edge of this dusty torus at the dust sublimation radius of the central engine (defined by the dust sublimation temperature $1000 - 1500$K). For a fixed torus scale height this would create a trend in the type-II fraction (i.e. those AGN seen *through* the torus) with luminosity (Lawrence 1991). Modifications to this receding torus model to account for changes in scale height have been tested (Simpson 2005). The trend for a decrease in the obscured fraction with luminosity is replicated in many X-ray observations, but there is mounting evidence in other observational regimes that the intrinsic fraction of type-II/obscured objects is down to selection effects, or incorrect handling of reddening (Lu et al. (2010), this work Chapter 3, Lawrence and Elvis (2010)) and that this fraction is actually fixed across many dex in luminosity (see further references in Chapter 1). The work of this chapter adds to the mounting evidence that the intrinsic type-II/obscured fraction is fixed, which may begin to spell the end for the receding torus model, or else demand a further modification such that the scale height-luminosity dependence counteracts the receding inner radius of the torus.

4.8 Conclusions

I have performed analysis on a sample of AGN selected according to FIR (250μm) emission, which is believed to be associated with cold dust. I find:

(i) No evidence for a type-II AGN fraction dependence on `[OIII]` luminosity. Instead I find the type-II fraction remains constant at around $f_2 = 0.8$. This result is at odds with the receding torus model and results from Simpson (2005), but in agreement with more recent results for Lu et al. (2010), along with those from mid-IR, radio and optical-volume limited samples.

(ii) Type-I and type-II AGN hosts are indistinguishable in many regards; their dust mass distributions, their star formation rate distributions, their stellar masses, their ages and the $L_{250\mu m}$ distributions.

(iii) I report a negative correlation in the AGN fraction vs. 250μm luminosity, $L_{250\mu m}$ and vs. dust mass, M_{dust} that is entirely dominated by the LINER population. The type-I+type-II AGN shows no significant change vs. t_{form}, $L_{250\mu m}$, M_{dust}, consistent with a fixed 2.5 percent of the total population.

(iv) LINERs have a lower dust content than AGN, star forming and passive galaxies in the sample. I note a trend for the oldest LINERs to have lower star formation rates than similarly aged and luminosity star forming objects. The LINERS have high $L_{250\mu m}$ compared to their stellar masses and star formation rates. I suggest that the bulk of this luminosity could be attributed to cirrus emission.

(v) I find a robust, though weak correlation between `[SII]`/Hα vs. age and `[OI]`/Hα vs. age for LINERs.

(vi) The passive population is more massive, more dusty (M_{dust}/M_*), more FIR luminous, more quiescent and older than the star-forming galaxy population.

In order to increase statistics for this sample, future works must include Herschel data from the Southern Galactic Plane (SGP) combined with spectroscopic measurements like those taken with SDSS+GAMA for the SGP. While work is underway for photometric surveys in the SGP with panStarrs, DES and the VST in the optical and near-IR, reliable classification of AGN will demand spectroscopic measurements.

Acknowledgements

The Herschel-ATLAS is a project with Herschel, which is an ESA space observatory with science instruments provided by European-led Principal Investigator consortia and with important participation from NASA. The H-ATLAS website is http://www.h-atlas.org/.

GAMA is a joint European-Australasian project based around a spectroscopic campaign using the Anglo- Australian Telescope. The GAMA input catalogue is based on data taken from the Sloan Digital Sky Survey and the UKIRT Infrared Deep Sky Survey. Complementary imaging of the GAMA regions is being obtained by a number of independent survey programs including GALEX MIS, VST KIDS, VISTA VIKING, WISE, Herschel-ATLAS, GMRT and ASKAP providing UV to radio coverage. GAMA is funded by the STFC (UK), the ARC (Australia), the AAO, and the participating institutions. The GAMA website is: http://www.gama-survey.org/.

Funding for the SDSS and SDSS-II has been provided by the Alfred P. Sloan Foundation, the Participating Institutions, the National Science Foundation, the U.S. Department of Energy, the National Aeronautics and Space Administration, the Japanese Monbukagakusho, the Max Planck Society, and the Higher Education Funding Council for England. The SDSS Web Site is http://www.sdss.org/. The SDSS is managed by the Astrophysical Research Consortium for the Participating Institutions. The Participating Institutions are the American Museum of Natural History, Astrophysical Institute Potsdam, University of Basel, University of Cambridge, Case Western Reserve University, University of Chicago, Drexel University, Fermilab, the Institute for Advanced Study, the Japan Participation Group, Johns Hopkins University, the Joint Institute for Nuclear Astrophysics, the Kavli Institute for Particle Astrophysics and Cosmology, the Korean Scientist Group, the Chinese Academy of Sciences (LAMOST), Los Alamos National Laboratory, the Max-Planck-Institute for Astronomy (MPIA), the Max-Planck-Institute for Astrophysics (MPA), New Mexico State University, Ohio State University, University of Pittsburgh, University of Portsmouth, Princeton University, the United States Naval Observatory, and the University of Washington.

Chapter 5

The Fraction of Obscured Quasars at Redshift ~ 1

5.1 Abstract

A proposal to gain optical spectra of a statistically significant sample of 24μm selected AGN was made and accepted in 2010. My role within this proposal was target selection, catalog construction and investigating instrumental limitations. Observations began in late 2010 and were carried over for two consecutive semesters. Ultimately, only three of eleven pointings were observed and so a statistical sample was not realised. The work below describes the reduction and analysis of the observed data set.

The aim was to construct an equivalent to the 12μm Galaxy Sample (12MGS) at $z \sim 1$, to directly compare the demographics of AGN at two epochs, i) the current day and ii) when the Universe was approximately half its current age. This involves selecting targets using 24μm fluxes such that sources have the same rest wavelength as the 12MGS.
A spectroscopic sample of 102 sources was realised (with spectral redshifts primarily derived from the 4000Å break). Of these sources, 2 were stellar M4-dwarf stars within the Galaxy, whilst the remaining extragalactic sources range from $z = 0.366$ to $z = 1.286$. The narrow emission line objects (those with visual `[OIII]`, Hβ and `[OII]` lines) amounted to 27 sources. Broad Line type-I AGN total 6 sources.

Overall the target sample selection based on photometric redshift was problematic; all broad line objects (which were believed, photometrically to lie between z= $0.6 - 0.9$ in fact were all at $z > 1.0$. Thus a fair comparison of Type-I and Type-II objects was not only not possible on a statistical level, but also impossible over a reasonable epoch (say z= $0.6 - 0.9$). Thus serious questions are raised as to the reliability of SED fitting of Quasars with the model templates adopted in this work.

5.2 Introduction

Determining the true obscured fraction (f_{obsc}) of AGN is crucial both for understanding the fueling and gas flow in AGN, and for understanding the growth of black holes over cosmic time, including their feedback on galaxy formation. It is predicted that accretion onto supermassive black holes contributes between 5 and 20 percent of the luminosity of the Universe (see Matt 2002, and references therein). The large uncertainty on this value is due to the ill-determined contribution from the obscured fraction

Most observations of AGN are biased towards Type-I/unobscured or radio loud AGN. For example, in the X-ray regime, unobscured objects are typically observed to be more luminous since their soft X-ray emission is unattenuated. In the optical regime Type-I objects typically appear more luminous since their BBB is unattenuated. In the radio regime one is obviously biased towards radio loud objects.

In order to mitigate biases associated with selection techniques we must target AGN in regimes where obscured/unobscured or Type-I/Type-II AGN are indistinguishable. The mid-IR goes some way to doing this. Since all AGN are believed to have a warm dusty *torus* which is heated by the radiation in the accretion disc, the mid-IR luminosity should be a relatively good proxy for the intrinsic luminosity of an AGN central engine. Mid-IR selection is, to first order, both obscuration and orientation-independent (see models from Nenkova et al. 2008). To second order, it is possible that the obscuring material is marginally optically thick at 12μm (Buchanan et al. 2006). One must also take care to consider Star formation contamination in the mid-IR, especially from PAH emission, which can become substantial (and dominant for low-luminosity AGN).

The definitive low-redshift sample, with comprehensive multiwavelength data, is the IRAS 12μm Galaxy Sample (12MGS Rush et al. 1993). This contains 893 galaxies in total, of which 118 are AGN (53 type-I and 63 type-II). Type-I AGN are relatively easy to find; the problem of course is separating type-II AGN from star-forming galaxies.

Using mid-IR photometry (e.g. Stern et al. 2005) it is possible to select AGN based on their colours. This method recovers $\sim$ 90 percent of known Type-I AGN but only $\sim$ 40 percent of the Type-II AGN (Davis et al. 2007). The only safe method for gaining an unbiased sample for populations statistics is to obtain optical spectra of a complete flux limited MIR sample.

5.3 Sample Selection

The aim is to produce an analogue to the local 12μm sample at $z \sim 1$ using 24μm sources; targets are taken from the SpUDS survey (detailed below) in the UDS field. Sources are selected to have photometric redshifts of $z = 0.6 - 0.9$ derived from optical photometric colours, and are followed-up with optical spectroscopy. Below I detail the available data in the field:

5.3.1 The Spitzer-UDS

The 24μm sample from which targets are selected is the Spitzer-UDS (SpUDS; Dunlop et al. 2007). The SpUDS field is centred on the UDS field at `J2000 RA` = 02h18m and `Dec` $= -5^\circ$. Photometric data exist in IRAC (3.6, 4.5, 5.8 and 8μm) with IRAC and 24, 70, and 160 μm with MIPS. The 24μm flux limit is $\sim 100\mu$Jy. Across the field this produces a 24μm catalog totalling 15370 sources.

5.3.2 Ancillary Data

As well as mid-IR photometry, I make use of X-ray, optical and near-IR photometry from the XMM telescope (X-ray), CFHT (U), Subaru telescope (B,V,R_c,i' and z') and UKIRT telescope (J,H,K) as well as spectroscopic redshift measurements from the UDSz:

X-ray

The XMM-Newton Space Telescope has acquired X-ray data in four channels the $0.5 - 10$keV energy band, over seven contiguous pointings in the UDS field, covering 1.14 deg^2 with a total exposure time of 400ks. The catalogue amounts to 1245 sources. Sensitivity varies from between 5×10^{-15}erg cm^{-2} s^{-1} in the $4.5 -$ 10keV channel to 6×10^{-16} erg cm^{-2} s^{-1} in the $0.5 - 2.0$keV channel. Limitations to these data come from vignetting in each individual pointing and non-uniform coverage between pointings (the central pointing having twice the exposure time over the six remaining pointings (Ueda et al. 2008).

Ultra-Violet

Data have been taken for the U band (centering at $\sim$ 3600Å) with the Canada France Hawaii Telescope (CFHT). The depth reached is $\mathrm{U_{AB}} = 26.75$ (Foucaud et al., in prep).

Optical

The Subaru Prime Focus Camera (SuPrime-Cam, see Miyazaki et al. 2002) has imaged 1.3 sq. degrees of UDS in five optical bands, B,V,R_c,i' and z' to 5σ point source AB magnitudes of 28.2, 27.6,27.5, 27.2 and 26.3 respectively. The catalog contains over 900,000 objects, made up of five pointings totalling 133 hours time-on-target (Furusawa et al. 2008).

Infra-Red

Near Infra-Red: UKIRT - Using the Wide Field CAMera (WFCAM) on UKIRT, as part of UKIDSS (Lawrence et al. 2007), the UDS field is imaged in J, H and K filters, with current depths of 24.9, 24.2, 24.6 (5σ; DR8), respectively. This survey field covers some 0.8 sq. deg.

The UDS Redshift Survey (UDSz)

This is a spectroscopic survey of K-band selected objects in the UDS field. Observations are taken with Visual Multi-Object Spectrograph (VIMOS) and FOcal Reducer and low dispersion Spectrograph (FORS2) at the Very Large Telescope (VLT), Chile, targeting over 4000 objects primarily with $z_{\mathrm{phot}} > 1$.

Figure 5.1 shows the footprints from the X-ray, optical and IR surveys, as well as the pointings with the VIMOS instrument (see later).

5.3.3 Auxiliary Data

As well as the photometric and spectroscopic data as detailed above, there are also further data available in the near-IR as part of the VISTA Deep Extragalactic Observations (VIDEO; Jarvis et al. 2013), far-IR as part of the Herschel Multi-tiered Extragalactic Survey (HerMES Oliver et al. 2012) and in the radio from the National Radio Astronomy Observatory (NRAO) Very Large Array (VLA). These data are not used here, but will undoubtedly be of importance for future work in the field.

5.4 Observations

5.4.1 Description of the Instrument - VIMOS

I make use of the Visual Multi-Object Spectrograph (VIMOS) at the VLT in Paranal, Chile to perform multi object spectroscopy. The VIMOS instrument has four 4k×2k CCD detectors each with a 7’×8’ field of view, the detectors are arranged in a square configuration with inner edges separated by 2’. In imaging mode the instrument has six band photometry covering the U’,B,V,R,I,z filters. In multi object spectroscopic (MOS) mode the instrument has several configurations :

- Low resolution (LR) spectroscopy, either in blue or red mode (5500-9500Å or 3700-6700Å) at resolutions of $R = 180$ and 210 respectively. Four-way multiplexing is possible.
- Medium resolution (MR) spectroscopy between 4800-1000Å at $R = 580$.
- High resolution (HR) spectroscopy in red, orange or blue mode (3700-5350Å, 5150-7600Å or 6500-8750Å) at resolutions of $R = 1150$, 2150 or 2500 respectively.

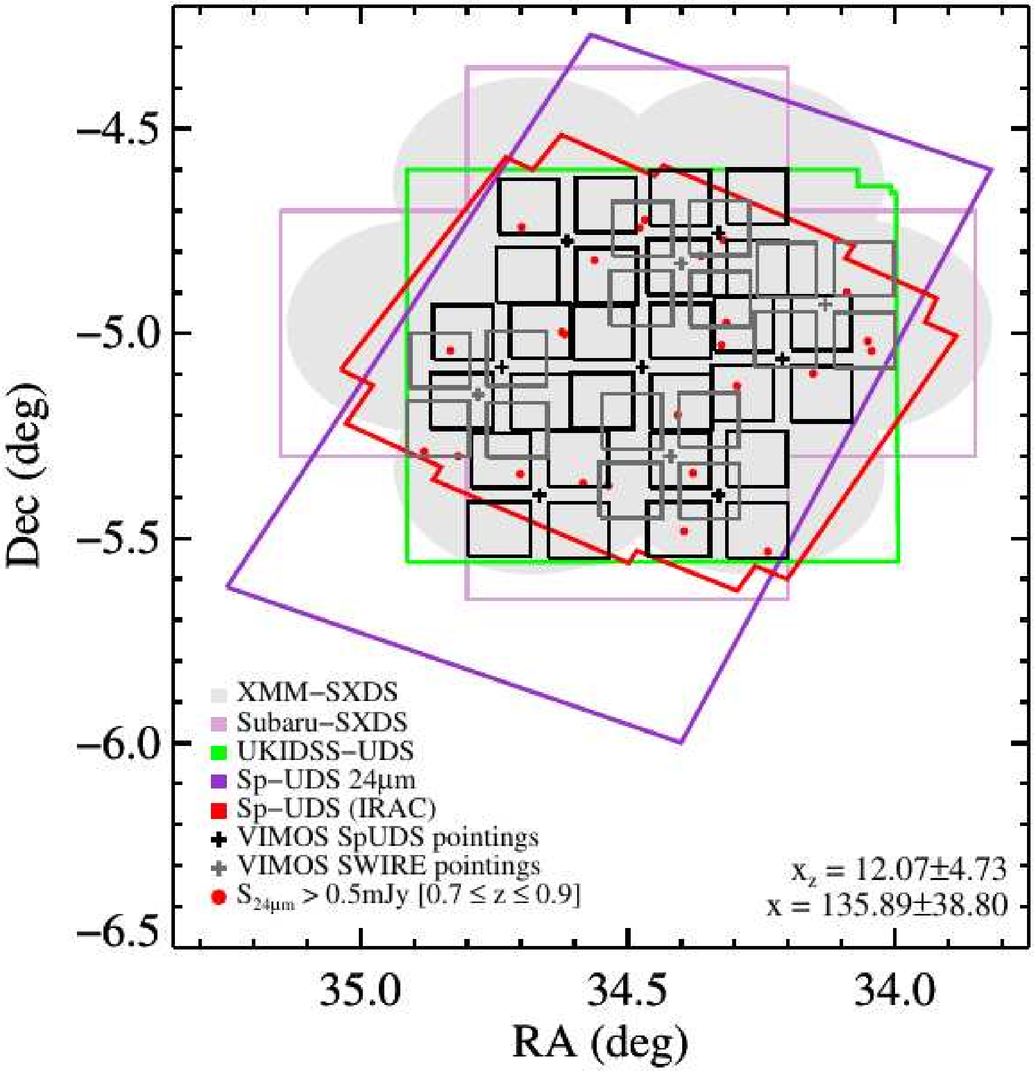

Figure 5.1: A plot of the coverage with different instruments in the UDS field. X-ray data from the XMM-Newton telescope is shown as the grey petal pattern in the background. Spitzer IRAC and MIPS coverage are shown in red and purple. UKIDSS near-IR data is shown in green. Subaru optical data is shown in pink. The deep (labelled SpUDS for historical reasons) VIMOS pointings are shown in black and the shallow (labelled SWIRE for historical reasons) VIMOS pointings are shown in dark grey. The brightest 24μm sources of 0.5mJy or greater in the z=0.7-0.9 redshift window are shown as red points. The statistics detailed in the bottom right show the number of 24μm sources with photometric redshifts $z_{\rm phot} = 0.7-0.9$ (x_z) and total number of 24μm sources with optical counterparts *per quadrant* (x).

Targets are isolated using a disposable slit mask, where slits can be curved, down to $0\overset{\prime\prime}{.}7$ in width and up to 30" in length for long slit spectroscopic purposes. The VIMOS instrument is also capable of fibre based integral field spectroscopy over a field of up to 54" arcsec^2, at a spectral resolution of either $0\overset{\prime\prime}{.}33$ or $0\overset{\prime\prime}{.}67$ per resolution element, making an array of 6400 fibres.

MOS-MR mode is adopted in order to have a balance between spectral range and a resolution sufficient to deblend lines.

An exposure time of four hours is necessary to achieve a 5σ signal-to-noise per pixel at the point, and $\sim 1.5\sigma$ per pixel at 9000Å, for a $I_{AB} < 23.5$ galaxy. This is adequate to detect the emission lines one would expect for moderately luminous AGN. For the more luminous sources an exposure time of only two hours is sufficient. Filling the overlapping SpUDS and UKIDSS-UDS fields most effectively requires 7 separate pointings with the VIMOS instrument. The observing strategy included 7 deep (4 hour) pointings and 4 shallow (2 hour) pointings used to fill gaps and observe interesting and luminous 24μm sources missed in the deep pointings.

5.4.2 Target Catalog and Final Sample

In order to optimise optical emission-line coverage, 24μm targets are selected to be in the redshift slice $0.6 < z < 0.9$, selected using photometric redshifts.

This allows us to probe the luminosity range $L = 43 - 45.5$ [$\mathrm{erg\,s^{-1}}$]. Sources outwith this luminosity range are either not detectable in the redshift window (at the low luminosity end) or are sufficiently rare to be poorly represented in the field area (at the high luminosity end; these sources can be located in the Wide-field Infrared Survey Explorer (WISE) all-sky survey ($\mathrm{S}_{23\mu m} > 2600\mu$Jy). Within the master catalog of possible sources, many have spectroscopic redshift information. Those found to have spectroscopic redshifts outside of the target window are immediately rejected.

The catalog construction software, known as the VIMOS Mask Preparation Software (VMMPS) requires two input catalogs for target selection. The first catalog, known as the *compulsory catalog* contains sources that must be observed. The second catalog, known as the *selectable catalog* contains sources that could otherwise be observed. VMMPS will assign slits to the compulsory sources, The user will then assign broad slits (boxes) to alignment stars (a minimum of three per pointing, over any of the four quadrants), other sources from the selectable catalog are then assigned, and VMMPS undertakes this assignment automatically so as to maximise the number of selectable sources.

The process for defining a target catalog begins with the shallow fields, which are assigned in the manner described above. Compulsory sources have having $z_{\rm phot} = 0.7 - 0.9$ and selectable sources are within $z_{\rm phot} \pm \delta z_{\rm phot} = 0.6 - 0.9$, or are otherwise interesting X-ray sources without spectroscopic data. Once VMMPS produces a target catalog for these shallow fields, any sources with $m_r < 24$ are removed from any other contributory catalogs, whilst those which have $m_r > 24$ and lie within deep pointings are made compulsory for that pointing. The target catalogs are then produced for the seven deep pointings.

There are two deep pointing quadrants which lie on the edge of the IRAC coverage, and so have no photometric redshift information in this regions. These quadrants (Deep-2-Quadrant-1 [D2-Q1] and Deep-6-Quadrant-3 [D6-Q3]) are managed separately; for D2-Q1 the contributory catalog is constructed from all $m_K > 19$ and $m_R < 24$ in the frame with all sources being selectable targets. For D6-Q3, the IRAC coverage splits the quadrant in half, and so for the region with IRAC coverage the targets were selected as per all other quadrants, whilst in the region without the IRAC data the targets were selected as per D2-Q1. After all target catalogs are constructed, every slit centre is checked by eye against K-band mosaic data to ensure that no sources have been mis-targeted.

In the 0.6 sq/ deg overlap region between SpUDS and UKIDSS-UDS there are 2532 24μm sources to a 5σ flux limit at $z_{\rm phot} < 1$. Based on photometric redshifts, 627 of these are in the redshift slice $0.7 < z_{\rm phot} < 0.9$

With VIMOS pointings having a covering factor of 77%, this makes a potential sample size of 486.

The chosen pointing centre coordinates are shown in Table 5.1 and Figure 5.1.

From a 24μm sample of 15370 unique sources, 6398 have optical counterparts. Of these 6398 sources, 770 have $0.7 < z_{\rm phot} < 0.9$ and 1133 have $0.6 < z_{\rm phot} < 0.9$. The final target catalog is made up of 865 targets, of which 850 are unique (15 are targeted to be observed in two overlapping pointings). Of these 850 unique targets, 58 are included based on the fact that they have X-ray emission, but lie outside the photometric redshift selection criteria.

Table 5.1: A table of the VIMOS pointing centres, including the number of target galaxies to be observed.

Name	RA (Centre)	Dec (Centre)	N^o Targets
Deep-1	34.33	-5.395	82
Deep-2	34.665	-5.395	92
Deep-3	34.21	-5.06194	91
Deep-4	34.4731	-5.08194	74
Deep-5	34.7361	-5.08194	61
Deep-6	34.33	-4.75389	73
Deep-7	34.6131	-4.77389	76
Shallow-1	34.13	-4.93	73
Shallow-2	34.78	-5.15	77
Shallow-3	34.42	-5.30	93
Shallow-4	34.4	-4.83	87

5.5 The Final Observed Sample

Due to the UDS having RA$\sim 2^{\mathrm{h}}$ observations were initially scheduled between Nov-Jan 2010. However, due to scheduling priorities only a subset of the data were aquired in this session, with the remaining data carried over for two following semesters. Eventually, the observations were terminated, leaving only a subset of the final sample, amounting to three pointings; Deep-1, Deep-7 and Shallow-1.

Figure 5.1 shows the layout of the deep (labelled SpUDS) and shallow (labelled SWIRE) VIMOS pointings in relation to the available photometric data. The Deep-1 pointing is at the bottom right, the Deep-7 pointing is at the top left and the Shallow-1 pointing is the right-most.

This amounts to 231 unique targets, with no sources being observed in two separate pointings. Of these 231 targets, 12 are sources which are selected based on their X-ray emission (2 in Deep-1, 6 in Deep-7 and 4 in Shallow-1.

5.6 Data Reduction

Data are reduced using the VIMOS data reduction pipeline. Details of the algorithms, input and output parameters/files are included in Appendix B. Raw data are wavelength calibrated and flux calibrated, sky subtracted, reduced and co-added for analysis. Each extracted and reduced spectrum is checked by eye for abnormal features or problematic reduction. Flux calibration is performed by using observations of standard stars at or near to the date and airmass as the target exposures, along with template spectra for each of these stars.

5.6.1 Quality of the Data

By masking at visible emission lines between $6000 < \lambda_{\rm obs} < 7000$, boxcar smoothing the remaining continuum, binning the residuals about the smoothed continuum and fitting a Gaussian to the histogram, I calculate an approximate signal-to-noise for each spectrum. This is shown for a subset of the sources in Figure 5.2 where the measured S/N values are plotted against the apparent R-band magnitudes as measured by Subaru. We can see that brighter objects (i.e. those with a lower R-band magnitude) typically have a higher signal to noise. The extreme outlier in this diagram, and the only source lying at $\rm R_{AB} > 25$ is source with 24μm $\rm ID_{24} = 23303$ (note that the two neighbouring data-points correspond to the two individual observations on 05/12/2010 and 08/12/2010). This source is discussed in more detail in Section 5.9.4. The wavelength calibration is accurate to $\delta\lambda \approx 0.24$Å.

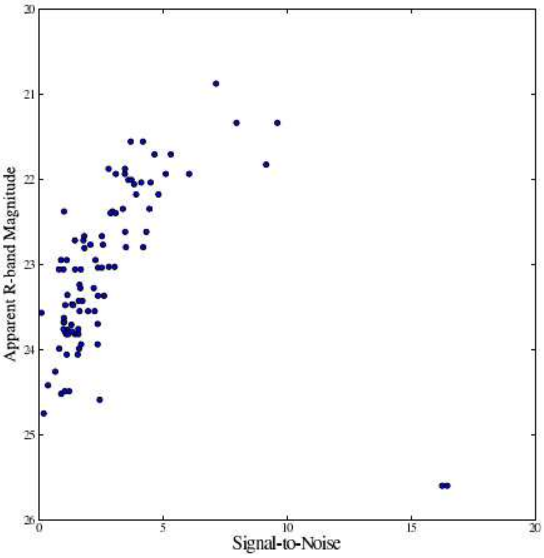

Figure 5.2: A plot of the measured optical spectroscopic signal-to-noise of a subset of the 24μm sources vs. R-band magnitude from Subaru.

5.6.2 Example Spectra

Shown in Figures 5.3 and 5.4 are reduced spectra of a Type-I and Type-II classified sources, respectively (details of their classification will be given in Section 5.7).

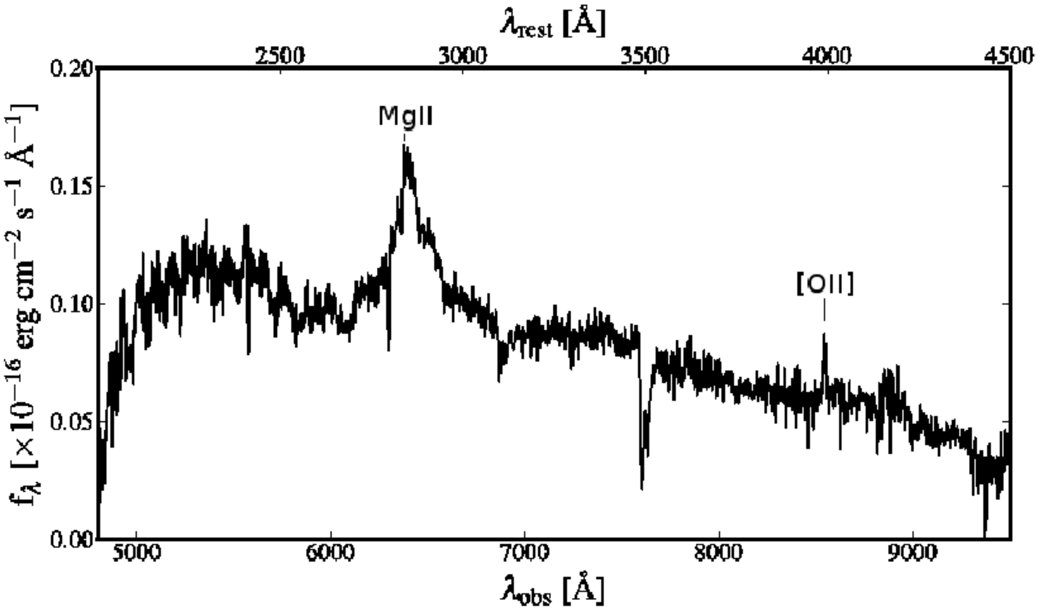

Figure 5.3: Fully reduced spectrum of Type-I AGN with 24μm ID 12136 at redshift 1.28. Note that the downturn in flux at the blue end (short-ward of 5000Å) is a sensitivity issue, and not necessarily a genuine downturn.

Spectral Redshifts and Population Statistics

With such a small target sample, spectroscopic redshifts are measured by eye, finding key spectral features such as the 4000Å break, broad `MgII` λ2800Å emission line, `[OII]` λ3726Å, `[OIII]` λ5007Å and Hβ λ4861Å emission lines.

Figure 5.5 shows a comparison of the photometric and spectroscopic redshifts of all extragalactic sources in the sample. The photometric redshift selection window is shown in dark and light grey. The dark grey represents redshift window

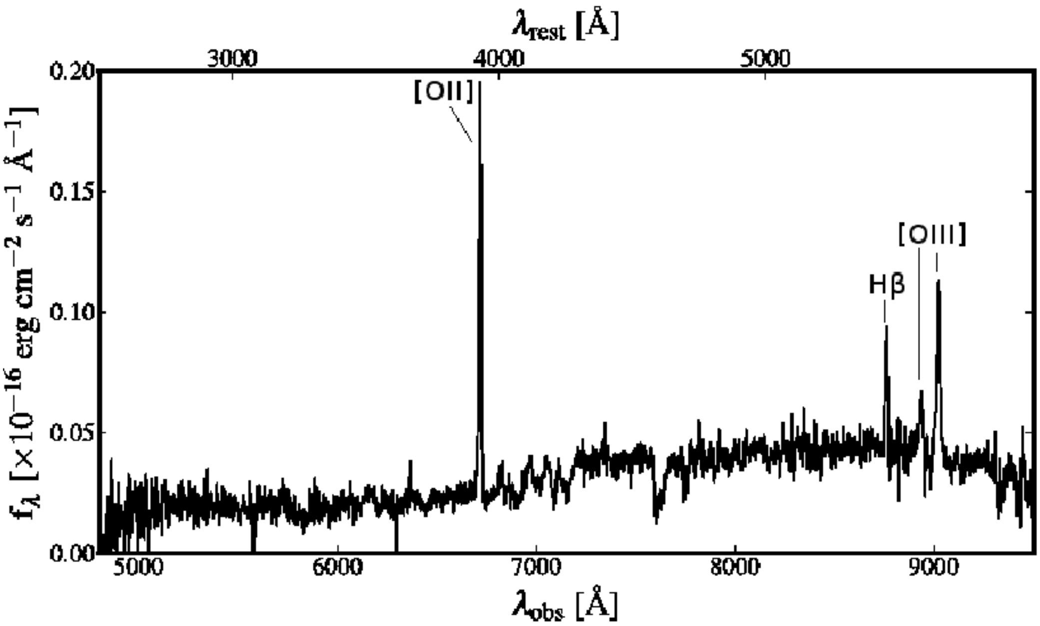

Figure 5.4: Fully reduced spectrum of Type-I AGN with 24μm ID 7229 at redshift 0.803.

$z = 0.7 - 0.9$ and the light grey area represents the redshift window $z = 0.6 - 0.7$. The red symbols shows the (12) objects which are X-ray sources (note that those lying outside the redshift selection window (including errors) are exclusively X-ray sources. The spearman rank correlation coefficient for the photometric and spectroscopic redshifts is 0.445, with a p-value of 1-(3.6 $\times 10^{-4}$) percent, showing a strong and reliable correlation.

Of the 231 targets, 228 had extractable spectra. There were 102 with spectra of sufficient quality to gain spectroscopic redshifts. Of these, 33 have strong (S/N > 3 in `[OIII]` and Hβ) emission lines. These are classified as shown in Table 5.2, along with other class statistics.

Note that the objects that have been classified as Type-II AGN in this sample also contain the LINER objects.

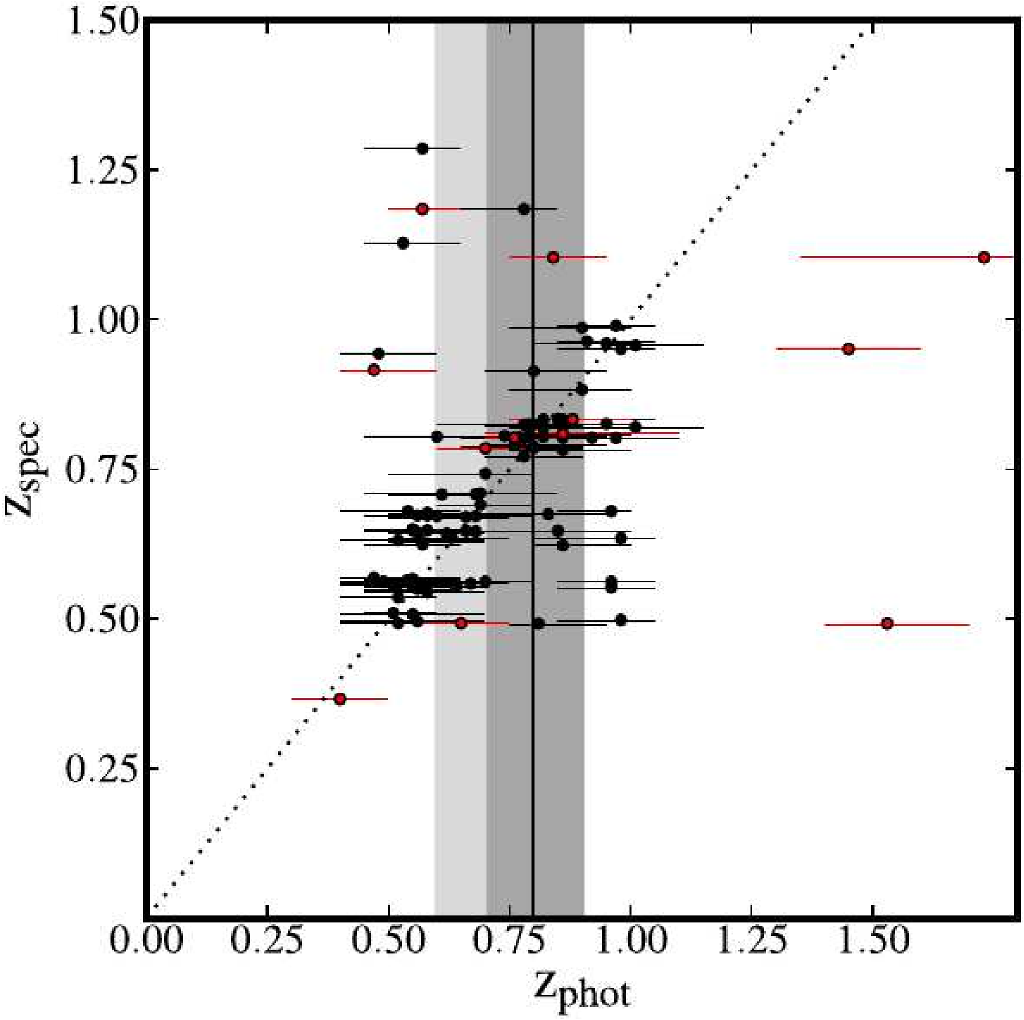

Figure 5.5: The photometric versus spectroscopic redshifts for all extragalactic sources with sufficient data quality. The dark and light grey areas represent the redshift selection windows ($z = 0.7 - 0.9$ and $z = 0.6 - 0.7$) from which the core sample was selected. The targets which are observed in the X-ray regime are shown in red.

5.7 Object Classification

The BPT technique described and used for the H-ATLAS data set in Chapter 4 relies on spectral coverage over both Hα and Hβ and so cannot be used for this VIMOS sample. The spectral window for the VIMOS medium resolution grism is around 5000-9500Å which means that Hα will be redshifted out of the window at $z > 0.45$. I adopt an alternative classification scheme that makes use of spectral

Table 5.2: Tabulation of the optical classification of VIMOS 24μm selected objects. Each object in this list has a spectral redshift.

Type-II AGN/LINER	6
Type-I AGN	6
Composite	11
Star Forming Galaxies	10
Passive Galaxies	66
Star	2
Unknown	1

features at higher frequencies.

5.7.1 Spectral Classification Techniques

A range of alternatives to the BPT technique exist. Some of the more popular ones are described here:

Lee et al. 2011 Technique

The Lee et al. (2011) technique uses `[OIII]`/Hβ vs. FWHM$_{\texttt{[OIII]}}$ to separate non AGN from narrow line AGN. The technique does not discriminate between bona fide AGN and LINERs, but Lee et al. report a 89 percent reliability of AGN diagnosis compared to the BPT technique. An identical technique (though different demarcation lines) is adopted by Zakamska et al. (2003), which is reported by Lee et al. (2011) to have a lower completeness but higher reliability of AGN diagnosis compared to the BPT diagnostic

Lamareille 2004,2010 Technique

The technique derived by Lamareille et al. (2004) and Lamareille (2010) uses bluer spectral line ratios than those adopted in the BPT diagnostics. The technique is compared to the BPT technique in Lamareille (2010) and found to be between 86 percent (Seyfert-II) and 99.7 percent (SF) reliable. The technique itself uses `[OII]`$\lambda\lambda$3726+3729Å /Hβ vs. `[OIII]`λ5007Å /Hβ. The demarcation lines are defined such that the misclassification of sources compared to the BPT technique is minimised.

Stasinska (DEW) 2006 Technique

The technique proposed by Stasińska et al. (2006) uses $\mathrm{D_n}(4000)$, the 4000Å break strength and the equivalent width (EW) of `[O II]` and `[Ne III]` to separate star forming galaxies from AGN. $\mathrm{D_n}(4000)$ is defined as:

$$\mathrm{D_n}(4000) = \frac{(\lambda_2^- - \lambda_1^-)\int_{\lambda_1^+}^{\lambda_2^+} F_\nu \,\mathrm{d}\lambda}{(\lambda_2^+ - \lambda_1^+)\int_{\lambda_1^-}^{\lambda_2^-} F_\nu \,\mathrm{d}\lambda} \tag{5.1}$$

where λ_1^-,λ_2^-,λ_1^+,$\lambda_2^+ = 3750,3950,4050,4250$Å (Bruzual A. 1983). Large $\mathrm{D_n}(4000)$ values are usually indicative of old stellar population passive galaxies (Cid Fernandes et al. 2005), but also of Type-II AGN hosts (Mateus et al. 2006). Star-forming galaxies typically have much lower $\mathrm{D_n}(4000)$ values. The presence of emission lines indicate that ionisation is taking place, whether due to stellar or accretion related emission. Therefore by combining emission line strength and $\mathrm{D_n}(4000)$ one can effectively discriminate between AGN and star forming galaxies. Since the spectral region used in this technique is very blue (compared to Hα) this allows for effective classification up to, and in excess of $z = 1.0$.

Marocco-Hache-Lamareille (MHL) 2011 Technique

The Marocco et al. (2011) technique was developed to be supplementary to the Lamareille technique described above. The MHL technique uses $\mathrm{D_n}(4000)$ vs. `[OII]`$\lambda\lambda$3726,3729Å to separate objects into two separation populations where in the Lamareille diagnostic they are classified very close to the demarcation.

Weiner et al. 2007 Diagnostic

Weiner et al. (2007) proposed a diagram using rest-frame H-band magnitude, $\mathrm{M_H}$, to replace the `[NII]`/Hα ratio, where $\mathrm{M_H}$ is used as a proxy for stellar mass. This method can distinguish Seyferts in relatively massive hosts from low-mass, low-metallicity star-forming galaxies. The separation of the two classes using this technique is not very clean, however, since it does not effectively distinguish transition objects from either pure star forming galaxies or AGN dominated galaxies.

Yan et al. 2011 C-Ex Diagnostic

The Colour-Excitation (C-Ex) technique developed by Yan et al. (2011) uses the rest frame U-B colour vs. `[OIII]`/Hβ ratio to separate star-forming galaxies from AGN (but not AGN from LINERS or transition objects). This techniques builds upon the Weiner et al. (2007) diagnostic. Almost every BPT-identified (narrow line) AGN (or LINER) is found in a red/green (i.e not blue) galaxy. This is because bluer galaxies are typically less massive, have smaller relative bulge components, and as such typically host smaller black holes (Magorrian et al. 1998, McLure et al. 2006). For a fixed Eddington ratio this will result in bluer galaxies typically having less luminous AGN. Again this method does not effectively distinguish transition objects from either pure star forming galaxies or AGN dominated galaxies.

5.7.2 Juneau+2011 M-Ex Diagnostic

The Mass-Excitation (M-Ex) technique developed by Juneau et al. (2011) uses the stellar mass vs. `[OIII]`/Hβ ratio to separate star-forming galaxies, transition objects and AGN. The stellar mass is used in replacement of the `[NII]`/Hα ratio in the BPT diagram as there is an empirical mass-metallicity relation (Tremonti et al. 2004) which suggests a physical connection between that line ratio and stellar mass. Also, AGN more commonly live in high stellar mass galaxies and so often lie above this relation.

5.7.3 Photometric Classification Techniques

Since there is a wealth of photometric data available, it will be interesting to compare spectroscopic classifications to photometric classifications. The C-Ex and M-Ex diagnostics detailed above use both photometric and spectroscopic data to classify objects (since stellar masses are typically derived from SED fitting of optical colours). In recent years, with the advent of the Spitzer Space Telescope, the use of IR colour-colour plots to classify objects has become very popular. There also exist analogous colour-colour diagnostics for data from the WISE telescope (Jarrett et al. 2011).

Stern-Lacy Plot

The diagnostics defined by Lacy et al. (2004), Sajina et al. (2005) and Stern et al. (2005) uses mid-IR colours from the IRAC bands of Spitzer to distinguish star-forming galaxies from AGN. AGN are considerable more red than star forming galaxies in the mid-IR. Due to PAH emission the spread in colours of star-forming galaxies is much larger than AGN, and so AGN can selected from wedges of colour-colour space in the Stern-Lacy plots. This method is very good as selecting broad-line AGN, but not as effective at selecting narrow-line AGN.

Donley et al. 2012 Plot - Donley et al. (2012) revisited the Stern-Lacy colour-colour selection techniques in order to assess high-redshift star forming galaxy contamination to the AGN samples. The AGN selection using these criteria are more reliable and complete than either the Lacy et al. (2004) or Stern et al. (2005) methods; A discussion of the Stern-Lacy selection techniques is given in Donley et al. (2012).

5.7.4 Ivison-Pope Plot

The diagnostic used by Ivison et al. (2004) and Pope et al. (2008) makes use of the MIPS 24μm and IRAC 8μm & 4.5μm data to produce a colour-colour plot to separate starburst galaxies from AGN.

5.7.5 X-ray selection

As described in Chapter 3, X-ray selection in AGN is dependent on two criteria. The first is the X-ray luminosity of the source; since star forming galaxies rarely have X-ray luminosities in excess of 10^{42} erg s^{-1} a luminosity cut for compact sources at this value is a fairly safe selection criterion. However, this luminosity cut will typically only select unobscured or the most luminous obscured objects. Since obscuration will lead to suppression of flux in the soft X-ray bands (typically below 2keV, but increasingly harder for high column obscuration), the inferred luminosity of the X-ray source using broad-band photometry will be much lower than the intrinsic luminosity.

In order to find these obscured sources a second level of selection must take place. Firstly the 2-10keV spectrum will show signs of obscuration and so much deeper observations capable of getting crude spectra will be needed. One typically bins the X-ray spectra into soft and hard bins, calculates a hardness ratio and infers a level of obscuration from this.

If these sources are Compton thick obscured however, observations from $2 -$ 10keV will be of little help and observations at much harder X-ray energies (e.g. $10 - 50$keV) will be needed.

5.8 Biases

Lone selection at 24μm would allow for a relatively unbiased sample of AGN. However, there will be heavy starburst contamination due to strong PAH lines in the mid-IR. With the introduction of photometric redshift selection the sample will begin to depend on the templates used in the photometric code; for example, if the templates do not include a quasar component then objects that appear blue will be taken to be younger star forming objects and possibly miscalculating photometric redshifts. This can be tested in the sample, since those objects classified as AGN, and especially Seyfert-I objects will have large discrepancies between the photometric and spectroscopic redshifts. This is discussed in Section 5.9.3.

5.9 Analysis

A combination of the Lee et al. (2011) and Juneau et al. (2011) diagnostic techniques is used to classify the 24μm since these diagrams use only `[OIII]` and Hβ lines to select bonafide AGN, mitigating the effects of reddening that would be present in the `[OII]`/Hβ ratio. Any source which is in the AGN region of the Lee et al. (2011) diagnostic and either the AGN or intermediate region of the Juneau et al. (2011) diagnostic is taken to be an AGN. On the other hand if a source is an AGN in the Lee et al. (2011) diagnostic but a star forming galaxy in the Juneau et al. (2011) diagnostic, or a star forming galaxy in the Lee et al. (2011) diagnostic and an intermediate in the Juneau et al. (2011) diagnostic is it taken to be a composite object. Finally, those sources which lie in the star forming region of both diagnostics are classified as star forming galaxies.

Only sources with a S/N of 3 or greater in both `[OIII]` and Hβ are considered for emission line classification. This leaves a sample of 27 narrow line sources for classification with these diagnostic techniques. The Lee et al. and Juneau et al. diagnostic diagrams for the sample are shown in Figures 5.6 and 5.7, respectively.

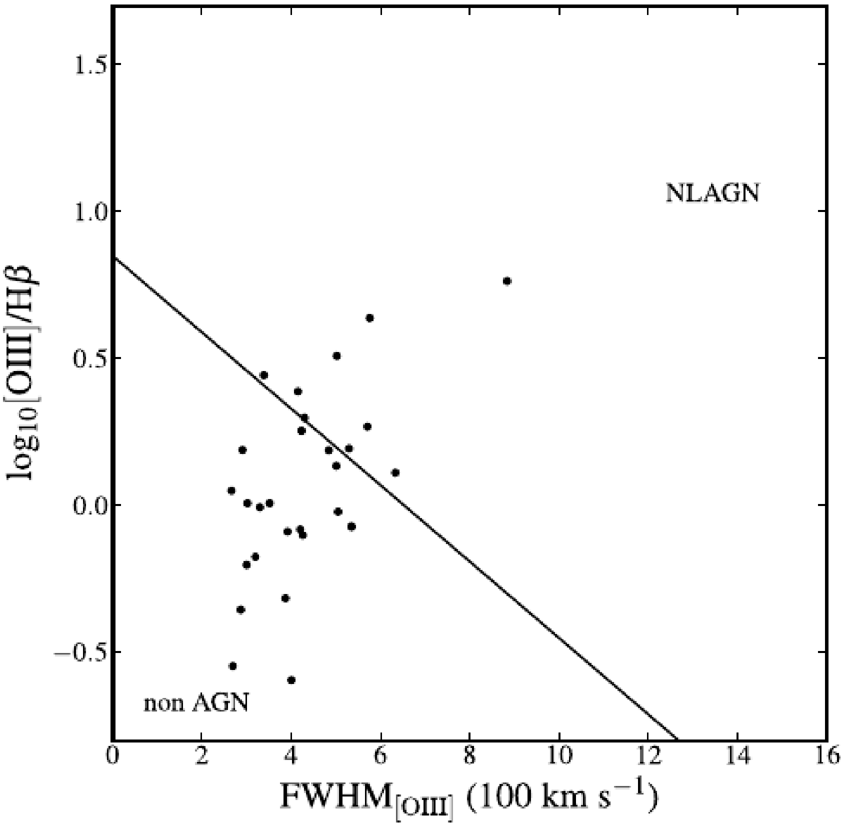

Figure 5.6: Lee et al. (2011) diagnostic diagram showing the result for all VIMOS narrow emission line objects (27).

5.9.1 Parameters

For this sample there exists 13 band optical-to-mid-IR photometry, X-ray fluxes, spectroscopic redshifts, `[OII]`, `[OIII]` and Hβ line fluxes and linewidths as well as diagnostic diagram derived object classifications. There are also SED derived star formation rates, stellar masses and ages:

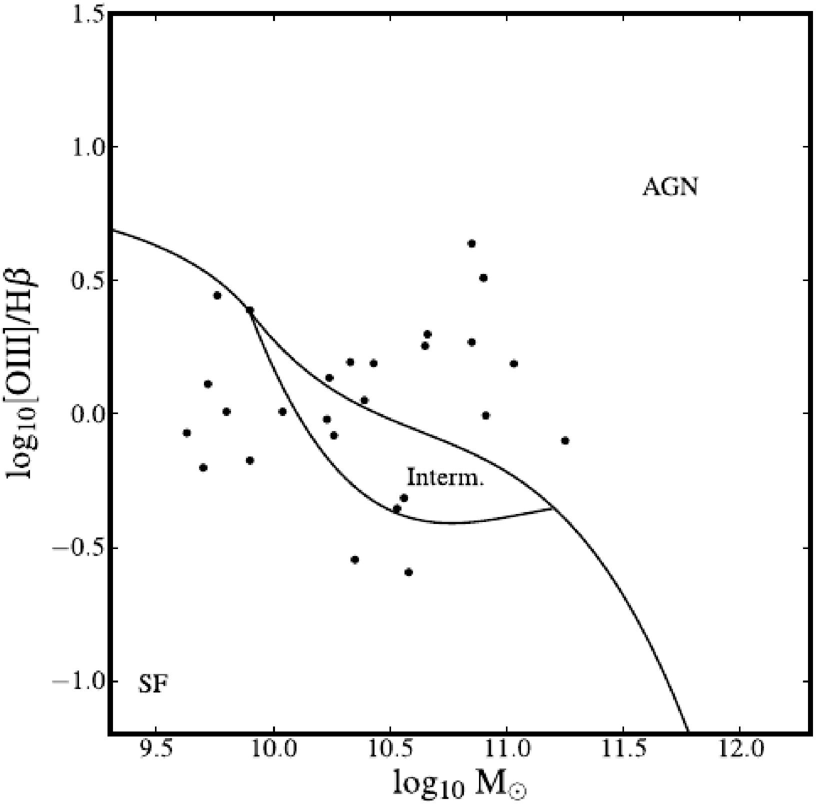

Figure 5.7: Juneau et al. (2011) diagnostic diagram showing all VIMOS narrow emission line objects (27).

5.9.2 SED derived parameters

Using the new spectroscopic redshift constraint, this allows for an improved, constrained SED fit, with tighter constraints on the star formation rates and stellar masses. Using the same routines used to previously derive photometric redshifts, SED fitting is re-run by V. Bruce (private communication), making use of the Hyper-Z code (Bolzonella et al. 2000) with templates from Bruzual and Charlot (2003). Constraints are: $0 < A_v < 4$, Age > 50Myr and exponentially declining star formation histories with $0.3 < \tau < 5$ Gyr. The sample has an SED derived median stellar mass of $\log_{10} \mathrm{M}_*(\mathrm{M}_\odot) = 10.52 \pm 0.53$.

5.9.3 Type-I Objects

All six type-I objects classfied here have spectral redshifts of $z > 1.0$. Of these, three have X-ray detections with XMM-Newton. While one of these sources was selected for observation based on its X-ray detection, the remaining 5 were targeted based on their photometric redshift values ($0.57 < z < 0.84$). This is obviously an issue for the photometric redshift code, which consistently underestimates the redshift by $dz \simeq 0.35$, with spectral redshifts lying even $dz \geq 0.25$ outside the maximum photometric redshift estimates. Given that this is the case, this places the `[OIII]`+Hβ complex at $\sim$ 5000Å outside the spectral window for all type-I objects in the sample. Optically classification as Seyfert-I type objects is taken from a detection of broad Mg-II 2800Å component.

5.9.4 Curious Objects

The objects ID$_{24}$=23303, ID$_{24}$=2143 and ID$_{24}$=17434 are curious objects in this sample. ID$_{24}$=2143 and ID$_{24}$=17434 are spectrally classified as stars (17434 is also an X-ray source):

ID$_{24}$=2143

The 24μm source ID$_{24}$=2143 is a star. Using a by-eye classification of this source alongside the M-dwarf sequence spectra in Gray and Corbally (2009, p. 343) I classify this source and similar source ID$_{24}$=17434 as M4-Dwarf stars. The spectrum of ID$_{24}$=2143 is shown in Figure 5.8.

ID$_{24}$=23303

The 24μm source ID$_{24}$=23303 is very much an anomalous result. In the photometry taken from the SXDS the object has an R-band magnitude of 25. However, on the observation dates for this source (5th/8th Dec, 2010) the spectrum is dominated by continuum, with absorption features dominated by atmospheric absorption features. The object has an integrated R-band magnitude of 20.5, some 4.5 magnitudes brighter than in previous photometry. Over the limited spectral range, it is not possible to discern whether the continuum is associated with a thermal spectrum, or a non-thermal power law. The best fit for both a thermal and a power law continuum to the optical spectrum is shown in Figure 5.9. The temperature of the best fit thermal continuum is 7200K (observed frame), while the best fit continuum slope for the power law continuum

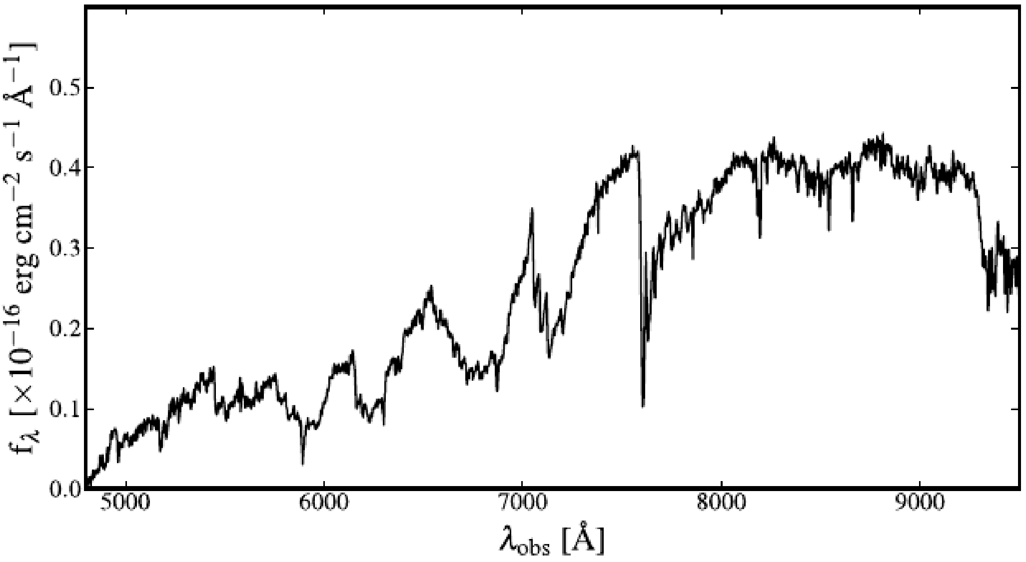

Figure 5.8: Fully reduced spectrum of an M-dwarf star with 24μm ID 2143

is $\beta = -1.68$ (corresponding to $\alpha = -0.32$ where $f_\nu \propto \nu^{-\alpha}$).

The UKIDSS J,H,K photometric data were mined for possible observations on, or near the date of these spectroscopic observations, however, the data are consistent with previous measured (note, that if one were to extrapolate either the thermal or non-thermal lines fit into the near-IR then the change in magnitude would be insignificant anyway, therefore this result is consistent with what was expected).

The spectrum of $\rm ID_{24}$=23303 looks remarkably like that of a GRB optical afterglow reported by Maiorano et al. (2006). I show in Figure 5.10 the spectrum of 23303 with prominent atmospheric absorption features labelled as $\oplus$ symbols. There is a prominent absorption feature 6555Å, which is not an atmospheric feature, which is labelled with a red vertical line. This feature could be any one of many species, especially if the spectrum is interpreted as a GRB afterglow feature. This absorption feature may even due to intervening material along the line of sight. I note that there are no reports of a GRB in the previous days/weeks/months from this region of the sky. The spectrum does not look to be that of a Supernova, as these typically have broader emission/absorption features than those shown in Figure 5.10. Note that the recorded flux between

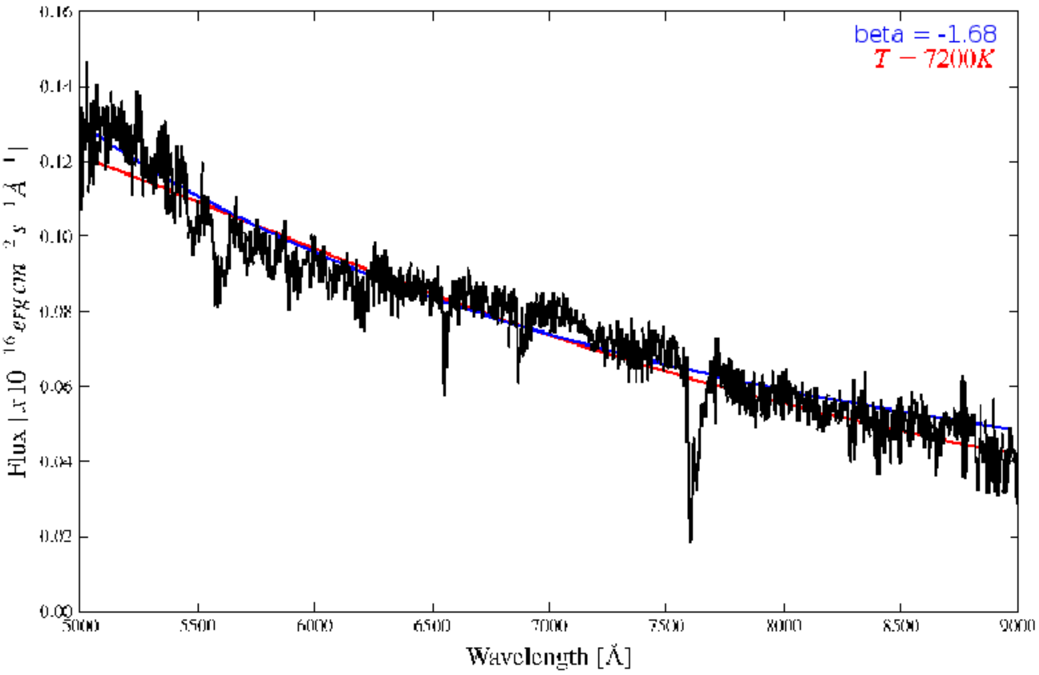

Figure 5.9: The curious source ID_{24}=23303. Spectrum taken from 5th December, 2012. The thermal and non-thermal (power law) best fit lines are also included in red and blue respectively.

the 5th of December and the 8th of December drops by a factor of two, thus it would appear that if the source is GRB afterglow then it is indeed decaying.

5.9.5 AGN vs. Star Forming Galaxies

in AGN, the 24μm is believed to be a good proxy for the intrinsic AGN luminosity. It is, however, well known that the PAH emission in starburst galaxies contributes a significant fraction of the mid-IR luminosity in those sources where PAHs are present. PAHs are seldom seen in mid-IR AGN spectra, and so the mid-IR luminosity in these sources should not have large amounts of contamination. In the optical region, the `[OIII]` luminosity is taken to be a good proxy for the intrinsic AGN luminosity, since the photons needed to produce the species responsible for this emission are produced in copious amounts in AGN accretion discs. One would therefore expect to see a good correlation between the `[OIII]` luminosity and 24μm in AGN. A plot of this is shown in Figure 5.11 (subplot 1)

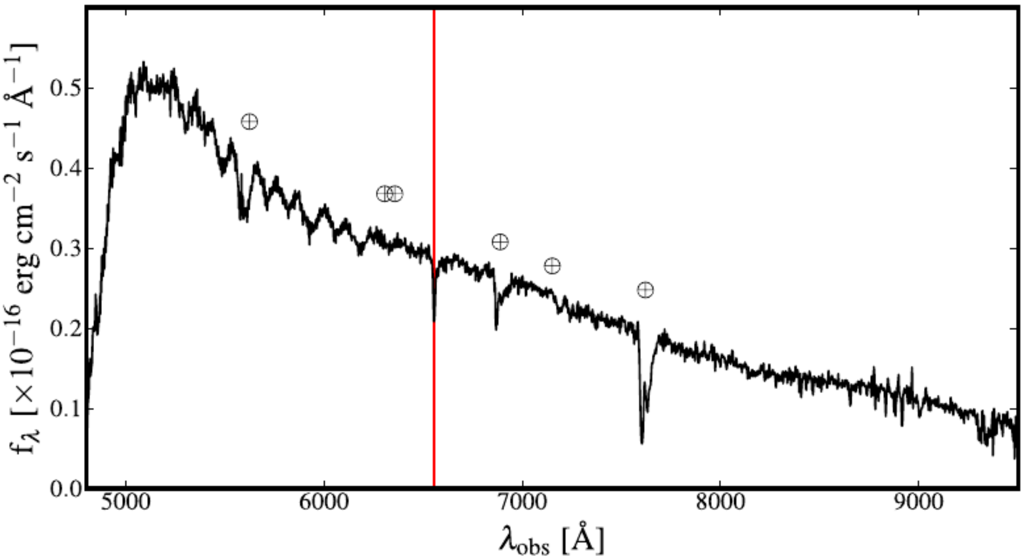

Figure 5.10: a plot of source ID_{24}=23303 Spectrum taken from 8th December, 2012, with prominant atmospheric absorption features labelled as ⊕ symbols. The feature labelled with a vertical red line is shown at λ_{obs}= 6555Å.

where all narrow emission line objects are plotted. Since the type-I AGN are at a redshift too high to probe the `[OIII]` emission line they cannot be included in this comparison. For the type-II AGN (blue circles) while there would appear to be a correlation between `[OIII]` luminosity and 24μm luminosity, the sample is very small, so this cannot be a firm result. A spearman rank correlation test on these data return a correlation coefficient of 0.2 put a p-value of only 30 percent (i.e. 70 percent chance that the two data are uncorrelated). The derived correlation between `[OIII]` and 13.5μm luminosity for local type-II objects taken from LaMassa et al. (2010) is shown in the plot as a dot-dashed line. All six of the type-II AGN are shown to lie below this line. This is interpreted as a suppression in the `[OIII]` luminosity due to a lack of redenning correction of the line fluxes; the continuum is generally quite weak in the spectra of these objects and so it is difficult to measure a stellar continuum reddening. Alternatively deriving an emission line reddening using Hβ/Hγ is very difficult since the Hγ line is also very weak.

By plotting the SED derived SFR vs. 24μm data (Figure 5.11, subplot 3) shows the spread in SFRs for across the entire sample. The type-II objects have a spread in SFRs from 1-15 $M_\odot$ yr^{-1}. The larger spread in the type-I

AGN must be taken with caution, since the SED fitting routine does not include quasar templates. This may result in the blue continua in the type-I objects forcing a young stellar population, with artificially high star formation rates. The dashed line in this subplot is taken from Rieke et al. (2009), which is the derived correlation in the LIRG/ULIRG regime.

Plotting the SED derived SFR vs. derived `[OIII]` luminosities of the sample (Figure 5.11, subplot 4) shows the `[OIII]` excess in the Type-II objects vs. the composite and star forming population.

5.9.6 Mid-IR photometric classification

Figure 5.12 shows that while all type-II objects lie within the selection wedges of Stern (left) and Lacy (right) colour-colour plots, not all of the type-I objects do. This plot also highlights the level of contamination of star forming galaxies in this photometric selection technique. The two large black star symbols represent the M-dwarf stars (note that ID_{24}=2143 lies within the Stern wedge but not the Lacy wedge, while ID_{24}=17434 lies outside the Stern wedge, but within the Lacy wedge).

5.9.7 Comparison to Rush et al. (1993)

In Rush et al. (1993), the authors construct a subsample of 12μm IRAS AGN containing 53 Seyfert-I and 63 Seyfert-II objects to a flux limit of 0.3Jy, which represents 13 percent of the parent 12μm sample. The total fraction of AGN is seen to increase as a function of 12μm luminosity, but shows no significant signs of intrinsic differences between the Seyfert-I and Seyfert-II objects. In this work a sample of 6 Seyfert-I and 6 Seyfert-II objects selected at 24μm to a flux limit of 0.1mJy are optically spectroscopically classified, which would translate to $\sim$ 22 Seyfert-Is and $\sim$ 22 Seyfert-IIs had the entire survey been completed.

For comparison with Rush et al. (1993) whilst maintaining maximum statistics, a mid-IR luminosity cut of $\log_{10} \nu \, L\nu > 43.7$ [erg s^{-1}] is used, which at the flux limits for Rush et al. (1993) and this 24μm sample imposes a redshift cut of $z < 0.02$ and $z < 0.9$ respectively. This produces a 12μm sample of 98 sources, of which 6 are type-I sources, 13 are type-II sources and a 24μm sample of 44 sources, of which 6 are classified as Type-II AGN, including LINERs. Note that in this limited sample there are no Type-I AGN since they all lie outside the redshift limit imposed for the 24μm sample. A plot of the luminosity vs. redshift is shown in Figure 5.13.

5.10 Discussion

The results and analysis undertaken above reveal that not only were the aims of the program unrealised, but that they would have unlikely to be fulfilled had the entire observational data been amassed. A significant fraction of the targeted sources did not contain spectra of sufficient quality to extract spectroscopic redshifts, and for many of the sources where the spectral quality was sufficient (most specifically, the Type-I broad-line objects) the spectroscopic redshifts were significantly different from those predicted by the photometric template fitting. Nonetheless, this analysis may be interesting for that very reason; the above work reveals that such a method of sample selection is not ideal for aims of the project; further work in the way of photometric redshift templates for AGN, as well as further target constraints (such as an optical magnitude cut to limit the number of *poor* quality spectra in the final observations) would be essential for progression. For example, the work of Salvato et al. (2009) reveal that many AGN are outliers of typical photometric redshift regimes, and thus require further considerations for photometric redshift calculations.

While the analysis undertaken by Salvato et al. (2009) reveals the importance of SED template selection in photometric redshift estimation, it also highlights just how difficult AGN SED fitting is; all of the sources in their sample were either X-ray or radio luminous objects, and known AGN. For a radio-quiet, X-ray obscured AGN, it appears that it would be necessary to first gain a spectroscopic redshift of the source before showing it to be an outlier in photometric vs. spectroscopic redshift.

It is unclear to the author whether any minor amendments to the sample selection technique as performed above would be sufficient to transform the method into a *much* more successful one for selecting AGN in a relatively unbiased fashion. Indeed a radical re-think of the technique may be necessary. As an example, if one wishes to increase the number of broad line objects in the sample, they could use the above technical shortfall to their advantage: they could perform more crude optical spectroscopy across a large sample of 24μm sources in order to obtain spectroscopic redshift measurements, compare these with photometric redshift measurements and select the outliers for follow up fine optical spectroscopy, since these sources are more likely to be Type-I AGN. However, such a technique would not help Type-II object statistics.

5.10.1 Type-II Fraction

With this sample of AGN, deriving statistically significant results for the Type-II AGN fraction is impossible, especially over a luminosity range comparable with that of the Rush et al. (1993) sample. Other work being undertaken by Toba et al. (2012a;b) controversially find the 18μm and 22μm Type-II fraction at $z < 0.3$ to be a decreasing function of luminosity. They also find a total type-II fraction of around 0.8 obtained from type-I and type-II luminosity functions between $0.006 < z < 0.7$. These results are at odds with those found from the Rush et al. (1993) sample, where there is no evidence for a luminosity dependence of the type-II AGN fraction, and a type-II AGN fraction of 0.55.

5.11 Conclusions

From a sample of 228 sources, 102 are of sufficient quality to gain spectroscopic redshifts (primarily from the 4000Å break). Of these 102 sources, two are stellar M4-dwarf stars (ID_{24}=2143 and ID_{24}= 17434), whilst the remaining extragalactic sources range from $z = 0.366$ to $z = 1.286$. The narrow emission line objects (those with visual `[OIII]`, Hβ and `[OII]` lines) amount to 27 sources. Broad Line type-I AGN total 6 sources.

Based on the initial aims of this program, both the target selection and target acquisition both had significant problems. The primary concern is that the selection technique did not find anywhere near the anticipated number of desirable AGN sources (i.e. not enough to create a statistically significant sample suitable for comparison with local sources). Secondly, there is obviously a significant bias against the selection of Type-I AGN within the desired redshift range. Any future works building on such a method as applied here must address two important questions:

1. The photometric redshift fitting code routinely underestimates the true redshifts of Type-I AGN, and must be adapted to include quasar templates to address this issue.
2. An optical or near-IR apparent magnitude cut for selectable targets will help to increase the detection rate among targets. However, careful consideration must be given to any biases that this will introduce. While selection in the near-IR (H-band, say) will target objects with large stellar masses (the stellar SEDs peaks at $\sim 1.6\mu$m), in which AGN are more common. This should not introduce a bias with regard to Type-II fraction population statistics (if indeed the unified scheme is to be believed, and Type-I and Type-II AGN have the same stellar mass distributions), but will effect the total AGN fraction.

The original aim was to spectroscopically follow up ~ 550 24μm sources, where ~ 120 (~ 20 percent) of the targets were AGN. With only 33 (14 percent) of final 228 targets showing emission lines and only 12 (5 percent) being classified as AGN/LINERs this is not as successful as anticipated. Addressing the issues raised above would undoubtedly go some way to improving the method of sample selection in future works, However, even with such amendments an increased target sample would also be necessary to increase AGN statistics.

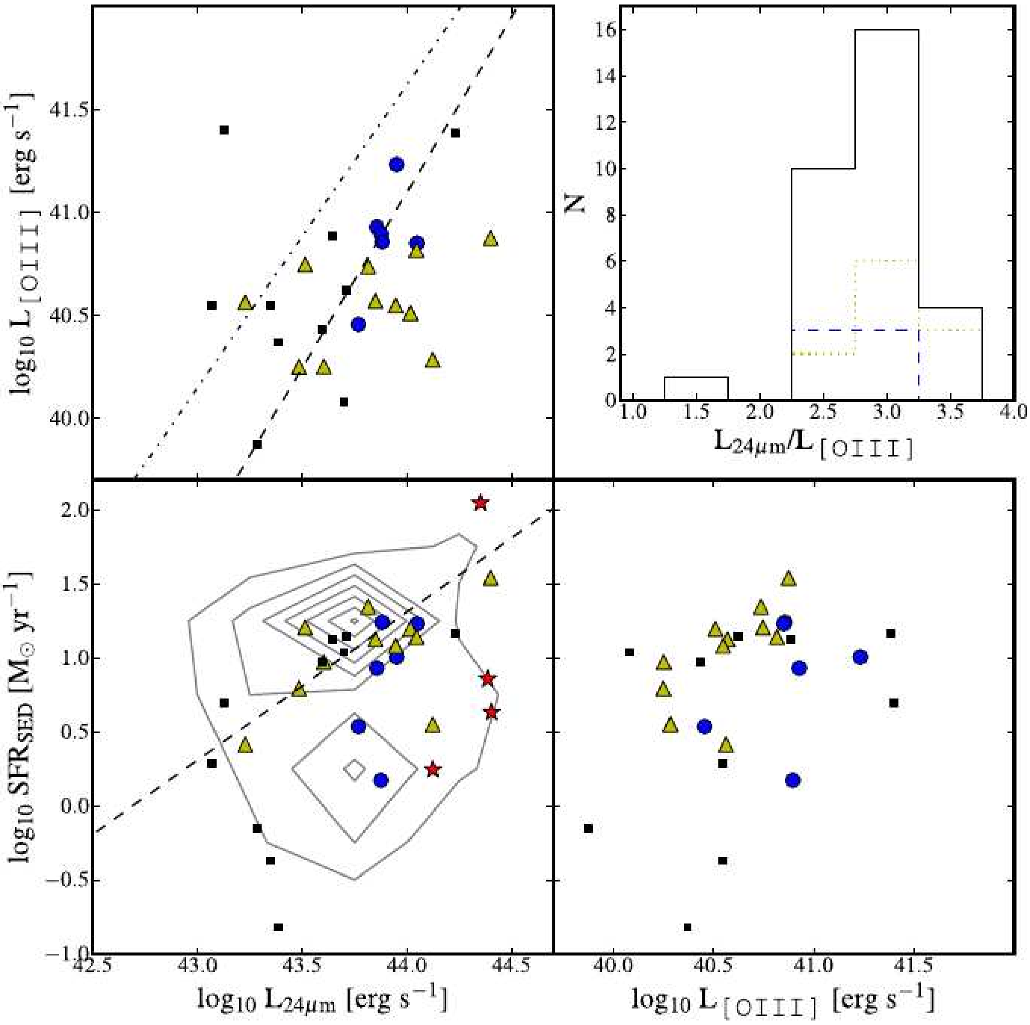

Figure 5.11: Subplot 1 (top-left) shows the 24μm luminosity vs `[OIII]` luminosity of these sources with spectral redshifts and `[OIII]` line measurements (S/N$>$ 3). Blue circles = type-II, yellow triangles = Composite, black squares = star forming galaxies. The dashed line represents the best fit to the data, while the dot-dashed line is taken from the correlation derived by LaMassa et al. (2010) for local type-II AGN, with the mid-IR continuum luminosity measured from low resolution spectra at $\lambda_{\rm rest} = 13.5\mu$m. Subplot 2 (top-left) shows the ratio of 24μm luminosity to `[OIII]` for the same sources. Blue dashed line = type-II, yellow dotted line = Composite, black solid line = all narrow emission line sources. Subplot 3 (bottom-left) shows the 24μm luminosity vs. SED derived SFR, symbols are as per figure one, except red stars = type-I, grey contour = passive galaxies. Dashed line represents the correlation derived by Rieke et al. (2009) for LIRG/ULIRG galaxies. Subplot 4 (bottom-right shows the `[OIII]` luminosity vs. SED derived SFR for the narrow emission line galaxies. Symbols are as per sub-plot 1.

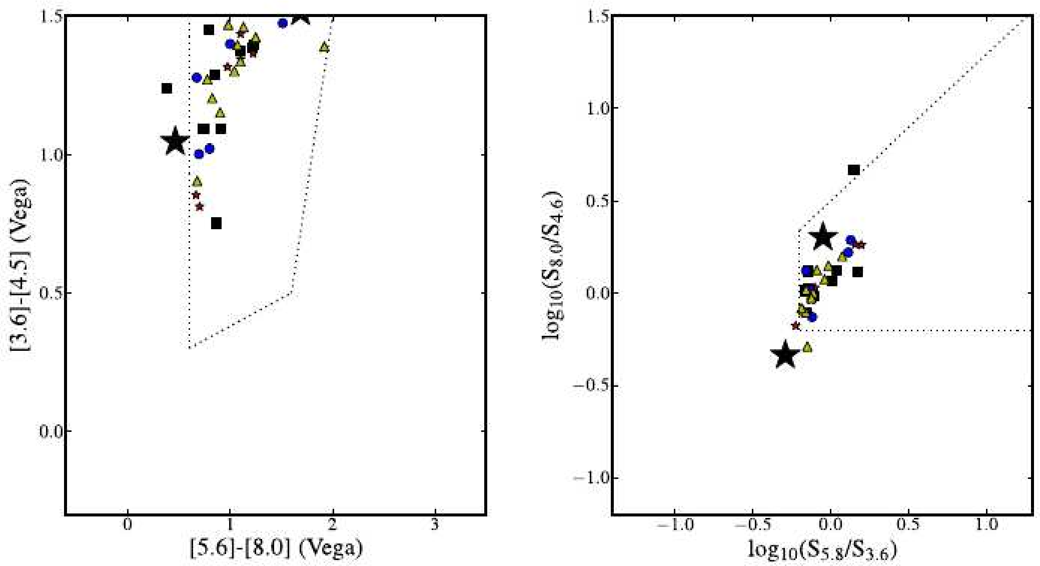

Figure 5.12: Data from the sample plotted in the Stern et al. (left) and Lacy et al. (right) colour-colour plots. The red star symbols represent those objects classified optically as Type-I AGN, Type-II objects are blue circles, star forming galaxies are black squares and composite objects are yellow triangles. The two large black star symbols represent the M-dwarf stars

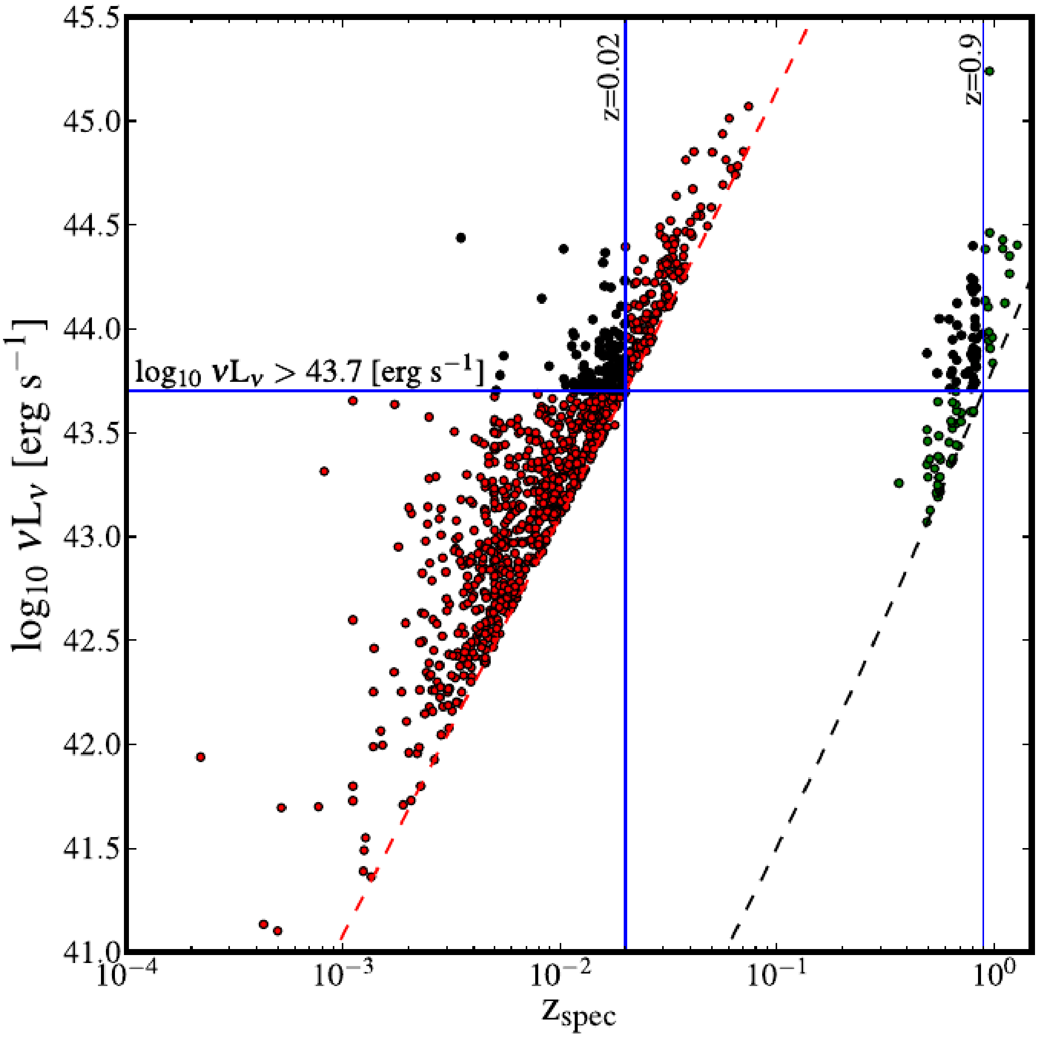

Figure 5.13: A plot of the luminosity vs. redshift for the Rush et al. (1993) and this sample, with the imposed redshift and luminosity cut to create comparative samples.

Chapter 6

Conclusions

6.1 The Aims of this Work

The primary aims of this work are: i) constraining the obscured/type-II AGN fraction, ii) to investigate a possible link between radio galaxy radio power and source overdensity at high redshift and iii) to investigate the nature of AGN host galaxies selected on their far-IR characteristics. The first aim was targeted in Chapters 3, 4 and 5, the second aim targeted in Chapter 2, and the third again in Chapter 4. Below I discuss the findings of each chapter, the impact each results has on the field and the future prospects.

6.2 Partial Obscuration

6.2.1 This Work

In Chapter 3 I have developed a model which uses partial obscuration as a means to explain the obscured AGN fraction vs. luminosity that is observed between 2 and 10 keV. The model uses Compton thick obscurers to partially cover the X-ray source, attenuating the X-ray flux within this region. With insufficient or crude data, any observer will be unaware of such an obscured region since the 2-10keV flux will be fully attenuated here. In a realistic scenario, a fraction of the remaining "uncovered" region will be obscured by a lower column of material, the effects of which *will* be measured in the X-ray spectrum and corrected for. The observer will classify the object as obscured and correct the "intrinsic" X-ray flux to that of the uncovered fraction. Given the level of partial covering that has been seen in a number of sources, such an effect could lead to a discrepancy between the inferred intrinsic and true intrinsic X-ray luminosities of some sources to differ by orders of magnitude. The overall effect will be a dearth of obscured objects at high X-ray luminosities, but equally an amplification of obscured sources at low X-ray luminosities, in line with what is actually observed.

If such an phenomenon were to be present in the population then this should also be easy to see in X-ray vs. IR AGN luminosity data. The IR luminosity is believed to be the least biased proxy of the intrinsic luminosity of AGN, and should correlated well with the intrinsic X-ray luminosity. One assesses the correlation between the X-ray and IR luminosities of AGN in unobscured objects which require little in the way of attenuation correction the X-ray regime. If there is a population of obscured AGN with their X-ray luminosities erroneously corrected (i.e. correcting for a lightly obscured partial column, but not for a CT partial column) then these will not lie on the correlation found for unobscured objects. This effect is tentatively observed in data from Brightman and Nandra (2011) and Asmus et al. (2011), and cannot reasonably be accounted for by source variability alone.

6.2.2 Limitations

This study draws upon a compilation of observations made by Hasinger (2008) in which the targets are not necessarily selected in a uniform manner, in which the X-ray luminosities are not necessarily calculated consistently, and in which the source classification is not necessarily consistent across all sources. Despite this, the sample is one the best available for 2-10 keV flux measurements and source classifications. One limitation to this dataset is central to the arguments made in Chapter 3; the X-ray spectra of the sources is crude, often only allowing hardness ratios to be extracted. If this limitation on the dataset is removed by high resolution and dynamic range observations, much of the effect being described will by nullified; *good* spectra will allow for detailed modeling and correction of heavy obscuration, allowing for more reliable intrinsic X-ray luminosity estimations.

Future Study

For this simple model to be developed further, future works must consider the obscured fraction luminosity dependence that has been seen (though disputed) in other observational regimes, such as the hard X-ray and `[OIII]`. One must investigates whether the same processes described in this model be used to reproduce the trend seen in these other regimes.

Physical models involving a range of clouds of different columns, proximities and locations with regard to the central X-ray source will need to be researched further. These models will need to be stable and long lived, or else generated at a rate high enough to counteract their destruction. To add to this, the dynamics of such cloud populations must also be carefully modeled to account for X-ray variability that is observed in many sources.

Observationally, long term observations will allow one to pin down the variability of sources in the X-ray (and indeed to a lesser extent in the IR). Current and future X-ray missions will create a wealth of data, allowing us to probe further free parameters of the model, and test the conclusions of the simple model I propose in chapter 3. With the increased sensitivity and dynamic range of next generation instruments, much of the effect of the partial covering described above (and in Chapter 3) will be corrected for in an increasingly detailed manner, which in turn will reduce the uncertainty of measurements in the X-ray vs. IR luminosity measurements.

Once such a matter has been fully resolved in the X-ray regime, the issue of contrasting results in optical-volume limited, IR and Radio regimes must also be addressed. High resolution imaging of emission regions around AGN will help to some degree; looking at the morphology of the `[OIII]` emission line region will help us model the obscuration morphology in the central regions. High resolution mid-IR spectroscopic observations will allow us to decouple PAH and torus contributions on parsec scales, and to measure the true intrinsic AGN luminosity at unprecedented levels.

6.3 Environments of High Redshift Radio Galaxies

6.3.1 This Work

In Chapter 2 I investigate the environments of high redshift radio galaxies (HzRGs), assessing the population statistics around these objects compared to field galaxies. The targeted observations of 63 HzRGs between redshifts of one and five at 24μm allows us to probe the starburst and AGN populations simultaneously. In this chapter I find that the vicinities of HzRGs are statistically overdense compared to field galaxies. I find that 32 percent of the sources have an overdensity of sources of $d_n > 3$ (i.e. $\mathrm{N}_{\mathrm{field}}+3\sigma_{\mathrm{field}}$), with 13 of these fields being new protocluster candidates.

This work is the first capable of statistically studying field overdensities around radio sources, and so it is also the first to probe any possible correlation between source overdensity and radio power. The common assumption is that the radio jets emanating from the central engine into the IGM may trigger star formation in the environments of HzRGs and since the more powerful jets are capable of injecting more energy into the IGM this should in turn trigger more star formation. In this work I find no correlation between radio power and source overdensity in the sample, casting doubt on the aforementioned assumption.

6.3.2 Limitations

Since the observations in this regime were single band photometry, a lot of the measured overdensities may just in fact be line-of-sight coincidences. This was hopefully addressed in the comparison to the blind targets in the survey fields, but may still be an issue. Equally important is the redshift dependence of the flux density of sources of a given luminosity. The portion of the luminosity function which is being probed at different results varies strongly, and therefore the observed excess surface density has a different meaning at each redshift. Barring evolutionary effects this will lead to an decrease in mean overdensity with increasing z above $z \sim 2$.

6.3.3 Future Work

This issue of true (3D) overdensities vs. surface (2D) overdensities is currently being addressed by full IR SED measurements of all possible target sources in overdense fields, getting photometric redshifts for all candidates and assessing the likelihood that each source is at - or close to - the redshift of the HzRG.

Addressing the issue of probing different populations at different redshifts can be addressed with optical spectroscopic follow-up of all candidates, from which spectroscopic redshift and line flux measurements will allow source luminosities and classes to be derived. As a byproduct of doing this, the results will also help to constrain the luminosity functions of different demographics at a range of epochs.

In particular, interesting targets/fields to follow up will be those that show large discrepancies in the ratio of passive to active galaxies (IRAC colour selection vs. 24μm selection), since these may reveal details of different evolutionary states of those protoclusters.

6.4 Characteristics and Environments of 250μm selected AGN

6.4.1 This Work

By selecting a sample of AGN from Far-IR emission, it is possible to compare Type-I, Type-II and LINER objects based on emission associated with stellar activities alone. In Chapter 4 I study a sample of 7433 250μm selected galaxies, below a redshift of 0.38, and with optical spectra sufficient to classify the sources as Type-I and Type-II AGN, LINERS, star forming galaxies, composite objects and passive galaxies. In this chapter I find that there is statistically no difference between Type-I and Type-II AGN so far as star formation related activities are concerned; type-I objects do not have a boost or suppression in star formation compared to type-II objects, they are no more dusty than Type-II objects, and they do not appear to have older or younger stellar populations. I find the fraction of type-I AGN constant across three decades in `[OIII]` luminosity. In this sample, there is a weak correlation found between stellar age and `[SII]`/Hα, and `[NII]`/Hα. I find LINERs to have a reduced star formation rate compared other objects of equal age and mass, and I find that Type-II AGN have a larger spread in Balmer decrement derived colour excess.

6.4.2 Limitations

The main limitation of this work is the relatively small AGN sample. When measuring a type-II AGN fraction - luminosity dependence, population statistics must be split across multiple luminosity bins, which increases the relative errors for each bin significantly. Also, the derived SED parameters that depend on FIR photometry do not have the most conservative criteria; only one far-IR band is needed for analysis, at 250μm (though many have at least 3 photometric bands). Another limitation of this sample is the lack of mid-IR data. Such data would allow for hot/dust + PAH contribution measurements, and allow for further testing of photometric diagnostics. The BPT diagnostic limits the redshift range over optical spectroscopic classification can take place, this in turn limits the size of the 250μm sample.

6.4.3 Future Work

In order to increase statistics for this sample, future works must include Herschel data from the Southern Galactic Plane (SGP) combined with spectroscopic measurements like those taken with SDSS+GAMA for the SGP. While work is underway for photometric surveys in the SGP with panStarrs, DES and the VST in the optical and near-IR, reliable classification of AGN will demand spectroscopic measurements.

Another direction that this research could undertake is in using alternative spectroscopic diagnostics for classifying AGN at higher redshifts, possibly finding evolutionary trends in the Type-II fraction or in the AGN population as a whole.

6.5 The Obscured Fraction at $z \sim 1$

The work of this chapter was set out in a proposal of 2010. The aim was to observe a statistically significant sample of AGN from a 24μm targets at $z \sim 1$ in order to constrain the type-II fraction from an unbiased sample. Unfortunately, the project was terminated prematurely, resulting in only three of eleven pointings being observed. Though no statistically significant results could be derived from the sample, I describe the reduction process and analyse the observed dataset. I create a catalog of spectroscopic redshifts for over 100 24μm sources, where possible classifying sources as star forming, AGN, composite or stellar. Outwith the scope of this work (classification and study of AGN) I find otherwise interesting objects; two M4-Dwarf stars, and an object which is likely an Gamma Ray Burst afterglow, for which there was no detection of the initial GRB.

6.5.1 Limitations

Due to a small subset of the total sample being observed, no statistically significant results could be derived from the sample. The targeting strategy was also not without problem; The statistics of desired AGN was not only below expectations, there was also a bias against the selection of type-I AGN within the desired redshift range, this bias was due to the photometric redshift templates not sufficiently accounting for AGN contributions, thus making significant discrepancies between the photometric redshift and spectroscopic redshifts of type-I AGN.

6.6 Future Work

The future direction that this work could take would involve the high luminosity WISE sources which will possibly already have SDSS spectra, by selecting these sources based on 22μm flux alone one would be able to possible derive a Type-II fraction without photometric redshift selection effects, or otherwise could use photometric redshifts from the SDSS photometry to preselect targets. This will only be of use at the highest end of the luminosity function (in the optical regime, SDSS DR-7 will reach $R_{AB} < 22.2$ and the WISE satellite will only probe down to $S_{22\mu m} > 2.6$Jy. This work would expand on that being undertaken by Yorhiki Toba and collaborators (Toba et al. (see 2012b, for example)), who controversially find in AKARI and WISE data that the Type-II AGN fraction decreases with 18μm luminosity, at odds local mid-IR results.

6.7 Concluding Remarks

There is still much to be understood about AGN, from even the relatively simple matter of the Type-II fraction, to the complex issues of *torus* morphology and creation, AGN feedback, dust creation and wind geometry, to name but a few. With the advent of the next generation of telescopes including the James Webb Space telescope, the Euclid mission, the Extremely Large Telescope, the Square Kilometer Array, the proposed Athena X-ray telescope and the proposed Space Infrared Telescope for Cosmology and Astrophysics (SPICA), the wealth of data will allow us to test existing models to the limits, but will demand ever increasingly detailed models to explain nuances that will exist is subpopulations of objects.

Appendix A

Photometry Parameters for HzRG Source Extraction - Basic SExtractor Parameters

- CLEANing was turned off
- NPIXEL, the minimum number of adjacent pixels above the detection threshold to qualify a source, is set to 4.
- DEBLEND_NTHRESH, the number of deblending sub-thresholds is set to 16.
- DEBLEND_MINCONT, the minimum contrast parameter for deblending is set to 0.01.
- PHOT_APERTURES, the fixed aperture **diameter** for photometry is set depending on whether the SWIRE frames of the HzRG frames are being analysed. Since the re-sampling is different this value must be set to 8.75 or 8.4 respectively.
- PHOT_AUTOPARAMS, The Kron−Factor and minimum Kron radius respectively are set to 2.55, 3.5.
- THRESH_TYPE, is set to RELATIVE. This constrains DETECT_THRESH to be *relative* to the background.
- DETECT_THRESH is set to 3.

- BACK_SIZE, the background mesh size is set to 32 pixels.
- BACK_FILTERSIZE, is set to 3.
- BACKPHOTO_TYPE, is set to LOCAL.
- SEEING_FWHM, the Stellar FWHM is set to 5.0 (arcseconds).
- GAIN is set to 0.0 (e-/ADU)
- WEIGHT_TYPE is set to MAP_VAR, since the weight map has been edited to be an absolute variance map.
- WEIGHT_GAIN is set to N

Appendix B

The VIMOS Pipeline

B.1 vmmoscalib - calibration files

The `vmmoscalib` routine brings together a series of more simple routines to create calibration files for the final science exposures. The routines are performed on arc lamp exposures, which are taken either before of after the science exposures with the same slit mask. Here I give an overview of the routines involved in taking raw data through to files used for final calibration. For a more complete picture of the mathematics involved at east step the reader is referred to the Vimos Data Reduction Pipeline Manual.

Bias & Dark Subtraction - The arc lamp exposures must first have the bias assosiated with the voltage across each pixel gate removed. This fixed pattern noise is not assosiated with Poisson noise or thermal noise on the chip, but simply that do with the reading out of data. The next step is to remove dark frames from the arc lamp exposures; these are exposure assosiated with the thermal noise of the chip. Together these two steps allow for the better detection of signal and characterisation of noise.

Arc Lamp Peak Detection - The next step in the calibration pipeline is the detection of peaks within each frame of each arc lamp exposure. The arc lamp is dispersed along the columns of the CCD, and so data are split into columns and peak detection is performed on each column individually. The algorithm itself searches for peaks between triplets of pixels, if a middle pixel has a higher value than the two surrounding it, and it is above a defined signal-to-noise threshold then it is taken to the location of a peak. The peak vertex is then approximated from parabolic interpolation of the data triplet. The process is continued for every pixel triplet in each column of the CCD.

Pattern Recognition - This routine makes use of an arc lamp calibration file which stores the intrinsic wavelengths of all emission lines expected from the diffraction. The pattern recognition task then takes triplets of detected peaks and finds the ratio of $y_1 \rightarrow y_2$ and $y_2 \rightarrow y_3$, the dispersion pixels of peak 1 (y_1), peak 2 (y_2) and peak 3 (y_3) respectively, and compares them to the ratios of contiguous emission lines in the calibration file λ_a to λ_b and λ_b to λ_c. Once a close match is found, each peak pixel location is provisionally assigned a wavelength, $y_1 \rightarrow \lambda_a$, $y_2 \rightarrow \lambda_b$ and $y_3 \rightarrow \lambda_c$, and each pair has an assosiated counter increased. This counter plays a vital role if peak pixels are assigned multiple wavelengths or vise versa, since in these cases the pairing with the highest counter is taken to be the true pairing. I note that the use of these ratios is dependent on the local dispersion of the arc lamps being roughly linear.

Initial Wavelength Calibration - Once each peak has been assigned a catalog wavelength, a arbitrary wavelength and CCD position pair are chosen as a reference to define the wavelength calibration and curvature models.

2-D Pattern Recognition - 2D pattern recognition is activated to match slit positions with physical position on the CCD. After this a coordinate transformation is determines to match the two coordinate systems.

Global Model of Curvature - The spatial curvature is calculate by tracing the slit spectra edges. A local spatial curvature model is derived for each spectral trace, fitted by a low-degree polynomial. If there are enough slits and enough spectra, then a global curvature model is derived from the local curvatures.

Arc Spectra Extration - Arc spectra are extracted by reading along the derived curvature. The arc spectra are then finally wavelength calibrated using the calibration method described above (1D peak detection and pattern recognition).

Input Items

- `MOS_ARC_SPECTRUM` - The arc lamp exposure.
- `MOS_ARC_FLAT` - flatfield frames, typically more than 1, can be stacked according to a method defined by the user (Average, Median, MinMax (mean after minimum and maximum rejection)).
- `BIAS` - There are usually 5 bias frames for each quadrant. These are stacked according to the method defined by the user (as for flat frames).
- `CCD_TABLE` - A table of known bad pixels.
- `CONFIG_TABLE` - a configuration table for the particular setup (MR with GG475 filter requires configuration file VIMOS_GRS_MR_GG475_1.fits). Includes expected dispersion in Å/pixel, wavelength calibration parameters, spatial curvature initial parameters, start and end wavelengths for spectral extration.
- `LINE_CATALOG` - A catalog of the lines for the arc lamp.

Output Items

- `mos_wavelength_map.fits` - map of wavelengths on CCD, each pixel has a wavelength assigned to its centre, if available.
- `mos_spectral_resolution.fits` - table of mean spectral resolution for each reference arc lamp line, with columns Wavelength, FWHM, FWHM RMS, Resolution and Resolution RMS.
- `mos_spatial_map.fits` - maps of spatial positions on the CCD.
- `mos_slit_location.fits` - split positions on CCD and rectified image (`mos_arc_spectrum_extracted.fits`) of arc lamp exposures.
- `mos_master_screen_flat.fits` - the master flat of the input flat files, stacking as defined by the user.
- `mos_disp_residuals_table.fits` - table of the residuals of the wavelength, compared with the reference line catalog.

- `mos_disp_coeff.fits` - table containing the wavelength calibration polynomial coefficients. item `mos_delta_image.fits` - Deviation from the linear term of the wavelength calibration fitting polynomials.
- `mos_curv_traces.fits` - Table with spectral edge detected x positions on the CCD at different y posititions, compared with those predicted by model.
- `mos_curv_coeff.fits` - Table of spatial curvature coefficients.
- `mos_combined_screen_flat.fits` - sum of all input flat files.
- `mos_arc_spectrum_extracted.fits` - wavelength calibrated and rectified arc lamp image (all extracted arc spectra contiguously placed in one image).
- `master_bias.fits` - The master bias of the input bias files, stacking as defined by the user.
- `qc0001.paf` - Quality control log file.
- `qc0000.paf` - Quality control log file.
- `esorex.log` - Log file of output from command-line command `esorex`.
- `global_distortion_table.fits` - Concatenation of `mos_curv_coeff.fits` and `mos_disp_coeff.fits`.

B.2 vmmosscience - science files

The `vmmoscience` routine brings together a series of more simple routines to extract, wavelength calibrate, rectify, flatfield and flux calibrate the science images. The routines are performed on science exposures, which are taken either before or after the arc frame images with the same slit mask. Here I give an overview of the routines involved in taking the raw data through to final reduced spectra. For a more complete picture of the mathematics involved at east step the reader is referred to the Vimos Data Reduction Pipeline Manual.

Sky Subtraction - There are three options here; local, median and global sky subtraction. In the local method, the sky trend is modelled along the dispersion axis for each spectrum on the CCD and subtracted individually. In the median method the median value for the sky is calculated at every wavelength and subtracted from each rectified slit spectrum accordingly. The global method is generally only used for objects that extend across the entire slit, so a global interpolation of the sky is used to calculate the sky within this spectrum. Cosmic ray removal can also be performed at this step, but is largely superfluous since these are removed optimal extraction of detected objects.

Alignment and Stacking - For multiple observations of the same targets, the science frames must be stacked in order to combine the spectra. The spectra are dithered to same location and (by default) mean stacked together.

Object Detection and Extraction - rectification and wavelength calibration of object spectra, using the calibration files produced by *vmmoscalib* and in the `CONFIG_TABLE`.

Flux Calibration - This step makes use of standard star observations around the date/time of the target objects. The raw standard star objects are processed by *vmmoscalib* along with an predicted intrinsic spectrum of the target star. A spectrophotometric correction table is then produced that can be used to flux calibrate the object spectra.

Input Items

- `MOS_SCIENCE` - The raw science frames, spectroscopic observations of the targets.
- `CONFIG_TABLE` - As per vmmoscalib input items.
- `EXTINCT_TABLE` - Atmospheric extinctin table.
- `MASTER_BIAS` - As per vmmoscalib output items.
- `MOS_CURV_COEFF` - As per vmmoscalib output items.
- `MOS_MASTER_SCREEN_FLAT` - As per vmmoscalib output items.

- `MOS_SLIT_LOCATION` - As per vmmoscalib output items.
- `MOS_SPECPHOT_TABLE` - Derived from performing vmmoscalib on standard star observations.

Output Items

- `mos_sci_disp_coeff_sky.fits` - Wavelength calibration polynomial coefficients fit after alignment to skylines.
- `mos_science_extracted.fits` - Extracted, rectified, wavelength calibrated and sky subtracted slit spectra.
- `mos_science_flux_extracted.fits` - Extracted, rectified, wavelength calibrated, sky subtracted and flux calibrated slit spectra.
- `mos_science_flux_reduced.fits` - 1D extracted, rectified, wavelength calibrated, sky subtracted, flux calibrated and reduced spectra, one per row.
- `mos_science_reduced.fits` - 1D extracted, rectified, wavelength calibrated, sky subtracted and reduced spectra, one per row.
- `mos_science_sky_extracted.fits` - Extracted, rectified, wavelength calibrated slit spectra.
- `mos_science_sky.fits` - Extracted, rectified, wavelength calibrated sky spectra.
- `mos_sci_error_flux_reduced.fits` - Image with statical errors corresponding to extracted and flux calibrated object spectra.
- `mos_sci_error_reduced.fits` - Image with statical errors corresponding to reduced object spectra.
- `mos_sci_skylines_offsets_slit.fits` - Table of observed sky line offsets that are used for adjusting the input wavelength solution.
- `mos_sci_sky_reduced.fits` - Image of sky corresponding to extracted, rectified, wavelength calibrated, sky subtracted and reduced spectra, one per row.

- `mos_sci_unmapped_sky.fits` - Image of sky spectra on the CCD frame.
- `mos_sci_wavelength_map_sky.fits` - Maps of wavelengths on the CCD after skyline adjustment of the wavelength solution.
- `mos_unmapped_science.fits` - Image of object spectra on the CCD frame.
- `object_sci_table.fits` - Table detailing the locations of each slit in the reduced and extracted spectral files.
- `esorex.log` - Log file of output from command-line command `esorex`.

At this stage the data reduction pipeline has produced rectified, wavelength calibrated, sky subtracted, flux calibrated and reduced spectra for each date. This finally need to be stacked together to produce final reduced spectra for each source.

enumerate

References

K. N. Abazajian, J. K. Adelman-McCarthy, M. A. Agüeros, S. S. Allam, C. Allende Prieto, D. An, K. S. J. Anderson, S. F. Anderson, J. Annis, N. A. Bahcall, and et al. The Seventh Data Release of the Sloan Digital Sky Survey. ApJS, 182:543, June 2009. doi: 10.1088/0067-0049/182/2/543.

J. Aird, K. Nandra, E. S. Laird, A. Georgakakis, M. L. N. Ashby, P. Barmby, A. L. Coil, J.-S. Huang, A. M. Koekemoer, C. C. Steidel, and C. N. A. Willmer. The evolution of the hard X-ray luminosity function of AGN. MNRAS, 401:2531–2551, February 2010. doi: 10.1111/j.1365-2966.2009.15829.x.

D. M. Alexander, F. E. Bauer, W. N. Brandt, D. P. Schneider, A. E. Hornschemeier, C. Vignali, A. J. Barger, P. S. Broos, L. L. Cowie, G. P. Garmire, L. K. Townsley, M. W. Bautz, G. Chartas, and W. L. W. Sargent. The Chandra Deep Field North Survey. XIII. 2 Ms Point-Source Catalogs. AJ, 126:539–574, August 2003. doi: 10.1086/376473.

D. M. Alexander, F. E. Bauer, S. C. Chapman, I. Smail, A. W. Blain, W. N. Brandt, and R. J. Ivison. The X-Ray Spectral Properties of SCUBA Galaxies. ApJ, 632: 736–750, October 2005. doi: 10.1086/444342.

D. M. Alexander, R.-R. Chary, A. Pope, F. E. Bauer, W. N. Brandt, E. Daddi, M. Dickinson, D. Elbaz, and N. A. Reddy. Reliable Identification of Compton-thick Quasars at z ˜ 2: Spitzer Mid-Infrared Spectroscopy of HDF-oMD49. ApJ, 687:835–847, November 2008. doi: 10.1086/591928.

W. N. Alston, S. Vaughan, and P. Uttley. Ultraviolet and X-ray variability of NGC 4051 over 45 days with XMM-Newton and Swift. MNRAS, 429:75–84, February 2013. doi: 10.1093/mnras/sts320.

R. R. J. Antonucci and J. S. Miller. Spectropolarimetry and the nature of NGC 1068. ApJ, 297:621–632, October 1985. doi: 10.1086/163559.

N. Arav, I. Shlosman, and R. J. Weymann, editors. *Mass ejection from AGN : proceedings of a workshop held at the Carnegie Observatories in Pasadena, California, 19-21 February 1997*, volume 128 of *Astronomical Society of the Pacific Conference Series*, 1997.

P. Arévalo, P. Uttley, S. Kaspi, E. Breedt, P. Lira, and I. M. McHardy. Correlated X-ray/optical variability in the quasar MR2251-178. MNRAS, 389:1479–1488, September 2008. doi: 10.1111/j.1365-2966.2008.13719.x.

K. A. Arnaud. XSPEC: The First Ten Years. In G. H. Jacoby and J. Barnes, editors, *Astronomical Data Analysis Software and Systems V*, volume 101 of *Astronomical Society of the Pacific Conference Series*, page 17, 1996.

D. Asmus, P. Gandhi, A. Smette, S. F. Hönig, and W. J. Duschl. Mid-infrared properties of nearby low-luminosity AGN at high angular resolution. A&A, 536:A36, December 2011. doi: 10.1051/0004-6361/201116693.

D. Asmus, P. Gandhi, S. F. Hoenig, and A. Smette. The largest mid-infrared atlas of active galactic nuclei at sub-arcsecond spatial scales. *ArXiv e-prints*, January 2013.

J. A. Baldwin, M. M. Phillips, and R. Terlevich. Classification parameters for the emission-line spectra of extragalactic objects. PASP, 93:5–19, February 1981. doi: 10.1086/130766.

D. R. Ballantyne. Obscuring Active Galactic Nuclei with Nuclear Starburst Disks. ApJ, 685:787–800, October 2008. doi: 10.1086/591048.

A. J. Barger and L. L. Cowie. The Number Density of Intermediate- and High-Luminosity Active Galactic Nuclei at z ˜ 2-3. ApJ, 635:115–122, December 2005. doi: 10.1086/497330.

P. Barr, N. E. White, and C. G. Page. The discovery of low-level iron K line emission from CYG X-1. MNRAS, 216:65P–70P, October 1985.

T. Beckert and W. J. Duschl. The dynamical state of a thick cloudy torus around an AGN. A&A, 426:445–454, November 2004. doi: 10.1051/0004-6361:20040336.

V. Beckmann, S. D. Barthelmy, T. J.-L. Courvoisier, N. Gehrels, S. Soldi, J. Tueller, and G. Wendt. Hard X-ray variability of active galactic nuclei. A&A, 475:827–835, December 2007. doi: 10.1051/0004-6361:20078355.

M. C. Bentz, B. M. Peterson, R. W. Pogge, and M. Vestergaard. The Black Hole Mass-Bulge Luminosity Relationship for Active Galactic Nuclei From Reverberation Mapping and Hubble Space Telescope Imaging. ApJ, 694:L166–L170, April 2009. doi: 10.1088/0004-637X/694/2/L166.

T. S. Bergmann. Resolved Outflows in Nearby AGN from Integral Field Spectroscopy. In G. Chartas, F. Hamann, and K. M. Leighly, editors, *AGN Winds in Charleston*, volume 460 of *Astronomical Society of the Pacific Conference Series*, page 133, August 2012.

E. Bertin and S. Arnouts. SExtractor: Software for source extraction. A&AS, 117: 393–404, June 1996.

P. N. Best. The cluster environments of the z~1 3CR radio galaxies. MNRAS, 317: 720–736, September 2000. doi: 10.1046/j.1365-8711.2000.03712.x.

S. Bianchi, A. Corral, F. Panessa, X. Barcons, G. Matt, L. Bassani, F. J. Carrera, and E. Jimnez-Bailn. Ngc 3147: a true type 2 seyfert galaxy without the broad-line region. *Monthly Notices of the Royal Astronomical Society*, 385(1): 195–199, 2008. ISSN 1365-2966. doi: 10.1111/j.1365-2966.2007.12625.x. URL `http://dx.doi.org/10.1111/j.1365-2966.2007.12625.x`.

S. Bianchi, F. Panessa, X. Barcons, F. J. Carrera, F. La Franca, G. Matt, F. Onori, A. Wolter, A. Corral, L. Monaco, Á. Ruiz, and M. Brightman. Simultaneous X-ray and optical observations of true type 2 Seyfert galaxies. MNRAS, 426:3225–3240, November 2012. doi: 10.1111/j.1365-2966.2012.21959.x.

R. D. Blandford and C. F. McKee. Reverberation mapping of the emission line regions of Seyfert galaxies and quasars. ApJ, 255:419–439, April 1982. doi: 10.1086/159843.

R. D. Blandford and D. G. Payne. Hydromagnetic flows from accretion discs and the production of radio jets. MNRAS, 199:883–903, June 1982.

R. D. Blandford and R. L. Znajek. Electromagnetic extraction of energy from Kerr black holes. MNRAS, 179:433–456, May 1977.

M. Bolzonella, J.-M. Miralles, and R. Pelló. Photometric redshifts based on standard SED fitting procedures. A&A, 363:476–492, November 2000.

I. A. Bond and M. Matsuoka. Radiative Reprocessing by Blobs Immersed in the X-Ray Emitting Regions of Active Galactic Nuclei. MNRAS, 265:619, December 1993.

A. Bongiorno, G. Zamorani, I. Gavignaud, B. Marano, S. Paltani, G. Mathez, P. Møller, J. P. Picat, M. Cirasuolo, F. Lamareille, D. Bottini, B. Garilli, V. Le Brun, O. Le Fèvre, D. Maccagni, R. Scaramella, M. Scodeggio, L. Tresse, G. Vettolani, A. Zanichelli, C. Adami, S. Arnouts, S. Bardelli, M. Bolzonella, A. Cappi, S. Charlot, P. Ciliegi, T. Contini, S. Foucaud, P. Franzetti, L. Guzzo, O. Ilbert, A. Iovino, H. J. McCracken, C. Marinoni, A. Mazure, B. Meneux, R. Merighi, R. Pellò, A. Pollo, L. Pozzetti, M. Radovich, E. Zucca, E. Hatziminaoglou, M. Polletta, M. Bondi, J. Brinchmann, O. Cucciati, S. de la Torre, L. Gregorini, Y. Mellier, P. Merluzzi, S. Temporin, D. Vergani, and C. J. Walcher. The VVDS type-1 AGN sample: the faint end of the luminosity function. A&A, 472:443–454, September 2007. doi: 10.1051/0004-6361:20077611.

R. G. Bower, A. J. Benson, R. Malbon, J. C. Helly, C. S. Frenk, C. M. Baugh, S. Cole, and C. G. Lacey. Breaking the hierarchy of galaxy formation. MNRAS, 370:645–655, August 2006. doi: 10.1111/j.1365-2966.2006.10519.x.

E. Breedt, P. Arévalo, I. M. McHardy, P. Uttley, S. G. Sergeev, T. Minezaki, Y. Yoshii, C. M. Gaskell, E. M. Cackett, K. Horne, and S. Koshida. Long-term optical and X-ray variability of the Seyfert galaxy Markarian 79. MNRAS, 394:427–437, March 2009. doi: 10.1111/j.1365-2966.2008.14302.x.

E. Breedt, I. M. McHardy, P. Arévalo, P. Uttley, S. G. Sergeev, T. Minezaki, Y. Yoshii, Y. Sakata, P. Lira, and N. G. Chesnok. Twelve years of X-ray and optical variability in the Seyfert galaxy NGC 4051. MNRAS, 403:605–619, April 2010. doi: 10.1111/j.1365-2966.2009.16146.x.

M. Brightman and K. Nandra. An XMM-Newton spectral survey of 12 μm selected galaxies - II. Implications for AGN selection and unification. MNRAS, 414:3084–3104, July 2011. doi: 10.1111/j.1365-2966.2011.18612.x.

G. Bruzual and S. Charlot. Stellar population synthesis at the resolution of 2003. MNRAS, 344:1000–1028, October 2003. doi: 10.1046/j.1365-8711.2003.06897.x.

G. Bruzual A. Spectral evolution of galaxies. I - Early-type systems. ApJ, 273:105–127, October 1983. doi: 10.1086/161352.

C. L. Buchanan, J. F. Gallimore, C. P. O'Dea, S. A. Baum, D. J. Axon, A. Robinson, M. Elitzur, and M. Elvis. Spitzer IRS Spectra of a Large Sample of Seyfert Galaxies: A Variety of Infrared Spectral Energy Distributions in the Local Active Galactic Nucleus Population. AJ, 132:401–419, July 2006. doi: 10.1086/505022.

D. Burlon, M. Ajello, J. Greiner, A. Comastri, A. Merloni, and N. Gehrels. Three-year Swift-BAT Survey of Active Galactic Nuclei: Reconciling Theory and Observations? ApJ, 728:58, February 2011. doi: 10.1088/0004-637X/728/1/58.

D. Calzetti, A. L. Kinney, and T. Storchi-Bergmann. Dust extinction of the stellar continua in starburst galaxies: The ultraviolet and optical extinction law. ApJ, 429: 582–601, July 1994. doi: 10.1086/174346.

D. Calzetti, L. Armus, R. C. Bohlin, A. L. Kinney, J. Koornneef, and T. Storchi-Bergmann. The Dust Content and Opacity of Actively Star-forming Galaxies. ApJ, 533:682–695, April 2000. doi: 10.1086/308692.

X. Cao. On the Dust Tori in Palomar-Green Quasars. ApJ, 619:86–92, January 2005. doi: 10.1086/425247.

M. Cappellari and E. Emsellem. Parametric Recovery of Line-of-Sight Velocity Distributions from Absorption-Line Spectra of Galaxies via Penalized Likelihood. PASP, 116:138–147, February 2004. doi: 10.1086/381875.

K. I. Caputi, G. Lagache, L. Yan, H. Dole, N. Bavouzet, E. Le Floc'h, P. I. Choi, G. Helou, and N. Reddy. The Infrared Luminosity Function of Galaxies at Redshifts z = 1 and z ˜ 2 in the GOODS Fields. ApJ, 660:97–116, May 2007. doi: 10.1086/512667.

J. A. Cardelli, G. C. Clayton, and J. S. Mathis. The relationship between infrared, optical, and ultraviolet extinction. ApJ, 345:245–256, October 1989. doi: 10.1086/167900.

C. L. Carilli, H. J. A. Roettgering, R. van Ojik, G. K. Miley, and W. J. M. van Breugel. Radio Continuum Imaging of High-Redshift Radio Galaxies. ApJS, 109:1–+, March 1997. doi: 10.1086/312973.

M. Casali, A. Adamson, C. Alves de Oliveira, O. Almaini, K. Burch, T. Chuter, J. Elliot, M. Folger, S. Foucaud, N. Hambly, M. Hastie, D. Henry, P. Hirst, M. Irwin, D. Ives, A. Lawrence, K. Laidlaw, D. Lee, J. Lewis, D. Lunney, S. McLay, D. Montgomery, A. Pickup, M. Read, N. Rees, I. Robson, K. Sekiguchi, A. Vick, S. Warren, and B. Woodward. The UKIRT wide-field camera. A&A, 467:777–784, May 2007. doi: 10.1051/0004-6361:20066514.

A. Cattaneo, S. M. Faber, J. Binney, A. Dekel, J. Kormendy, R. Mushotzky, A. Babul, P. N. Best, M. Brüggen, A. C. Fabian, C. S. Frenk, A. Khalatyan, H. Netzer, A. Mahdavi, J. Silk, M. Steinmetz, and L. Wisotzki. The role of black holes in galaxy formation and evolution. Nature, 460:213–219, July 2009. doi: 10.1038/nature08135.

A. Celotti, A. C. Fabian, and M. J. Rees. Dense thin clouds in the central regions of active galactic nuclei. MNRAS, 255:419–422, April 1992.

G. Chabrier. Galactic Stellar and Substellar Initial Mass Function. PASP, 115:763–795, July 2003. doi: 10.1086/376392.

S. C. Chapman, P. J. McCarthy, and S. E. Persson. Radio Galaxy-selected Clusters at High Redshift and Associated Extremely Red Object Overdensities. AJ, 120: 1612–1625, October 2000. doi: 10.1086/301579.

S. Charlot and S. M. Fall. A Simple Model for the Absorption of Starlight by Dust in Galaxies. ApJ, 539:718–731, August 2000. doi: 10.1086/309250.

R. Cid Fernandes, A. Mateus, L. Sodré, G. Stasińska, and J. M. Gomes. Semi-empirical analysis of Sloan Digital Sky Survey galaxies - I. Spectral synthesis method. MNRAS, 358:363–378, April 2005. doi: 10.1111/j.1365-2966.2005.08752.x.

A. Cimatti, D. Villani, L. Pozzetti, and S. di Serego Alighieri. The density of extremely red objects around high-z radio-loud active galactic nuclei. MNRAS, 318:453–461, October 2000. doi: 10.1046/j.1365-8711.2000.03736.x.

A. L. Coil, J. F. Hennawi, J. A. Newman, M. C. Cooper, and M. Davis. The DEEP2 Galaxy Redshift Survey: Clustering of Quasars and Galaxies at z = 1. ApJ, 654: 115–124, January 2007. doi: 10.1086/509099.

A. L. Coil, A. Georgakakis, J. A. Newman, M. C. Cooper, D. Croton, M. Davis, D. C. Koo, E. S. Laird, K. Nandra, B. J. Weiner, C. N. A. Willmer, and R. Yan. AEGIS: The Clustering of X-Ray Active Galactic Nucleus Relative to Galaxies at z ˜ 1. ApJ, 701:1484–1499, August 2009. doi: 10.1088/0004-637X/701/2/1484.

A. Constantin and M. S. Vogeley. The Clustering of Low-Luminosity Active Galactic Nuclei. ApJ, 650:727–748, October 2006. doi: 10.1086/507087.

M. C. Cooper, J. A. Newman, D. J. Croton, B. J. Weiner, C. N. A. Willmer, B. F. Gerke, D. S. Madgwick, S. M. Faber, M. Davis, A. L. Coil, D. P. Finkbeiner, P. Guhathakurta, and D. C. Koo. The DEEP2 Galaxy Redshift Survey: the relationship between galaxy properties and environment at z ˜ 1. MNRAS, 370: 198–212, July 2006. doi: 10.1111/j.1365-2966.2006.10485.x.

M. C. Cooper, A. L. Coil, B. F. Gerke, J. A. Newman, K. Bundy, C. J. Conselice, D. J. Croton, M. Davis, S. M. Faber, P. Guhathakurta, D. C. Koo, L. Lin, B. J. Weiner, C. N. A. Willmer, and R. Yan. Absence of evidence is not evidence of absence: the colour-density relation at fixed stellar mass persists to z ˜ 1. MNRAS, 409:337–345, November 2010. doi: 10.1111/j.1365-2966.2010.17312.x.

A. Corral, R. Della Ceca, A. Caccianiga, P. Severgnini, H. Brunner, F. J. Carrera, M. J. Page, and A. D. Schwope. The X-ray spectral properties of the AGN population in the XMM-Newton bright serendipitous survey. A&A, 530:A42, June 2011. doi: 10.1051/0004-6361/201015227.

L. L. Cowie, A. J. Barger, M. W. Bautz, W. N. Brandt, and G. P. Garmire. The Redshift Evolution of the 2-8 keV X-Ray Luminosity Function. ApJ, 584:L57–L60, February 2003. doi: 10.1086/368404.

S. Croft, J. Kurk, W. van Breugel, S. A. Stanford, W. de Vries, L. Pentericci, and H. Röttgering. The Filamentary Large-Scale Structure around the z=2.16 Radio Galaxy PKS 1138-262. AJ, 130:867–872, September 2005. doi: 10.1086/431956.

B. Czerny and K. Hryniewicz. The hypothesis of the dust origin of the Broad Line Region in Active Galactic Nuclei. *Journal of Physics Conference Series*, 372(1): 012013, July 2012. doi: 10.1088/1742-6596/372/1/012013.

E. da Cunha, S. Charlot, and D. Elbaz. A simple model to interpret the ultraviolet, optical and infrared emission from galaxies. MNRAS, 388:1595–1617, August 2008. doi: 10.1111/j.1365-2966.2008.13535.x.

R. I. Davies, F. Müller Sánchez, R. Genzel, L. J. Tacconi, E. K. S. Hicks, S. Friedrich, and A. Sternberg. A Close Look at Star Formation around Active Galactic Nuclei. ApJ, 671:1388–1412, December 2007. doi: 10.1086/523032.

M. Davis, P. Guhathakurta, N. P. Konidaris, J. A. Newman, M. L. N. Ashby, A. D. Biggs, P. Barmby, K. Bundy, S. C. Chapman, A. L. Coil, C. J. Conselice, M. C. Cooper, D. J. Croton, P. R. M. Eisenhardt, R. S. Ellis, S. M. Faber, T. Fang, G. G. Fazio, A. Georgakakis, B. F. Gerke, W. M. Goss, S. Gwyn, J. Harker, A. M. Hopkins, J.-S. Huang, R. J. Ivison, S. A. Kassin, E. N. Kirby, A. M. Koekemoer, D. C. Koo, E. S. Laird, E. Le Floc'h, L. Lin, J. M. Lotz, P. J. Marshall, D. C. Martin, A. J. Metevier, L. A. Moustakas, K. Nandra, K. G. Noeske, C. Papovich, A. C. Phillips, R. M. Rich, G. H. Rieke, D. Rigopoulou, S. Salim, D. Schiminovich, L. Simard, I. Smail, T. A. Small, B. J. Weiner, C. N. A. Willmer, S. P. Willner, G. Wilson, E. L. Wright, and R. Yan. The All-Wavelength Extended Groth Strip International Survey (AEGIS) Data Sets. ApJ, 660:L1–L6, May 2007. doi: 10.1086/517931.

C. De Breuck, W. van Breugel, H. J. A. Röttgering, and G. Miley. A sample of 669 ultra steep spectrum radio sources to find high redshift radio galaxies. A&AS, 143: 303–333, April 2000. doi: 10.1051/aas:2000181.

C. De Breuck, W. van Breugel, S. A. Stanford, H. Röttgering, G. Miley, and D. Stern. Optical and Near-Infrared Imaging of Ultra-Steep-Spectrum Radio Sources: The K-z Diagram of Radio-selected and Optically Selected Galaxies. AJ, 123:637–677, February 2002. doi: 10.1086/324632.

C. De Breuck, N. Seymour, D. Stern, S. P. Willner, P. R. M. Eisenhardt, G. G. Fazio, A. Galametz, M. Lacy, A. Rettura, B. Rocca-Volmerange, and J. Vernet. The Spitzer High-redshift Radio Galaxy Survey. ApJ, 725:36–62, December 2010. doi: 10.1088/0004-637X/725/1/36.

M. H. K. de Grijp, W. C. Keel, G. K. Miley, P. Goudfrooij, and J. Lub. Warm IRAS sources. II - Optical spectroscopy of objects from the point source catalog. A&AS, 96:389–428, December 1992.

G. de Zotti and C. M. Gaskell. Orientation effects and the reddening of the lines and continua of Seyfert galaxies. A&A, 147:1–12, June 1985.

S. di Serego Alighieri, R. A. E. Fosbury, C. N. Tadhunter, and P. J. Quinn. Polarized light in high-redshift radio galaxies. Nature, 341:307–309, September 1989. doi: 10.1038/341307a0.

M. Doherty, M. Tanaka, C. De Breuck, C. Ly, T. Kodama, J. Kurk, N. Seymour, J. Vernet, D. Stern, B. Venemans, M. Kajisawa, and I. Tanaka. Optical and near-IR spectroscopy of candidate red galaxies in two z ˜ 2.5 proto-clusters. A&A, 509:A83+, January 2010. doi: 10.1051/0004-6361/200912868.

C. Done and S. Nayakshin. Observational Signatures of X-Ray-irradiated Accretion Disks. ApJ, 546:419–428, January 2001. doi: 10.1086/318245.

C. Done, M. Gierliński, M. Sobolewska, and N. Schurch. The Origin of the Soft Excess in AGN. In L. C. Ho and J.-W. Wang, editors, *The Central Engine of Active Galactic Nuclei*, volume 373 of *Astronomical Society of the Pacific Conference Series*, page 121, October 2007.

C. Done, S. W. Davis, C. Jin, O. Blaes, and M. Ward. Intrinsic disc emission and the soft X-ray excess in active galactic nuclei. MNRAS, 420:1848–1860, March 2012. doi: 10.1111/j.1365-2966.2011.19779.x.

J. L. Donley, G. H. Rieke, P. G. Pérez-González, J. R. Rigby, and A. Alonso-Herrero. Spitzer Power-Law Active Galactic Nucleus Candidates in the Chandra Deep Field-North. ApJ, 660:167–190, May 2007. doi: 10.1086/512798.

J. L. Donley, G. H. Rieke, D. M. Alexander, E. Egami, and P. G. Pérez-González. The AGN, Star-forming, and Morphological Properties of Luminous IR-bright/optically-faint Galaxies. ApJ, 719:1393–1407, August 2010. doi: 10.1088/0004-637X/719/2/1393.

J. L. Donley, A. M. Koekemoer, M. Brusa, P. Capak, C. N. Cardamone, F. Civano, O. Ilbert, C. D. Impey, J. S. Kartaltepe, T. Miyaji, M. Salvato, D. B. Sanders, J. R. Trump, and G. Zamorani. Identifying Luminous Active Galactic Nuclei in Deep Surveys: Revised IRAC Selection Criteria. ApJ, 748:142, April 2012. doi: 10.1088/0004-637X/748/2/142.

A. G. Doroshkevich and I. D. Novikov. Mean Density of Radiation in the Metagalaxy and Certain Problems in Relativistic Cosmology. *Soviet Physics Doklady*, 9:111, August 1964.

S. P. Driver, D. T. Hill, L. S. Kelvin, A. S. G. Robotham, J. Liske, P. Norberg, I. K. Baldry, S. P. Bamford, A. M. Hopkins, J. Loveday, J. A. Peacock, E. Andrae, J. Bland-Hawthorn, S. Brough, M. J. I. Brown, E. Cameron, J. H. Y. Ching, M. Colless, C. J. Conselice, S. M. Croom, N. J. G. Cross, R. de Propris, S. Dye, M. J. Drinkwater, S. Ellis, A. W. Graham, M. W. Grootes, M. Gunawardhana, D. H. Jones, E. van Kampen, C. Maraston, R. C. Nichol, H. R. Parkinson, S. Phillipps, K. Pimbblet, C. C. Popescu, M. Prescott, I. G. Roseboom, E. M. Sadler, A. E. Sansom, R. G. Sharp, D. J. B. Smith, E. Taylor, D. Thomas, R. J. Tuffs, D. Wijesinghe, L. Dunne, C. S. Frenk, M. J. Jarvis, B. F. Madore, M. J. Meyer, M. Seibert, L. Staveley-Smith, W. J. Sutherland, and S. J. Warren. Galaxy and Mass Assembly (GAMA): survey diagnostics and core data release. MNRAS, 413: 971–995, May 2011. doi: 10.1111/j.1365-2966.2010.18188.x.

G. Drouart, C. De Breuck, J. Vernet, R. A. Laing, N. Seymour, D. Stern, M. Haas, E. A. Pier, and B. Rocca-Volmerange. Jet and Torus Orientations in High Redshift Radio Galaxies. *ArXiv e-prints*, September 2012.

J. Dunlop, M. Akiyama, D. Alexander, O. Almaini, C. Borys, R. Bouwens, M. Bremer, A. Cimatti, M. Cirasuolo, L. Clewley, C. Conselice, K. Coppin, G. Dalton, M. Damen, L. Dunne, S. Dye, S. Eales, A. Edge, E. Egami, M. Fall, D. Farrah, H. Ferguson, A. Finoguenov, S. Foucaud, M. Franx, H. Furusawa, J. Huang, E. Ibar, G. Illingworth, R. Ivison, M. Jarvis, I. Labbe, A. Lawrence, S. Maddox, R. McLure, A. Mortier, S. Oliver, M. Ouchi, M. Page, C. Papovich, R. Quadri, S. Rawlings, G. Rieke, D. Schiminovich, K. Sekiguchi, S. Serjeant, C. Simpson, I. Smail, E. Stanway, A. Taylor, M. Watson, R. Williams, T. Yamada, C. van Breukelen, and P. van Dokkum. A Spitzer Public Legacy survey of the UKIDSS Ultra Deep Survey. *Spitzer Proposal*, page 40021, May 2007.

J. S. Dunlop and J. A. Peacock. The Redshift Cut-Off in the Luminosity Function of Radio Galaxies and Quasars. MNRAS, 247:19, November 1990.

J. S. Dunlop, R. J. McLure, M. J. Kukula, S. A. Baum, C. P. O'Dea, and D. H. Hughes. Quasars, their host galaxies and their central black holes. MNRAS, 340:1095–1135, April 2003. doi: 10.1046/j.1365-8711.2003.06333.x.

S. Eales, L. Dunne, D. Clements, A. Cooray, G. de Zotti, S. Dye, R. Ivison, M. Jarvis, G. Lagache, S. Maddox, M. Negrello, S. Serjeant, M. A. Thompson, E. van Kampen, A. Amblard, P. Andreani, M. Baes, A. Beelen, G. J. Bendo, D. Benford, F. Bertoldi,

J. Bock, D. Bonfield, A. Boselli, C. Bridge, V. Buat, D. Burgarella, R. Carlberg, A. Cava, P. Chanial, S. Charlot, N. Christopher, P. Coles, L. Cortese, A. Dariush, E. da Cunha, G. Dalton, L. Danese, H. Dannerbauer, S. Driver, J. Dunlop, L. Fan, D. Farrah, D. Frayer, C. Frenk, J. Geach, J. Gardner, H. Gomez, J. González-Nuevo, E. González-Solares, M. Griffin, M. Hardcastle, E. Hatziminaoglou, D. Herranz, D. Hughes, E. Ibar, W.-S. Jeong, C. Lacey, A. Lapi, A. Lawrence, M. Lee, L. Leeuw, J. Liske, M. López-Caniego, T. Müller, K. Nandra, P. Panuzzo, A. Papageorgiou, G. Patanchon, J. Peacock, C. Pearson, S. Phillipps, M. Pohlen, C. Popescu, S. Rawlings, E. Rigby, M. Rigopoulou, A. Robotham, G. Rodighiero, A. Sansom, B. Schulz, D. Scott, D. J. B. Smith, B. Sibthorpe, I. Smail, J. Stevens, W. Sutherland, T. Takeuchi, J. Tedds, P. Temi, R. Tuffs, M. Trichas, M. Vaccari, I. Valtchanov, P. van der Werf, A. Verma, J. Vieria, C. Vlahakis, and G. J. White. The Herschel ATLAS. PASP, 122:499–515, May 2010. doi: 10.1086/653086.

J. Ebrero, F. J. Carrera, M. J. Page, J. D. Silverman, X. Barcons, M. T. Ceballos, A. Corral, R. Della Ceca, and M. G. Watson. The XMM-Newton serendipitous survey. VI. The X-ray luminosity function. A&A, 493:55–69, January 2009. doi: 10.1051/0004-6361:200810919.

D. O. Edge, J. R. Shakeshaft, W. B. McAdam, J. E. Baldwin, and S. Archer. A survey of radio sources at a frequency of 159 Mc/s. MmRAS, 68:37–60, 1959.

M. Elitzur and I. Shlosman. The AGN-obscuring Torus: The End of the "Doughnut" Paradigm? ApJ, 648:L101–L104, September 2006. doi: 10.1086/508158.

M. Elvis. Quasar Atmospheres: Toward a 'Low' Theory for Quasars. In G. T. Richards and P. B. Hall, editors, *AGN Physics with the Sloan Digital Sky Survey*, volume 311 of *Astronomical Society of the Pacific Conference Series*, page 109, June 2004.

M. Elvis, T. Maccacaro, A. S. Wilson, M. J. Ward, M. V. Penston, R. A. E. Fosbury, and G. C. Perola. Seyfert galaxies as X-ray sources. MNRAS, 183:129–157, April 1978.

M. Elvis, M. Marengo, and M. Karovska. Smoking Quasars: A New Source for Cosmic Dust. ApJ, 567:L107–L110, March 2002. doi: 10.1086/340006.

Martin Elvis, Belinda J. Wilkes, Jonathan C. McDowell, Richard F. Green, Jill Bechtold, S. P. Willner, M. S. Oey, Elisha Polomski, and Roc Cutri. Atlas of quasar energy distributions. *ApJS*, 95:1, November 1994. ISSN 0067-0049. doi: 10.1086/192093. URL `http://adsabs.harvard.edu/abs/1994ApJS...95....1E`.

R. T. Emmering, R. D. Blandford, and I. Shlosman. Magnetic acceleration of broad emission-line clouds in active galactic nuclei. ApJ, 385:460–477, February 1992. doi: 10.1086/170955.

M. Eracleous and J. P. Halpern. Doubled-peaked emission lines in active galactic nuclei. ApJS, 90:1–30, January 1994. doi: 10.1086/191856.

J. E. Everett. Radiative Transfer and Acceleration in Magnetocentrifugal Winds. ApJ, 631:689–706, October 2005. doi: 10.1086/432678.

A. C. Fabian. Observational Evidence of Active Galactic Nuclei Feedback. ARA&A, 50:455–489, September 2012. doi: 10.1146/annurev-astro-081811-125521.

A. C. Fabian, X. Barcons, O. Almaini, and K. Iwasawa. Do nuclear starbursts obscure the X-ray background? MNRAS, 297:L11, June 1998. doi: 10.1046/j.1365-8711.1998.01645.x.

J. T. Falder, J. A. Stevens, M. J. Jarvis, M. J. Hardcastle, M. Lacy, R. J. McLure, E. Hatziminaoglou, M. J. Page, and G. T. Richards. The environments of z ~ 1 active galactic nuclei at 3.6μm. MNRAS, 405:347–358, June 2010. doi: 10.1111/j.1365-2966.2010.16444.x.

B. L. Fanaroff and J. M. Riley. The morphology of extragalactic radio sources of high and low luminosity. MNRAS, 167:31P–36P, May 1974.

E. A. Fath. The Spectra of Some Spiral Nebulae and Globular Star Clusters. *Popular Astronomy*, 17:504–508, October 1909.

G. G. Fazio, J. L. Hora, L. E. Allen, M. L. N. Ashby, P. Barmby, L. K. Deutsch, J.-S. Huang, S. Kleiner, M. Marengo, S. T. Megeath, G. J. Melnick, M. A. Pahre, B. M. Patten, J. Polizotti, H. A. Smith, R. S. Taylor, Z. Wang, S. P. Willner, W. F. Hoffmann, J. L. Pipher, W. J. Forrest, C. W. McMurty, C. R. McCreight, M. E. McKelvey, R. E. McMurray, D. G. Koch, S. H. Moseley, R. G. Arendt, J. E. Mentzell, C. T. Marx, P. Losch, P. Mayman, W. Eichhorn, D. Krebs, M. Jhabvala, D. Y. Gezari, D. J. Fixsen, J. Flores, K. Shakoorzadeh, R. Jungo, C. Hakun, L. Workman, G. Karpati, R. Kichak, R. Whitley, S. Mann, E. V. Tollestrup, P. Eisenhardt, D. Stern, V. Gorjian, B. Bhattacharya, S. Carey, B. O. Nelson, W. J. Glaccum, M. Lacy, P. J. Lowrance, S. Laine, W. T. Reach, J. A. Stauffer, J. A. Surace, G. Wilson, E. L. Wright, A. Hoffman, G. Domingo, and M. Cohen. The Infrared Array Camera (IRAC) for the Spitzer Space Telescope. ApJS, 154:10–17, September 2004. doi: 10.1086/422843.

L. Ferrarese and D. Merritt. A Fundamental Relation between Supermassive Black Holes and Their Host Galaxies. ApJ, 539:L9–L12, August 2000. doi: 10.1086/312838.

J. Ferreira. MHD Disc Winds. In J. Ferreira, C. Dougados, and E. Whelan, editors, *Lecture Notes in Physics, Berlin Springer Verlag*, volume 723 of *Lecture Notes in Physics, Berlin Springer Verlag*, page 181, 2007.

S. Fine, M. J. Jarvis, and T. Mauch. Orientation effects in quasar spectra: the broad- and narrow-line regions. MNRAS, 412:213–222, March 2011. doi: 10.1111/j.1365-2966.2010.17898.x.

D. J. E. Floyd, M. J. Kukula, J. S. Dunlop, R. J. McLure, L. Miller, W. J. Percival, S. A. Baum, and C. P. O'Dea. The host galaxies of luminous quasars. MNRAS, 355: 196–220, November 2004. doi: 10.1111/j.1365-2966.2004.08315.x.

H. Furusawa, G. Kosugi, M. Akiyama, T. Takata, K. Sekiguchi, I. Tanaka, I. Iwata, M. Kajisawa, N. Yasuda, M. Doi, M. Ouchi, C. Simpson, K. Shimasaku, T. Yamada, J. Furusawa, T. Morokuma, C. M. Ishida, K. Aoki, T. Fuse, M. Imanishi, M. Iye, H. Karoji, N. Kobayashi, T. Kodama, Y. Komiyama, Y. Maeda, S. Miyazaki, Y. Mizumoto, F. Nakata, J. Noumaru, R. Ogasawara, S. Okamura, T. Saito, T. Sasaki, Y. Ueda, and M. Yoshida. The Subaru/XMM-Newton Deep Survey (SXDS). II. Optical Imaging and Photometric Catalogs. ApJS, 176:1–18, May 2008. doi: 10.1086/527321.

A. Galametz. *The Environments of AGN out to z = 2*. PhD thesis, University of Strasbourg, March 2010.

A. Galametz, C. De Breuck, J. Vernet, D. Stern, A. Rettura, C. Marmo, A. Omont, M. Allen, and N. Seymour. Large scale structures around radio galaxies at z ˜ 1.5. A&A, 507:131–145, November 2009. doi: 10.1051/0004-6361/200912177.

A. Galametz, D. Stern, S. A. Stanford, C. De Breuck, J. Vernet, R. L. Griffith, and F. A. Harrison. Spectroscopic confirmation of a galaxy cluster associated with 7C 1756+6520 at z = 1.416. A&A, 516:A101+, June 2010. doi: 10.1051/0004-6361/201014356.

P. Gandhi, H. Horst, A. Smette, S. Hönig, A. Comastri, R. Gilli, C. Vignali, and W. Duschl. Resolving the mid-infrared cores of local Seyferts. A&A, 502:457–472, August 2009. doi: 10.1051/0004-6361/200811368.

C. M. Gaskell. What broad emission lines tell us about how active galactic nuclei work. , 53:140–148, July 2009. doi: 10.1016/j.newar.2009.09.006.

C. M. Gaskell, R. W. Goosmann, R. R. J. Antonucci, and D. H. Whysong. The Nuclear Reddening Curve for Active Galactic Nuclei and the Shape of the Infrared to X-Ray Spectral Energy Distribution. ApJ, 616:147–156, November 2004. doi: 10.1086/423885.

C. M. Gaskell, E. S. Klimek, and L. S. Nazarova. NGC 5548: The AGN Energy Budget Problem and the Geometry of the Broad-Line Region and Torus. *ArXiv e-prints*, November 2007.

N. Gehrels. Confidence limits for small numbers of events in astrophysical data. ApJ, 303:336–346, April 1986. doi: 10.1086/164079.

A. Georgakakis, K. Nandra, M. C. Cooper, and AEGIS Collaboration. The Environment of X-ray AGN at z1. In J. Afonso, H. C. Ferguson, B. Mobasher, and R. Norris, editors, *Deepest Astronomical Surveys*, volume 380 of *Astronomical Society of the Pacific Conference Series*, page 157, December 2007.

G. Ghisellini, F. Haardt, and G. Matt. The Contribution of the Obscuring Torus to the X-Ray Spectrum of Seyfert Galaxies - a Test for the Unification Model. MNRAS, 267:743, April 1994.

M. Gierliński and C. Done. Is the soft excess in active galactic nuclei real? MNRAS, 349:L7–L11, March 2004. doi: 10.1111/j.1365-2966.2004.07687.x.

F. C. Gillett, W. J. Forrest, and K. M. Merrill. 8 - 13-micron spectra of NGC 7027, BD +30 3639, and NGC 6572. ApJ, 183:87–93, July 1973. doi: 10.1086/152211.

R. Gilli. The X-ray background and the deep X-ray surveys. *Advances in Space Research*, 34:2470–2477, January 2004. doi: 10.1016/j.asr.2003.03.073.

R. Gilli, M. Salvati, and G. Hasinger. Testing current synthesis models of the X-ray background. A&A, 366:407–417, February 2001. doi: 10.1051/0004-6361:20000105.

G. L. Granato, L. Silva, P. Monaco, P. Panuzzo, P. Salucci, G. De Zotti, and L. Danese. Joint formation of QSOs and spheroids: QSOs as clocks of star formation in spheroids. MNRAS, 324:757–768, June 2001. doi: 10.1046/j.1365-8711.2001.04369.x.

G. L. Granato, G. De Zotti, L. Silva, A. Bressan, and L. Danese. A Physical Model for the Coevolution of QSOs and Their Spheroidal Hosts. ApJ, 600:580–594, January 2004. doi: 10.1086/379875.

R. O. Gray and C. Corbally, J. *Stellar Spectral Classification*. 2009.

J. E. Greene and L. C. Ho. The M_{BH}-σ_* Relation in Local Active Galaxies. ApJ, 641: L21–L24, April 2006. doi: 10.1086/500507.

M. J. Griffin, A. Abergel, A. Abreu, P. A. R. Ade, P. André, J.-L. Augueres, T. Babbedge, Y. Bae, T. Baillie, J.-P. Baluteau, M. J. Barlow, G. Bendo, D. Benielli, J. J. Bock, P. Bonhomme, D. Brisbin, C. Brockley-Blatt, M. Caldwell, C. Cara, N. Castro-Rodriguez, R. Cerulli, P. Chanial, S. Chen, E. Clark, D. L. Clements, L. Clerc, J. Coker, D. Communal, L. Conversi, P. Cox, D. Crumb, C. Cunningham, F. Daly, G. R. Davis, P. de Antoni, J. Delderfield, N. Devin, A. di Giorgio, I. Didschuns, K. Dohlen, M. Donati, A. Dowell, C. D. Dowell, L. Duband, L. Dumaye, R. J. Emery, M. Ferlet, D. Ferrand, J. Fontignie, M. Fox, A. Franceschini, M. Frerking, T. Fulton, J. Garcia, R. Gastaud, W. K. Gear, J. Glenn, A. Goizel, D. K. Griffin, T. Grundy, S. Guest, L. Guillemet, P. C. Hargrave, M. Harwit, P. Hastings, E. Hatziminaoglou, M. Herman, B. Hinde, V. Hristov, M. Huang, P. Imhof, K. J. Isaak, U. Israelsson, R. J. Ivison, D. Jennings, B. Kiernan, K. J. King, A. E. Lange, W. Latter, G. Laurent, P. Laurent, S. J. Leeks, E. Lellouch, L. Levenson, B. Li, J. Li, J. Lilienthal, T. Lim, S. J. Liu, N. Lu, S. Madden, G. Mainetti, P. Marliani, D. McKay, K. Mercier, S. Molinari, H. Morris, H. Moseley, J. Mulder, M. Mur, D. A. Naylor, H. Nguyen, B. O'Halloran, S. Oliver, G. Olofsson, H.-G. Olofsson, R. Orfei, M. J. Page, I. Pain, P. Panuzzo, A. Papageorgiou, G. Parks, P. Parr-Burman, A. Pearce, C. Pearson, I. Pérez-Fournon, F. Pinsard, G. Pisano, J. Podosek, M. Pohlen, E. T. Polehampton, D. Pouliquen, D. Rigopoulou, D. Rizzo, I. G. Roseboom, H. Roussel, M. Rowan-Robinson, B. Rownd, P. Saraceno, M. Sauvage, R. Savage, G. Savini, E. Sawyer, C. Scharmberg, D. Schmitt, N. Schneider, B. Schulz, A. Schwartz, R. Shafer, D. L. Shupe, B. Sibthorpe, S. Sidher, A. Smith, A. J. Smith, D. Smith, L. Spencer, B. Stobie, R. Sudiwala, K. Sukhatme, C. Surace,

J. A. Stevens, B. M. Swinyard, M. Trichas, T. Tourette, H. Triou, S. Tseng, C. Tucker, A. Turner, M. Vaccari, I. Valtchanov, L. Vigroux, E. Virique, G. Voellmer, H. Walker, R. Ward, T. Waskett, M. Weilert, R. Wesson, G. J. White, N. Whitehouse, C. D. Wilson, B. Winter, A. L. Woodcraft, G. S. Wright, C. K. Xu, A. Zavagno, M. Zemcov, L. Zhang, and E. Zonca. The Herschel-SPIRE instrument and its in-flight performance. A&A, 518:L3, July 2010. doi: 10.1051/0004-6361/201014519.

J. A. Grimes, S. Rawlings, and C. J. Willott. Implications for unified schemes from the quasar fraction and emission-line luminosities in radio-selected samples. MNRAS, 349:503–517, April 2004. doi: 10.1111/j.1365-2966.2004.07510.x.

K. Gültekin, D. O. Richstone, K. Gebhardt, T. R. Lauer, S. Tremaine, M. C. Aller, R. Bender, A. Dressler, S. M. Faber, A. V. Filippenko, R. Green, L. C. Ho, J. Kormendy, J. Magorrian, J. Pinkney, and C. Siopis. The M-σ and M-L Relations in Galactic Bulges, and Determinations of Their Intrinsic Scatter. ApJ, 698:198–221, June 2009. doi: 10.1088/0004-637X/698/1/198.

H. Gursky, E. M. Kellogg, C. Leong, H. Tananbaum, and R. Giacconi. Detection of X-Rays from the Seyfert Galaxies NGC 1275 and NGC 4151 by the UHURU Satellite. ApJ, 165:L43, April 1971. doi: 10.1086/180713.

D. Haggard, P. J. Green, S. F. Anderson, A. Constantin, T. L. Aldcroft, D.-W. Kim, and W. A. Barkhouse. The Field X-ray AGN Fraction to z = 0.7 from the Chandra Multiwavelength Project and the Sloan Digital Sky Survey. ApJ, 723:1447–1468, November 2010. doi: 10.1088/0004-637X/723/2/1447.

P. B. Hall, M. Sawicki, P. Martini, R. A. Finn, C. J. Pritchet, P. S. Osmer, D. W. McCarthy, A. S. Evans, H. Lin, and F. D. A. Hartwick. Galaxies in the Fields of Z˜1.5 Radio-Loud Quasars. AJ, 121:1840–1862, April 2001. doi: 10.1086/319964.

P. B. Hall, D. Hutsemékers, S. F. Anderson, J. Brinkmann, X. Fan, D. P. Schneider, and D. G. York. VLT+UVES Spectroscopy of the Ca II Low-Ionization Broad Absorption Line Quasar SDSS J030000.56+004828.0. ApJ, 593:189–202, August 2003. doi: 10.1086/376409.

L. Hao, H. W. W. Spoon, G. C. Sloan, J. A. Marshall, L. Armus, A. G. G. M. Tielens, B. Sargent, I. M. van Bemmel, V. Charmandaris, D. W. Weedman, and J. R. Houck. The Detection of Silicate Emission from Quasars at 10 and 18 Microns. ApJ, 625: L75–L78, June 2005. doi: 10.1086/431227.

L. Hao, D. W. Weedman, H. W. W. Spoon, J. A. Marshall, N. A. Levenson, M. Elitzur, and J. R. Houck. The Distribution of Silicate Strength of AGNs and ULIRGs. In L. C. Ho and J.-W. Wang, editors, *The Central Engine of Active Galactic Nuclei*, volume 373 of *Astronomical Society of the Pacific Conference Series*, page 574, October 2007.

N. Häring and H.-W. Rix. On the Black Hole Mass-Bulge Mass Relation. ApJ, 604: L89–L92, April 2004. doi: 10.1086/383567.

G. Hasinger. The X-ray background and AGNs. *Nuclear Physics B Proceedings Supplements*, 132:86–96, June 2004. doi: 10.1016/j.nuclphysbps.2004.04.127.

G. Hasinger. Absorption properties and evolution of active galactic nuclei. A&A, 490: 905–922, November 2008. doi: 10.1051/0004-6361:200809839.

G. Hasinger, B. Altieri, M. Arnaud, X. Barcons, J. Bergeron, H. Brunner, M. Dadina, K. Dennerl, P. Ferrando, A. Finoguenov, R. E. Griffiths, Y. Hashimoto, F. A. Jansen, D. H. Lumb, K. O. Mason, S. Mateos, R. G. McMahon, T. Miyaji, F. Paerels, M. J. Page, A. F. Ptak, T. P. Sasseen, N. Schartel, G. P. Szokoly, J. Trümper, M. Turner, R. S. Warwick, and M. G. Watson. XMM-Newton observation of the Lockman Hole. I. The X-ray data. A&A, 365:L45–L50, January 2001. doi: 10.1051/0004-6361:20000046.

G. Hasinger, T. Miyaji, and M. Schmidt. Luminosity-dependent evolution of soft X-ray selected AGN. New Chandra and XMM-Newton surveys. A&A, 441:417–434, October 2005. doi: 10.1051/0004-6361:20042134.

C. Hazard, M. B. Mackey, and A. J. Shimmins. Investigation of the Radio Source 3C 273 By The Method of Lunar Occultations. Nature, 197:1037–1039, March 1963. doi: 10.1038/1971037a0.

T. M. Heckman, L. Blitz, A. S. Wilson, L. Armus, and G. K. Miley. A millimeter-wave survey of CO emission in Seyfert galaxies. ApJ, 342:735–758, July 1989. doi: 10.1086/167633.

T. M. Heckman, A. Ptak, A. Hornschemeier, and G. Kauffmann. The Relationship of Hard X-Ray and Optical Line Emission in Low-Redshift Active Galactic Nuclei. ApJ, 634:161–168, November 2005. doi: 10.1086/491665.

G. J. Hill, R. W. Goodrich, and D. L. Depoy. Observations of Paschen alpha in a Complete Sample of Radio Galaxies. ApJ, 462:163, May 1996. doi: 10.1086/177139.

K. D. Hiner, G. Canalizo, M. Lacy, A. Sajina, L. Armus, S. Ridgway, and L. Storrie-Lombardi. An Infrared Comparison of Type-1 and Type-2 Quasars. ApJ, 706: 508–515, November 2009. doi: 10.1088/0004-637X/706/1/508.

L. C. Ho, A. V. Filippenko, and W. L. W. Sargent. A Search for “Dwarf” Seyfert Nuclei. V. Demographics of Nuclear Activity in Nearby Galaxies. ApJ, 487:568, October 1997. doi: 10.1086/304638.

L. C. Ho, A. V. Filippenko, and W. L. W. Sargent. A Search for “Dwarf” Seyfert Nuclei. VI. Properties of Emission-Line Nuclei in Nearby Galaxies. ApJ, 583:159–177, January 2003. doi: 10.1086/345354.

D. W. Hogg, M. R. Blanton, D. J. Eisenstein, J. E. Gunn, D. J. Schlegel, I. Zehavi, N. A. Bahcall, J. Brinkmann, I. Csabai, D. P. Schneider, D. H. Weinberg, and D. G. York. The Overdensities of Galaxy Environments as a Function of Luminosity and Color. ApJ, 585:L5–L9, March 2003. doi: 10.1086/374238.

S. S. Holt, R. F. Mushotzky, E. A. Boldt, P. J. Serlemitsos, R. H. Becker, A. E. Szymkowiak, and N. E. White. X-ray spectral constraints on the broad-line cloud geometry of NGC 4151. ApJ, 241:L13–L17, October 1980. doi: 10.1086/183350.

E. P. Hubble. Extragalactic nebulae. ApJ, 64:321–369, December 1926. doi: 10.1086/143018.

B. Husemann, S. F. Sánchez, L. Wisotzki, K. Jahnke, D. Kupko, D. Nugroho, and M. Schramm. Mapping the ionised gas around the luminous QSO HE 1029-1401: evidence for minor merger events? A&A, 519:A115, September 2010. doi: 10.1051/0004-6361/201014559.

E. Ibar, R. J. Ivison, A. Cava, G. Rodighiero, S. Buttiglione, P. Temi, D. Frayer, J. Fritz, L. Leeuw, M. Baes, E. Rigby, A. Verma, S. Serjeant, T. Müller, R. Auld, A. Dariush, L. Dunne, S. Eales, S. Maddox, P. Panuzzo, E. Pascale, M. Pohlen, D. Smith, G. de Zotti, M. Vaccari, R. Hopwood, A. Cooray, D. Burgarella, and M. Jarvis. H-ATLAS: PACS imaging for the Science Demonstration Phase. MNRAS, 409:38–47, November 2010. doi: 10.1111/j.1365-2966.2010.17620.x.

A. Iovino, O. Cucciati, M. Scodeggio, C. Knobel, K. Kovač, S. Lilly, M. Bolzonella, L. A. M. Tasca, G. Zamorani, E. Zucca, K. Caputi, L. Pozzetti, P. Oesch, F. Lamareille, C. Halliday, S. Bardelli, A. Finoguenov, L. Guzzo, P. Kampczyk, C. Maier, M. Tanaka, D. Vergani, C. M. Carollo, T. Contini, J.-P. Kneib, O. Le Fèvre, V. Mainieri, A. Renzini, A. Bongiorno, G. Coppa, S. de la Torre, L. de Ravel, P. Franzetti, B. Garilli, J.-F. Le Borgne, V. Le Brun, M. Mignoli, R. Pellò, Y. Peng, E. Perez-Montero, E. Ricciardelli, J. D. Silverman, L. Tresse, U. Abbas, D. Bottini, A. Cappi, P. Cassata, A. Cimatti, A. M. Koekemoer, A. Leauthaud, D. Maccagni, C. Marinoni, H. J. McCracken, P. Memeo, B. Meneux, C. Porciani, R. Scaramella, D. Schiminovich, and N. Scoville. The zCOSMOS redshift survey: how group environment alters global downsizing trends. A&A, 509:A40, January 2010. doi: 10.1051/0004-6361/200912558.

J. C. Ives, P. W. Sanford, and M. V. Penston. The variability and absorption of the X-ray emission from NGC 4151. ApJ, 207:L159–L162, August 1976. doi: 10.1086/182203.

Ž. Ivezić, K. Menou, G. R. Knapp, M. A. Strauss, R. H. Lupton, D. E. Vanden Berk, G. T. Richards, C. Tremonti, M. A. Weinstein, S. Anderson, N. A. Bahcall, R. H. Becker, M. Bernardi, M. Blanton, D. Eisenstein, X. Fan, D. Finkbeiner, K. Finlator, J. Frieman, J. E. Gunn, P. B. Hall, R. S. J. Kim, A. Kinkhabwala, V. K. Narayanan, C. M. Rockosi, D. Schlegel, D. P. Schneider, I. Strateva, M. SubbaRao, A. R. Thakar, W. Voges, R. L. White, B. Yanny, J. Brinkmann, M. Doi, M. Fukugita, G. S. Hennessy, J. A. Munn, R. C. Nichol, and D. G. York. Optical and Radio Properties of Extragalactic Sources Observed by the FIRST Survey and the Sloan Digital Sky Survey. AJ, 124:2364–2400, November 2002. doi: 10.1086/344069.

R. J. Ivison, T. R. Greve, S. Serjeant, F. Bertoldi, E. Egami, A. M. J. Mortier, A. Alonso-Herrero, P. Barmby, L. Bei, H. Dole, C. W. Engelbracht, G. G. Fazio,

D. T. Frayer, K. D. Gordon, D. C. Hines, J.-S. Huang, E. Le Floc'h, K. A. Misselt, S. Miyazaki, J. E. Morrison, C. Papovich, P. G. Pérez-González, M. J. Rieke, G. H. Rieke, J. Rigby, D. Rigopoulou, I. Smail, G. Wilson, and S. P. Willner. Spitzer Observations of MAMBO Galaxies: Weeding Out Active Nuclei in Starbursting Protoellipticals. ApJS, 154:124–129, September 2004. doi: 10.1086/423249.

K. Iwasawa and Y. Taniguchi. The X-ray Baldwin effect. ApJ, 413:L15–L18, August 1993. doi: 10.1086/186948.

W. Jaffe, K. Meisenheimer, H. J. A. Röttgering, C. Leinert, A. Richichi, O. Chesneau, D. Fraix-Burnet, A. Glazenborg-Kluttig, G.-L. Granato, U. Graser, B. Heijligers, R. Köhler, F. Malbet, G. K. Miley, F. Paresce, J.-W. Pel, G. Perrin, F. Przygodda, M. Schoeller, H. Sol, L. B. F. M. Waters, G. Weigelt, J. Woillez, and P. T. de Zeeuw. The central dusty torus in the active nucleus of NGC 1068. Nature, 429:47–49, May 2004. doi: 10.1038/nature02531.

K. G. Jansky. Radio Waves from Outside the Solar System. Nature, 132:66, July 1933. doi: 10.1038/132066a0.

T. H. Jarrett, M. Cohen, F. Masci, E. Wright, D. Stern, D. Benford, A. Blain, S. Carey, R. M. Cutri, P. Eisenhardt, C. Lonsdale, A. Mainzer, K. Marsh, D. Padgett, S. Petty, M. Ressler, M. Skrutskie, S. Stanford, J. Surace, C. W. Tsai, S. Wheelock, and D. L. Yan. The Spitzer-WISE Survey of the Ecliptic Poles. ApJ, 735:112, July 2011. doi: 10.1088/0004-637X/735/2/112.

M. J. Jarvis, S. Rawlings, C. J. Willott, K. M. Blundell, S. Eales, and M. Lacy. On the redshift cut-off for steep-spectrum radio sources. MNRAS, 327:907–917, November 2001. doi: 10.1046/j.1365-8711.2001.04778.x.

M. J. Jarvis, D. G. Bonfield, V. A. Bruce, J. E. Geach, K. McAlpine, R. J. McLure, E. González-Solares, M. Irwin, J. Lewis, A. K. Yoldas, S. Andreon, N. J. G. Cross, J. P. Emerson, G. Dalton, J. S. Dunlop, S. T. Hodgkin, F. O. Le, M. Karouzos, K. Meisenheimer, S. Oliver, S. Rawlings, C. Simpson, I. Smail, D. J. B. Smith, M. Sullivan, W. Sutherland, S. V. White, and J. T. L. Zwart. The VISTA Deep Extragalactic Observations (VIDEO) survey. MNRAS, 428:1281–1295, January 2013. doi: 10.1093/mnras/sts118.

L. Jiang, X. Fan, Ž. Ivezić, G. T. Richards, D. P. Schneider, M. A. Strauss, and B. C. Kelly. The Radio-Loud Fraction of Quasars is a Strong Function of Redshift and Optical Luminosity. ApJ, 656:680–690, February 2007. doi: 10.1086/510831.

H. L. Johnson. The Brightness of 3c 273 AT 2.2 μ. ApJ, 139:1022, April 1964. doi: 10.1086/147842.

R. A. Johnson, A. Lawrence, R. Terlevich, and D. Carter. A High-Excitation HII Region in the faint dwarf elliptical galaxy A0951+68. MNRAS, 287:333–340, May 1997.

S. Juneau, M. Dickinson, D. M. Alexander, and S. Salim. A New Diagnostic of Active Galactic Nuclei: Revealing Highly Absorbed Systems at Redshift ¿ 0.3. ApJ, 736: 104, August 2011. doi: 10.1088/0004-637X/736/2/104.

M. Kajisawa, T. Kodama, I. Tanaka, T. Yamada, and R. Bower. Protoclusters with evolved populations around radio galaxies at z ˜ 2.5. MNRAS, 371:577–582, September 2006. doi: 10.1111/j.1365-2966.2006.10704.x.

G. Kauffmann, T. M. Heckman, C. Tremonti, J. Brinchmann, S. Charlot, S. D. M. White, S. E. Ridgway, J. Brinkmann, M. Fukugita, P. B. Hall, Ž. Ivezić, G. T. Richards, and D. P. Schneider. The host galaxies of active galactic nuclei. MNRAS, 346:1055–1077, December 2003. doi: 10.1111/j.1365-2966.2003.07154.x.

G. Kauffmann, S. D. M. White, T. M. Heckman, B. Ménard, J. Brinchmann, S. Charlot, C. Tremonti, and J. Brinkmann. The environmental dependence of the relations between stellar mass, structure, star formation and nuclear activity in galaxies. MNRAS, 353:713–731, September 2004. doi: 10.1111/j.1365-2966.2004.08117.x.

W. C. Keel. Inclination effects on the recognition of Seyfert galaxies. AJ, 85:198–203, March 1980. doi: 10.1086/112662.

K. I. Kellermann, R. Sramek, M. Schmidt, D. B. Shaffer, and R. Green. VLA observations of objects in the Palomar Bright Quasar Survey. AJ, 98:1195–1207, October 1989. doi: 10.1086/115207.

R. C. Kennicutt, Jr. Star Formation in Galaxies Along the Hubble Sequence. ARA&A, 36:189–232, 1998. doi: 10.1146/annurev.astro.36.1.189.

L. J. Kewley, B. Groves, G. Kauffmann, and T. Heckman. The host galaxies and classification of active galactic nuclei. MNRAS, 372:961–976, November 2006. doi: 10.1111/j.1365-2966.2006.10859.x.

É. Y. Khachikyan and D. W. Weedman. A spectroscopic study of luminous galactic nuclei. *Astrophysics*, 7:231–240, July 1971. doi: 10.1007/BF01001021.

O. Klein and T. Nishina. ber die streuung von strahlung durch freie elektronen nach der neuen relativistischen quantendynamik von dirac. *Zeitschrift fr Physik*, 52:853–868, 1929. ISSN 0044-3328. doi: 10.1007/BF01366453.

G. P. Knopp and K. C. Chambers. Deep Imaging of the Field of the High-Redshift Radio Source 4C 23.56. ApJS, 109:367–+, April 1997. doi: 10.1086/312981.

W. Kollatschny and M. Zetzl. Accretion disk wind as explanation for the broad-line region structure in NGC 5548. A&A, 551:L6, March 2013. doi: 10.1051/0004-6361/201220923.

A. Koratkar and O. Blaes. The Ultraviolet and Optical Continuum Emission in Active Galactic Nuclei: The Status of Accretion Disks. PASP, 111:1–30, January 1999. doi: 10.1086/316294.

K. Korista, G. Ferland, and J. Baldwin. Do the Broad Emission Line Clouds See the Same Continuum That We See? ApJ, 487:555, October 1997. doi: 10.1086/304659.

S. Kozłowski, C. S. Kochanek, D. Stern, M. L. N. Ashby, R. J. Assef, J. J. Bock, C. Borys, K. Brand, M. Brodwin, M. J. I. Brown, R. Cool, A. Cooray, S. Croft, A. Dey, P. R. Eisenhardt, A. Gonzalez, V. Gorjian, R. Griffith, N. Grogin, R. Ivison, J. Jacob, B. T. Jannuzi, A. Mainzer, L. Moustakas, H. Röttgering, N. Seymour, H. A. Smith, S. A. Stanford, J. R. Stauffer, I. S. Sullivan, W. van Breugel, S. P. Willner, and E. L. Wright. Mid-infrared Variability from the Spitzer Deep Wide-field Survey. ApJ, 716:530–543, June 2010. doi: 10.1088/0004-637X/716/1/530.

J. H. Krolik. *Active galactic nuclei : from the central black hole to the galactic environment*. 1999.

J. H. Krolik. AGN Obscuring Tori Supported by Infrared Radiation Pressure. ApJ, 661:52–59, May 2007. doi: 10.1086/515432.

J. H. Krolik and M. C. Begelman. Molecular tori in Seyfert galaxies - Feeding the monster and hiding it. ApJ, 329:702–711, June 1988. doi: 10.1086/166414.

J. H. Krolik and T. R. Kallman. Fe K features as probes of the nuclear reflection region in Seyfert galaxies. ApJ, 320:L5–L8, September 1987. doi: 10.1086/184966.

J. H. Krolik, P. Madau, and P. T. Zycki. X-ray bumps, iron K-alpha lines, and X-ray suppression by obscuring tori in Seyfert galaxies. ApJ, 420:L57–L61, January 1994. doi: 10.1086/187162.

E. Kuiper, N. A. Hatch, H. J. A. Röttgering, G. K. Miley, R. A. Overzier, B. P. Venemans, C. De Breuck, S. Croft, M. Kajisawa, T. Kodama, J. D. Kurk, L. Pentericci, S. A. Stanford, I. Tanaka, and A. W. Zirm. A galaxy populations study of a radio-selected protocluster at z ˜ 3.1. MNRAS, 405:969–986, June 2010. doi: 10.1111/j.1365-2966.2010.16537.x.

E. Kuiper, N. A. Hatch, B. P. Venemans, G. K. Miley, H. J. A. Röttgering, J. D. Kurk, R. A. Overzier, L. Pentericci, J. Bland-Hawthorn, and J. Cepa. Discovery of a high-z protocluster with tunable filters: the case of 6C0140+326 at z= 4.4. MNRAS, pages 1376–+, September 2011. doi: 10.1111/j.1365-2966.2011.19324.x.

E Kuiper, BP Venemans, NA Hatch, GK Miley, and HJA Röttgering. A z 3 radio galaxy and its protocluster: evidence for a superstructure? *Monthly Notices of the Royal Astronomical Society*, 425(2):801–813, 2012.

J. D. Kurk, L. Pentericci, R. A. Overzier, H. J. A. Röttgering, and G. K. Miley. A search for clusters at high redshift. IV. Spectroscopy of Hα emitters in a proto-cluster at z = 2.16. A&A, 428:817–821, December 2004a. doi: 10.1051/0004-6361:20041819.

J. D. Kurk, L. Pentericci, H. J. A. Röttgering, and G. K. Miley. A search for clusters at high redshift. III. Candidate Hα emitters and EROs in the PKS 1138-262 proto-cluster at z = 2.16. A&A, 428:793–815, December 2004b. doi: 10.1051/0004-6361:20040075.

M. Lacy. HST Imaging of Two z ¿ 4 Radio Galaxies. In A. J. Bunker & W. J. M. van Breugel, editor, *The Hy-Redshift Universe: Galaxy Formation and Evolution at High Redshift*, volume 193 of *Astronomical Society of the Pacific Conference Series*, pages 94–+, 1999.

M. Lacy, L. J. Storrie-Lombardi, A. Sajina, P. N. Appleton, L. Armus, S. C. Chapman, P. I. Choi, D. Fadda, F. Fang, D. T. Frayer, I. Heinrichsen, G. Helou, M. Im, F. R. Marleau, F. Masci, D. L. Shupe, B. T. Soifer, J. Surace, H. I. Teplitz, G. Wilson, and L. Yan. Obscured and Unobscured Active Galactic Nuclei in the Spitzer Space Telescope First Look Survey. ApJS, 154:166–169, September 2004. doi: 10.1086/422816.

M. Lacy, A. O. Petric, A. Sajina, G. Canalizo, L. J. Storrie-Lombardi, L. Armus, D. Fadda, and F. R. Marleau. Optical Spectroscopy and X-Ray Detections of a Sample of Quasars and Active Galactic Nuclei Selected in the Mid-Infrared from Two Spitzer Space Telescope Wide-Area Surveys. AJ, 133:186–205, January 2007. doi: 10.1086/509617.

F. Lamareille. Spectral classification of emission-line galaxies from the Sloan Digital Sky Survey. I. An improved classification for high-redshift galaxies. A&A, 509:A53, January 2010. doi: 10.1051/0004-6361/200913168.

F. Lamareille, M. Mouhcine, T. Contini, I. Lewis, and S. Maddox. The luminosity-metallicity relation in the local Universe from the 2dF Galaxy Redshift Survey. MNRAS, 350:396–406, May 2004. doi: 10.1111/j.1365-2966.2004.07697.x.

S. M. LaMassa, T. M. Heckman, A. Ptak, L. Martins, V. Wild, and P. Sonnentrucker. Indicators of Intrinsic Active Galactic Nucleus Luminosity: A Multi-wavelength Approach. ApJ, 720:786–810, September 2010. doi: 10.1088/0004-637X/720/1/786.

S. M. LaMassa, T. M. Heckman, A. Ptak, L. Martins, V. Wild, P. Sonnentrucker, and A. Hornschemeier. Uncovering Obscured Active Galactic Nuclei in Homogeneously Selected Samples of Seyfert 2 Galaxies. ApJ, 729:52, March 2011. doi: 10.1088/0004-637X/729/1/52.

A. Lamastra, S. Bianchi, G. Matt, G. C. Perola, X. Barcons, and F. J. Carrera. The bolometric luminosity of type 2 AGN from extinction-corrected [OIII]. No evidence of Eddington-limited sources. A&A, 504:73–79, September 2009. doi: 10.1051/0004-6361/200912023.

G. Lanzuisi, E. Piconcelli, F. Fiore, C. Feruglio, C. Vignali, M. Salvato, and C. Gruppioni. Revealing X-ray obscured quasars in SWIRE sources with extreme mid-IR/optical flux ratios. A&A, 498:67–81, April 2009. doi: 10.1051/0004-6361/200811282.

A. Laor. On the Nature of Low-Luminosity Narrow-Line Active Galactic Nuclei. ApJ, 590:86–94, June 2003. doi: 10.1086/375008.

A. Lawrence. The relative frequency of broad-lined and narrow-lined active galactic nuclei - Implications for unified schemes. MNRAS, 252:586–592, October 1991.

A. Lawrence. Warped discs and the Unified Scheme. In V. Karas and G. Matt, editors, *IAU Symposium*, volume 238 of *IAU Symposium*, pages 117–122, April 2007. doi: 10.1017/S1743921307004814.

A. Lawrence. The UV peak in active galactic nuclei: a false continuum from blurred reflection? MNRAS, 423:451–463, June 2012. doi: 10.1111/j.1365-2966.2012.20889.x.

A. Lawrence and M. Elvis. Obscuration and the various kinds of Seyfert galaxies. ApJ, 256:410–426, May 1982. doi: 10.1086/159918.

A. Lawrence and M. Elvis. Misaligned Disks as Obscurers in Active Galaxies. ApJ, 714:561–570, May 2010. doi: 10.1088/0004-637X/714/1/561.

A. Lawrence, S. J. Warren, O. Almaini, A. C. Edge, N. C. Hambly, R. F. Jameson, P. Lucas, M. Casali, A. Adamson, S. Dye, J. P. Emerson, S. Foucaud, P. Hewett, P. Hirst, S. T. Hodgkin, M. J. Irwin, N. Lodieu, R. G. McMahon, C. Simpson, I. Smail, D. Mortlock, and M. Folger. The UKIRT Infrared Deep Sky Survey (UKIDSS). MNRAS, 379:1599–1617, August 2007. doi: 10.1111/j.1365-2966.2007.12040.x.

O. Le Fevre, J. M. Deltorn, D. Crampton, and M. Dickinson. Clustering around the Radio Galaxy MRC 0316-257 at Z = 3.14. ApJ, 471:L11, November 1996. doi: 10.1086/310319.

J. C. Lee, H. S. Hwang, M. G. Lee, M. Kim, and S. C. Kim. Optical spectral classification of southern ultraluminous infrared galaxies. MNRAS, 414:702–712, June 2011. doi: 10.1111/j.1365-2966.2011.18437.x.

N. A. Levenson, M. M. Sirocky, L. Hao, H. W. W. Spoon, J. A. Marshall, M. Elitzur, and J. R. Houck. Deep Mid-Infrared Silicate Absorption as a Diagnostic of Obscuring Geometry toward Galactic Nuclei. ApJ, 654:L45–L48, January 2007. doi: 10.1086/510778.

A. Li. Dust in Active Galactic Nuclei. *ArXiv e-prints*, August 2008.

S. J. Lilly, O. Le Fevre, F. Hammer, and D. Crampton. The Canada-France Redshift Survey: The Luminosity Density and Star Formation History of the Universe to Z approximately 1. ApJ, 460:L1, March 1996. doi: 10.1086/309975.

Y. Liu and S. N. Zhang. Dusty Torus Formation by Anisotropic Radiative Pressure Feedback of Active Galactic Nuclei. ApJ, 728:L44, February 2011. doi: 10.1088/2041-8205/728/2/L44.

M. S. Longair. *High energy astrophysics. Volume 2. Stars, the Galaxy and the interstellar medium.* 1994.

C. J. Lonsdale, H. E. Smith, M. Rowan-Robinson, J. Surace, D. Shupe, C. Xu, S. Oliver, D. Padgett, F. Fang, T. Conrow, A. Franceschini, N. Gautier, M. Griffin, P. Hacking, F. Masci, G. Morrison, J. O'Linger, F. Owen, I. Pérez-Fournon, M. Pierre, R. Puetter, G. Stacey, S. Castro, M. d. C. Polletta, D. Farrah, T. Jarrett, D. Frayer, B. Siana, T. Babbedge, S. Dye, M. Fox, E. Gonzalez-Solares, M. Salaman, S. Berta, J. J. Condon, H. Dole, and S. Serjeant. SWIRE: The SIRTF Wide-Area Infrared Extragalactic Survey. PASP, 115:897–927, August 2003. doi: 10.1086/376850.

Y. Lu, T.-G. Wang, X.-B. Dong, and H.-Y. Zhou. Type 1 active galactic nucleus fraction in the SDSS/FIRST survey. MNRAS, 404:1761–1774, June 2010. doi: 10.1111/j.1365-2966.2010.16434.x.

B. Luo, W. N. Brandt, Y. Q. Xue, D. M. Alexander, M. Brusa, F. E. Bauer, A. Comastri, A. C. Fabian, R. Gilli, B. D. Lehmer, D. A. Rafferty, D. P. Schneider, and C. Vignali. Revealing a Population of Heavily Obscured Active Galactic Nuclei at z $\sim 0.5 - 1$ in the Chandra Deep Field-South. ApJ, 740:37, October 2011. doi: 10.1088/0004-637X/740/1/37.

D. Lynden-Bell. Galactic Nuclei as Collapsed Old Quasars. Nature, 223:690–694, August 1969. doi: 10.1038/223690a0.

D. Lynden-Bell. Note on N Galaxies and mini-quasars. MNRAS, 155:119, 1971.

J. T. Macklin. An investigation of the properties of double radio sources using the Spearman partial rank correlation coefficient. MNRAS, 199:1119–1136, June 1982.

P. Madau, H. C. Ferguson, M. E. Dickinson, M. Giavalisco, C. C. Steidel, and A. Fruchter. High-redshift galaxies in the Hubble Deep Field: colour selection and star formation history to z˜4. MNRAS, 283:1388–1404, December 1996.

S. C. Madden, F. Galliano, A. P. Jones, and M. Sauvage. ISM properties in low-metallicity environments. A&A, 446:877–896, February 2006. doi: 10.1051/0004-6361:20053890.

J. Magorrian, S. Tremaine, D. Richstone, R. Bender, G. Bower, A. Dressler, S. M. Faber, K. Gebhardt, R. Green, C. Grillmair, J. Kormendy, and T. Lauer. The Demography of Massive Dark Objects in Galaxy Centers. AJ, 115:2285–2305, June 1998. doi: 10.1086/300353.

R. Maiolino and G. H. Rieke. Low-Luminosity and Obscured Seyfert Nuclei in Nearby Galaxies. ApJ, 454:95, November 1995. doi: 10.1086/176468.

R. Maiolino, G. Risaliti, M. Salvati, P. Pietrini, G. Torricelli-Ciamponi, M. Elvis, G. Fabbiano, V. Braito, and J. Reeves. "Comets" orbiting a black hole. A&A, 517:A47, July 2010. doi: 10.1051/0004-6361/200913985.

E. Maiorano, N. Masetti, E. Palazzi, S. Savaglio, E. Rol, P. M. Vreeswijk, E. Pian, P. A. Price, B. A. Peterson, M. Jelínek, L. Amati, M. I. Andersen, A. J. Castro-Tirado, J. M. Castro Cerón, A. de Ugarte Postigo, F. Frontera, A. S. Fruchter, J. P. U.

Fynbo, J. Gorosabel, A. A. Henden, J. Hjorth, B. L. Jensen, S. Klose, C. Kouveliotou, G. Masi, P. Møller, L. Nicastro, E. O. Ofek, S. B. Pandey, J. Rhoads, N. R. Tanvir, R. A. M. J. Wijers, and E. P. J. van den Heuvel. Physics of the GRB 030328 afterglow and its environment. A&A, 455:423–431, August 2006. doi: 10.1051/0004-6361:20054728.

D. Makovoz and I. Khan. Mosaicking with MOPEX. In P. Shopbell, M. Britton, and R. Ebert, editors, *Astronomical Data Analysis Software and Systems XIV*, volume 347 of *Astronomical Society of the Pacific Conference Series*, pages 81–+, December 2005.

M. A. Malkan, V. Gorjian, and R. Tam. A Hubble Space Telescope Imaging Survey of Nearby Active Galactic Nuclei. ApJS, 117:25, July 1998. doi: 10.1086/313110.

S. P. Maran. *The astronomy and astrophysics encyclopedia.* 1992.

O. Marco and K. J. Brooks. VLT 3-5 micron spectroscopy and imaging of NGC 1068: Does the AGN hide nuclear starburst activity? A&A, 398:101–106, January 2003. doi: 10.1051/0004-6361:20021619.

J. Marocco, E. Hache, and F. Lamareille. Spectral classification of emission-line galaxies from the Sloan Digital Sky Survey. II. A supplementary diagnostic for AGNs using the $D_n(4000)$ index. A&A, 531:A71, July 2011. doi: 10.1051/0004-6361/201016143.

F. Maschietto, N. A. Hatch, B. P. Venemans, H. J. A. Röttgering, G. K. Miley, R. A. Overzier, M. A. Dopita, P. R. Eisenhardt, J. D. Kurk, G. R. Meurer, L. Pentericci, P. Rosati, S. A. Stanford, W. van Breugel, and A. W. Zirm. [OIII] emitters in the field of the MRC0316-257 protocluster. MNRAS, 389:1223–1232, September 2008. doi: 10.1111/j.1365-2966.2008.13571.x.

R. Mason, G. Wright, A. Adamson, and Y. Pendleton. Nuclear Dust in the Seyfert II Galaxy, NGC1068. In *American Astronomical Society Meeting Abstracts*, volume 35 of *Bulletin of the American Astronomical Society*, page 1298, December 2003.

A. Mateus, L. Sodré, R. Cid Fernandes, G. Stasińska, W. Schoenell, and J. M. Gomes. Semi-empirical analysis of Sloan Digital Sky Survey galaxies - II. The bimodality of the galaxy population revisited. MNRAS, 370:721–737, August 2006. doi: 10.1111/j.1365-2966.2006.10565.x.

J. C. Mather, E. S. Cheng, R. E. Eplee, Jr., R. B. Isaacman, S. S. Meyer, R. A. Shafer, R. Weiss, E. L. Wright, C. L. Bennett, N. W. Boggess, E. Dwek, S. Gulkis, M. G. Hauser, M. Janssen, T. Kelsall, P. M. Lubin, S. H. Moseley, Jr., T. L. Murdock, R. F. Silverberg, G. F. Smoot, and D. T. Wilkinson. A preliminary measurement of the cosmic microwave background spectrum by the Cosmic Background Explorer (COBE) satellite. ApJ, 354:L37–L40, May 1990. doi: 10.1086/185717.

J. S. Mathis, W. Rumpl, and K. H. Nordsieck. The size distribution of interstellar grains. ApJ, 217:425–433, October 1977. doi: 10.1086/155591.

Y. Matsuda, T. Yamada, T. Hayashino, H. Tamura, R. Yamauchi, T. Murayama, T. Nagao, K. Ohta, S. Okamura, M. Ouchi, K. Shimasaku, Y. Shioya, and Y. Taniguchi. Large-Scale Filamentary Structure around the Protocluster at Redshift z = 3.1. ApJ, 634:L125–L128, December 2005. doi: 10.1086/499071.

M. Matsuoka, L. Piro, M. Yamauchi, and T. Murakami. X-ray spectral variability and complex absorption in the Seyfert 1 galaxies NGC 4051 and MCG -6-30-15. ApJ, 361:440–458, October 1990. doi: 10.1086/169209.

G. Matt. Obscured active galactic nuclei: the hidden side of the X-ray Universe. *Royal Society of London Philosophical Transactions Series A*, 360:2045, September 2002. doi: 10.1098/rsta.2002.1052.

T. A. Matthews and A. R. Sandage. Optical Identification of 3c 48, 3c 196, and 3c 286 with Stellar Objects. ApJ, 138:30, July 1963. doi: 10.1086/147615.

T. A. Matthews, W. W. Morgan, and M. Schmidt. A Discussion of Galaxies Indentified with Radio Sources. ApJ, 140:35, July 1964. doi: 10.1086/147890.

I. McHardy, A. Lawson, A. Newsam, A. P. Marscher, A. S. Sokolov, C. M. Urry, and A. E. Wehrle. Simultaneous X-ray and infrared variability in the quasar 3C273 - II. Confirmation of the correlation and X-ray lag. MNRAS, 375:1521–1527, March 2007. doi: 10.1111/j.1365-2966.2006.11420.x.

K. K. McLeod and G. H. Rieke. Near-infrared imaging of low-redshift quasar host galaxies. ApJ, 420:58–67, January 1994. doi: 10.1086/173542.

R. J. McLure and J. S. Dunlop. On the black hole-bulge mass relation in active and inactive galaxies. MNRAS, 331:795–804, April 2002. doi: 10.1046/j.1365-8711.2002.05236.x.

R. J. McLure and J. S. Dunlop. The cosmological evolution of quasar black hole masses. MNRAS, 352:1390–1404, August 2004. doi: 10.1111/j.1365-2966.2004.08034.x.

R. J. McLure, M. J. Jarvis, T. A. Targett, J. S. Dunlop, and P. N. Best. On the evolution of the black hole: spheroid mass ratio. MNRAS, 368:1395–1403, May 2006. doi: 10.1111/j.1365-2966.2006.10228.x.

M. Meléndez, S. B. Kraemer, H. R. Schmitt, D. M. Crenshaw, R. P. Deo, R. F. Mushotzky, and F. C. Bruhweiler. Constraining the Active Galactic Nucleus Contribution in a Multiwavelength Study of Seyfert Galaxies. ApJ, 689:95–107, December 2008. doi: 10.1086/592724.

G. Miley and C. De Breuck. Distant radio galaxies and their environments. A&A Rev., 15:67–144, February 2008. doi: 10.1007/s00159-007-0008-z.

G. K. Miley, R. A. Overzier, Z. I. Tsvetanov, R. J. Bouwens, N. Benítez, J. P. Blakeslee, H. C. Ford, G. D. Illingworth, M. Postman, P. Rosati, M. Clampin, G. F. Hartig, A. W. Zirm, H. J. A. Röttgering, B. P. Venemans, D. R. Ardila, F. Bartko, T. J.

Broadhurst, R. A. Brown, C. J. Burrows, E. S. Cheng, N. J. G. Cross, C. De Breuck, P. D. Feldman, M. Franx, D. A. Golimowski, C. Gronwall, L. Infante, A. R. Martel, F. Menanteau, G. R. Meurer, M. Sirianni, R. A. Kimble, J. E. Krist, W. B. Sparks, H. D. Tran, R. L. White, and W. Zheng. A large population of 'Lyman-break' galaxies in a protocluster at redshift z ˜ 4.1. Nature, 427:47–50, January 2004.

C. J. Miller, R. C. Nichol, P. L. Gómez, A. M. Hopkins, and M. Bernardi. The Environment of Active Galactic Nuclei in the Sloan Digital Sky Survey. ApJ, 597: 142–156, November 2003. doi: 10.1086/378383.

S. Miyazaki, Y. Komiyama, M. Sekiguchi, S. Okamura, M. Doi, H. Furusawa, M. Hamabe, K. Imi, M. Kimura, F. Nakata, N. Okada, M. Ouchi, K. Shimasaku, M. Yagi, and N. Yasuda. Subaru Prime Focus Camera – Suprime-Cam. PASJ, 54: 833–853, December 2002.

A. D. Montero-Dorta, D. J. Croton, R. Yan, M. C. Cooper, J. A. Newman, A. Georgakakis, F. Prada, M. Davis, K. Nandra, and A. Coil. The DEEP2 Galaxy Redshift Survey: the red sequence AGN fraction and its environment and redshift dependence. MNRAS, 392:125–134, January 2009. doi: 10.1111/j.1365-2966.2008.13893.x.

R. Morrison and D. McCammon. Interstellar photoelectric absorption cross sections, 0.03-10 keV. ApJ, 270:119–122, July 1983. doi: 10.1086/161102.

J. S. Mulchaey, A. Koratkar, M. J. Ward, A. S. Wilson, M. Whittle, R. R. J. Antonucci, A. L. Kinney, and T. Hurt. Multiwavelength tests of the dusty torus model for Seyfert galaxies. ApJ, 436:586–598, December 1994. doi: 10.1086/174933.

K. D. Murphy and T. Yaqoob. An X-ray spectral model for Compton-thick toroidal reprocessors. MNRAS, 397:1549–1562, August 2009. doi: 10.1111/j.1365-2966.2009.15025.x.

K. Nandra and I. M. George. X-Ray Reprocessing by Cold Clouds in Active Galactic Nuclei. MNRAS, 267:974, April 1994.

K. Nandra and K. A. Pounds. GINGA Observations of the X-Ray Spectra of Seyfert Galaxies. MNRAS, 268:405, May 1994.

K. Nandra, E. S. Laird, and C. C. Steidel. The space density of moderate-luminosity active galaxies at z= 3. MNRAS, 360:L39–L44, June 2005. doi: 10.1111/j.1745-3933.2005.00042.x.

S. Nayakshin. Warped accretion discs and the unification of active galactic nuclei. MNRAS, 359:545–550, May 2005. doi: 10.1111/j.1365-2966.2005.08913.x.

M. Nenkova, M. M. Sirocky, R. Nikutta, Ž. Ivezić, and M. Elitzur. AGN Dusty Tori. II. Observational Implications of Clumpiness. ApJ, 685:160–180, September 2008. doi: 10.1086/590483.

H. Netzer. Accretion and star formation rates in low-redshift type II active galactic nuclei. MNRAS, 399:1907–1920, November 2009. doi: 10.1111/j.1365-2966.2009.15434.x.

H. Netzer and B. M. Peterson. Reverberation Mapping and the Physics of Active Galactic Nuclei. In D. Maoz, A. Sternberg, and E. M. Leibowitz, editors, *Astronomical Time Series*, volume 218 of *Astrophysics and Space Science Library*, page 85, 1997.

M. Nikołajuk, B. Czerny, and J. Ziółkowski. Geometry of the Broad Line Region in AGN. In T. Bulik, B. Rudak, and G. Madejski, editors, *Astrophysical Sources of High Energy Particles and Radiation*, volume 801 of *American Institute of Physics Conference Series*, pages 220–223, November 2005. doi: 10.1063/1.2141869.

K. Noguchi, Y. Terashima, Y. Ishino, Y. Hashimoto, M. Koss, Y. Ueda, and H. Awaki. Scattered X-rays in Obscured Active Galactic Nuclei and Their Implications for Geometrical Structure and Evolution. ApJ, 711:144–156, March 2010. doi: 10.1088/0004-637X/711/1/144.

P. Ogle, D. Whysong, and R. Antonucci. Spitzer Reveals Hidden Quasar Nuclei in Some Powerful FR II Radio Galaxies. ApJ, 647:161–171, August 2006. doi: 10.1086/505337.

J. B. Oke. The Optical Spectrum of 3c 273. ApJ, 141:6, January 1965. doi: 10.1086/148086.

S. J. Oliver, J. Bock, B. Altieri, A. Amblard, V. Arumugam, H. Aussel, T. Babbedge, A. Beelen, M. Béthermin, A. Blain, A. Boselli, C. Bridge, D. Brisbin, V. Buat, D. Burgarella, N. Castro-Rodríguez, A. Cava, P. Chanial, M. Cirasuolo, D. L. Clements, A. Conley, L. Conversi, A. Cooray, C. D. Dowell, E. N. Dubois, E. Dwek, S. Dye, S. Eales, D. Elbaz, D. Farrah, A. Feltre, P. Ferrero, N. Fiolet, M. Fox, A. Franceschini, W. Gear, E. Giovannoli, J. Glenn, Y. Gong, E. A. González Solares, M. Griffin, M. Halpern, M. Harwit, E. Hatziminaoglou, S. Heinis, P. Hurley, H. S. Hwang, A. Hyde, E. Ibar, O. Ilbert, K. Isaak, R. J. Ivison, G. Lagache, E. Le Floc'h, L. Levenson, B. L. Faro, N. Lu, S. Madden, B. Maffei, G. Magdis, G. Mainetti, L. Marchetti, G. Marsden, J. Marshall, A. M. J. Mortier, H. T. Nguyen, B. O'Halloran, A. Omont, M. J. Page, P. Panuzzo, A. Papageorgiou, H. Patel, C. P. Pearson, I. Pérez-Fournon, M. Pohlen, J. I. Rawlings, G. Raymond, D. Rigopoulou, L. Riguccini, D. Rizzo, G. Rodighiero, I. G. Roseboom, M. Rowan-Robinson, M. Sánchez Portal, B. Schulz, D. Scott, N. Seymour, D. L. Shupe, A. J. Smith, J. A. Stevens, M. Symeonidis, M. Trichas, K. E. Tugwell, M. Vaccari, I. Valtchanov, J. D. Vieira, M. Viero, L. Vigroux, L. Wang, R. Ward, J. Wardlow, G. Wright, C. K. Xu, and M. Zemcov. The Herschel Multi-tiered Extragalactic Survey: HerMES. MNRAS, 424:1614–1635, August 2012. doi: 10.1111/j.1365-2966.2012.20912.x.

D. E. Osterbrock and G. J. Ferland. *Astrophysics of gaseous nebulae and active galactic nuclei*. 2006.

R. A. Overzier, R. J. Bouwens, N. J. G. Cross, B. P. Venemans, G. K. Miley, A. W. Zirm, N. Benítez, J. P. Blakeslee, D. Coe, R. Demarco, H. C. Ford, N. L. Homeier, G. D. Illingworth, J. D. Kurk, A. R. Martel, S. Mei, I. Oliveira, H. J. A. Röttgering, Z. I. Tsvetanov, and W. Zheng. Lyman Break Galaxies, Lyα Emitters, and a Radio Galaxy in a Protocluster at z = 4.1. ApJ, 673:143–162, January 2008. doi: 10.1086/524342.

F. N. Owen and R. A. White. Surface photometry of radio galaxies. II - Cluster sources. MNRAS, 249:164–171, March 1991.

A. G. Pacholczyk and W. Z. Wisniewski. Infrared Radiation from the Seyfert Galaxy NGC 1068. ApJ, 147:394, January 1967. doi: 10.1086/149020.

K. L. Page, J. N. Reeves, P. T. O'Brien, and M. J. L. Turner. XMM-Newton spectroscopy of high-redshift quasars. MNRAS, 364:195–207, November 2005. doi: 10.1111/j.1365-2966.2005.09550.x.

C. Papovich. The Angular Clustering of Distant Galaxy Clusters. ApJ, 676:206–217, March 2008. doi: 10.1086/527665.

E. Pascale, R. Auld, A. Dariush, L. Dunne, S. Eales, S. Maddox, P. Panuzzo, M. Pohlen, D. J. B. Smith, S. Buttiglione, A. Cava, D. L. Clements, A. Cooray, S. Dye, G. de Zotti, J. Fritz, R. Hopwood, E. Ibar, R. J. Ivison, M. J. Jarvis, L. Leeuw, M. López-Caniego, E. Rigby, G. Rodighiero, D. Scott, M. W. L. Smith, P. Temi, M. Vaccari, and I. Valtchanov. The first release of data from the Herschel ATLAS: the SPIRE images. MNRAS, 415:911–917, July 2011. doi: 10.1111/j.1365-2966.2011.18756.x.

S. M. Pascarelle, R. A. Windhorst, W. C. Keel, and S. C. Odewahn. Sub-galactic clumps at a redshift of 2.39 and implications for galaxy formation. Nature, 383: 45–50, September 1996. doi: 10.1038/383045a0.

H. Patel, D. L. Clements, M. Vaccari, D. J. Mortlock, M. Rowan-Robinson, I. Pérez-Fournon, and A. Afonso-Luis. Evolution of the far-infrared luminosity functions in the Spitzer Wide-area Infrared Extragalactic Legacy Survey. MNRAS, 428:291–306, January 2013. doi: 10.1093/mnras/sts013.

L. Pentericci, J. D. Kurk, H. J. A. Röttgering, G. K. Miley, W. van Breugel, C. L. Carilli, H. Ford, T. Heckman, P. McCarthy, and A. Moorwood. A search for clusters at high redshift. II. A proto cluster around a radio galaxy at z=2.16. A&A, 361: L25–L28, September 2000.

L. Pentericci, J. D. Kurk, C. L. Carilli, D. E. Harris, G. K. Miley, and H. J. A. Röttgering. A Chandra study of X-ray sources in the field of the z=2.16 radio galaxy MRC 1138-262. A&A, 396:109–115, December 2002. doi: 10.1051/0004-6361:20021368.

A. A. Penzias and R. W. Wilson. A Measurement of Excess Antenna Temperature at 4080 Mc/s. ApJ, 142:419–421, July 1965. doi: 10.1086/148307.

B. M. Peterson. *An Introduction to Active Galactic Nuclei.* February 1997.

B. M. Peterson and A. Wandel. Keplerian Motion of Broad-Line Region Gas as Evidence for Supermassive Black Holes in Active Galactic Nuclei. ApJ, 521:L95–L98, August 1999. doi: 10.1086/312190.

B. M. Peterson and A. Wandel. Evidence for Supermassive Black Holes in Active Galactic Nuclei from Emission-Line Reverberation. ApJ, 540:L13–L16, September 2000. doi: 10.1086/312862.

V. Petrosian. Surface brightness and evolution of galaxies. ApJ, 209:L1–L5, October 1976. doi: 10.1086/182253.

E. A. Pier and J. H. Krolik. Infrared spectra of obscuring dust tori around active galactic nuclei. I - Calculational method and basic trends. ApJ, 401:99–109, December 1992. doi: 10.1086/172042.

E. A. Pier, R. Antonucci, T. Hurt, G. Kriss, and J. Krolik. The intrinsic nuclear spectrum of NGC 1068. ApJ, 428:124–129, June 1994. doi: 10.1086/174225.

G. L. Pilbratt, J. R. Riedinger, T. Passvogel, G. Crone, D. Doyle, U. Gageur, A. M. Heras, C. Jewell, L. Metcalfe, S. Ott, and M. Schmidt. Herschel Space Observatory. An ESA facility for far-infrared and submillimetre astronomy. A&A, 518:L1, July 2010. doi: 10.1051/0004-6361/201014759.

K. A. Pimbblet, S. S. Shabala, C. P. Haines, A. Fraser-McKelvie, and D. J. E. Floyd. The drivers of AGN activity in galaxy clusters: AGN fraction as a function of mass and environment. MNRAS, 429:1827–1839, February 2013. doi: 10.1093/mnras/sts470.

L. Piro, M. Yamauchi, and M. Matsuoka. X-ray spectral signatures of very thick cold matter in the spectra of the Seyfert 1 galaxies NGC 7469 and IC 4329A. ApJ, 360: L35–L38, September 1990. doi: 10.1086/185806.

L. Piro, M. Yamauchi, and M. Matsuoka. X-ray spectral signatures of very thick cold matter in the spectra of Seyfert galaxies. *Nuovo Cimento C Geophysics Space Physics C*, 15:811–818, October 1992. doi: 10.1007/BF02507855.

A. Poglitsch, C. Waelkens, N. Geis, H. Feuchtgruber, B. Vandenbussche, L. Rodriguez, O. Krause, E. Renotte, C. van Hoof, P. Saraceno, J. Cepa, F. Kerschbaum, P. Agnèse, B. Ali, B. Altieri, P. Andreani, J.-L. Augueres, Z. Balog, L. Barl, O. H. Bauer, N. Belbachir, M. Benedettini, N. Billot, O. Boulade, H. Bischof, J. Blommaert, E. Callut, C. Cara, R. Cerulli, D. Cesarsky, A. Contursi, Y. Creten, W. De Meester, V. Doublier, E. Doumayrou, L. Duband, K. Exter, R. Genzel, J.-M. Gillis, U. Grözinger, T. Henning, J. Herreros, R. Huygen, M. Inguscio, G. Jakob, C. Jamar, C. Jean, J. de Jong, R. Katterloher, C. Kiss, U. Klaas, D. Lemke, D. Lutz, S. Madden, B. Marquet, J. Martignac, A. Mazy, P. Merken, F. Montfort, L. Morbidelli, T. Müller, M. Nielbock, K. Okumura, R. Orfei, R. Ottensamer,

S. Pezzuto, P. Popesso, J. Putzeys, S. Regibo, V. Reveret, P. Royer, M. Sauvage, J. Schreiber, J. Stegmaier, D. Schmitt, J. Schubert, E. Sturm, M. Thiel, G. Tofani, R. Vavrek, M. Wetzstein, E. Wieprecht, and E. Wiezorrek. The Photodetector Array Camera and Spectrometer (PACS) on the Herschel Space Observatory. A&A, 518: L2, July 2010. doi: 10.1051/0004-6361/201014535.

M. Polletta, D. Weedman, S. Hnig, C. J. Lonsdale, H. E. Smith, and J. Houck. Obscuration in extremely luminous quasars. *The Astrophysical Journal*, 675(2):960, 2008. URL `http://stacks.iop.org/0004-637X/675/i=2/a=960`.

A. Pope, R.-R. Chary, D. M. Alexander, L. Armus, M. Dickinson, D. Elbaz, D. Frayer, D. Scott, and H. Teplitz. Mid-Infrared Spectral Diagnosis of Submillimeter Galaxies. ApJ, 675:1171–1193, March 2008. doi: 10.1086/527030.

K. Pounds and S. Vaughan. X-ray reflection in the nearby Seyfert 2 galaxy NGC 1068. MNRAS, 368:707–714, May 2006. doi: 10.1111/j.1365-2966.2006.10139.x.

D. Raban, W. Jaffe, H. Röttgering, K. Meisenheimer, and K. R. W. Tristram. Resolving the obscuring torus in NGC 1068 with the power of infrared interferometry: revealing the inner funnel of dust. MNRAS, 394:1325–1337, April 2009. doi: 10.1111/j.1365-2966.2009.14439.x.

N. A. Reddy, C. C. Steidel, D. Fadda, L. Yan, M. Pettini, A. E. Shapley, D. K. Erb, and K. L. Adelberger. Star Formation and Extinction in Redshift z˜2 Galaxies: Inferences from Spitzer MIPS Observations. ApJ, 644:792–812, June 2006. doi: 10.1086/503739.

J. N. Reeves and M. J. L. Turner. X-ray spectra of a large sample of quasars with ASCA. MNRAS, 316:234–248, August 2000. doi: 10.1046/j.1365-8711.2000.03510.x.

G. A. Reichert, R. F. Mushotzky, S. S. Holt, and R. Petre. Soft X-ray spectral observations of low-luminosity active galaxies. ApJ, 296:69–89, September 1985. doi: 10.1086/163421.

C. S. Reynolds, A. C. Fabian, K. Makishima, Y. Fukazawa, and T. Tamura. The Reflection-Dominated X-Ray Spectrum of NGC6552. MNRAS, 268:L55, June 1994.

J. H. Rhee and J. E. Larkin. Probing the Dust Obscuration in Seyfert Galaxies using Infrared Spectroscopy. II. Implication for the Unification of Seyfert Galaxies. ApJ, 620:151–164, February 2005. doi: 10.1086/426884.

C. Ricci, S. Paltani, H. Awaki, P.-O. Petrucci, Y. Ueda, and M. Brightman. Luminosity-dependent unification of active galactic nuclei and the X-ray Baldwin effect. A&A, 553:A29, May 2013. doi: 10.1051/0004-6361/201220324.

G. H. Rieke. The infrared emission of Seyfert galaxies. ApJ, 226:550–558, December 1978. doi: 10.1086/156639.

G. H. Rieke, E. T. Young, C. W. Engelbracht, D. M. Kelly, F. J. Low, E. E. Haller, J. W. Beeman, K. D. Gordon, J. A. Stansberry, K. A. Misselt, J. Cadien, J. E. Morrison, G. Rivlis, W. B. Latter, A. Noriega-Crespo, D. L. Padgett, K. R. Stapelfeldt, D. C. Hines, E. Egami, J. Muzerolle, A. Alonso-Herrero, M. Blaylock, H. Dole, J. L. Hinz, E. Le Floc'h, C. Papovich, P. G. Pérez-González, P. S. Smith, K. Y. L. Su, L. Bennett, D. T. Frayer, D. Henderson, N. Lu, F. Masci, M. Pesenson, L. Rebull, J. Rho, J. Keene, S. Stolovy, S. Wachter, W. Wheaton, M. W. Werner, and P. L. Richards. The Multiband Imaging Photometer for Spitzer (MIPS). ApJS, 154:25–29, September 2004. doi: 10.1086/422717.

G. H. Rieke, A. Alonso-Herrero, B. J. Weiner, P. G. Pérez-González, M. Blaylock, J. L. Donley, and D. Marcillac. Determining Star Formation Rates for Infrared Galaxies. ApJ, 692:556–573, February 2009. doi: 10.1088/0004-637X/692/1/556.

E. E. Rigby, S. J. Maddox, L. Dunne, M. Negrello, D. J. B. Smith, J. González-Nuevo, D. Herranz, M. López-Caniego, R. Auld, S. Buttiglione, M. Baes, A. Cava, A. Cooray, D. L. Clements, A. Dariush, G. de Zotti, S. Dye, S. Eales, D. Frayer, J. Fritz, R. Hopwood, E. Ibar, R. J. Ivison, M. Jarvis, P. Panuzzo, E. Pascale, M. Pohlen, G. Rodighiero, S. Serjeant, P. Temi, and M. A. Thompson. Herschel-ATLAS: first data release of the Science Demonstration Phase source catalogues. MNRAS, 415:2336–2348, August 2011. doi: 10.1111/j.1365-2966.2011.18864.x.

G. Risaliti. X-ray spectral properties of Seyfert 2s observed with BeppoSAX. *Nuclear Physics B Proceedings Supplements*, 132:229–231, June 2004. doi: 10.1016/j.nuclphysbps.2004.04.040.

G. Risaliti, R. Maiolino, and M. Salvati. The Distribution of Absorbing Column Densities among Seyfert 2 Galaxies. ApJ, 522:157–164, September 1999. doi: 10.1086/307623.

G. Risaliti, M. Elvis, G. Fabbiano, A. Baldi, and A. Zezas. Rapid Compton-thick/Compton-thin Transitions in the Seyfert 2 Galaxy NGC 1365. ApJ, 623:L93–L96, April 2005. doi: 10.1086/430252.

G. Risaliti, M. Elvis, G. Fabbiano, A. Baldi, A. Zezas, and M. Salvati. Occultation Measurement of the Size of the X-Ray-emitting Region in the Active Galactic Nucleus of NGC 1365. ApJ, 659:L111–L114, April 2007. doi: 10.1086/517884.

G. Risaliti, G. Miniutti, M. Elvis, G. Fabbiano, M. Salvati, A. Baldi, V. Braito, S. Bianchi, G. Matt, J. Reeves, R. Soria, and A. Zezas. Variable Partial Covering and A Relativistic Iron Line in NGC 1365. ApJ, 696:160–171, May 2009. doi: 10.1088/0004-637X/696/1/160.

P. F. Roche, D. K. Aitken, C. H. Smith, and M. J. Ward. An atlas of mid-infrared spectra of galaxy nuclei. MNRAS, 248:606–629, February 1991.

G. Rodighiero, M. Vaccari, A. Franceschini, L. Tresse, O. Le Fevre, V. Le Brun, C. Mancini, I. Matute, A. Cimatti, L. Marchetti, O. Ilbert, S. Arnouts, M. Bolzonella,

E. Zucca, S. Bardelli, C. J. Lonsdale, D. Shupe, J. Surace, M. Rowan-Robinson, B. Garilli, G. Zamorani, L. Pozzetti, M. Bondi, S. de la Torre, D. Vergani, P. Santini, A. Grazian, and A. Fontana. Mid- and far-infrared luminosity functions and galaxy evolution from multiwavelength Spitzer observations up to z ˜ 2.5. A&A, 515:A8, June 2010. doi: 10.1051/0004-6361/200912058.

H. J. A. Roettgering, M. J. West, G. K. Miley, and K. C. Chambers. The optical counterparts and the environments of ultra-steep-spectrum radio sources. A&A, 307:376–384, March 1996.

P. Rosati, P. Tozzi, R. Giacconi, R. Gilli, G. Hasinger, L. Kewley, V. Mainieri, M. Nonino, C. Norman, G. Szokoly, J. X. Wang, A. Zirm, J. Bergeron, S. Borgani, R. Gilmozzi, N. Grogin, A. Koekemoer, E. Schreier, and W. Zheng. The Chandra Deep Field-South: The 1 Million Second Exposure. ApJ, 566:667–674, February 2002. doi: 10.1086/338339.

M. Rowan-Robinson. On the unity of activity in galaxies. ApJ, 213:635–647, May 1977. doi: 10.1086/155195.

M. Rowan-Robinson, G. Helou, and D. Walker. Studies of IRAS sources at high galactic latitudes. III - Luminosity functions at 25, 60, and 100 microns and the correlation of optical and infrared luminosities. MNRAS, 227:589–606, August 1987.

M. Rowan-Robinson, C. Lonsdale, G. Smith, J. Surace, D. Shupe, M. Polletta, B. Siana, T. Babbedge, S. Oliver, I. Perez-Fournon, A. Franceschini, A. Afonso, C. D. Luis, P. Davoodi, D. Domingue, A. Efstathiou, F. Fang, D. Farrah, D. Frayer, E. Hatziminaoglou, E. Gonzalez-Solares, K. Xu, D. Padgett, and M. Vaccari. Understanding Infrared Galaxy Populations: the SWIRE Legacy Survey. In R. R. Chary, H. I. Teplitz, and K. Sheth, editors, *Infrared Diagnostics of Galaxy Evolution*, volume 381 of *Astronomical Society of the Pacific Conference Series*, page 216, March 2008.

B. Rush, M. A. Malkan, and L. Spinoglio. The extended 12 micron galaxy sample. ApJS, 89:1–33, November 1993. doi: 10.1086/191837.

A. Sajina, M. Lacy, and D. Scott. Simulating the Spitzer Mid-Infrared Color-Color Diagrams. ApJ, 621:256–268, March 2005. doi: 10.1086/426536.

S. Salim, R. M. Rich, S. Charlot, J. Brinchmann, B. D. Johnson, D. Schiminovich, M. Seibert, R. Mallery, T. M. Heckman, K. Forster, P. G. Friedman, D. C. Martin, P. Morrissey, S. G. Neff, T. Small, T. K. Wyder, L. Bianchi, J. Donas, Y.-W. Lee, B. F. Madore, B. Milliard, A. S. Szalay, B. Y. Welsh, and S. K. Yi. UV Star Formation Rates in the Local Universe. ApJS, 173:267–292, December 2007. doi: 10.1086/519218.

M. Salvato, G. Hasinger, O. Ilbert, G. Zamorani, M. Brusa, N. Z. Scoville, A. Rau, P. Capak, S. Arnouts, H. Aussel, M. Bolzonella, A. Buongiorno, N. Cappelluti, K. Caputi, F. Civano, R. Cook, M. Elvis, R. Gilli, K. Jahnke, J. S. Kartaltepe,

C. D. Impey, F. Lamareille, E. Le Floc'h, S. Lilly, V. Mainieri, P. McCarthy, H. McCracken, M. Mignoli, B. Mobasher, T. Murayama, S. Sasaki, D. B. Sanders, D. Schiminovich, Y. Shioya, P. Shopbell, J. Silverman, V. Smolčić, J. Surace, Y. Taniguchi, D. Thompson, J. R. Trump, M. Urry, and M. Zamojski. Photometric Redshift and Classification for the XMM-COSMOS Sources. ApJ, 690:1250–1263, January 2009. doi: 10.1088/0004-637X/690/2/1250.

D. B. Sanders, B. T. Soifer, J. H. Elias, B. F. Madore, K. Matthews, G. Neugebauer, and N. Z. Scoville. Ultraluminous infrared galaxies and the origin of quasars. ApJ, 325:74–91, February 1988. doi: 10.1086/165983.

D. B. Sanders, E. S. Phinney, G. Neugebauer, B. T. Soifer, and K. Matthews. Continuum energy distribution of quasars - Shapes and origins. ApJ, 347:29–51, December 1989. doi: 10.1086/168094.

M. Sarzi, J. Falcón-Barroso, R. L. Davies, R. Bacon, M. Bureau, M. Cappellari, P. T. de Zeeuw, E. Emsellem, K. Fathi, D. Krajnović, H. Kuntschner, R. M. McDermid, and R. F. Peletier. The SAURON project - V. Integral-field emission-line kinematics of 48 elliptical and lenticular galaxies. MNRAS, 366:1151–1200, March 2006. doi: 10.1111/j.1365-2966.2005.09839.x.

M. Sauvage and T. X. Thuan. On the use of far-infrared luminosity as a star formation indicator in galaxies. ApJ, 396:L69–L73, September 1992. doi: 10.1086/186519.

K. Schawinski, D. Thomas, M. Sarzi, C. Maraston, S. Kaviraj, S.-J. Joo, S. K. Yi, and J. Silk. Observational evidence for AGN feedback in early-type galaxies. MNRAS, 382:1415–1431, December 2007. doi: 10.1111/j.1365-2966.2007.12487.x.

M. Schmidt. 3C 273 : A Star-Like Object with Large Red-Shift. Nature, 197:1040, March 1963. doi: 10.1038/1971040a0.

H. R. Schmitt, J. E. Pringle, C. J. Clarke, and A. L. Kinney. The Orientation of Jets Relative to Dust Disks in Radio Galaxies. ApJ, 575:150–155, August 2002. doi: 10.1086/341211.

S. Serjeant, F. Bertoldi, A. W. Blain, D. L. Clements, A. Cooray, L. Danese, J. Dunlop, L. Dunne, S. Eales, J. Falder, E. Hatziminaoglou, D. H. Hughes, E. Ibar, M. J. Jarvis, A. Lawrence, M. G. Lee, M. Michałowski, M. Negrello, A. Omont, M. Page, C. Pearson, P. P. van der Werf, G. White, A. Amblard, R. Auld, M. Baes, D. G. Bonfield, D. Burgarella, S. Buttiglione, A. Cava, A. Dariush, G. de Zotti, S. Dye, D. Frayer, J. Fritz, J. Gonzalez-Nuevo, D. Herranz, R. J. Ivison, G. Lagache, L. Leeuw, M. Lopez-Caniego, S. Maddox, E. Pascale, M. Pohlen, E. Rigby, G. Rodighiero, S. Samui, B. Sibthorpe, D. J. B. Smith, P. Temi, M. Thompson, I. Valtchanov, and A. Verma. Herschel ATLAS: The cosmic star formation history of quasar host galaxies. A&A, 518:L7, July 2010. doi: 10.1051/0004-6361/201014565.

N. Seymour, D. Stern, C. De Breuck, J. Vernet, A. Rettura, M. Dickinson, A. Dey, P. Eisenhardt, R. Fosbury, M. Lacy, P. McCarthy, G. Miley, B. Rocca-Volmerange,

H. Röttgering, S. A. Stanford, H. Teplitz, W. van Breugel, and A. Zirm. The Massive Hosts of Radio Galaxies across Cosmic Time. ApJS, 171:353–375, August 2007. doi: 10.1086/517887.

Z. Shang, M. S. Brotherton, R. F. Green, G. A. Kriss, J. Scott, J. K. Quijano, O. Blaes, I. Hubeny, J. Hutchings, M. E. Kaiser, A. Koratkar, W. Oegerle, and W. Zheng. Quasars and the Big Blue Bump. ApJ, 619:41–59, January 2005. doi: 10.1086/426134.

O. Shemmer, W. N. Brandt, H. Netzer, R. Maiolino, and S. Kaspi. The Hard X-Ray Spectrum as a Probe for Black Hole Growth in Radio-Quiet Active Galactic Nuclei. ApJ, 682:81–93, July 2008. doi: 10.1086/588776.

D. L. Shupe, M. Rowan-Robinson, C. J. Lonsdale, F. Masci, T. Evans, F. Fang, S. Oliver, M. Vaccari, G. Rodighiero, D. Padgett, J. A. Surace, C. K. Xu, S. Berta, F. Pozzi, A. Franceschini, T. Babbedge, E. Gonzales-Solares, B. D. Siana, D. Farrah, D. T. Frayer, H. E. Smith, M. Polletta, F. Owen, and I. Pérez-Fournon. Galaxy Counts at 24 μm in the SWIRE Fields. AJ, 135:1050–1056, March 2008. doi: 10.1088/0004-6256/135/3/1050.

R. Siebenmorgen and E. Krügel. Dust in starburst nuclei and ULIRGs. SED models for observers. A&A, 461:445–453, January 2007. doi: 10.1051/0004-6361:20065700.

R. Siebenmorgen, M. Haas, E. Kruegel, and B. Schulz. Discovery of 10 Mu.m silicate emission in quasars. - Evidence of the AGN unification scheme. *Astronomische Nachrichten*, 326:556–556, August 2005.

J. D. Silverman, P. J. Green, W. A. Barkhouse, D.-W. Kim, M. Kim, B. J. Wilkes, R. A. Cameron, G. Hasinger, B. T. Jannuzi, M. G. Smith, P. S. Smith, and H. Tananbaum. The Luminosity Function of X-Ray-selected Active Galactic Nuclei: Evolution of Supermassive Black Holes at High Redshift. ApJ, 679:118–139, May 2008. doi: 10.1086/529572.

R. Simcoe, K. K. McLeod, J. Schachter, and M. Elvis. Obscuration in the Host Galaxies of Soft X-Ray–selected Seyfert Nuclei. ApJ, 489:615, November 1997. doi: 10.1086/304819.

C. Simpson. The luminosity dependence of the type 1 active galactic nucleus fraction. MNRAS, 360:565–572, June 2005. doi: 10.1111/j.1365-2966.2005.09043.x.

J. Singal, V. Petrosian, A. Lawrence, and Ł. Stawarz. On the Radio and Optical Luminosity Evolution of Quasars. ApJ, 743:104, December 2011. doi: 10.1088/0004-637X/743/2/104.

V. M. Slipher. The spectrum and velocity of the nebula N.G.C. 1068 (M 77). *Lowell Observatory Bulletin*, 3:59–62, 1917.

D. J. B. Smith, L. Dunne, E. da Cunha, K. Rowlands, S. J. Maddox, H. L. Gomez, D. G. Bonfield, S. Charlot, S. P. Driver, C. C. Popescu, R. J. Tuffs, J. S. Dunlop, M. J. Jarvis, N. Seymour, M. Symeonidis, M. Baes, N. Bourne, D. L. Clements, A. Cooray, G. De Zotti, S. Dye, S. Eales, D. Scott, A. Verma, P. van der Werf, E. Andrae, R. Auld, S. Buttiglione, A. Cava, A. Dariush, J. Fritz, R. Hopwood, E. Ibar, R. J. Ivison, L. Kelvin, B. F. Madore, M. Pohlen, E. E. Rigby, A. Robotham, M. Seibert, and P. Temi. Herschel-ATLAS: multi-wavelength SEDs and physical properties of 250 um selected galaxies at z ¡ 0.5. MNRAS, 427:703–727, November 2012. doi: 10.1111/j.1365-2966.2012.21930.x.

J. E. Smith, A. Robinson, S. Young, D. J. Axon, and E. A. Corbett. Equatorial scattering and the structure of the broad-line region in Seyfert nuclei: evidence for a rotating disc. MNRAS, 359:846–864, May 2005. doi: 10.1111/j.1365-2966.2005.08895.x.

H. W. W. Spoon, J. A. Marshall, J. R. Houck, M. Elitzur, L. Hao, L. Armus, B. R. Brandl, and V. Charmandaris. Mid-Infrared Galaxy Classification Based on Silicate Obscuration and PAH Equivalent Width. ApJ, 654:L49–L52, January 2007. doi: 10.1086/511268.

V. Springel, S. D. M. White, A. Jenkins, C. S. Frenk, N. Yoshida, L. Gao, J. Navarro, R. Thacker, D. Croton, J. Helly, J. A. Peacock, S. Cole, P. Thomas, H. Couchman, A. Evrard, J. Colberg, and F. Pearce. Simulations of the formation, evolution and clustering of galaxies and quasars. Nature, 435:629–636, June 2005. doi: 10.1038/nature03597.

M. Stalevski, J. Fritz, M. Baes, T. Nakos, and L. Č. Popović. 3D radiative transfer modelling of the dusty tori around active galactic nuclei as a clumpy two-phase medium. MNRAS, 420:2756–2772, March 2012. doi: 10.1111/j.1365-2966.2011.19775.x.

G. Stasińska, R. Cid Fernandes, A. Mateus, L. Sodré, and N. V. Asari. Semi-empirical analysis of Sloan Digital Sky Survey galaxies - III. How to distinguish AGN hosts. MNRAS, 371:972–982, September 2006. doi: 10.1111/j.1365-2966.2006.10732.x.

D. Stern, P. Eisenhardt, V. Gorjian, C. S. Kochanek, N. Caldwell, D. Eisenstein, M. Brodwin, M. J. I. Brown, R. Cool, A. Dey, P. Green, B. T. Jannuzi, S. S. Murray, M. A. Pahre, and S. P. Willner. Mid-Infrared Selection of Active Galaxies. ApJ, 631:163–168, September 2005. doi: 10.1086/432523.

D. Stern, R.-R. Chary, P. R. M. Eisenhardt, and L. A. Moustakas. Spitzer Observations of the Prototypical Extremely Red Objects HR 10 and LBDS 53W091: Separating Dusty Starbursts from Old Elliptical Galaxies. AJ, 132:1405–1414, September 2006. doi: 10.1086/506347.

T. Storchi-Bergmann, D. Calzetti, and A. L. Kinney. Ultraviolet to near-infrared spectral distributions of star-forming galaxies: Metallicity and age effects. ApJ, 429:572–581, July 1994. doi: 10.1086/174345.

J. P. Stott, R. C. Hickox, A. C. Edge, C. A. Collins, M. Hilton, C. D. Harrison, A. K. Romer, P. J. Rooney, S. T. Kay, C. J. Miller, M. Sahlén, E. J. Lloyd-Davies, N. Mehrtens, B. Hoyle, A. R. Liddle, P. T. P. Viana, I. G. McCarthy, J. Schaye, and C. M. Booth. The XMM Cluster Survey: the interplay between the brightest cluster galaxy and the intracluster medium via AGN feedback. MNRAS, 422:2213–2229, May 2012. doi: 10.1111/j.1365-2966.2012.20764.x.

E. Sturm, M. Schweitzer, D. Lutz, A. Contursi, R. Genzel, M. D. Lehnert, L. J. Tacconi, S. Veilleux, D. S. Rupke, D.-C. Kim, A. Sternberg, D. Maoz, S. Lord, J. Mazzarella, and D. B. Sanders. Silicate Emissions in Active Galaxies: From LINERs to QSOs. ApJ, 629:L21–L23, August 2005. doi: 10.1086/444359.

E. Sturm, G. Hasinger, I. Lehmann, V. Mainieri, R. Genzel, M. D. Lehnert, D. Lutz, and L. J. Tacconi. Mid-Infrared Spitzer Spectra of X-Ray-Selected Type 2 QSOs: QSO2s Are Not Ultraluminous Infrared Galaxies. ApJ, 642:81–86, May 2006. doi: 10.1086/500828.

M. Suganuma, Y. Yoshii, Y. Kobayashi, T. Minezaki, K. Enya, H. Tomita, T. Aoki, S. Koshida, and B. A. Peterson. Reverberation Measurements of the Inner Radius of the Dust Torus in Nearby Seyfert 1 Galaxies. ApJ, 639:46–63, March 2006. doi: 10.1086/499326.

W. Sutherland and W. Saunders. On the likelihood ratio for source identification. MNRAS, 259:413–420, December 1992.

G. P. Szokoly, J. Bergeron, G. Hasinger, I. Lehmann, L. Kewley, V. Mainieri, M. Nonino, P. Rosati, R. Giacconi, R. Gilli, R. Gilmozzi, C. Norman, M. Romaniello, E. Schreier, P. Tozzi, J. X. Wang, W. Zheng, and A. Zirm. The Chandra Deep Field-South: Optical Spectroscopy. I. ApJS, 155:271–349, December 2004. doi: 10.1086/424707.

I. Tanaka, C. D. Breuck, J. D. Kurk, Y. Taniguchi, T. Kodama, Y. Matsuda, C. Packham, A. Zirm, M. Kajisawa, T. Ichikawa, N. Seymour, D. Stern, A. Stockton, B. P. Venemans, and J. Vernet. Discovery of an Excess of Hα Emitters around 4C 23.56 at z = 2.48. PASJ, 63:415–, March 2011.

R. C. Telfer, W. Zheng, G. A. Kriss, and A. F. Davidsen. The Rest-Frame Extreme-Ultraviolet Spectral Properties of Quasi-stellar Objects. ApJ, 565:773–785, February 2002. doi: 10.1086/324689.

T. A. Thompson, E. Quataert, and N. Murray. Radiation Pressure-supported Starburst Disks and Active Galactic Nucleus Fueling. ApJ, 630:167–185, September 2005. doi: 10.1086/431923.

Y. Toba, S. Oyabu, H. Matsuhara, D. Ishihara, M. Malkan, T. Wada, H. Kataza, Y. Ohyama, and S. Takita. The Mid-Infrared luminosity function of galaxies using the AKARI mid-infrared All-Sky Survey Catalogue. In R. J. Tuffs and C. C. Popescu, editors, *IAU Symposium*, volume 284 of *IAU Symposium*, pages 228–230, August 2012a. doi: 10.1017/S1743921312009118.

Y. Toba, S. Oyabu, H. Matsuhara, M. A. Malkan, D. Ishihara, T. Wada, Y. Ohyama, S. Takita, and C. Yamauchi. Luminosity and redshift dependence of covering factor of dust torus viewed with AKARI and WISE. In R. Mason, A. Alonso-Herrero, and C. Packham, editors, *Torus Workshop, 2012*, page 58, December 2012b.

P. Todini and A. Ferrara. Dust formation in primordial Type II supernovae. MNRAS, 325:726–736, August 2001. doi: 10.1046/j.1365-8711.2001.04486.x.

P. Tozzi, P. Rosati, M. Nonino, J. Bergeron, S. Borgani, R. Gilli, R. Gilmozzi, G. Hasinger, N. Grogin, L. Kewley, A. Koekemoer, C. Norman, E. Schreier, G. Szokoly, J. X. Wang, W. Zheng, A. Zirm, and R. Giacconi. New Results from the X-Ray and Optical Survey of the Chandra Deep Field-South: The 300 Kilosecond Exposure. II. ApJ, 562:42–51, November 2001. doi: 10.1086/322492.

C. A. Tremonti, T. M. Heckman, G. Kauffmann, J. Brinchmann, S. Charlot, S. D. M. White, M. Seibert, E. W. Peng, D. J. Schlegel, A. Uomoto, M. Fukugita, and J. Brinkmann. The Origin of the Mass-Metallicity Relation: Insights from 53,000 Star-forming Galaxies in the Sloan Digital Sky Survey. ApJ, 613:898–913, October 2004. doi: 10.1086/423264.

J. Tueller, W. H. Baumgartner, C. B. Markwardt, G. K. Skinner, R. F. Mushotzky, M. Ajello, S. Barthelmy, A. Beardmore, W. N. Brandt, D. Burrows, G. Chincarini, S. Campana, J. Cummings, G. Cusumano, P. Evans, E. Fenimore, N. Gehrels, O. Godet, D. Grupe, S. Holland, J. Kennea, H. A. Krimm, M. Koss, A. Moretti, K. Mukai, J. P. Osborne, T. Okajima, C. Pagani, K. Page, D. Palmer, A. Parsons, D. P. Schneider, T. Sakamoto, R. Sambruna, G. Sato, M. Stamatikos, M. Stroh, T. Ukwata, and L. Winter. The 22 Month Swift-BAT All-Sky Hard X-ray Survey. ApJS, 186:378–405, February 2010. doi: 10.1088/0067-0049/186/2/378.

T. J. Turner, L. Miller, S. B. Kraemer, J. N. Reeves, and K. A. Pounds. Suzaku Observation of a Hard Excess in 1H 0419 - 577: Detection of a Compton-Thick Partial-Covering Absorber. ApJ, 698:99–105, June 2009. doi: 10.1088/0004-637X/698/1/99.

Y. Ueda, M. Akiyama, K. Ohta, and T. Miyaji. Cosmological Evolution of the Hard X-Ray Active Galactic Nucleus Luminosity Function and the Origin of the Hard X-Ray Background. ApJ, 598:886–908, December 2003. doi: 10.1086/378940.

Y. Ueda, M. G. Watson, I. M. Stewart, M. Akiyama, A. D. Schwope, G. Lamer, J. Ebrero, F. J. Carrera, K. Sekiguchi, T. Yamada, C. Simpson, G. Hasinger, and S. Mateos. The Subaru/XMM-Newton Deep Survey (SXDS). III. X-Ray Data. ApJS, 179:124–141, November 2008. doi: 10.1086/591083.

P. Uttley, R. Edelson, I. M. McHardy, B. M. Peterson, and A. Markowitz. Correlated Long-Term Optical and X-Ray Variations in NGC 5548. ApJ, 584:L53–L56, February 2003. doi: 10.1086/373887.

E. Valiante, D. Lutz, E. Sturm, R. Genzel, L. J. Tacconi, M. D. Lehnert, and A. J. Baker. A Mid-Infrared Spectroscopic Study of Submillimeter Galaxies: Luminous Starbursts at High Redshift. ApJ, 660:1060–1071, May 2007. doi: 10.1086/513306.

R. Valiante, R. Schneider, S. Bianchi, and A. C. Andersen. Stellar sources of dust in the high-redshift Universe. MNRAS, 397:1661–1671, August 2009. doi: 10.1111/j.1365-2966.2009.15076.x.

R. Valiante, R. Schneider, S. Salvadori, and S. Bianchi. The origin of the dust in high-redshift quasars: the case of SDSS J1148+5251. MNRAS, 416:1916–1935, September 2011. doi: 10.1111/j.1365-2966.2011.19168.x.

R. V. Vasudevan, A. C. Fabian, P. Gandhi, L. M. Winter, and R. F. Mushotzky. The power output of local obscured and unobscured AGN: crossing the absorption barrier with Swift/BAT and IRAS. MNRAS, 402:1081–1098, February 2010. doi: 10.1111/j.1365-2966.2009.15936.x.

S. Veilleux, D. S. N. Rupke, D.-C. Kim, R. Genzel, E. Sturm, D. Lutz, A. Contursi, M. Schweitzer, L. J. Tacconi, H. Netzer, A. Sternberg, J. C. Mihos, A. J. Baker, J. M. Mazzarella, S. Lord, D. B. Sanders, A. Stockton, R. D. Joseph, and J. E. Barnes. Spitzer Quasar and Ulirg Evolution Study (QUEST). IV. Comparison of 1 Jy Ultraluminous Infrared Galaxies with Palomar-Green Quasars. ApJS, 182:628–666, June 2009. doi: 10.1088/0067-0049/182/2/628.

B. Venemans, G. Miley, J. Kurk, H. Röttgering, and L. Pentericci. Tracing the Formation and Evolution of Clusters and their Central Massive Galaxies to z¿4: a Progress Report. *The Messenger*, 111:36–39, March 2003.

B. P. Venemans, J. D. Kurk, G. K. Miley, H. J. A. Röttgering, W. van Breugel, C. L. Carilli, C. De Breuck, H. Ford, T. Heckman, P. McCarthy, and L. Pentericci. The Most Distant Structure of Galaxies Known: A Protocluster at z=4.1. ApJ, 569: L11–L14, April 2002. doi: 10.1086/340563.

B. P. Venemans, H. J. A. Röttgering, G. K. Miley, J. D. Kurk, C. De Breuck, R. A. Overzier, W. J. M. van Breugel, C. L. Carilli, H. Ford, T. Heckman, L. Pentericci, and P. McCarthy. Properties of Lyα emitters around the radio galaxy MRC 0316 257'. A&A, 431:793–812, March 2005. doi: 10.1051/0004-6361:20042038.

B. P. Venemans, H. J. A. Röttgering, G. K. Miley, W. J. M. van Breugel, C. de Breuck, J. D. Kurk, L. Pentericci, S. A. Stanford, R. A. Overzier, S. Croft, and H. Ford. Protoclusters associated with z ¿ 2 radio galaxies . I. Characteristics of high redshift protoclusters. A&A, 461:823–845, January 2007. doi: 10.1051/0004-6361:20053941.

M.-P. Véron-Cetty, P. Véron, and A. C. Gonçalves. A spectrophotometric atlas of Narrow-Line Seyfert 1 galaxies. A&A, 372:730–754, June 2001. doi: 10.1051/0004-6361:20010489.

M. Vika, S. P. Driver, E. Cameron, L. Kelvin, and A. Robotham. The near-IR M_{bh}-L and M_{bh}-n relations. MNRAS, 419:2264–2292, January 2012. doi: 10.1111/j.1365-2966.2011.19881.x.

K. Wada and C. A. Norman. Obscuring Material around Seyfert Nuclei with Starbursts. ApJ, 566:L21–L24, February 2002. doi: 10.1086/339438.

D. A. Wake, C. J. Miller, T. Di Matteo, R. C. Nichol, A. Pope, A. S. Szalay, A. Gray, D. P. Schneider, and D. G. York. The Clustering of Active Galactic Nuclei in the Sloan Digital Sky Survey. ApJ, 610:L85–L88, August 2004. doi: 10.1086/423317.

B. P. Wakker and J. S. Mathis. Dependence of Gas-Phase Abundances in the Interstellar Medium on Column Density. ApJ, 544:L107–L110, December 2000. doi: 10.1086/317316.

J. Wang and J. Y. Wei. Understanding the AGN-Host Connection in Partially Obscured Active Galactic Nuclei. I. The Nature of AGN+H II Composites. ApJ, 679:86–100, May 2008. doi: 10.1086/587048.

J. X. Wang and P. Jiang. On the Fraction of X-Ray-obscured Quasars in the Local Universe. ApJ, 646:L103–L106, August 2006. doi: 10.1086/507100.

R. S. Warwick, K. A. Pounds, and T. J. Turner. Variable low-energy absorption in the X-ray spectrum of ESO 103-G35. MNRAS, 231:1145–1152, April 1988.

D. Weedman, M. Polletta, C. J. Lonsdale, B. J. Wilkes, B. Siana, J. R. Houck, J. Surace, D. Shupe, D. Farrah, and H. E. Smith. Active Galactic Nucleus and Starburst Classification from Spitzer Mid-Infrared Spectra for High-Redshift SWIRE Sources. ApJ, 653:101–111, December 2006. doi: 10.1086/508647.

D. W. Weedman. A Photometric Study of Markarian Galaxies. ApJ, 183:29–40, July 1973. doi: 10.1086/152205.

D. W. Weedman, L. Hao, S. J. U. Higdon, D. Devost, Y. Wu, V. Charmandaris, B. Brandl, E. Bass, and J. R. Houck. Mid-Infrared Spectra of Classical AGNs Observed with the Spitzer Space Telescope. ApJ, 633:706–716, November 2005. doi: 10.1086/466520.

B. J. Weiner, C. Papovich, K. Bundy, C. J. Conselice, M. C. Cooper, R. S. Ellis, R. J. Ivison, K. G. Noeske, A. C. Phillips, and R. Yan. AEGIS: Extinction and Star Formation Tracers from Line Emission. ApJ, 660:L39–L42, May 2007. doi: 10.1086/517925.

M. W. Werner, T. L. Roellig, F. J. Low, G. H. Rieke, M. Rieke, W. F. Hoffmann, E. Young, J. R. Houck, B. Brandl, G. G. Fazio, J. L. Hora, R. D. Gehrz, G. Helou, B. T. Soifer, J. Stauffer, J. Keene, P. Eisenhardt, D. Gallagher, T. N. Gautier, W. Irace, C. R. Lawrence, L. Simmons, J. E. Van Cleve, M. Jura, E. L. Wright, and D. P. Cruikshank. The Spitzer Space Telescope Mission. ApJS, 154:1–9, September 2004. doi: 10.1086/422992.

B. J. Wilkes, G. D. Schmidt, R. M. Cutri, H. Ghosh, D. C. Hines, B. Nelson, and P. S. Smith. The X-Ray Properties of 2MASS Red Active Galactic Nuclei. ApJ, 564: L65–L68, January 2002. doi: 10.1086/338908.

R. Willingale, R. L. C. Starling, A. P. Beardmore, N. R. Tanvir, and P. T. O'Brien. Calibration of X-ray absorption in our Galaxy. MNRAS, 431:394–404, May 2013. doi: 10.1093/mnras/stt175.

C. J. Willott, S. Rawlings, K. M. Blundell, and M. Lacy. The quasar fraction in low-frequency-selected complete samples and implications for unified schemes. MNRAS, 316:449–458, August 2000. doi: 10.1046/j.1365-8711.2000.03447.x.

C. J. Willott, S. Rawlings, K. M. Blundell, M. Lacy, and S. A. Eales. The radio luminosity function from the low-frequency 3CRR, 6CE and 7CRS complete samples. MNRAS, 322:536–552, April 2001. doi: 10.1046/j.1365-8711.2001.04101.x.

A. S. Wilson, J. A. Braatz, T. M. Heckman, J. H. Krolik, and G. K. Miley. The Ionization Cones in the Seyfert Galaxy NGC 5728. ApJ, 419:L61, December 1993. doi: 10.1086/187137.

L. M. Winter, R. F. Mushotzky, C. S. Reynolds, and J. Tueller. X-Ray Spectral Properties of the BAT AGN Sample. ApJ, 690:1322–1349, January 2009. doi: 10.1088/0004-637X/690/2/1322.

J.-H. Woo and C. M. Urry. Active Galactic Nucleus Black Hole Masses and Bolometric Luminosities. ApJ, 579:530–544, November 2002. doi: 10.1086/342878.

J.-H. Woo, T. Treu, A. J. Barth, S. A. Wright, J. L. Walsh, M. C. Bentz, P. Martini, V. N. Bennert, G. Canalizo, A. V. Filippenko, E. Gates, J. Greene, W. Li, M. A. Malkan, D. Stern, and T. Minezaki. The Lick AGN Monitoring Project: The M $_{BH}$-σ_* Relation for Reverberation-mapped Active Galaxies. ApJ, 716:269–280, June 2010. doi: 10.1088/0004-637X/716/1/269.

Y. Wu, V. Charmandaris, J. Huang, L. Spinoglio, and S. Tommasin. Spitzer/IRS 5-35 μm Low-resolution Spectroscopy of the 12 μm Seyfert Sample. ApJ, 701:658–676, August 2009. doi: 10.1088/0004-637X/701/1/658.

D. Wylezalek, J. Vernet, C. De Breuck, D. Stern, A. Galametz, N. Seymour, M. Jarvis, P. Barthel, G. Drouart, T. R. Greve, M. Haas, N. Hatch, R. Ivison, M. Lehnert, K. Meisenheimer, G. Miley, N. Nesvadba, H. J. A. Röttgering, and J. A. Stevens. The Herschel view of the environment of the radio galaxy 4C+41.17 at z = 3.8. MNRAS, 428:3206–3219, February 2013. doi: 10.1093/mnras/sts264.

R. Yan, L. C. Ho, J. A. Newman, A. L. Coil, C. N. A. Willmer, E. S. Laird, A. Georgakakis, J. Aird, P. Barmby, K. Bundy, M. C. Cooper, M. Davis, S. M. Faber, T. Fang, R. L. Griffith, A. M. Koekemoer, D. C. Koo, K. Nandra, S. Q. Park, V. L. Sarajedini, B. J. Weiner, and S. P. Willner. AEGIS: Demographics of X-ray and Optically Selected Active Galactic Nuclei. ApJ, 728:38, February 2011. doi: 10.1088/0004-637X/728/1/38.

T. Yaqoob and K. Murphy. Where are the Compton-thick AGN? In *American Astronomical Society Meeting Abstracts 215*, volume 42 of *Bulletin of the American Astronomical Society*, page 353.01, January 2010.

T. Yaqoob and U. Padmanabhan. The Cores of the Fe K Lines in Seyfert 1 Galaxies Observed by the Chandra High Energy Grating. ApJ, 604:63–73, March 2004. doi: 10.1086/381731.

B. Yencho, A. J. Barger, L. Trouille, and L. M. Winter. The OPTX Project. II. Hard X-Ray Luminosity Functions of Active Galactic Nuclei for z lsim 5. ApJ, 698:380–396, June 2009. doi: 10.1088/0004-637X/698/1/380.

D. G. York, J. Adelman, J. E. Anderson, Jr., S. F. Anderson, J. Annis, N. A. Bahcall, J. A. Bakken, R. Barkhouser, S. Bastian, E. Berman, W. N. Boroski, S. Bracker, C. Briegel, J. W. Briggs, J. Brinkmann, R. Brunner, S. Burles, L. Carey, M. A. Carr, F. J. Castander, B. Chen, P. L. Colestock, A. J. Connolly, J. H. Crocker, I. Csabai, P. C. Czarapata, J. E. Davis, M. Doi, T. Dombeck, D. Eisenstein, N. Ellman, B. R. Elms, M. L. Evans, X. Fan, G. R. Federwitz, L. Fiscelli, S. Friedman, J. A. Frieman, M. Fukugita, B. Gillespie, J. E. Gunn, V. K. Gurbani, E. de Haas, M. Haldeman, F. H. Harris, J. Hayes, T. M. Heckman, G. S. Hennessy, R. B. Hindsley, S. Holm, D. J. Holmgren, C.-h. Huang, C. Hull, D. Husby, S.-I. Ichikawa, T. Ichikawa, Ž. Ivezić, S. Kent, R. S. J. Kim, E. Kinney, M. Klaene, A. N. Kleinman, S. Kleinman, G. R. Knapp, J. Korienek, R. G. Kron, P. Z. Kunszt, D. Q. Lamb, B. Lee, R. F. Leger, S. Limmongkol, C. Lindenmeyer, D. C. Long, C. Loomis, J. Loveday, R. Lucinio, R. H. Lupton, B. MacKinnon, E. J. Mannery, P. M. Mantsch, B. Margon, P. McGehee, T. A. McKay, A. Meiksin, A. Merelli, D. G. Monet, J. A. Munn, V. K. Narayanan, T. Nash, E. Neilsen, R. Neswold, H. J. Newberg, R. C. Nichol, T. Nicinski, M. Nonino, N. Okada, S. Okamura, J. P. Ostriker, R. Owen, A. G. Pauls, J. Peoples, R. L. Peterson, D. Petravick, J. R. Pier, A. Pope, R. Pordes, A. Prosapio, R. Rechenmacher, T. R. Quinn, G. T. Richards, M. W. Richmond, C. H. Rivetta, C. M. Rockosi, K. Ruthmansdorfer, D. Sandford, D. J. Schlegel, D. P. Schneider, M. Sekiguchi, G. Sergey, K. Shimasaku, W. A. Siegmund, S. Smee, J. A. Smith, S. Snedden, R. Stone, C. Stoughton, M. A. Strauss, C. Stubbs, M. SubbaRao, A. S. Szalay, I. Szapudi, G. P. Szokoly, A. R. Thakar, C. Tremonti, D. L. Tucker, A. Uomoto, D. Vanden Berk, M. S. Vogeley, P. Waddell, S.-i. Wang, M. Watanabe, D. H. Weinberg, B. Yanny, N. Yasuda, and SDSS Collaboration. The Sloan Digital Sky Survey: Technical Summary. AJ, 120:1579–1587, September 2000. doi: 10.1086/301513.

Q. Yu and S. Tremaine. Observational constraints on growth of massive black holes. MNRAS, 335:965–976, October 2002. doi: 10.1046/j.1365-8711.2002.05532.x.

N. L. Zakamska, M. A. Strauss, J. H. Krolik, M. J. Collinge, P. B. Hall, L. Hao, T. M. Heckman, Ž. Ivezić, G. T. Richards, D. J. Schlegel, D. P. Schneider, I. Strateva, D. E. Vanden Berk, S. F. Anderson, and J. Brinkmann. Candidate Type II Quasars from the Sloan Digital Sky Survey. I. Selection and Optical Properties of a Sample at 0.3 $<$ z $<$ 0.83. AJ, 126:2125–2144, November 2003. doi: 10.1086/378610.

W. Zheng, G. A. Kriss, R. C. Telfer, J. P. Grimes, and A. F. Davidsen. A Composite HST Spectrum of Quasars. ApJ, 475:469, February 1997. doi: 10.1086/303560.

Publications

Mayo, J. H.; Vernet, J.; De Breuck, C.; Galametz, A.; Seymour, N.; Stern, D. *Overdensities of 24um Sources in the Vicinities of High-Redshift Radio Galaxies.* Astronomy & Astrophysics, 539, 33. **2012**.

Mayo; Jack. H., Lawrence, Andy. *The Effect of Partial Obscuration on the Luminosity Dependence of the Obscured Fraction in Active Galactic Nuclei.*. Monthly Notices of the Royal Astronomical Society. accepted. **2013**.

Mayo; Jack. H., et al. *Herschel-ATLAS Active Galactic Nuclei - Host Galaxy Characteristics and Population Statistics.*. in prep **2013**

Galametz, Audrey; Stern, Daniel; De Breuck, Carlos; Hatch, Nina; **Mayo, Jack**; Miley, George; Rettura, Alessandro; Seymour, Nick; Stanford, S. Adam; Vernet, Jol. *The Mid-infrared Environments of High-redshift Radio Galaxies.* Astrophysical Journal, 749, 159. **2012**.

Lawrence, Andy; Roseboom, Isaac; **Mayo, Jack**; Elvis, Martin; Shen, Yue; Hao, Heng; Petty, Sara. *The Distribution of AGN Covering Factors.* Proceedings of the Torus Workshop 2012 held at the University of Texas at San Antonio, 5-7 December. **2012**.